TECHNISCHE UNIVERSITÄT MÜNCHEN
Lehrstuhl für Physikalische Chemie

Kinetic and Mechanistic Studies of Methane Activation Mediated by Free Tantalum and Tantalum Oxide Clusters

Jan Frederik Eckhard

Vollständiger Abdruck der von der Fakultät für Chemie der Technischen Universität München zur Erlangung des akademischen Grades eines

Doktors der Naturwissenschaften

genehmigten Dissertation.

Vorsitzender:	Hon.-Prof. Dr. Richard W. Fischer
Prüfer der Dissertation:	1. Prof. Dr. Ulrich K. Heiz
	2. Prof. Dr. Klaus Köhler
	3. Prof. Dr. Helmut Schwarz

Die Dissertation wurde am 26.02.2018 bei der Technischen Universität München eingereicht und durch die Fakultät für Chemie am 09.04.2018 angenommen.

Abstract

Gas-phase clusters serve as model systems for active sites in catalytic processes. In this work, tantalum-based clusters are generated in a laser vaporization source, mass selected in a quadrupole mass filter, and exposed to reactive gases under multi-collision conditions in a cryogenic ring electrode ion trap. The reaction time is systematically varied and products of consecutive reactions are analyzed in a reflectron time-of-flight spectrometer. Subsequent modeling facilitates the kinetic and mechanistic characterization of reactions, which are focused on the C–H bond activation of methane. The effect of cluster size and the properties of tantalum cluster oxides with a specific number of oxygen atoms are special topics of this thesis.

Small cationic clusters comprising fewer than five tantalum atoms mediate the dehydrogenation of methane and concomitant elimination of dihydrogen, the reactivity decreases monotonically with cluster size, and the latter also determines the product composition. When exposed to oxygen, tantalum-methylene complexes release the equivalent of formaldehyde, and the size of the cluster core affects the selectivity of this C–O coupling process. In tantalum cluster oxides, oxygen atoms may act as ligands that alter the electronic structure and thus reduce C–H bond scission barriers in the reaction with methane. A radical oxygen atom in the stoichiometric tantalum dimer pentoxide cation mediates a direct hydrogen atom transfer from methane, and molecular adsorption in a parallel channel seemingly promote the formation of a Lewis acid-base pair, which subsequently also abstracts atomic hydrogen from a second methane molecule.

Zusammenfassung

Freie Cluster fungieren als Modellsysteme für aktive Zentren in katalytischen Vorgängen. In dieser Arbeit werden Cluster auf der Basis von Tantal in einer Laserverdampfungsquelle dargestellt, in einem Quadrupolmassenfilter selektiert, und unter Mehrstoß-Bedingungen in einer kryogenen Ringelektroden-Ionenfalle Reaktivgasen ausgesetzt. Die Reaktionszeit wird systematisch variiert und die Produkte von Folgereaktionen werden mithilfe eines Reflektron-Flugzeit-Massenspektrometers analysiert. Durch anschließende Modellierung werden die Reaktionen, deren Hauptaugenmerk auf der C–H-Bindungsaktivierung in Methan liegt, kinetisch und mechanistisch charakterisiert. Dabei sind der Einfluss der Clustergröße und die Eigenschaften der Tantalclusteroxide mit einer spezifischen Anzahl an Sauerstoffatomen von besonderem Interesse.

Kleine kationische Cluster mit weniger als fünf Tantalatomen ermöglichen die Dehydrierung von Methan unter Eliminierung eines Wasserstoffmoleküls. Die Reaktivität nimmt monoton mit der Clustergröße ab, und letztere bestimmt auch die Zusammensetzung der resultierenden Produkte. Tantal-Methylen-Komplexe setzen ein Formaldehydäquivalent frei, wenn sie Sauerstoff ausgesetzt werden, und die Größe des Clusterkerns beeinflusst die Selektivität dieses C–O-Kopplungsprozesses. In Tantalclusteroxiden können sich Sauerstoffatome wie Liganden verhalten, die die elektronische Struktur verändern und somit Barrieren der C–H-Bindungsspaltung verringern. In dem stöichiometrischen Ditantalpentoxidkation spaltet ein radikalisches Sauerstoffatom ein Wasserstoffatom aus einem Methanmolekül direkt ab, und in einer Parallelreaktion führt die molekulare Adsorption von Methan vermutlich zur Ausbildung eines Lewis-Base-Säure-Paares, das in einem zweiten Schritt ebenfalls atomaren Wasserstoff eines zweiten Methanmoleküls abspaltet.

CONTENTS

LIST OF FIGURES

LIST OF TABLES

INTRODUCTION 1

"I have learnt that all our theories are not Truth itself, but resting places or stages on the way to the conquest of Truth, and that we must be contented to have obtained for the strivers after Truth such a resting place which, if it is on a mountain, permits us to view the provinces already won and those still to be conquered."

— Justus von Liebig

Life is based upon the conversion of chemical energy; the most prominent examples ranging from photosynthesis in plants, which consumes carbon-dioxide, water and sunlight to produce glucose and oxygen [1], to the reduction of glucose as an integral part in the metabolism of animals [2]. Without the presence of a catalyst, these processes are greatly hindered and would not occur with significant rates. Per definition, a catalyst mediates a reaction by reducing the required activation energy without being consumed itself [3], and specific proteins, enzymes, perform this task in nature. Man-made catalysis has shaped today's society: specially designed catalysts enable the synthesis of fine chemicals [4], for example drugs, and artificial nitrogen fertilizers made it feasible to feed billions of people [5]. Nitrogen fertilizers are produced from ammonia, which is synthesized in the famous Haber-Bosch process. This important industrial procedure utilizes iron oxide- or ruthenium-based catalysts to fixate atmospheric nitrogen and react it with hydrogen at elevated pressure and temperature, resulting in the formation of ammonia [6]. Since its early conception by Fritz Haber in 1904, the Haber-Bosch process has been studied from a scientific point of view and continuously developed from an applied, technical approach [7]. These advances also benefited from fundamental investigations that elucidated the underlying mechanisms, where ground-breaking contributions by Gerhardt Ertl played a significant role [8, 9]. As a result, ammonia synthesis is one of the most well understood and heavily optimized catalytic processes, and the losses in thermodynamic efficiency of the overall procedure are mostly attributed to steam reforming of methane to obtain the required hydrogen [6, 10].

Methane makes up the largest share of natural gas and has traditionally been used to generate electricity and heat [11]. Nevertheless, the role of methane is not limited to an energy carrier or a source of hydrogen. Due to its high abundance in nature, methane is an ideal feedstock to be used as a molecular building block for the synthesis of value-added chemicals [12]. However, intrinsic molecular properties hamper the purposeful activation of methane, and the number of viable industrial processes to achieve this goal is limited. Over the last four decades, fundamental studies by the groups of Schwarz, Armentrout, He and others contributed significantly to the clarification of mechanisms for the activation of carbon-hydrogen bonds (see Ref. [13] and references therein). Moreover, continuous advances in technology facilitate the synthesis and characterization of designed catalysts and sophisticated materials that are structured on the nanoscale. Sub-nanometer metal clusters, for instance, demonstrate properties advantageous in catalysis, including a high surface-to-volume ratio and a reactivity tunable as a function of size [14–16]. Atom-precise metal clusters in the gas phase have furthermore been shown to serve as model systems in catalytic processes [17]. For example, natural photosynthesis systems that were mentioned in the beginning rely on a protein-bound Mn_4CaO_5 cluster (photosystem II) to convert water into oxygen. Fundamental effects therein were unraveled by investigating the reaction of free manganese oxide clusters and water [18–20]. This thesis aims to illuminate the reactions of metal clusters isolated in the gas phase as prototypical models of reactive centers in the activation of methane. The presented studies are conducted under well-defined conditions in order to obtain insights about cluster properties as well as mechanisms that are operative on the molecular level.

ACTIVATION OF METHANE 2

Methane, the smallest saturated hydrocarbon, is very stable (free enthalpy of formation of -50.8 kJmol^{-1}) [21, 22] and comprises four strong sp^3-hybridized C–H bonds (bond strength of 439 kJmol^{-1}) [21, 23]. Methane demonstrates a negligibly low, or even negative electron affinity [24–26], a very high ionization potential (12.6 eV [27] to 14.4 eV [25, 28] for an adiabatic and a vertical ionization, respectively), and a large HOMO/LUMO gap [21, 25]. These molecular properties render methane rather inert and turn the activation of C–H bonds into a challenging goal [13]. Additionally, products of partial methane oxidation, *e.g.* methanol or carbon monoxide, are kinetically more labile than the reactant alkane and consequently prone to thermodynamically favorable over-oxidation to CO_2 [29, 30]. In industry, methane is used as a feedstock primarily in the generation of syngas (CO/H_2) [29, 31], and secondarily in reactions with ammonia to yield hydrogen cyanide [32] or, more recently, in the conversion to methanesulfonic acid [33]. These heterogeneous processes (*i.e.* catalyst and reactants in different phases) will be briefly discussed in the following chapter and recent fundamental studies will be shown thereafter. This overview is partially based on the review publication "Methane activation: the past and future" [29].

2.1. Industrial processes

Steam reforming is a procedure that converts methane and water into carbon monoxide and dihydrogen (syngas) as illustrated in Equation 2.1. Highly dispersed Ni particles supported on metal oxides catalyze this endothermic reaction [31], which is industrially conducted at elevated temperatures (>1000 K) [29].

$$CH_4 + H_2O \rightleftharpoons CO + 3H_2 \tag{2.1}$$

Additionally, methane is partially oxidized in the presence of oxygen, also producing syngas, albeit with a lower H_2/CO ratio (see Eq. 2.2).

$$2CH_4 + O_2 \rightleftharpoons 2CO + 4H_2 \tag{2.2}$$

Employing the **water-gas shift reaction** [31] increases the hydrogen yield (Eq. 2.3). However, this reaction turns carbon monoxide into carbon dioxide, which is less available for further chemical transformations.

$$CO + H_2O \rightleftharpoons CO_2 + H_2 \tag{2.3}$$

Ni dispersed on metal oxide supports catalyzes **dry reforming** of methane. In this comproportionation reaction (shown in Eq. 2.4), methane and carbon dioxide are converted into carbon monoxide and dihydrogen.

$$CH_4 + CO_2 \rightleftharpoons 2CO + 2H_2 \tag{2.4}$$

Syngas obtained in these procedures may subsequently be utilized as a feed in the **Fischer-Tropsch process** in order to successively build up longer hydrocarbon chains under the use of a cobalt- or iron-based catalyst [29, 34].
Next to syngas, hydrogen cyanide is another valuable product industrially formed from methane. The reaction shown in Equation 2.5 occurs in the **Degussa process**, which is also known as the **BMA process** due to the involvement of hydrogen cyanide, methane and ammonia (in german: Blausäure, Methan and Ammoniak) [35–37].

$$CH_4 + NH_3 \rightarrow HCN + 3H_2 \tag{2.5}$$

In the Degussa process, platinum catalyzes the dehydrogenation of methane and the subsequent coupling to ammonia. The formation of HCN/H_2 (Eq. 2.5) is strongly endothermic ($\Delta_r H = 251$ kJmol^{-1}) [35]. Hydrogen cyanide is also produced by the **Andrussow process**, albeit under consumption of dioxygen and formation of water: [35, 37, 38]

$$2CH_4 + 2NH_3 + 3O_2 \rightarrow 2HCN + 6H_2O \tag{2.6}$$

The reaction depicted in Equation 2.6 is exothermic ($\Delta_r H = -481$ kJmol^{-1}) and similarly mediated by Pt catalysts. The Andrussow process, however, suffers from the formation of side products, CO and N_2 [35, 37, 38]. Lastly, the **sulfonation of methane** has gained interest and might become industrially viable. The transformation of methane into methane sulfonic acid (CH_3SO_3H) consumes SO_2

and O_2 and is catalyzed by Pd and Cu [33]. Alternatively, CH_4 and SO_3 also produce methane sulfonic acid in the presence of metal peroxides [39].

The industrial procedures summarized in this section demonstrate potential for optimization. The synthesis of longer-chained hydrocarbons *via* syngas production and subsequent Fischer-Tropsch reactions is a multi-step process, whereas the direct transformation of methane to methanol or ethane is potentially more efficient. Some of the previously mentioned industrial reactions are highly endothermic or are conducted under harsh conditions, resulting in high-operative costs, or suffer from the formation of side products. Consequently, the goal of many fundamental studies is to find efficient and selective routes for the transformation of methane, and a brief overview will be given in the next section.

2.2. Homo- and heterogeneous studies

An abundance of fundamental investigations focuses on metal oxide support materials decorated with reactive sites in order to study the activation of methane, *viz.* oxidative and non-oxidative coupling reactions as well as the direct methane-to-methanol conversion [29]. Due to the relevance for this thesis, the first part of this section showcases two supported Ta-based catalysts, whereas the second part highlights selected homogeneous systems.

Silica-supported Ta clusters (0.3-0.8 nm in diameter) catalyze the reaction of methane with *n*-butane: [40]

$$CH_4 + C_4H_{10} \rightarrow C_2H_6 + C_3H_8 \tag{2.7}$$

The product distribution is not limited to ethane and propane as *n*-butane additionally undergoes a disproportionation, yielding propane and pentane. While smaller Ta clusters demonstrate a higher turn-over frequency, clusters of all sizes lose their catalytic activity after 20 h of continuous reactions, which was attributed to oxidation of the particles [40].

Another coupling reaction is mediated by the silica-supported tantalum hydride [41, 42], namely the catalytic transformation of two methane molecules into ethane and dihydrogen as shown in Equation 2.8.

$$2CH_4 \rightarrow C_2H_6 + H_2 \tag{2.8}$$

The authors of the study identified a tantalum-methylidene-methyl intermediate to play a key role [41]. The catalytic process is characterized by a high selectivity

(98%) and activity for over 200 h, but demonstrates a low conversion of 0.05% at 300 K [29].

Heterogeneous systems also provide routes for the activation of methane [29, 43, 44]. A schematic catalytic cycle of the Shilov system [43] is shown in Figure 2.1. In the Shilov system, a Pt(II) complex reacts with methane to form a Pt(II)-CH_3 species, which is oxidized to a Pt(IV)-CH_3 intermediate that subsequently eliminates a functionalized methane derivate [44]. The drawbacks of this catalytic system are a low activity, decomposition due to side reactions and stoichiometric consumption of an oxidant [44]. Extensive efforts were undertaken by the Periana group to develop systems that overcome these issues [44]. These catalysts include Pd complexes to convert methane into acetic acid [45] and a Pt-based system, which is highly stable and less prone to overoxidation that typically leads to deactivation [46].

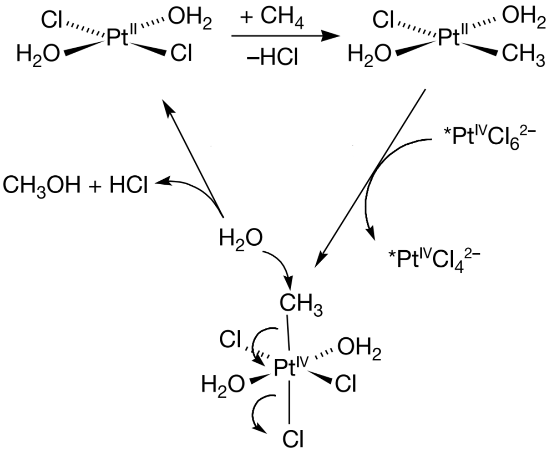

Figure 2.1: *Catalytic cycle for the functionalization of methane by a platinum complex (Shilov system) [43, 47]. Reproduced (adapted) by permission from Springer Nature: Springer, Nature, Reference [48], Copyright 2002.*

2.3. Gas-phase studies

The investigation of methane activation in the gas phase aims to uncover fundamental phenomena in order to identify molecular properties and mechanisms of general importance. The study of isolated gas-phase systems benefits from an easy characterization by mass-spectrometric techniques and the absence of many otherwise perturbing effects, for example solvation in homogeneous phases or interactions of the active center and the support material in heterogeneous catalysis. In addition, the restriction to a single reactive site rules out mass-transport phenomena and allows a theoretical treatment of the full system. Figure 2.2 illustrates the range of environmental parameters, structural complexity and pressure, from single crystals in vacuum to technical catalysis. The relevance of fundamental studies in the gas phase is under scrutiny due to low-pressure conditions and systems, which are more simplistic than industrial catalysts [17]. However, the complexity of free clusters (*e.g.*, geometric and electronic isomerism) is often underestimated, and the corresponding properties serve as descriptors for the reactivity of active centers on surfaces [49] or in enzymes [20]. Moreover, buffer gas employed in flow-tube and ion trap reactors acts as a "heat bath" and facilitates reactions at elevated pressure conditions, which bridges the so called "pressure gap" (see Fig. 2.2). Gas-phase clusters consequently represent ideal model systems for catalysis.

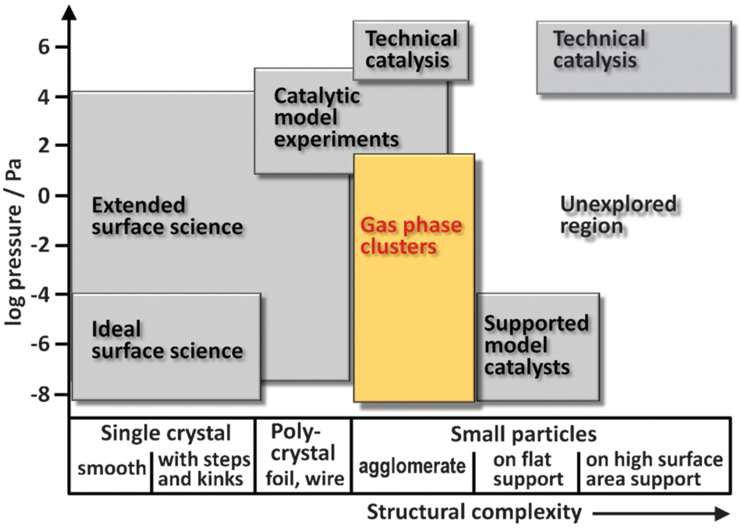

Figure 2.2: *Characteristics of different reaction environments. Technical catalysis employs complex materials and occurs at elevated pressures, whereas many fundamental studies are conducted at ultra-high vacuum (UHV) conditions. The structural complexity of isolated clusters lies between highly periodic single crystals and particles on a disordered support material. Gas-phase reactions are studied under single-collision conditions (UHV) or under multi-collision conditions through the use of buffer gas, thereby closing the "pressure gap". Reproduced from Ref. [17] with permission from the PCCP Owner Societies.*

The following section discusses general reaction mechanisms in the activation of methane by metallic systems in the gas phase. Specific insights from previous findings in literature are furthermore available in the introduction of each chapter that discusses experimental results. Major parts of this brief overview are based on two comprehensive review publications by Helmut Schwarz, "Chemistry with Methane: Concepts Rather than Recipes" [12] and "How and Why Do Cluster Size, Charge State, and Ligands Affect the Course of Metal-Mediated Gas-Phase Activation of Methane?" [13], and on results of his group, who elucidated many previously unidentified effects.
Gas-phase metal and metal oxide systems demonstrate three principal mechanisms in the reaction with methane:

(1) metal-mediated dehydrogenation and concurrent dihydrogen elimination,

(2) transfer of atomic hydrogen to a metal oxide system and

(3) a direct conversion of methane to methanol or formaldehyde.

These mechanisms are schematically illustrated in Figure 2.3. During the reaction with methane, transition metal atoms may insert into C–H bonds, causing the formation of H–[M]–CH_3 species. When two C–H bonds are cleaved in this manner and the hydrogen atoms recombine, this process leads to the **elimination of dihydrogen** and generation of a metal-methylidene species. This **dehydrogenation** reaction is one of the methane activation mechanisms shown in Figure 2.3 (marked

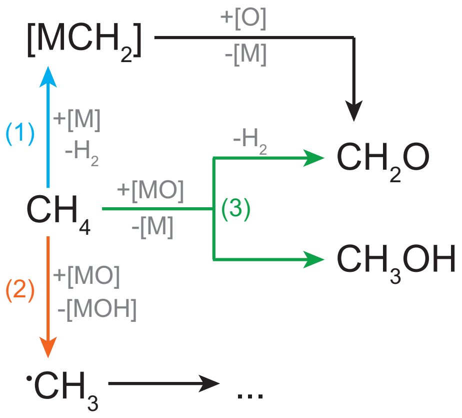

Figure 2.3: *Reactivity modes in the activation of methane involving free metal [M] and metal oxide [MO] systems as well as oxidants [O]. Reproduced (adapted) from Reference [12]. Copyright © WILEY-VCH Verlag GmbH & Co. KGaA, Weinheim.*

by 1). Coupling the methylidene group of the [M]CH_2 species to a substrate in a subsequent step may generate value-added products, for example formaldehyde or hydrogen cyanide.[1] The metal-methylidene bond strength has to be larger than the methane dehydrogenation enthalpy ($\Delta_r H\,(CH_4 \rightarrow CH_2 + H_2) = 464$ kJmol^{-1}) for an exothermic energy balance [12]. Accordingly, this reaction only occurs for a limited number of elements. The group of Diethard Böhme exposed monoatomic cations of many elements to CH_4 in a flow-tube reactor and analyzed the reaction products [53]. The largest share of cations does not react with methane or adsorbs the molecule in absence of H_2 elimination. Five of the seven atomic cations that bring about dehydrogenation are concentrated in the 5d row (Ta^+, W^+, Os^+, Ir^+ and Pt^+) due to relativistic effects. The 6s orbital of these cations is stabilized and close in energy to the 5d orbital, which facilitates the formation of very strong M–CH_2 bonds [12, 54–56]. The group of Peter Armentrout obtained thermochemical information about the reactions of many cationic atoms and clusters in a guided ion beam experiment that also allows the investigation of very endothermic reactions [56–59]. Their data illustrates the effect of orbital stabilization: the metal-methylidene bond strengths are 335, 428 and 464 kJmol^{-1} for the homologous vanadium [60], niobium [61] and tantalum cation [62], respectively. While Au^+ does not mediate methane dehydrogenation under experimental conditions employed by Böhme and co-workers [53], the cationic gold dimer is very reactive as observed in ion trap studies by the group of Thorsten Bernhardt [63]. In the reaction with methane, the actual catalyst $[Au_2\,(CH_4)]^+$ is formed. At temperatures above 250 K, the reaction with a second CH_4 molecules enables the formation of an ethylene unit and concomitant H_2 elimination *via* cooperative co-adsorption. The adsorption of a third molecule triggers the release of the ethylene molecule and this step was found to be rate-limiting [64]. Lower temperatures facilitate the adsorption of O_2 to the $[Au_2\,(CH_4)_2]^+$ intermediate, which leads to the ejection of formaldehyde and regeneration of $[Au_2\,(CH_4)]^+$. The cationic gold dimer subsequently represents a highly selective catalyst that mediates coupling or partial oxidation of methane as a function of temperature [65]. H_2 elimination is also mediated by clusters of other elements. The previous studies of Armentrout and co-workers demonstrated endothermic methane dehydrogenation reactions of Fe [57], Ni[58] and Co [59] cluster cations. For near-room temperature

---

[1] Elementary steps in the Degussa process were identified with the insights obtained from coupling reactions of $[PtCH_2]^+$ [50–52].

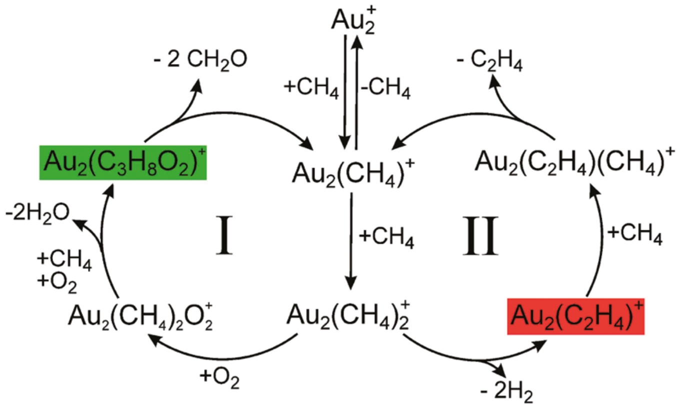

Figure 2.4: *Catalytic cycles in the reaction of the cationic gold dimer with methane and oxygen. Below 250 K, formaldehyde is mainly produced and ethylene is predominantly formed at higher temperatures. Reprinted (adapted) with permission from [63]. Copyright 2011 American Chemical Society.*

conditions (and single-element species), however, methane dehydrogenation is limited to a few noble metal clusters in addition to the gold dimer. Platinum clusters were heavily studied by the groups of Cox and Kaldor [66], Beyer and Bondybey [67–69], Adlhart and Uggerud [70, 71], and Schwarz [72–74]. Methane dehydrogenation by cationic Rh clusters was observed by the group of Beyer and Bondybey [75]; Pd clusters were studied by Lang and Bernhardt [65, 76], who also worked on binary AuPd clusters [64, 77], whereas binary AuPt clusters were examined by Schwarz and co-workers [74].

Many more gas-phase systems **abstract atomic hydrogen** from methane [78]. In this process, metal oxides induce a C–H bond cleavage and a methyl radical is released (reaction marked by 2 in Fig. 2.3). The abstraction of atomic hydrogen can furthermore be categorized in a proton-coupled electron transfer (PCET) mechanism and a direct hydrogen atom transfer (HAT) mechanism [78–80]. The groups of Helmut Schwarz [78–85] and Sheng-Gui He [86–93] obtained extensive insights of these mechanisms. HAT reactions are characterized by a high unpaired spin density, *i.e.* the presence of a radical oxygen center that readily accepts a hydrogen radical from methane [78]. Terminal oxygen atoms with unpaired spin are typically present in stoichiometric metal oxide cations (for example $(M_2O_5)^+_{1,2}$, M = V, Nb, Ta) [87, 91], and detailed mechanistic results were unraveled in a combined experimental and theoretical study of $[V_4O_{10}]^+$ [81]. On the other hand, a PCET mechanism leads to abstraction of atomic hydrogen when a Lewis acid-base pair is present, *e.g.* in the reaction of $[Al_2O_2]^{\bullet+}$ with methane. In this reaction, a bridging O atom acts as a Lewis base to accept a proton from CH_4 and the CH_3^- fragment (including the electron pair from the heterolytically cleaved C–H bond) binds to a Lewis acidic Al atom [79].

The **direct transformation of methane** to methanol or formaldehyde is the ultimate goal in methane activation and has been observed for several gas-phase systems [12, 94–98] (process 3 in Fig. 2.3). When the diatomic iron oxide cation, FeO^+, is exposed to CH_4, methanol and Fe^+ are primarily formed [12]. This reaction was extensively studied by experimental [95, 96] and theoretical means [99] due to its exemplary nature for an intricate two-state reactivity (TSR) scenario [12]. In the course of the reaction, the $[FeO\,(CH_4)]^+$ adsorption complex crosses from the sextet ground state into the quartet spin state, which is facilitated by spin-orbit mediated coupling [12]. Thus, high-energy transition states (in excess of endothermicity) of the sextet state are circumvented and the reaction becomes accelerated. TSR mechanisms are operative in many more reactions, *e.g.* methanol formation from $[CuO]^+/CH_4$ [97], ligand exchange in $[NiH]^+/CH_4$ [100] and dihydrogen elimination in Ta^+/CH_4 [62]. Lastly, a platinum aliminum oxide anion $[PtAl_2O_4]^-$ directly converts methane to formaldehyde (forming $[PtAl_2O_3H_2]^-$) [101]. This cluster system serves as an interesting model for atoms deposited on metal oxide surfaces: the Pt atom is almost neutral and performs the initial activation of the C–H bond, whereas oxygen and aluminum atoms act as a "support" [101].

In summary, gas-phase studies of model systems are helpful to illuminate reaction mechanisms that govern the activation of C–H bonds. Relativistic effects, radical centers and spin cross-over play important roles in the activation of methane by active sites composed of transition metals and metal oxides. Tantalum clusters and the corresponding oxides are promising candidates to mediate CH_4 activation that have yet to be fully explored.

EXPERIMENTAL SETUP AND METHODOLOGY

3

> *"We must trust to nothing but facts: these are presented to us by nature and cannot deceive. We ought, in every instance, to submit our reasoning to the test of experiment, and never to search for truth but by the natural road of experiment and observation."*
>
> — Antoine Lavoisier

The experimental apparatus consists of four main components: a laser vaporization cluster source, a quadrupole mass filter (QMF), a ring electrode ion trap (RET) and a reflectron time-of-flight mass spectrometer (ReTOF-MS) as illustrated in Figure 3.1. A list of pumps used for the evacuation of the chambers is provided in the Appendix (see Tab. A.1). Similarly, Table A.2 supplies all carrier, buffer and reactive gases employed in the experiments. This section serves as an overview, which is followed by a description of the main components and the experimental methodology.

In brief, a pulsed vaporization laser (100 Hz, 532 nm, Innolas Spitlight DPSS) creates a plasma plume on the metal disk located in the cluster source. A pulse of helium carrier gas (He 5.0, Westfalen) cools the metal plasma and the resulting conglomerate of metal particles and carrier gas undergoes a directed expansion into the vacuum chamber, thereby generating a beam of clusters. Several ion-guiding elements (einzel lenses, quadrupole bender) create electrostatic potentials to transfer the charged portion of the cluster beam into a quadrupole mass filter (Model 5221, Extrel). A combination of radio-frequency (RF) and constant (direct current, DC) potentials applied to the QMF rods guide ions of a previously specified mass and suppress the others. Subsequently, the mass-selected ions are transferred into the home-built RET, which is typically filled with 0.77 Pa of helium buffer gas. RF potentials on the ring electrodes provide radial confinement, whereas additional DC potentials on the outer electrodes enable an axial confinement of the charged particles. When the ions initially enter the trap, many collisions with the He buffer gas atoms disperse their excess kinetic energy. At 0.77 Pa, each thermalized ion undergoes approximately 100 collisions with a He atom per millisecond. High-energy ions undergo more collisions when the ion beam is initially collected, and trapped ions are consequently in constant thermal equilibration with the buffer gas. After a specified storage time, a DC gradient on the ring electrode assembly ejects the ions into a home-built, Wiley-McLaren-type time-of-flight mass spectrometer with a reflectron stage. Therein, a high-voltage DC pulse accelerates all ions to the same kinetic energy and onto a micro-channel plate (MCP) detector, which amplifies the measured signal. Ions are therefore separated based on an arrival time (of flight) as a function of the mass-to-charge ratio (m/z). An oscilloscope (triggered at the same time as the acceleration potential) subsequently records the MCP signal. When reactive gas in addition to the buffer gas (see Chapter A.3) is introduced into the RET, collisions with the stored ions generate reaction products in consecutive steps. Through systematic variation of the storage time, the progression of the reaction is followed based on the change of ion abundances. Kinetic modeling is employed to mimic the progression of the reaction, which enables the determination of reactions schemes and rate coefficients associated with each step.

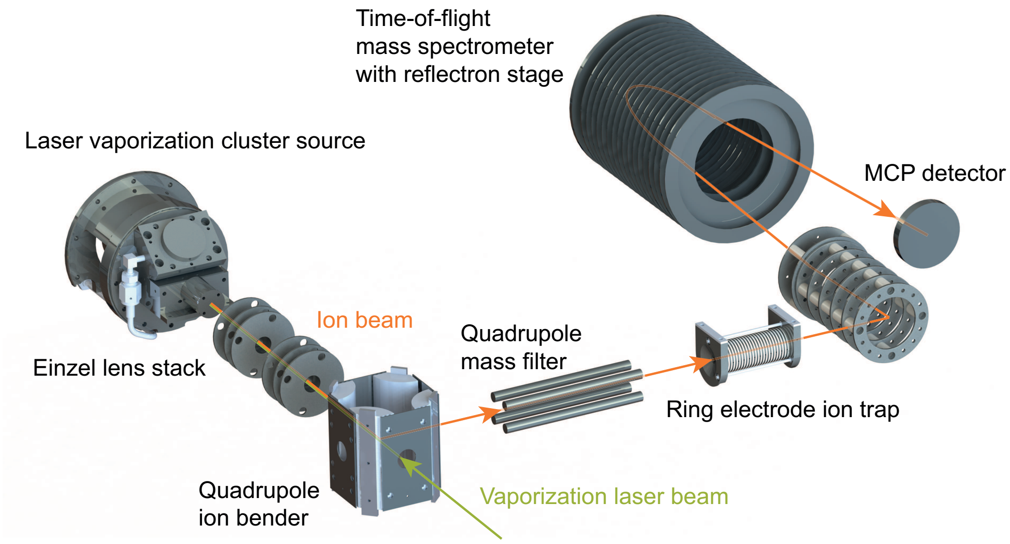

Figure 3.1: *Rendering of the experimental apparatus. For the sake of clarity, the illustration neglects many einzel lens stacks (exemplarily shown between the cluster source and the ion bender), and displays shortened distances between the main components of the setup.*

3.1. Generation of mass-selected metal clusters

Details on the laser vaporization source are available in previous publications, *e.g.* reference [102] and further publications cited therein, and this section summarizes the general working principle as well as the operation with a quadrupole mass filter. In the cluster source, the constant rotation and translation of a metal target disc (50 mm in diameter, tantalum for the following studies) in a hypocycloidal motion exposes a different surface spot for each irradiation pulse of the high-intensity vaporization laser (~60-120 mJ, ~10 ns pulse width). The laser pulse initially vaporizes atoms and ablates particles from the metal surface and subsequently causes the formation of a plasma plume in the so-called "waiting room" of the source, which contains neutral, anionic and cationic atoms and particles. A home-built piezo valve introduces helium carrier gas (stagnation pressure of ~8 bar) with a variable pulse width (typically between 300 and 450 μs). The helium gas pulse removes energy from the metal plasma and induces an agglomeration of the atoms to form clusters of all charge states, $M_n^{-/0/+}$ (with the metal M and the number of atoms per cluster n). The variation of laser pulse energy and carrier gas pulse width enable a tuning of the cluster size distribution, and a wide size range ($n \approx 1 - 100$) is accessible [102]. Due to a significant pressure difference in the cluster source and the vacuum chamber, the helium gas/clusters mixture is carried into the expansion channel of the source nozzle. In there, many more collisions between clusters and carrier gas occur. The small orifice of the expansion channel in conjunction with the pressure gradient cause a directed, supersonic expansion of the clusters into the vacuum chamber. Collisional cooling during the adiabatic expansion process removes vibronic energy from the clusters, and the internal energy of the clusters is consequently expected to be below room temperature [103, 104]. The resulting cluster beam furthermore passes a skimmer, thereby selecting the central portion of the beam, which contains clusters with less kinetic energy perpendicular to the direction of expansion. The skimmer additionally functions as an aperture that facilitates differential pumping of the cluster source chamber in order to maintain high-vacuum conditions in the adjacent section of the apparatus. A high pressure is generally detrimental to the guiding of ions and also hampers mass-spectrometric techniques. To avoid the presence of He carrier gas from the cluster source or He buffer gas from the RET in the other chambers, cluster source, quadrupole bender, QMF, RET and ReTOF-MS chambers are connected *via* apertures.

The **quadrupole bender** is composed of four quarter-circle based cylinders and a positive potential (or ground) is applied to one diagonal pair, while a negative potential is applied to the other pair of cylinders. As a result, the ion bender redirects the cluster beam from the initial trajectory and steers the ions into the quadrupole mass filter. The **quadrupole mass filter** consists of four rods that are addressed as diagonal pairs. An alternating potential is applied at a frequency of 440 kHz with opposite phases for the two pairs. Without any DC potential in the so called "RF only mode", the QMF transmits all ions within a certain m/z range and the mass-to-charge ratio with maximum transmission is a function of the RF amplitude. When a certain mass is selected in the QMF software (Merlin Automation Data System, Extrel), the corresponding RF amplitude is applied to the rods. With additional DC potential on the rods, ions in a much smaller mass range are transmitted according to the region of stability as described by Mathieu's equation [105, 106]. The combination of RF and DC potentials puts ions of smaller or larger mass-to-charge ratios onto a trajectory that collides them with the rods or the QMF housing. High RF amplitudes typically form a low-mass filter, whereas low DC potentials suppress high-mass ions. As a result, only ions

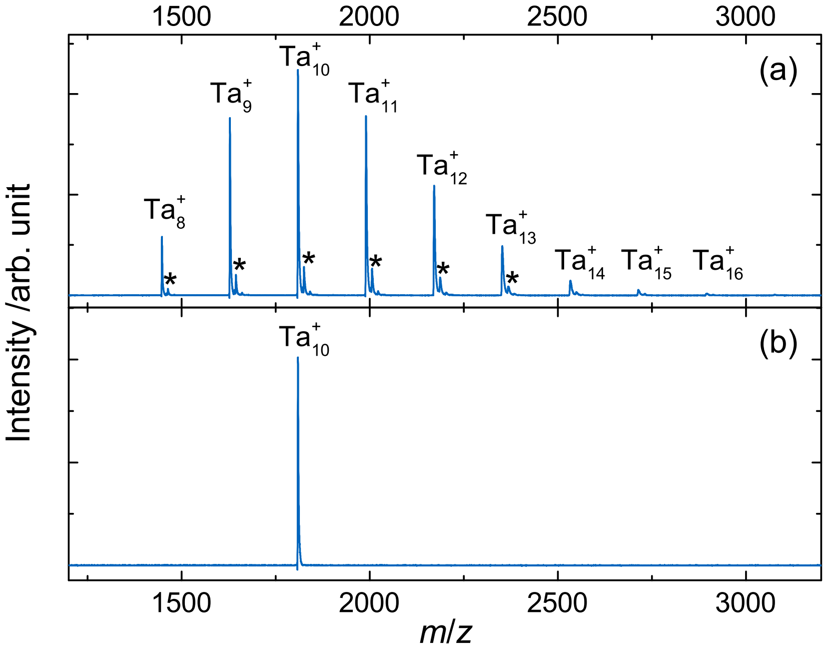

Figure 3.2: *Time-of-flight mass spectra with experimental parameters optimized around* Ta_{10}^+*. Ions are guided to the ReTOF-MS in absence of mass selection (a) and filtering by the QMF solely transmits* Ta_{10}^+ *(b). Cluster monoxides are marked by asterisks.*

with a previously chosen mass-to-charge ratio reach the exit lens of the QMF. A typical size distribution of cationic tantalum clusters is depicted in Figure 3.2a. As the abundance of multiply charged species is negligible, m/z will be used as a direct indicator of m and the two terms are used synonymously. Note that the relative cluster intensity does not correspond to the natural size distribution. Each ion-guiding element (einzel lenses, ion bender, QMF) uses mass-dependent potentials that affect the intensity shown in Figure 3.2a. Experimental parameters were optimized for the generation and transmission of Ta_{10}^{+} (m = 1810 u)[1] to obtain these mass spectra. Each cluster is accompanied by a minor species that correspond to a relative mass shift of 16 u, *i.e.* small amounts of cluster monoxides are additionally formed. Residual air in the piezo valve gas line causes the formation of oxide species and typically vanishes as the gas line is flushed with the helium carrier gas. More importantly, mass selection with the QMF suppresses every ion except the Ta_{10}^{+} species of interest (see Fig. 3.2b). As shown in Chapter 6, the mass selection of minority species, *e.g.* monoxides in presence of the bare clusters, is similarly feasible.

Thus, the combination of a laser vaporization cluster source and a quadrupole mass filter allows the study of single, atom-precise clusters in a wide size range. Additional modifications to the laser vaporization source (discussed in Chapter 4.3) enable the generation of chemically modified clusters, which are subsequently investigated in Chapters 6 and 8.

3.2. Time-of-flight mass spectrometry

Multipole and ring electrode ion traps are typically coupled with quadrupole mass spectrometers (combination of QMF and ion detector) or time-of-flight mass spectrometers. Reactivity experiments in ion traps produce ion bunches, *i.e.* charged species are stored for a specified time and extracted as a cloud of ions with different masses, and each experiment is repeated several times to obtain a temporal resolution of the reaction. With a quadrupole mass spectrometer, ion masses are probed in a scanning fashion, *i.e.* one mass at a time, and each temporal data point has to be scanned several times for the determination of all present masses. In contrast, time-of-flight mass spectrometers are operated in a pulsed mode. Ideally, an ion cloud is extracted from the ion trap and transferred as a

---

[1] The mass is typically given in unified atomic mass units, 1 u $\approx 1.66 \cdot 10^{-27}$ kg.

whole into the acceleration stage of the TOF-MS, thereby analyzing all charged species at the same time.[2]

In a two-stage TOF-MS, ions enter between the so called repeller (REP) and extractor plate (EXT) and are orthogonally accelerated to pass into a field-free drift region. To do so, a pulsed high-voltage potential U is applied to the repeller and extractor plate (with up to 5000 V and $U_{REP} > U_{EXT}$). This potential energy translates into kinetic energy of the ions E_{kin}, which is a function of the charge q and the mass m: [108–110]

$$E_{kin} = qU = \frac{1}{2}mv^2 \tag{3.1}$$

with q being a multiple z of the elementary charge e. The ions subsequently leave the acceleration stage, enter a field-free drift region and eventually collide with a detector. In a simplified model, the time t between acceleration and detection is a function of the distance to the detector x and the velocity v. The resulting expression for the time of flight and ion mass is shown in the following equation:

$$t = \frac{x}{v} = x\sqrt{\frac{m}{2qU}} \Leftrightarrow m = t^2 x^2 2qU \tag{3.2}$$

At the same kinetic energy, heavier ion posses a smaller velocity than lighter ions, *i.e.* smaller masses equal shorter times of flight. However, uncertainties affect the time of flight and two effects will be briefly discussed in the following, whereas a more detailed analysis is provided in literature [108–110]. Ions may be closer to the repeller plate or closer to the extractor plate due to a finite spatial distribution of the ion cloud. Ions in proximity to the repeller plate will obtain a higher final velocity than those further away, which will result in different times of flight for ions of the same mass (peak broadening). On the other hand, former ions need to travel a longer distance to the detector. At some point in space, the enhanced velocity and increased travel distance cancel each other out, as depicted in Figure 3.3a. In a two-stage TOF-MS, this so called space focus is manipulated with the acceleration potentials and is ideally projected onto the detector. Low acceleration potentials mitigate the effect of spatial ion distribution on the uncertainty in the time of flight and additionally increase the time resolution (the temporal spacing of ions arriving at the detector increases). Ions may furthermore posses

---

[2] The extraction process can cause a temporal separation of ions as a function of mass [107]. Especially for ions of significantly different relative masses (*e.g.*, different cluster sizes), this requires the repetition of a reactivity measurement for a few temporal delays between extraction and acceleration of the ions.

an initial velocity distribution in the acceleration trajectory, and the resulting uncertainty is reduced through the use of large acceleration potentials [108–110]. However, larger acceleration potentials decrease the temporal resolution and enhance the effects of spatial distribution. In order to overcome this issue, an ion reflector may be used to modify the ion trajectory, as depicted in Figure 3.3b. With a reflectron setup, the travel distance of ions in the field-free drift region is significantly increased, enabling the use of larger acceleration potentials. A reflectron also compensates the energy distribution of ions: high-velocity ions penetrate deeper into the reflecting field, thereby increasing the travel distance, and the

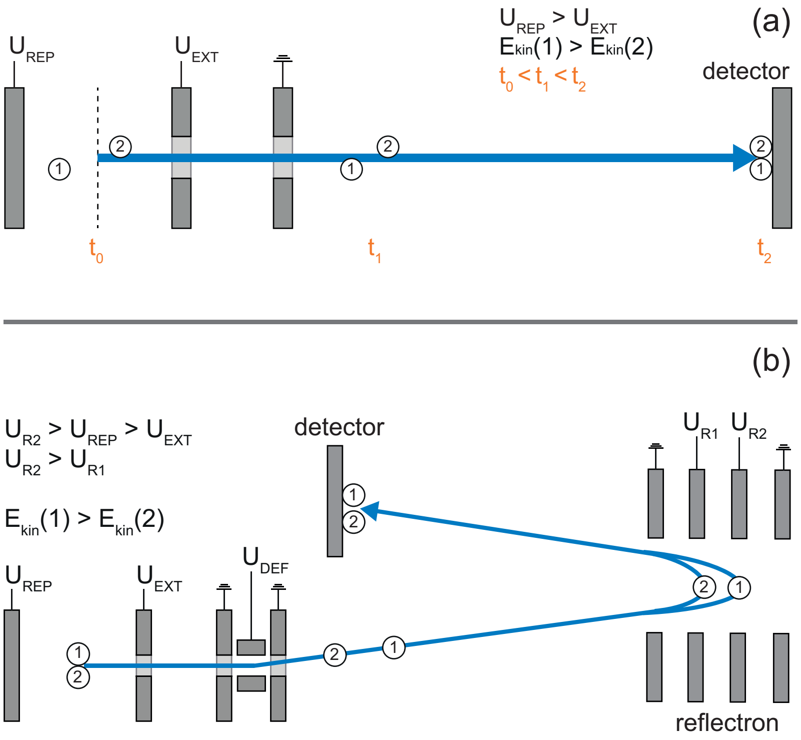

Figure 3.3: *Schematic illustration of a linear two-stage TOF-MS (a). Due to the potential gradient between the acceleration plates and a spatial distribution, ions of the same mass (marked by 1 and 2) obtain different kinetic energies (t_0). At the space focus (depicted to be identical with the detector position, t_2), ions with shorter travel distances and smaller velocities (2) arrive simultaneously to high-velocity ions with longer travel distances (1). The retardation potential in a reflectron setup (b) compensates the energy distribution of ions. Ions with a naturally high velocity in the acceleration direction (1) travel further in the ion reflector and the increased travel distance causes a time of flight coinciding with ions of the same mass and a smaller initial velocity (2). Reproduced (adapted) from Reference [108]. Copyright 1992 Elsevier.*

times of flight for high-energy and low-energy ions are equalized (see Fig. 3.3b). Through careful optimization of acceleration and reflecting potentials, a mass resolution ($R = m/\Delta m = t/2\Delta t$) of 2000 is routinely achieved during operation of the RET, *i.e.* under introduction of buffer gas [107].

This mass resolution would allow, for example, the discrimination of Ta_{10}^{+} from $[\mathrm{Ta}_{10}\mathrm{H}]^{+}$ and will be required to investigate hydrocarbon moieties attached to metal clusters. The pulsed operation mode furthermore enables the simultaneous determination of many products that could stem from consecutive parallel reactions. A reflectron time-of-flight mass spectrometer accordingly represents a powerful and time-efficient tool to analyze the charged products from chemical reactions under multi-collision conditions in an ion trap.

3.3. Design and operation of the ring electrode ion trap

This section focuses on important characteristics of the cryogenic ring electrode ion trap, whereas a previous publication, "Using controlled ion extraction to combine a ring electrode trap with a reflectron time-of-flight mass spectrometer" by D. Neuwirth and myself, gives detailed insights into the electronics unit that drives the trap and specifics on the RET itself [107]. The home-built ring electrode ion trap is based on a design, which was originally conceived by Dieter Gerlich [111] and was developed further by the group of Knut Asmis [112]. In the trap, two larger outer electrodes house a stack of concentric ring electrodes made out of molybdenum that are separated by sapphire rings (see Fig. 3.4). Compared to "open" multipole traps, this relatively **gas-tight design** facilitates the introduction of high-pressure buffer gas. Another distinction lies in the application of the radio-frequency (RF) potentials to store ions. Typically, power supply and electrodes form an oscillating (LC) circuit when sinusoidal RF potentials are applied [111]. As a result, such an assembly is usually driven at a fixed frequency and the RF amplitude is adapted to enable the storage of ions over a wider mass range, which is accompanied by significant power dissipation. **Square-wave RF potentials** circumvent the formation of an oscillating circuit (see Fig. 3.4) [107]. This consequently enables the use of variable RF amplitudes and frequencies, thereby facilitating the storage of ions over a very **wide mass range**, *e.g.* up to Ta_{90}^{+} (m = 16290 u) [107].

Moreover, the ring electrodes are individually connected to a home-built electronics unit and adjacent electrodes have alternating phases with respect to the RF voltage, *i.e* a positive RF voltage is applied to even-numbered electrodes when a negative RF voltage is applied to odd-numbered electrodes and vice versa. Figure 3.4 (top right) illustrates the alternating RF voltage on a single electrode. Additionally, a DC voltage offset may be superimposed onto the RF voltage (also shown in Fig. 3.4, top right). A specific DC amplitude may be used for each ring electrode. During collection and storage of ions, for example, a DC potential is applied to the outer "entrance" electrode and a larger potential is applied to the outer "exit" electrode, whereas the ring electrodes remain grounded (see Fig. 3.4, bottom right). As a result, high-velocity ions pass the entrance electrode potential

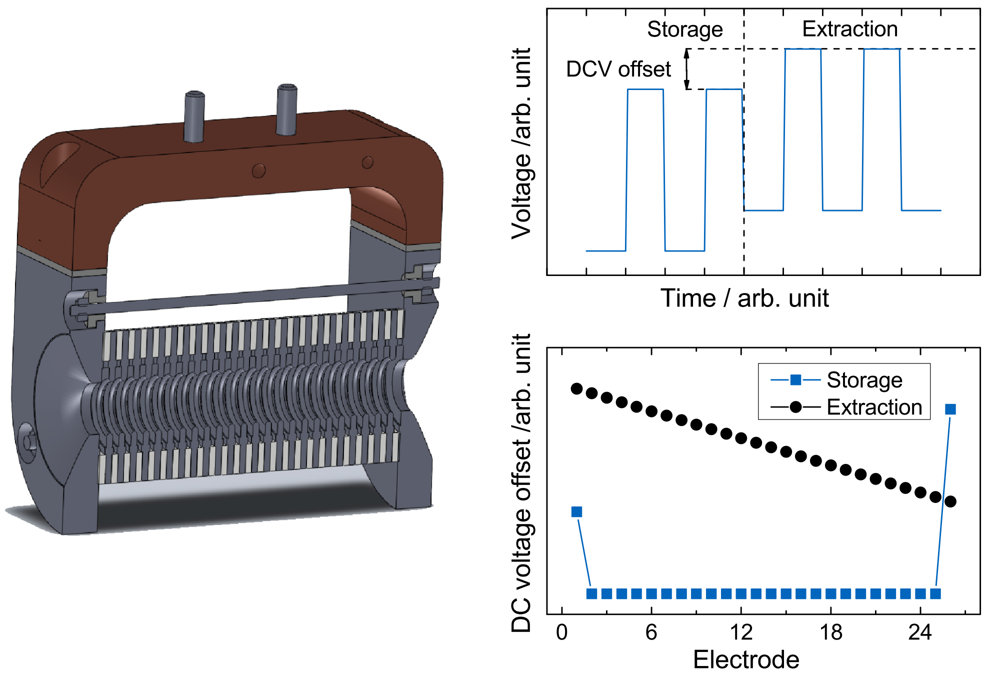

Figure 3.4: *Rendering of the ring electrode ion trap (left), voltage applied to a single electrode as a function of time (top right) and DC voltage offset applied to all electrodes during ion storage and extraction (bottom right). The RET consists of 24 circular electrodes plus two larger outer electrodes, which are individually addressed. The RF voltage alternates with a specified, variable frequency and amplitude. A DC voltage may be added to the outer electrodes in order to confine the ions, or to all electrodes in order to achieve a potential gradient that ejects the ions. Reprinted (adapted) from Ref. [107], Copyright (2015), with permission from Elsevier.*

and are repelled by the exit electrode potential. Collisions with buffer gas atoms in the meanwhile remove the excess kinetic energy of the ions, and they are thus also reflected by the entrance electrode potential. The RF potential on the ring electrodes therefore provides a radial confinement, while the DC potential on the outer electrodes repulses in axial direction. On the other hand, a linear DC voltage gradient is applied in axial direction in order to bring about a **controlled extraction**. Ideally, ions closer to the entrance electrode receive slightly more kinetic energy upon extraction than ions in proximity of the exit electrode, thereby creating an ion bunch that arrives simultaneously at the acceleration stage of the ReTOF-MS [107]. As a result of the efficient ion extraction, mass-selected ions produced by a single pulse of the (100 Hz) vaporization laser are collected and stored: accumulation of ions over a long period of time is unnecessary and the collection of a single ion beam within a few milliseconds produces high signal intensities upon detection.

The outer electrodes of the RET are mounted to a copper block (the cold head of a closed-circuit helium cryostat, RW2 by Leybold), and the electrode assembly is surrounded by a copper shield to reduce heating through black-body radiation. As a result, cooling the RET down to low temperatures is feasible, and a resistive heating cartridge in the copper block may heat the components to a constant, specified **temperature between 20 and 325 K**. The temperature of the copper block and one of the outer electrodes is probed by cryogenic temperature sensors (Cernox, Lake Shore Cryotronics), which are connected to a controller (Model 335 Cryogenic Temperature Controller, Lake Shore Cryotronics) that also provides the heating current.

A Teflon capillary connects a channel in one of the center ring electrodes to a mass flow controller with a variable flow rate (model 179C, MKS), typically set to 35 sccm, thereby facilitating a constant pressure of 0.77 Pa in the RET (monitored by a baratron model 722B, MKS, $1 \cdot 10^{-5}$–1 mbar range). The mass flow controller is in turn connected to a gas reservoir. The gas reservoir is contained within a home-built UHV chamber for gas-mixing purposes, that produces **clean gas mixtures with high dilutions** of reactive gas in helium buffer gas (He 6.0, Westfalen). Gas compositions are determined by absolute pressure measurements in the gas-mixing chamber and evaluated by a residual gas analyzer (RGA200, SRS), as is shown in Chapter A.3.

In conclusion, employing a ring electrode ion trap driven by square-wave RF potentials enables the efficient storage of ions over a wide mass range. A controlled collection and extraction of ions circumvents long accumulation times. Moreover, coupling the ion trap with a helium cryostat and a gas-mixing chamber facilitates the study of reactions at variable temperatures and reactive gas concentrations. The presented apparatus therefore demonstrates characteristics ideally suited for the investigation of ion-molecule reactions under multi-collision conditions.

3.4. Evaluation of ion-molecule reactions

As ion-molecule reactions are studied in this thesis, the conceptual description of these reactions is discussed in this chapter. Principal reactions kinetics, energy transfer mechanisms and interpretations of experimental data are included in the following.

3.4.1. Kinetic modeling

Simple reaction kinetics will be illustrated on a bimolecular association reaction of a metal cluster M_n and a reactant gas X in equal amounts:

$$M_n + X \rightarrow M_nX \tag{3.3}$$

The reaction rate r to form the product M_nX is defined as the change in cluster $[M_n]$ or reactant gas concentration $[X]$ as a function of time t [113]. This reaction rate is moreover proportional to product of the reactant (cluster and gas) concentrations: [113]

$$r = -\frac{d\,[M_n]}{dt} = -\frac{d\,[X]}{dt} = k\,[M_n]\,[X] \tag{3.4}$$

The proportionality factor in Equation 3.4 is the rate coefficient k, which is characteristic for a reaction. As two reactant particles are involved, the reaction depicted in Equation 3.3 is generally of second order. However, an approximation is used for the evaluation of reactions in the ion trap. A constant stream of reactant gas is supplied to the ion trap and the corresponding density exceeds the cluster density by several orders of magnitude (see Chapter A.3). The reactant gas concentration is therefore approximated to be constant [114, 115] and another rate coefficient is introduced:

$$k' = k\,[X] \tag{3.5}$$

This approximation reduces the order of the reaction, *i.e.* k' is a pseudo-first order rate coefficient, and simplifies the expression for the reaction rate:

$$r = -\frac{d\,[M_n]}{dt} = k'\,[M_n] \tag{3.6}$$

The differential equation depicted above is subsequently integrated to obtain the concentration of a cluster at a specific reaction time $[M_n]_t$ as a function of the initial concentration $[M_n]_{t=0}$ [113].

$$\int \frac{1}{[M_n]} d\,[M_n] = \int -k' dt \tag{3.7}$$

$$ln \frac{[M_n]_t}{[M_n]_{t=0}} = -k' t \tag{3.8}$$

$$[M_n]_t = [M_n]_{t=0} \cdot e^{-k' t} \tag{3.9}$$

Experimentally, tracking the relative abundance of a cluster species during the reaction reveals the associated rate coefficient. For such a simple reaction, the rate coefficient corresponds to the slope in a plot of the logarithmic cluster abundances as a function of reaction time. For more complicated reactions, *e.g.* involving subsequent steps or parallel reactions, a set of interdependent differential equations describes the concentration of participating species and has to be solved in order to obtain the rate coefficients. At a certain degree of complexity, the differential equations of a complex reaction network can no longer be solved analytically and require a numerical solution.

To analyze a specific reaction, a list of all ion abundances as a function of reaction time is parsed by a home-written program based on Python 2 [116]. The program translates a proposed reaction model, entered *via* a graphical user interface, into a set of differential equations, which are subsequently treated by a LSODE (Livermore Solver for Ordinary Differential Equations) algorithm [117]. A Levenberg-Marquardt algorithm fits the resulting time-dependent theoretical ion abundances to the experimental values according to a least-squares method [118]. Each reaction step is associated with a fitting parameter, which corresponds to the pseudo-first order rate coefficient k' of that specific step. This **kinetic modeling procedure** is repeated for several reaction networks, *e.g.* including or excluding back reactions for specific steps. A reaction model is accepted when the experimental findings are replicated with a high congruence. If multiple candidates produce the same result, the simplest model is assigned to be correct. In consequence, kinetic modeling facilitates the determination of a reaction sequence and of the apparent rate coefficients associated with each step. A high number of species (>20) does not limit this procedure, as reaction networks with multiple parallel and consecutive step were analyzed in this fashion [119, 120]. The pseudo-first order rate coefficients obtained from the kinetic simulations depend on the reactant gas concentration as, at higher reactant particle densities, ions undergo more collisions per time that lead to reactions. For studies conducted at a constant total pressure, concentration and particle density are directly proportional and the two terms are used synonymously:

$$[X] = \frac{p_X}{p_{total}} = \frac{\left(\frac{n}{V}\right)_X k_B T}{\left(\frac{n}{V}\right)_{total} k_B T} \tag{3.10}$$

Equation 3.10 depicts the relationship of a reactant gas concentration [X] to the corresponding particle density $(n/V)_X$, with the partial and total pressure p_X and p_{total}, the Boltzmann constant k_B, and the temperature T. Normalizing the apparent rate coefficient of pseudo-first order k' to the reactant gas particle density results in a bimolecular rate coefficient $k^{(2)}$:

$$k^{(2)} = \frac{k'}{\left(\frac{n}{V}\right)_X} \tag{3.11}$$

Chapter A.3 provides details on the determination of reactant gas particle density and illustrates the validity of the normalization depicted in Equation 3.11. First-order rate coefficients describe the change of a relative abundance as a function of time (in the dimension s^{-1}), and particle densities indicate a number of particles per volumetric unit (typically cm^{-3}). Bimolecular rate coefficients are consequently displayed in units of cubic centimeters per second.

3.4.2. Energy transfer mechanisms

The experimentally obtained rate coefficients are of an apparent nature as they usually do not correspond to a single elementary step. Instead, the combination of multiple elementary reaction steps leads to the formation of a species, *e.g.* including collisional stabilization with buffer gas atoms. The Lindemann model is helpful to describe reactions in the presence of buffer gas [115, 121, 122]. The collision of a cluster M_n and a reactant gas molecule X may yield an energized association complex M_nX^*.

$$M_n + X \underset{k_d}{\overset{k_a}{\rightleftharpoons}} M_nX^* \xrightarrow[k_s]{+\mathrm{He}} M_nX + \mathrm{He}^* \tag{3.12}$$

While k_a denotes the rate coefficient for the formation of the intermediate complex, k_d describes the dissociation of the energized species back to the reactants. Alternatively, a collision with a buffer gas atom stabilizes the energized association complex. The resulting formation of the product M_nX and an energized He atom is characterized by k_s. In a steady-state approximation, formation and decay of M_nX^* cancel each other out, and the corresponding concentration remains constant: [115, 121]

$$\frac{d\,[M_nX]^*}{dt} = 0 = k_a\,[M_n]\,[X] - k_d\,[M_nX^*] - k_s\,[M_nX^*]\,[\mathrm{He}] \tag{3.13}$$

$$[M_nX^*] = \frac{k_a\,[M_n]\,[X]}{k_d + k_s\,[\mathrm{He}]} \tag{3.14}$$

The steady-state approximation thus leads to a simplified expression for the overall reaction rate:

$$r = \frac{d\,[M_nX]}{dt} = k_s\,[M_nX^*]\,[\mathrm{He}] = \frac{k_s k_a\,[M_n]\,[X]\,[\mathrm{He}]}{k_d + k_s\,[\mathrm{He}]} \tag{3.15}$$

The overall reaction rate consequently depends on the rate coefficients k_a, k_d and k_s (see Eq. 3.15) which may be formulated to a termolecular rate coefficient $k^{(3)}$. In the kinetic-low pressure regime, the dissociation of the energized intermediate is much faster than a stabilization process, resulting in a further simplified expression for the termolecular rate constant [115, 122].

$$k^{(3)} = \frac{k_s k_a}{k_d + k_s\,[\mathrm{He}]} = \frac{k_s k_a}{k_d} \qquad \text{for} \qquad k_d >> k_s\,[\mathrm{He}] \tag{3.16}$$

Experimentally, normalizing an apparent pseudo-first order rate coefficient to the product of He and reactant gas particle densities yields the termolecular rate coefficient (in units of $\mathrm{cm^6 s^{-1}}$):

$$k^{(3)} = \frac{k^{(2)}}{[\mathrm{He}]} = \frac{k'}{[X]\,[\mathrm{He}]} \tag{3.17}$$

The formation and stabilization of the energized intermediate correspond to ion-molecule collisions. These processes are largely independent of temperature, and theoretical collision rates (see Chapter 3.4.3) nicely model the corresponding rate coefficients. In contrast, the dissociation of the intermediate complex is a function of the internal degrees of freedom and the temperature. Less thermal energy supplied at lower temperatures suppresses the dissociation, leading to an enhanced rate of the overall reaction. Under operation of such an energy-transfer mechanism, decreasing the reaction temperature may therefore increase the apparent rate coefficient, which may bring about a negative apparent activation energy of the overall process. However, modeling the formation and stabilization of the energized intermediate with theoretical collision rates allows access to the temperature dependence of the dissociation process. Rice-Ramsperger-Kassel-Marcus (RRKM) theory may be employed to model the dissociation step and comparison with experimental values subsequently yields the binding energy of the involved reactants [123–126]. The group of Thorsten Bernhardt, for example, used this approach to determine binding energies of many cluster-molecule complexes [114, 115, 123, 127].

In consequence, the Lindemann mechanism of energy transfer represents a model to describe the temperature-dependence of a reaction and, moreover, illustrates **collisional stabilization** by buffer gas atoms. Latter is a distinct characteristic of multi-collision studies as buffer gas is typically not present when ions of interest are studied under single-collision conditions. A Fourier-transform ion cyclotron resonance (FT-ICR) apparatus, for example, traps ions in a magnetic field to analyze their mass under UHV conditions ($p_{total} = 10^{-10} - 10^{-7}$ mbar). In order to study ion-molecule reactions therein, ions are typically thermalized (*via* collisions with inert gas atoms) prior to the injection into the ICR cell, where the ions undergo a single collision with a reactant particle at a partial pressure of approximately 10^{-8} mbar [95, 128]. Under single-collision conditions, an intermediate of ion-molecular association will proceed "downhill" on the potential energy surface of the reaction, resulting in the exothermic formation of a product (see Fig. 3.5). The absence of additional collisions limits the means of energy transfer: solely emission of radiation or ejection of a neutral fragment will remove excess energy from the system. In contrast, collisional stabilization of intermediates may occur through the use of a buffer gas. Reactions of cationic niobium clusters with benzene exemplify this distinction. Under single-collision conditions in an FT-ICR mass spectrometer, most clusters produce fully dehydrogenated $[Nb_nC_6]^+$ species with a few $[Nb_nC_6H_6]^+$ minority products [129, 130]. Under multi-collision conditions in a flow-tube reactor, however, many partially and non-dehydrogenated $[Nb_nC_6H_{2,4,6}]^+$ species are additionally generated [131]. Furthermore, small cationic gold clusters are inert when exposed to methane in an FT-ICR apparatus [74], but demonstrate a size-dependent reactivity under multi-collision conditions [127, 132]. For endothermic reactions, another effect has to be considered. The ensemble of buffer gas atoms adheres to a Maxwell-

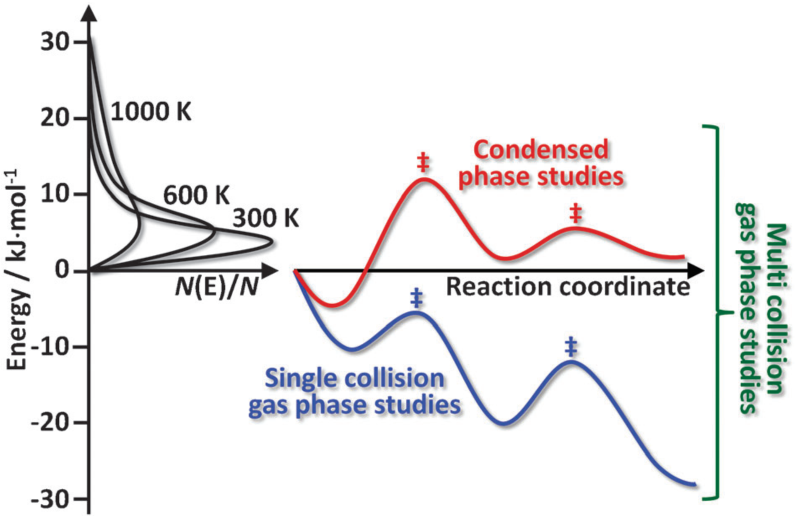

Figure 3.5: *Comparison of available energy and accessible reaction pathways in condensed phase studies, single-collision conditions in the gas phase and multi-collision conditions in the gas phase. Reproduced from Ref. [17] with permission from the PCCP Owner Societies.*

Boltzmann energy distribution and constantly equilibrates with ions stored in a trap. Collisions with buffer gas atoms may therefore supply external energy to the stored ions [114]. Energy provided by collisions promotes ion-molecule complexes to **overcome reaction barriers** that exceed the initial total energy of the ion and molecule in isolation (see Fig. 3.5). Similarly, externally supplied energy facilitates the endothermic formation of products. The rate coefficient k introduced in Equation 3.4 is moreover a function of temperature T and the corresponding relationship is expressed in the Arrhenius equation: [113, 133]

$$k = A \cdot e^{\frac{-E_A}{RT}} \tag{3.18}$$

where the pre-exponential factor A is the so-called frequency factor, E_A denotes the activation energy of a reaction and R describes the universal gas constant. The exponential Boltzmann term characterizes the fraction of energized complexes that may overcome the reaction barrier at a given temperature [113]. Variation of the reaction temperature therefore allows the determination of the activation energy. To do so, the natural logarithm of the experimentally determined rate coefficient is typically plotted against T^{-1} and E_A is obtained from the slope:

$$\ln(k) = \ln(A) - \frac{E_A}{R} \cdot \frac{1}{T} \tag{3.19}$$

In summary, the reaction conditions define the outcome, and employing a buffer gas with a dilute amount of reactant gas results in well-defined multi-collision conditions. Collisions with the buffer gas provide the means to stabilize reaction intermediates, as described by the Lindemann mechanism. Through the inverse transfer of energy from buffer gas atoms to ions, reaction pathways with transition states and products in excess of endothermicity become accessible.

3.4.3. Theoretical collision rates

The reaction efficiency of a system, *i.e.* the fraction of collisions that lead to a reaction, is calculated as the ratio of an experimental rate coefficient to the theoretical collision rate. In addition, apparent processes may consist of multiple elementary steps and using theoretical coefficients of individual steps helps to understand temperature-dependent phenomena, *e.g.* in the Lindemann mechanism (see Chapter 3.4.2). Thus, a theoretical description of the collision between an ion and a molecule benefits the interpretation of experimental results. Models relevant to this thesis are briefly summarized in this section.

Giousmousis and Stevenson developed a model based on theorems by Langevin [134] and Eyring [135] in order to describe reaction rates as a result of the interaction of an ion and a non-polar molecule [136]. In the so-called **Langevin-Giousmousis-Stevenson** (LGS) model, the interaction potential of a neutral molecule and an ion is given as:

$$\phi(r) = -\frac{q^2\alpha}{2r^4} \tag{3.20}$$

with the charge of the ion q, the polarizability of the molecule α and the center-of-mass distance r [136]. The interaction determines trajectories as a function of distance, and a critical impact parameter b_0 is introduced,[3] which defines a spatial limit for orbits of two particles to lead to a reaction.

$$b_0 = \left(\frac{4q^2\alpha}{\mu g^2}\right)^{\frac{1}{4}} \qquad \text{with} \qquad \mu = \frac{m_1 \cdot m_2}{m_1 + m_2} \tag{3.21}$$

---

[3] See the original publication of Giousmousis and Stevenson for a discussion of the orbit parameter and details on the volume integral to determine the reaction rate [136].

where g describes the relative velocity, μ is the reduced mass of the ion-molecule complex, m_1 and m_2 denote the mass of the ion and the molecule, respectively. With the help of the critical impact parameter, a reaction cross section σ is defined:

$$\sigma = \pi b_0^2 = \frac{\pi}{g}\left(\frac{4q^2\alpha}{\mu}\right)^{\frac{1}{2}} \tag{3.22}$$

Under the assumption of Maxwell-Boltzmann velocity distributions and additional considerations,[3] a reaction rate is obtained, thereby allowing the formulation of the LGS rate coefficient k^{LGS}: [136]

$$k^{\mathrm{LGS}} = 2\pi\left(\frac{q^2\alpha}{\mu}\right)^{\frac{1}{2}} \tag{3.23}$$

Note that Eqn. 3.20–3.23 use the centimetre-gram-second (cgs) system of units, *e.g.* with the charge in units of a statcoulomb (statC= $\mathrm{cm}^{3/2}\mathrm{g}^{1/2}\mathrm{s}^{-1}$) and the rate coefficient in $\mathrm{cm}^3\mathrm{s}^{-1}$. The theoretical rate coefficient according to the LGS model consequently only depends on the polarizability of the neutral (non-polar) molecule and on the reduced mass of the ion-molecule pair, whereas other properties are not taken into account.

Sun, Bowers and co-workers furthermore developed the **average-dipole-orientation** (ADO) theory to model the collisions between ions and polar molecules [137]. Due to the non-polar nature of particles investigated in this thesis (He, O_2, CH_4 and CD_4), solely the essence of this model will be discussed. More information is instead available in literature [138–142]. In the presence of a dipole in the neutral molecule, the interaction potential of ion and molecule additionally contains a term that depends on the charge q, the distance r, the dipole moment μ_D, and the orientation of the dipole (the angle θ between the dipole moment and the line of centers) [139]. Su and Bowers found that, in the electric field of the ion, the dipole should only be partially oriented, not fully locked, and the dipole orientation is thus averaged: [137–139]

$$\phi\left(r,\bar{\theta}\right) = \phi(r) - \frac{q\mu_D}{r^2} cos\bar{\theta}\left(r\right) \tag{3.24}$$

The resulting expression for the theoretical rate coefficient k^{ADO} contains the dipole-locking constant C, which depends on the ratio of the dipole moment to the square-root of the polarizability: [139]

$$k^{\mathrm{ADO}} = \frac{2\pi q}{\mu^{\frac{1}{2}}}\left(\alpha^{\frac{1}{2}} + \frac{2C\mu_D}{\pi k_B T}\right)^{\frac{1}{2}} \tag{3.25}$$

where k_B describes the Boltzmann constant and T is the temperature. The LGS and ADO models treat particles as point charges, and this becomes an insufficient description for increasingly larger metal clusters. Likewise, purely geometrical models (*e.g.*, the collision of two hard spheres) also fall short in the prediction of collision rates [143]. The **surface charge capture** (SCC) model by Kummerlöwe and Beyer improves on these findings. Charged metal clusters are treated as spheres with finite size and, in order to capture a molecule during a collision, the charge moves to the point on the cluster surface, which is closest to the neutral molecule [143]. The corresponding impact parameter b^{SCC} contains a geometric term r_{cluster} and the critical impact parameter from ADO theory b_0^{ADO}. Latter is derived from the calculated ADO rate coefficient (see also the original publication [143] by Kummerlöwe and Beyer):

$$b_0^{\text{ADO}}(v) = \frac{\left(k^{\text{ADO}}(v)\right)^{\frac{1}{2}}}{\pi v} \tag{3.26}$$

where v denotes the velocity. Furthermore, the cluster is assumed to be spherical and to have the same density as the bulk metal. The calculated cluster radius r_{cluster} consequently depends on the number of atoms n with the individual mass m and the bulk density ρ:

$$r_{\text{cluster}} = \left(\frac{3nm}{4\pi\rho}\right)^{\frac{3}{2}} \tag{3.27}$$

The full expression of the SCC impact parameter is depicted in the following equation.

$$b^{\text{SCC}}(v) = r_{\text{cluster}} + b_0^{\text{ADO}}(v) = \left(\frac{3nm}{4\pi\rho}\right)^{\frac{3}{2}} + \frac{\left(k^{\text{ADO}}(v)\right)^{\frac{1}{2}}}{\pi v} \tag{3.28}$$

The corresponding cross section $\pi(b^{\text{SCC}})^2$ is convoluted with the Maxwell distribution $f(v)$ to obtain k^{SCC}, the collision rate predicted by surface charge capture theory:

$$k^{\text{SCC}} = \int_0^\infty \pi\left(b^{\text{SCC}}(v)\right)^2 v f(v)\, dv \tag{3.29}$$

SCC theory provides an upper limit for rate coefficients, *e.g.* in the reaction of charged cobalt clusters with carbon monoxide, whereas other models predict rates that are exceeded by the experimental values of larger clusters [143]. However, certain effects (asymmetric charge distribution in the reaction of charged rhodium clusters and carbon monoxide, for example) may also cause SCC theory to fall short [143]. In this thesis, LGS as well as SCC theory will be used to analyze experimental rate coefficients of cationic Ta-based systems.

3.4.4. Kinetic isotope effect

Isotopic substitution of atoms in a molecule may affect reaction barriers, thereby changing the associated rate coefficient. The magnitude of this change is furthermore indicative of the nature of the transition state in the step that limits the reaction rate. Thus, reactions with isotopically labeled reactants provide additional insights and a short theoretical description of the responsible effect will be given in this chapter. In an idealized picture, a very heavy atom with the mass m_2 is bonded to a very light atom with the mass m_1 ($m_1 \ll m_2$), which may vibrate along the bond axis to change the interatomic distance. The frequency ν of this vibration will depend on a force constant k_f and the reduced mass of the diatomic system μ (see Eq. 3.30). For a very large mass difference, the reduced mass can be approximated as the mass of the lighter atom: [144, 145]

$$\nu = \frac{1}{2\pi}\sqrt{\frac{k_f}{\mu}} \approx \frac{1}{2\pi}\sqrt{\frac{k_f}{m_1}} \tag{3.30}$$

As an effect purely due to mass, substitution of the lighter atom by a heavier isotope will subsequently reduce the vibrational frequency. A large change is expected for a drastic relative mass difference of the two isotopes, *e.g.* when hydrogen in a C–H bond is replaced by a deuterium atom ($m_D = 2m_H$): [146]

$$\frac{\nu_D}{\nu_H} = \frac{\frac{1}{2\pi}\sqrt{\frac{k_f}{2m_H}}}{\frac{1}{2\pi}\sqrt{\frac{k_f}{m_H}}} = \sqrt{\frac{1}{2}} \tag{3.31}$$

Experimental C–H stretch vibrations are associated with wavenumbers ($\tilde{\nu} = \nu/c$, with the speed of light c) of approximately 3000 cm^{-1}, whereas C–D stretch vibrations occur around 2000 cm^{-1} [147]. As a result of this mass effect, a C–D bond demonstrates a lower zero-point vibrational energy (E_{zpe}) than a C–H bond: [146]

$$\Delta E_{\text{zpe}} = -\frac{1}{2}h\left(\nu_H - \nu_D\right) \tag{3.32}$$

where h denotes the Planck constant. Assuming the free dissociation of a C–H(D) bond, the dissociation rate k is a function of the bond-dissociation energy D_0 (the difference of the potential well depth D_e and the zero-point energy): [145]

$$D_0 = -k_B T \ln(k) = D_e - E_{\text{zpe}} \tag{3.33}$$

with the Boltzmann constant k_B and the temperature T. Using latter relationship and the difference in zero-point energy (see Eq. 3.32), the theoretical ratio of the rate coefficient for the C–H bond scission to the rate coefficient for the C–D cleavage is obtained: [145]

$$\frac{k_H}{k_D} = e^{\frac{1}{2}h\left(1-\sqrt{\frac{1}{2}}\right)\nu_H/k_BT} \tag{3.34}$$

This ratio is known as the kinetic isotope effect (KIE). As bond dissociation in CH_4 and CD_4 is the topic of this thesis, only primary kinetic isotope effects are discussed in the following, *i.e.* isotopic substitution occurs directly at the bond that is to be cleaved. For a free bond dissociation, a maximum KIE value of around 8 is expected (excluding non-classical effects, *e.g.* tunneling) [147]. However, a more complex potential energy surface for a reaction between two species may involve several transition states, *e.g.* C–H bond scission is followed by the formation and cleavage of additional bonds. Experimentally, the KIE of the overall product formation is obtained. This KIE relates to the rate-determining step (RDS) of the reaction, which is defined by the highest total energy of a transition state. A publication by Schröder and Schwarz provides an overview of the KIE magnitude as a function of the RDS process [148]. Phenomenologically, when a methane dehydrogenation reaction is limited by cleavage of the C–H(D) bond in an intermediate of an insertion reaction, the magnitude of the KIE will be above 2.50 [148]. An elevated KIE may also occur in σ-bond metathesis reactions, *e.g.* for NiF^+/CH_4 [100], and PCET mechanisms, for example in the reaction of $Al_2O_2^+$ with methane [79, 80]. On the other hand, when the rate is determined by the elimination of H_2 (D_2), *e.g.* in the reaction of Pt^+ with methane [149, 150], a KIE below 1.35 is expected. In general, product liberation in the RDS, *e.g.* HBr from $PtBr^+/CH_4$ [151], will cause low KIE magnitudes between 1.00 and 1.35. Medium KIE magnitudes (1.35–2.50) are observed when hydrogen radicals are directly abstracted from methane, *e.g.* in the HAT reaction of $V_4O_{10}^+$ with methane [81].

To summarize, isotopic substitution leads to a change in zero-point vibrational energy, which affects the reaction rate, and the reaction mechanism determines the magnitude of the rate change. The kinetic isotope effect therefore represents a mechanistic probe in methane activation reactions [148]. In hydrogen atom abstraction reactions, the KIE allows a discrimination of HAT and PCET mechanisms. For methane dehydrogenation and concomitant hydrogen elimination, the KIE indicates whether the rate is limited by C–H scission or H_2 elimination. These kinetic insights may furthermore validate results from quantum-chemical calculations, *e.g.* relative transition state energy and/or spin-crossover processes [99].

3.5. Motivation and approach

Gas-phase experiments aim to draw a relationship between the properties of reactants and the resulting mechanism that leads to the formation of products. To that end, the reactivity of single reactive species, *e.g.* isolated metal clusters, is investigated. Through variation of the clustering metal, the cluster size, and the charge state, a systematic study of a "designed" active site becomes feasible. Addition of (organic) ligands or non-metallic atoms furthermore tailors these

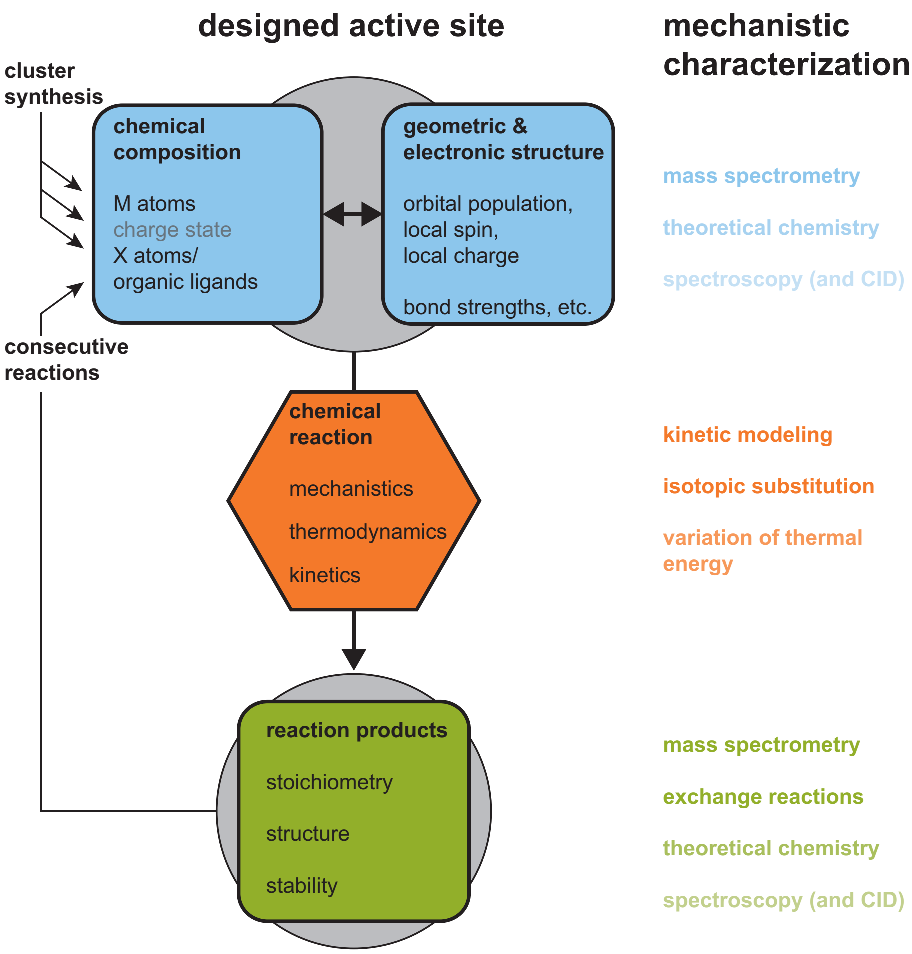

Figure 3.6: *Schematic approach for the systematic investigation of the reactions of gas-phase clusters. The properties of specially designed clusters, composed of metal and non-metal atoms (M and X) and organic ligands, are expressed in chemical reactions, which are characterized in kinetics studies. Faded text displays collision-induced dissociation (CID) and spectroscopy as these characterization techniques are not employed in this thesis.*

model systems, and affects the electronic and geometric structure. Latter properties distinctly define the reaction mechanism that is operative when the clusters are exposed to reactive molecules. In this work, mass-selected clusters react under multi-collision conditions at a defined temperature, and time-of-flight mass spectrometry characterizes ionic reactants and products as a function of the reaction time. Modeling the reaction kinetics subsequently allows a comparative analysis of different cluster sizes and compositions. Furthermore, gas-phase systems facilitate quantum-chemical calculations, which also identify the structures and reaction mechanisms of selected clusters in this thesis. Although not employed in this work, gas-phase spectroscopy and collision-induced dissociation (CID) provide additional means to analyze the isolated particles. As a result of the multi-collision reaction conditions in the ion trap, ligated clusters from a first reaction step undergo consecutive reactions, and the ensuing reaction scheme is analyzed in the same fashion.

This thesis focuses on bare tantalum cluster cations of different sizes and various tantalum oxide clusters. While initial studies investigate consecutive reactions toward oxygen (Chapter 4), the main topic of this work is the C–H bond activation of methane. Small tantalum and tantalum oxide systems have previously been demonstrated to mediate the transformation of methane into more valuable products [41, 98, 152] and to benefit from strong Ta–C bonds [62, 153], resulting in a thermodynamic driving force. Small tantalum clusters are therefore promising candidates for the activation of methane. In the first step, size-selected, bare tantalum clusters are exposed to methane and compared based on the products and kinetics of the consecutive reactions (Chapter 5). The reaction mechanism is moreover probed through the use of isotopically labeled methane, as the kinetic isotope effect is indicative of the reactivity mode in the rate-determining step. A cluster source modification, described in Chapter 4.3, allows the generation of tantalum cluster oxides with a precise amount of oxygen atoms. Through the mass selection of specific cluster oxides, the influence of oxygen atoms as components of the tantalum clusters on the methane activation reactions is evaluated in Chapters 6 and 7. Lastly, tantalum-methylene complexes are exposed to dioxygen in order to probe C–O coupling reactions (Chapter 8). Thus, the studies presented in this thesis will unravel the activation of methane mediated by tantalum-based systems as a function of the chemical composition.

CONSECUTIVE OXIDATION REACTIONS OF TANTALUM CLUSTER CATIONS

4

Molecular oxygen is a commonly used oxidant and may be utilized to transform methane into value-added products *via* oxidative coupling. The reactivity of tantalum clusters toward dioxygen was investigated, thus revealing cluster properties and simultaneously providing a basis for the analysis of more complicated reactions.

The following chapter covers studies of cationic tantalum clusters Ta_{4-40}^{+} reacting with O_2 in a cryogenic ring electrode ion trap in the presence of helium buffer gas. Two reactivity modes, intact oxidation and oxidative degradation, are accessible depending on cluster size. The reaction mechanisms are elucidated with the help of density functional theory (DFT) calculations. Kinetic insights furthermore facilitate the description of the unique reactivity of larger clusters.
The presented findings are the result of the work by my former colleague Dr. Daniel Neuwirth and myself. While many of these insights are included in the doctoral thesis of D. Neuwirth, subsequent considerations and additional computational results by the group of Prof. Dr. Karsten Reuter lead to an improved description of the observed phenomena. Ultimately, the results on the oxidation reactions were published in a three part series.[1] These publications are specially referenced (see the List of Publications, Chapter 10.2) and their essence will be briefly discussed here.

---

[1] "*Two reaction regimes in the oxidation of larger cationic tantalum clusters (Ta_n^+, n = 13 - 40) under multi-collision conditions*" [119], "*Consecutive reactions of small, free tantalum clusters with dioxygen controlled by relaxation dynamics*" [154] and "*From oxidative degradation to direct oxidation: Size regimes in the consecutive reaction of cationic tantalum clusters with dioxygen*" [120].

4.1. Reaction mechanisms

When tantalum and tantalum oxide clusters ($Ta_nO_x^+$, $x \geq 0$) collide with an oxygen molecule, an energized intermediate, $([Ta_nO_x(O_2)]^+)^*$, is formed. For unsaturated clusters, the O–O bond of the oxygen molecule is readily cleaved and Ta–O bonds are formed. This process releases energy into the system and some clusters relax *via* ejection of a neutral TaO fragment. A scheme for reactions of this type, called oxidative degradation, is shown in Equation 4.1.

$$[Ta_nO_x]^+ + O_2 \rightleftharpoons ([Ta_nO_x(O_2)]^+)^* \rightarrow \left(\left[Ta_nO_{y+2}\right]^+\right)^* \rightarrow [Ta_{n-1}O_{x+1}]^+ + TaO \tag{4.1}$$

Oxidative degradation typically occurs for small, bare clusters ($n < 13$ and $x = 0$) and for small oxide clusters with a low oxygen content ($n \geq x$). A reaction channel in absence of the release of a neutral molecule, intact oxidation, is additionally observed for larger clusters ($n > 8$) or a higher number of oxygen atoms ($n \leq x$) as depicted in Equation 4.2.

$$[Ta_nO_x]^+ + O_2 \rightleftharpoons ([Ta_nO_x(O_2)]^+)^* \xrightarrow[\text{He}]{} [Ta_nO_{x+2}]^+ \tag{4.2}$$

The consecutive oxidation of Ta_4^+ illustrates the branching between the two reaction channels:

$$Ta_4^+ \xrightarrow[\text{-TaO}]{+O_2} Ta_3O^+ \xrightarrow[\text{-TaO}]{+O_2} Ta_2O_2^+ \xrightarrow[\text{-TaO}_2]{+O_2} TaO_2^+ \qquad (90\%) \tag{4.3a}$$

$$Ta_2O_2^+ \xrightarrow{+O_2} Ta_2O_4^+ \xrightarrow{+O_2} Ta_2O_6^+ \qquad (10\%) \tag{4.3b}$$

Twofold oxidative degradation yields $Ta_2O_2^+$ and the majority of the clusters fragment to TaO_2^+ and TaO_2. However, $Ta_2O_2^+$ also undergoes intact oxidation to $Ta_2O_4^+$, which in turn reacts to $Ta_2O_6^+$.

DFT investigations on the oxidation reactions of four Ta_4^+ oxides demonstrate that the two reaction channels, intact oxidation and oxidative degradation, correspond to two different relaxation mechanisms and that the degradation product stability determines the branching ratio.

4.2. Ion trap studies

4.2.1. Competitive relaxation pathways of smaller clusters

Comparing three $Ta_4O_x^+$ clusters ($x = 3 - 5$), the intact oxidation products $Ta_4O_{x+2}^+$ are formed exothermically for every cluster. On the other hand, the oxidative degradation products become increasingly less stable with an increasing oxidation state of the reactants and the selectivity for intact oxidation changes from 0% for $Ta_4O_3^+$ to 100% for $Ta_4O_5^+$ (see Figure 4.1). The oxidative degradation product of $Ta_4O_3^+$ is the most stable and more than 2.5 eV would have to be removed through collisional stabilization with the buffer gas atoms in order to render the fragmentation channel inaccessible. Consequently, the clusters relax via ejection of TaO before a sufficient amount of collisional stabilization with the He atoms can occur. As the oxidative degradation products of $Ta_4O_4^+$ are less stable, less energy has to be quenched, collisional stabilization starts to compete and 55% of the clusters undergo intact oxidation. Lastly, reaction intermediates of $Ta_4O_5^+$ are quickly thermalized below the fragmentation threshold, preventing oxidative degradation. In general, oxidative degradation is found to decrease with a higher oxygen content of the reactants and the same mechanism is assumed to be operative for other cluster sizes. The consecutive oxidation reactions produce

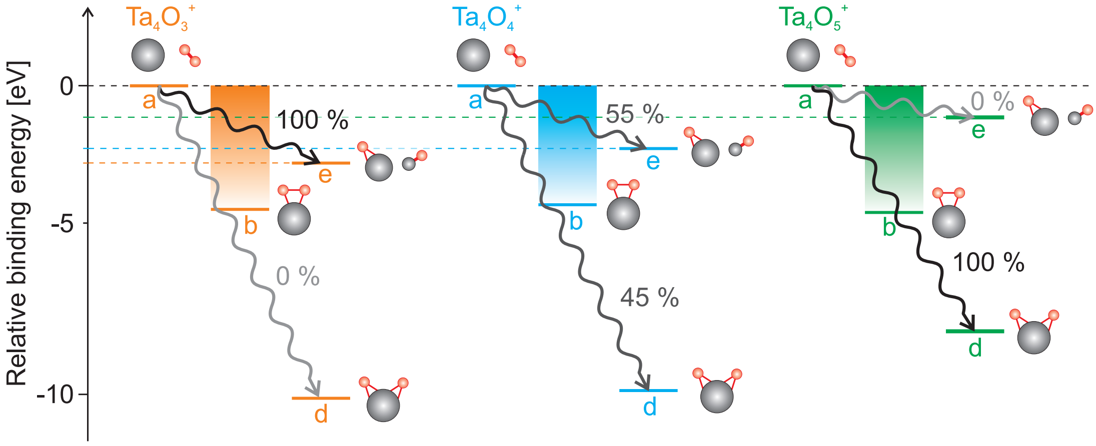

Figure 4.1: *Schematic of potential energy diagrams for the reaction of* $Ta_4O_x^+$ *(*$x = 3 - 5$*) with molecular oxygen. The oxidation progresses from the reactant clusters and* O_2 *(a) via an intermediate with chemisorbed oxygen,* $Ta_4O_x(O_2)^+$ *(b), and results either in* $Ta_4O_{x+2}^+$ *(d) or in the oxidative degradation products,* $Ta_3O_{x+1}^+$ *and TaO (e). [154] - Reproduced by permission of the PCCP Owner Societies.*

increasingly smaller tantalum oxide clusters with higher oxidation states, until a $Ta_nO^+_{x\geq n}$ cluster is formed that (additionally) undergoes intact oxidation (*e.g.* $Ta_4O_5^+$ in the reaction of Ta_9^+, $Ta_4O_4^+$ from Ta_8^+ and $Ta_3O_4^+$ from Ta_7^+). For cationic tantalum clusters larger than Ta_{12}^+, only trace amounts of oxidative degradation products are observed during the oxidation reactions and size-specific intact oxidation products are generated instead. Compared to smaller species, these larger clusters possess more degrees of freedom that facilitate internal vibrational relaxation. As a consequence, the energy released by O–O bond scission and Ta–O bond formation is stored in vibrational modes until collisions with the buffer gas occur, and fragmentation processes are subsequently prevented.

4.2.2. Surface oxidation in two kinetic regimes

The oxidation of Ta_{20}^+ exemplifies the findings for larger clusters. The reactions occur in two kinetic regimes as depicted in Figure 4.2: consecutive adsorption and dissociation of O_2 leads to the formation of a size-specific intermediate ($Ta_nO_m^+$, *e.g.* $Ta_{20}O_{14}^+$) and consecutive molecular adsorption subsequently yields a size-specific product (*e.g.* $Ta_{20}O_{26}^+$). The first kinetic regime is characterized by nearly constant apparent activation energies (between 0.3 and 0.4 $kJmol^{-1}$) and a slow decrease of apparent bimolecular rate coefficients (from 1.8 to $1.5{\cdot}10^{-9}cm^3s^{-1}$), suggesting a quick dissociative adsorption of oxygen that saturates surface Ta sites. On the other hand, rate coefficients quickly decrease in the second regime (from 1.5 to $0.2{\cdot}10^{-9}cm^3s^{-1}$) and apparent activation energies monotonically drop

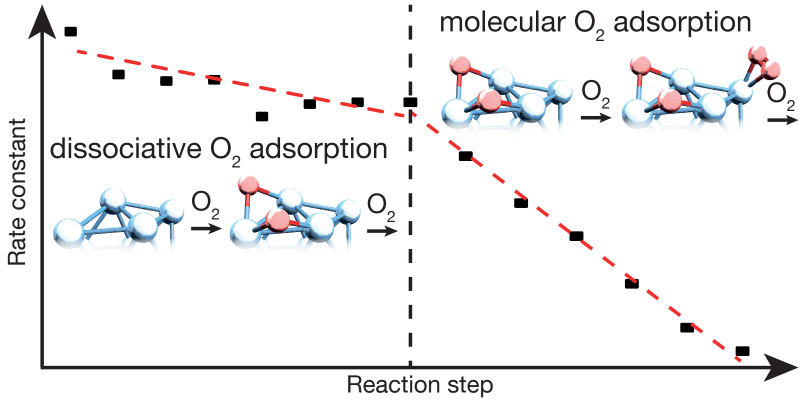

Figure 4.2: *Kinetic regimes in the consecutive oxidation of larger tantalum cluster cations (shown for Ta_{20}^+) caused by two characteristic reactivity modes. [119] - Published by the PCCP Owner Societies.*

to small negative values, evidencing molecular adsorption that is enhanced at lower reaction temperatures. Moreover, the Ta-O atom ratio of the intermediate species $Ta_nO_m^+$ is found to scale with $n^{-\frac{1}{3}}$, *i.e.* the surface-to-volume ratio of the clusters, which furthermore implies that these larger clusters consist of a metal core that is oxidized on its surface.

4.2.3. Final oxidation product regimes

Plotting the final reaction products with the highest oxidation state unravels additional information. As shown in section 4.2.1, small reactant tantalum clusters form increasingly smaller oxide clusters that undergo additional oxidation reactions. This process generates, for example, $Ta_2O_6^+$ from Ta_4^+ and $Ta_4O_{11}^+$ from Ta_9^+. A linear regression in the small size regime of the reaction products ($n = 1 - 10$) yields a slope of 5 O atoms per 2 Ta atoms (see Figure 4.3). Products in this regime correspond to fully oxidized tantalum oxide clusters $(Ta_2O_5)_y^+$ ($y = 1 - 10$), similar to the bulk phase, and some of them contain more oxygen as terminal O

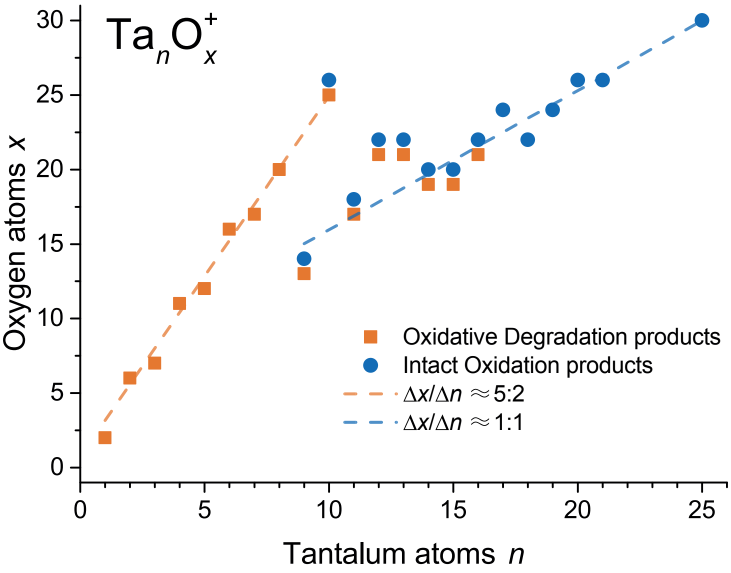

Figure 4.3: *Final products $Ta_nO_x^+$ of consecutive reactions with dioxygen. For each n, the product with the highest oxidation state is plotted. Orange squares indicate products of one or more oxidative degradation steps followed by intact oxidation steps and blue circles depict products solely from intact oxidation. Dashed lines demonstrate two regimes of the relative oxidation state. [154] - Reproduced by permission of the PCCP Owner Societies.*

atoms were replaced by O_2 groups. Oxidation products with a large metal core ($n > 10$) demonstrate a much lower oxygen content, consistent with a conserved metal core and the oxidation being restricted to the cluster surface. In the large size regime of the oxidation product composition, the slope amounts to approximately 1 O atom per 1 Ta atom. Interestingly, $Ta_9O_x^+$ product clusters contain few oxygen atoms as expected for large clusters, whereas intact oxidation of Ta_{10}^+ results in a highly oxidized $Ta_{10}O_{26}^+$ clusters. Ta_{10}^+ apparently facilitates extensive rearrangement of the cluster structure to allow the formation of many Ta–O bonds without previous degradation, and is an exemption from the composition of oxide clusters in the large size regime.

4.2.4. Conclusion and outlook

Cationic tantalum clusters readily react with dioxygen and consequently form different characteristic species due to inherent cluster properties and underlying reaction mechanisms. The products include partially oxidized clusters, *e.g.* $Ta_2O_2^+$, metal oxide clusters with a stoichiometric composition, *e.g.* $Ta_2O_5^+$, surface-oxidized clusters, *e.g.* $Ta_{20}O_{14}^+$, and surface-oxidized clusters with additional molecularly adsorbed oxygen, *e.g.* $Ta_{20}O_{26}^+$. Therefore, tantalum oxide clusters may serve as a platform to investigate methane oxidation as a function of not only the cluster size but additionally of the oxygen content.

The reaction of these different types of metal oxides towards methane could be studied by storing bare tantalum cluster cations and simultaneously exposing them to O_2 and CH_4. An abundance of parallel reactions is a major drawback of this approach. The spatial separation of the reaction with oxygen and with methane, *i.e.* generation of a target metal oxide cluster and subsequent storage in the ion trap, is greatly simplifying the unperturbed investigation of individual reactions. To this end, a source modification for the controlled chemical modification of metal clusters was developed, which is discussed in the next section.

4.3. In-source oxidation reactions

The previous cluster source design had to be modified in order to inject reactive gas in a controlled fashion. The adapted expansion nozzle geometry was designed by my co-worker Dr. Tsugunosuke Masubuchi. We implemented sets of the modular, modified source parts and evaluated them experimentally. The comparison of the obtained data to the results of the ion trap studies lead to an interpretation of the processes in the cluster source. The work was published with the title "*An efficient laser vaporization source for chemically modified metal clusters characterized by thermodynamics and kinetics*" [155], authored by T. Masubuchi, and will be summarized in this section.

4.3.1. Modifications to the laser vaporization cluster source

A solenoid valve (General valve, Series 9, Parker) was installed and connected to the expansion channel of the cluster source. Furthermore, the final section of the expansion nozzle was modified to include a second "waiting room" that functions as a pulsed high-pressure collision cell (see Figure 4.4). When a backing pressure of oxygen gas is applied, the solenoid valve may be used to introduce a pulse of oxygen into the expansion channel and the second waiting room becomes pre-filled with the reactive gas. Using a specific triggering scheme (shown in the Appendix), the solenoid valve pulse, the helium carrier gas pulse and the ablation laser pulse are sequenced to generate clusters in the first waiting room and expose them to oxygen in the second waiting room.

In order to evaluate the performance of the laser ablation source with the modified nozzle, cationic tantalum clusters were generated over a wide size range and guided (without mass selection) into the ion trap. The cluster beam was subsequently bunched in the ion trap and analyzed with the TOF-MS. Initially, the triggering sequence and the backing gas pressure levels were optimized and, ultimately, the amount of introduced oxygen gas was varied by systematically increasing the solenoid valve pulse width Δt_{open} and the resulting change in the distribution of metal oxide abundances was recorded.

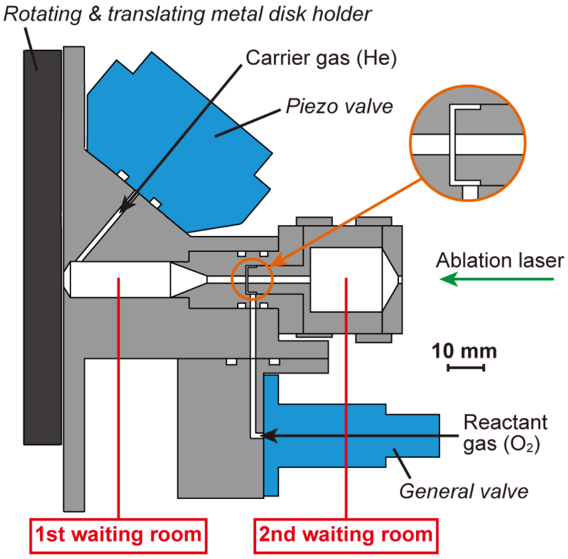

Figure 4.4: *Schematic cross-section of the modified laser vaporization cluster source. A pulsed solenoid valve fills the second waiting room in the expansion nozzle with oxygen gas. In the first waiting room, the ablation laser evaporates atoms and clusters from the metal target and a piezo-electric valve introduces the helium carrier gas ($p_{He} > p_{O_2}$). Consequently, metal clusters are formed, collide with many He atoms and oxygen molecules, and undergo an expansion into the vacuum chamber. Adapted with permission from [155]. Copyright AIP PUBLISHING LLC.*

4.3.2. Results

Similar to the ion trap studies, Ta_{20}^+ exemplifies the reactions of tantalum clusters toward dioxygen inside the nozzle of the cluster source. As the backing pressure of O_2 is applied, $Ta_{20}O_y^+$ clusters, predominantly with an even number of O atoms, are formed. With an increasing pulse duration of the solenoid valve, more O_2 units are picked up (see Figure 4.5) until $Ta_{20}O_{26}^+$ is formed, which is the same final product as observed during the oxidation in the ion trap.

These findings indicate a consecutive reaction with O_2 driven by an increased oxygen molecule density in the second waiting room as the solenoid valve remains open for longer durations. The oxygen gas pulse seemingly does not interfere with the cluster formation process, evidenced by a largely unaffected signal intensity of $Ta_{20}O_y^+$ clusters and the production of surface-oxidized species. Likewise, oxidative degradation seemingly occurs for small tantalum clusters as the even-odd alteration in the number of oxygen atoms is not observed in the lower

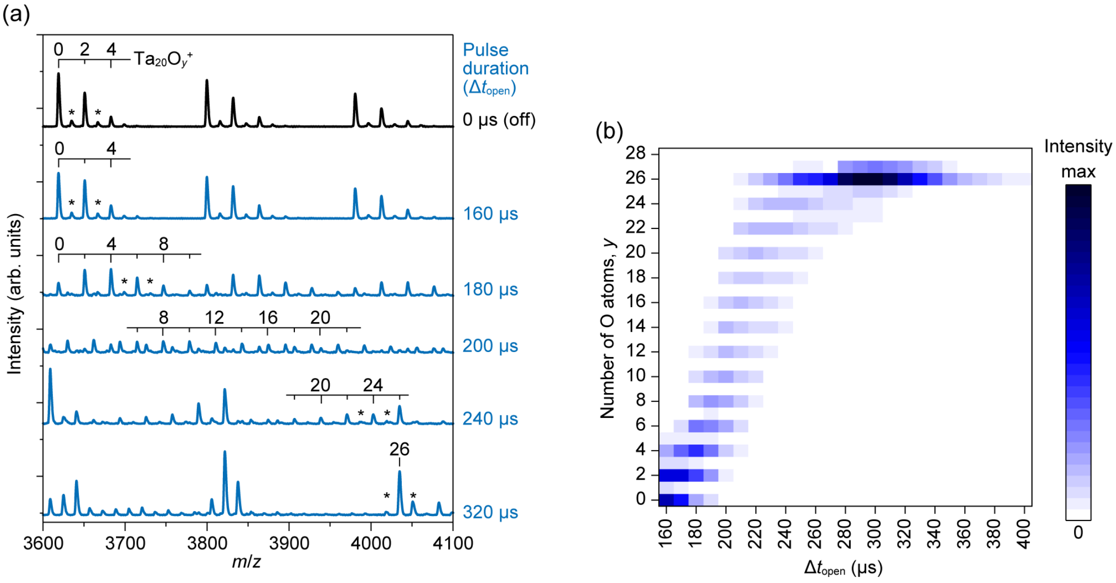

Figure 4.5: *Excerpts of time-of-flight mass spectra for increasing O_2 pulse durations, depicting the consecutive oxidation of Ta_{20}^{+} (a). Distribution of Ta_{20}^{+} oxides as a function of the pulse duration (b). Adapted with permission from [155]. Copyright AIP PUBLISHING LLC.*

mass range. Moreover, the final oxidation products associated with sensibly long O_2 pulse durations match the final oxides produced in the ion trap. The reaction conditions in the source nozzle are therefore similar to the well-defined multi-collision conditions inside of the ion trap.

Analyzing the pseudo-first order reaction kinetics reveals additional information. In general, the rate of these oxidation reactions depends on the product of the corresponding rate coefficient k, the oxygen molecule density $[O_2]$ and the reaction time t. While $[O_2]$ is kept constant in the ion trap studies and t is systematically varied, the specified O_2 pulse duration Δt_{open} is changed for reactions in the source. Due to a non-linear response of the solenoid valve, Δt_{open} is not directly proportional to the logarithmic change in reactant intensity, for example of Ta_{20}^{+}. Consequently, the parameter $\tau = [O_2] \cdot t$ is introduced and obtained *via* a power-function fit of the change in Ta_{20}^{+} intensity to Δt_{open}. One should note that this approach does not suffice to determine normalized rate coefficients as $[O_2]$ and t remain undetermined. The linearized results are subsequently compared to the findings obtained from the investigations using the ion trap. Each species $Ta_{20}O_{2,4,6,\ldots,24}^{+}$ occurs with a maximum relative abundance at a specific reaction time t_{max} or at a specific τ_{max}. Values for t_{max} are available from ion trap studies

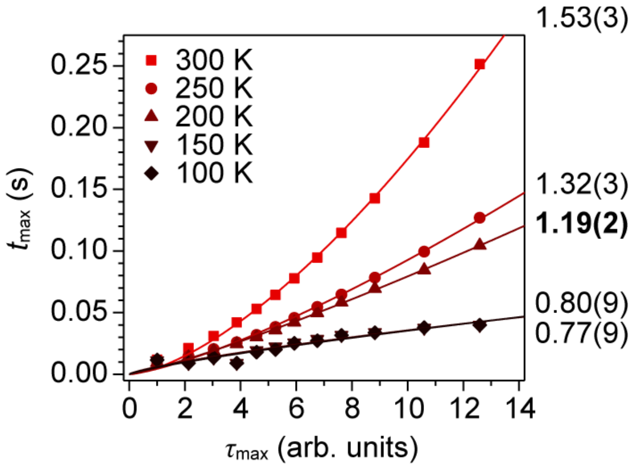

Figure 4.6: *Comparative evaluation of the reaction temperature inside of the cluster source nozzle. Species in the oxidation of* Ta_{20}^+ *occur in the ion trap with maximum abundance at specific reaction times* t_{max} *that depend on temperature. The corresponding* τ_{max} *obtained from the reaction in the source is fitted with a power function to five temperature data sets and an exponent (depicted on the right) of 1 is expected for matching temperatures. Reproduced with permission from [155]. Copyright AIP PUBLISHING LLC.*

at several reaction temperatures and τ_{max} is expected to scale linearly with t_{max}, if the reaction in the source is conducted at the same temperature. Figure 4.6 illustrates this relationship with fit functions $t_{max} = a \cdot \tau_{max}^b$ using five data sets for the oxidation reaction inside the ion trap at different temperatures. The exponent b increases from 0.77 for 100 K to 1.53 for 300 K. These results suggest a b value of 1 for a source reaction temperature between 200 K (b = 1.19) and 150 K (b = 0.80). Due to a high backing pressure and a pulsed operation of the carrier and reactive gas valves, there is a low stationary pressure in the volumes inside of the cluster source. Upon opening of the valves, the gases are introduced into the source in an adiabatic expansion, which cools them down. Even though the metal clusters are formed from a hot plasma, collisions with the carrier gas apparently reduce their internal energy and the reactions in the source nozzle occur below room temperature.

4.3.3. Conclusion and outlook

A laser vaporization cluster source was equipped with a secondary collision volume downstream in the expansion nozzle. A solenoid valve with variable pulse duration was used to introduce O_2 into the nozzle. The generation process of bare clusters is unaffected and the subsequent oxidation occurs in a consecutive manner that may be described by pseudo-first order kinetics, similar to the thermalized multi-collision conditions in the ion trap. The reaction kinetics are furthermore indicative of a reaction temperature below room temperature.

As the variation of the O_2 pulse duration controls the extent of the reaction, this cluster source design facilitates the selective formation of target species. Such species of interest may subsequently be mass selected, stored in the ion trap and exposed to an additional reactive gas, which circumvents convoluted multi-collision mass spectra when two reactive gases are introduced at once. The modified cluster source efficiently generates tantalum clusters with a specific number of oxygen atoms, which are subsequently reacted with CH_4 in the following chapters, and the methane activation potential is studied as a function of the oxygen content. As shown in Chapter 8, the cluster source modification is also used to react the tantalum clusters with methane inside of the source nozzle.

THERMAL METHANE ACTIVATION MEDIATED BY BARE TANTALUM CLUSTER CATIONS

5

Cationic tantalum clusters Ta_n^+ are exposed to methane under multi-collision conditions in a cryogenic ring electrode ion trap. The cluster size drastically affects the reaction rate and the number of consecutively dehydrogenated methane molecules. Small clusters ($n = 1 - 4$) dehydrogenate CH_4 and concurrently eliminate H_2, while larger clusters ($n > 5$) demonstrate molecular adsorption of methane. Underlying mechanisms and cluster properties responsible for the change in reactivity are unraveled with the help of experimental insights.

5.1. Introduction

Due to its high abundance in natural resources, the direct transformation of methane into value-added products, *e.g.* methanol, formaldehyde or ethylene, is a tempting goal. CH_4 could, in principle, be utilized as a molecular building block with the help of selective C–H bond activation [12, 13]. However, the high stability, amongst other molecular properties, of methane and easy overoxidation to CO_2 turn the purposeful activation into a demanding task that requires an understanding of operative mechanisms [12, 13]. To that end, the investigation of gas-phase systems is useful as effects are limited to a single reactive center and obstructing interactions are excluded, *e.g.* occurring at interfaces or between reactive sites and support material. Thus, gas-phase studies under well-defined conditions facilitate the observation of molecular-level processes and mechanisms [156].

In extensive studies of many elements, the cationic atoms of various transition metals were found to bind methane, and especially third-row transition metal cations (including Ta^+) dehydrogenate a specific number of CH_4 molecules and simultaneously liberate dihydrogen [53, 54, 56]. The Ta^+/CH_4 system has been studied previously in a Fourier-transform ion cyclotron resonance (FT-ICR) mass spectrometer [54, 152, 157], a guided ion beam experiment [62], a flow-tube reactor [53], with dissociation spectroscopy [158] and by theoretical means [55, 62, 159]. In comparison to single atoms, metal clusters may represent more realistic models of reactive centers, *e.g.* under-coordinated sites of metallic surfaces [17]. However, the findings of bare metal clusters mediating room-temperature methane activation are limited to a few noble metals, *viz.* Pt [66–70, 72], Pd [65, 76] Au [63, 127, 160], and Rh [75] clusters (as well as binary AuPd [64, 77] and AuPt [74] clusters). The corresponding reactivity modes are distinct for the respective elements: on the one hand, small cationic Au, Rh and Pd clusters react with a CH_4 molecule in absence of H_2 liberation (with the exception of Rh_2^+ [75] and Pd_3^+ [64, 76]). Binding modes in this initial activation of methane have been investigated spectroscopically for $[M_nCH_4]^+$ (M = Au [161], Pt [162]). Cooperative coadsorption of additional CH_4 molecules to $[M_2CH_4]^+$ (M = Au [127, 160], Pd [76]) facilitates dihydrogen elimination and C–C bond formation, consequently releasing C_{2-3} hydrocarbons in catalytic cycles. On the other hand, Pt cluster cations directly dehydrogenate methane and concurrently eliminate H_2 [68–70, 72], and some of the resulting Pt cluster methylene complexes undergo the same reaction with a second CH_4 molecule [73]. Lastly, the binary AuPt and AuPd clusters share traits of Au clusters, if the respective content is higher, and traits of Pt/Pd clusters otherwise [64, 74]. Interestingly, $AuPd_2^+$ couples carbon atoms in a catalytic cycle similar to the cationic gold dimer. The important step of C–C bond formation has also been probed in $[Ta(CH_2)_{2-4}]^+$ products generated in the reaction of Ta^+ with methane, but has not been shown conclusively [54, 157].

Closing the gap between the reactive Ta^+ and the inert bulk material may aid in the search of catalysts composed of metals less costly than platinum. The investigation of size-selected clusters in the non-scalable regime may furthermore reveal effects and properties beneficial in the design of catalytic systems for the selective transformation of methane. In this study, cationic tantalum clusters (Ta_n^+, $n = 1 - 10$) are exposed to methane in a cryogenic ring electrode ion trap under well-defined multi-collision conditions that allow the observation of consecutive reactions and promote reactions in excess of endothermicity [17]. In addition to reaction products, size-dependent reaction kinetics are obtained. The reaction mechanisms and product structures are additionally probed with the help of isotopically labeled methane. Ultimately, fundamental effects in methane activation are shown as a function of cluster size.

5.2. Results

5.2.1. Reaction pathways and products

In general, there are two distinct types of reaction: dehydrogenation of methane and concomitant elimination of dihydrogen as well as adsorption of methane in absence of H_2 liberation. Former may occur multiple times in sequence depending on cluster size, schematically shown in Equation 5.1.

$$\mathrm{Ta}_n^+ \xrightarrow[-\mathrm{H_2}]{+\mathrm{CH_4}} [\mathrm{Ta}_n\mathrm{CH_2}]^+ \rightarrow \cdots \rightarrow [\mathrm{Ta}_n\,(\mathrm{CH_2})_x]^+ \qquad \text{with } x \geq 1 \tag{5.1}$$

The molecular nature of hydrogen is not probed as neutral fragments are not detected in this experiment. It is, however, more likely and generally accepted that the two hydrogen atoms are ejected as an H_2 molecule. In case of small clusters ($n = 1 - 4$), molecular adsorption of methane occurs after one or more dehydrogenation steps, whereas it is the sole reaction pathway for larger clusters:

$$[\mathrm{Ta}_n\,(\mathrm{CH_2})_x]^+ \xrightarrow{+\mathrm{CH_4}} \cdots \xrightarrow{+\mathrm{CH_4}} \left[\mathrm{Ta}_n\,(\mathrm{CH_2})_x\,(\mathrm{CH_4})_y\right]^+ \tag{5.2}$$

$$\text{with } x \geq 0, y > 0$$

The atomic cation of tantalum readily reacts when exposed to methane and, in the main reaction channel, the dehydrogenation reaction occurs four subsequent times, yielding $[\mathrm{Ta}\,(\mathrm{CH_2})_4]^+$ as seen in Figure 5.1. Reaction species are noted as $[\mathrm{Ta}\,(\mathrm{CH_2})_x\,(\mathrm{CH_4})_y]^+$ in order to emphasize the lack of structural information obtained from mass spectra and to enable an easier assignment of each species to individual reaction steps. Adsorption of CH_4 in absence of H_2 elimination ultimately generates the major reaction product, $[\mathrm{Ta}\,(\mathrm{CH_2})_4\,(\mathrm{CH_4})]^+$. Intermittent adsorption of CH_4 followed by stabilization through collisions with helium buffer gas atoms may terminate the consecutive dehydrogenation reaction prematurely. As a result, this process leads to the formation of $[\mathrm{Ta}\,(\mathrm{CH_2})\,(\mathrm{CH_4})]^+$ and $[\mathrm{Ta}\,(\mathrm{CH_2})_2\,(\mathrm{CH_4})]^+$, which also adsorb CH_4 in absence of H_2 elimination to form $[\mathrm{Ta}\,(\mathrm{CH_2})\,(\mathrm{CH_4})_2]^+$ and $[\mathrm{Ta}\,(\mathrm{CH_2})_2\,(\mathrm{CH_4})_2]^+$, respectively, as two minor products.

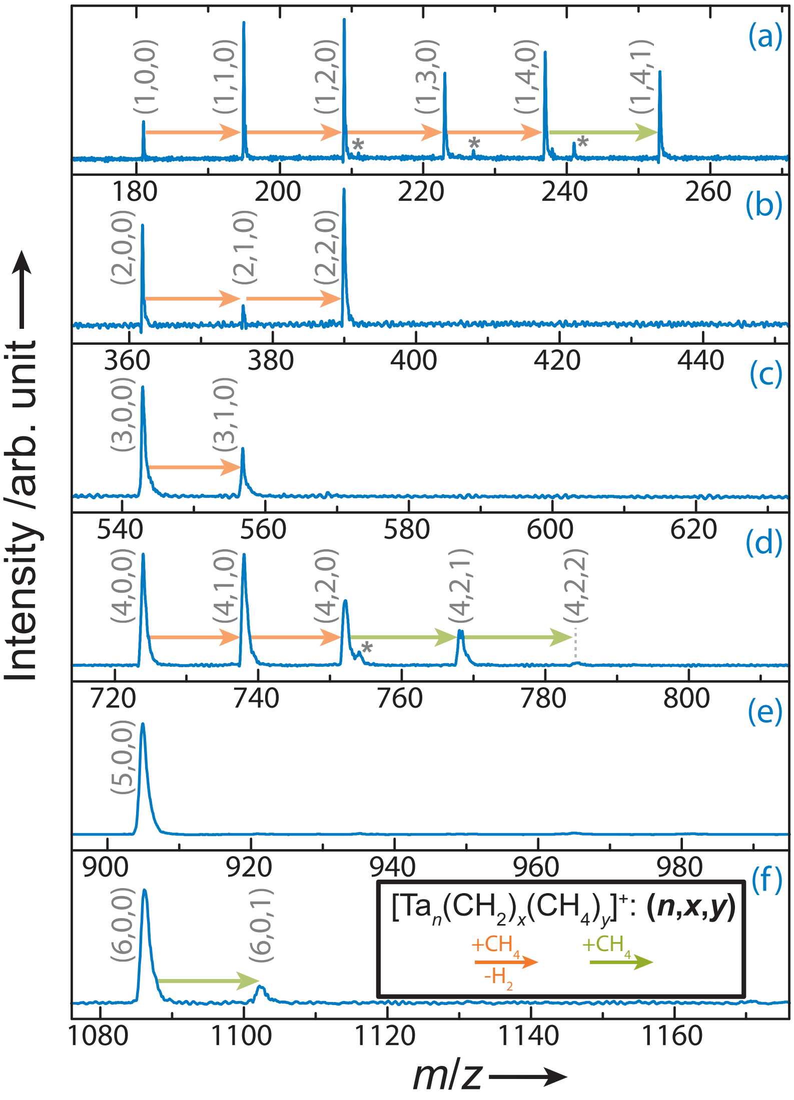

Figure 5.1: *Time-of-flight mass spectra of size-selected* Ta^+_{1-6} *reacting with* CH_4 *for selected storage times to illustrate the size-dependent extent of the dehydrogenation reactions. Orange arrows indicate dissociative adsorption and concomitant* H_2 *elimination, whereas green arrows depict molecular adsorption of methane. Four methane molecules are dehydrogenated in the reaction of* Ta^+ *with* $8.6 \cdot 10^{-4}$ *Pa* CH_4 *after 13 ms (a). In the reaction of* Ta^+_2 *with* $9.2 \cdot 10^{-4}$ *Pa* CH_4*, two methane molecules are dehydrogenated (b, 150 ms) and a single methane molecule is dehydrogenated in the reaction of* Ta^+_3 *(c,* $4.6 \cdot 10^{-2}$ *Pa* CH_4*, 15 ms). Two methane molecules are dehydrogenated in the reaction of* Ta^+_4 *with* $2.2 \cdot 10^{-2}$ *Pa* CH_4*, followed by molecular adsorption (d, 100 ms).* Ta^+_5 *shows no reaction when exposed to* $4.4 \cdot 10^{-2}$ *Pa* CH_4 *(e, after 300 ms) and* Ta^+_6 *demonstrates slow molecular adsorption (f,* $4.4 \cdot 10^{-2}$ *Pa* CH_4*, 500 ms). All reactions are conducted at 300 K in the presence of helium buffer gas at a total pressure of 0.77 Pa. Products of side reactions are marked by an asterisk and are specified in the main text. Chapter A.6 in the Appendix provides additional spectra of larger clusters and of the clusters stored in pure helium.*

Reacting the cationic tantalum dimer, Ta_2^+, with methane at 300 K generates an intermediate, $[Ta_2CH_2]^+$ and a final product, $[Ta_2(CH_2)_2]^+$. In the consecutive reaction of Ta_3^+ with CH_4 a single methane molecule is dehydrogenated under elimination of H_2 to generate $[Ta_3CH_2]^+$. This species also reacts with methane, albeit *via* slow molecular adsorption. When Ta_4^+ is exposed to methane, $[Ta_4CH_2]^+$ forms as an intermediate. Similar to $[Ta_2CH_2]^+$, this species facilitates dehydrogenation of a second CH_4 molecule, concurrently eliminating H_2. The reaction proceeds *via* reversible adsorption of two methane molecules to the resulting $[Ta_4(CH_2)_2]^+$. Additionally, molecular adsorption of methane to $[Ta_4CH_2]^+$ generates $[Ta_4(CH_2)(CH_4)]^+$ as a minor product. Cationic clusters composed of more than four tantalum atoms demonstrate a remarkably low reactivity towards methane. The pentamer cluster, Ta_5^+, undergoes no reaction with CH_4 at a temperature of 300 K (see Fig. A.3). Similar to all $n \geq 2$ species, the formation of weakly bound adducts of the cluster with multiple methane molecules becomes feasible at lower temperatures (see Chapter 5.5.2). At 300 K, Ta_6^+ forms $[Ta_6CH_4]^+$ *via* slow molecular adsorption. Larger cationic tantalum clusters, Ta_n^+ ($n \geq 7-10$), similarly demonstrate an insignificant reactivity towards methane. Dehydrogenation and concomitant ejection of hydrogen is not observed and adsorption of molecular methane proceeds analogously to Ta_6^+. Chapter 5.5.2 provides detailed time-of-flight mass spectra, including some obtained at lower reaction temperatures.

5.2.2. Reaction kinetics

Kinetic modeling subsequently enables the determination of rate coefficients for each reaction step in the consecutive reactions of cationic tantalum clusters toward methane. The simulated results nicely replicate the experimentally determined ion abundances as a function of reaction time (see Chapter 5.5.2). Table 5.1 in Chapter 5.5.2 shows the adapted bimolecular rate coefficients for all of the steps observed in the reaction of the tantalum cation and methane. Interestingly, rate coefficients in the order of $3.5\text{-}4.1 \cdot 10^{-10}$ cm^3s^{-1} are found for the first three and the last step that are part of the main reaction channel of Ta^+, while the formation of $[Ta(CH_2)_4]^+$ is associated with a significantly increased coefficient of $5.5 \cdot 10^{-10}$ cm^3s^{-1}. Another phenomenon is observed in the formation of the two minor products: although the initial reactions in absence of dehydrogenation (to generate $[Ta(CH_2)_{1-2}(CH_4)]^+$) are relatively slow, the following adsorption of CH_4 (to give $[Ta(CH_2)_{1-2}(CH_4)_2]^+$) is increased 30-fold.

In the reaction of the tantalum dimer, the abundance of the intermediate, $[Ta_2CH_2]^+$, remains small throughout, *i.e.* the subsequent reaction of $[Ta_2CH_2]^+$ is much faster than its formation. The bimolecular rate coefficient corresponding to the formation of $[Ta_2CH_2]^+$ is $1.7{\cdot}10^{-11}$ cm^3s^{-1}, more than an order of magnitude smaller than the values determined in the reaction of Ta^+. The second reaction step, however, is associated with an increased rate coefficient of $1.0{\cdot}10^{-10}$ cm^3s^{-1}.
A small rate coefficient of $9.0{\cdot}10^{-13}$ cm^3s^{-1} is determined for the dehydrogenation reaction step mediated by Ta_3^+ (for the kinetic simulation results see Fig. 5.6). In the reaction of the tetramer cluster, the rate coefficients obtained by kinetic modeling (see Fig. 5.7) are comparable to the coefficient found for Ta_3^+. The first and second dehydrogenation steps by Ta_4^+ are associated with an apparent rate coefficient of 7.1 and $6.4{\cdot}10^{-13}$ cm^3s^{-1}, respectively. An equilibrium constant of 0.92 is found for the first molecular adsorption reaction, while the equilibrium of the subsequent reaction is less balanced with a value of 0.25.
The rate coefficients determined in this experiment are of an apparent nature (see Chapter 3.4.2) and the reactions demonstrate negligible or even negative apparent activation energies, which are determined by repeating the experiments at several temperatures between 150 and 300 K. Chapter 5.5.2 illustrates these findings that are caused by a Lindemann energy transfer mechanism. In brief, clusters and methane form an energized association complex, which is either stabilized or dissociates back to the reactants. The dissociation of the complex becomes hindered at lowered temperatures, resulting in an enhanced overall reaction rate. Nevertheless, Chapter 5.5.2 discusses an approach to access the activation energy of the dehydrogenation reactions (indicating barriers that increase from the dimer to the tetramer cluster).

5.2.3. Kinetic isotope effect and exchange reactions

Repeating the reactions with fully deuterated methane confirms the initial mass assignment and corresponding mass spectra are available in Chapter 5.5.4. Exposing Ta^+ to CD_4 generates the analogous intermediates and products $[Ta\,(CD_2)_x\,(CD_4)_y]^+$ ($x = 0 - 4, y = 0 - 2$; see Fig. 5.8). The dehydrogenation of CD_4 is slower compared to the reactions with CH_4. The ratio of the corresponding reaction efficiencies is defined as the kinetic isotope effect (KIE). Table 5.1 in Chapter 5.5.4 displays the KIE of all dehydrogenation reactions. For the dehydrogenation steps in the reaction of Ta^+, KIE values between 1.43±0.41

and 2.01±0.58 are found. This indicates that H_2 formation and elimination limits the rate in these reactions [148]. The intact adsorption to generate the intermediates $[Ta\,(CX_2)\,(CX_4)]^+$ and $[Ta\,(CX_2)_2\,(CX_4)]^+$ (X=H,D) is enhanced for CD_4, *i.e.* there is an inverse KIE (of 0.10±0.03 and 0.38±0.11, respectively). The following adsorption in absence of H_2 elimination, which generates the byproducts $[Ta\,(CX_2)_{1,2}\,(CX_4)_2]^+$, shows no KIE within the error of the experiment. When $[TaCH_2]^+$ reacts with CD_4, H/D exchange generates $[TaCHD]^+$ and subsequently $[TaCD_2]^+$ (see Fig. 5.8). Firstly, this indicates a structure including accessible H atoms, *e.g.* a tantalum carbene, and secondly demonstrates the reversibility of methane adsorption:

$$[TaCH_2]^+ \xrightarrow{+CD_4} [TaCH_2(CD_4)]^+ \rightarrow [TaC_2H_2D_4]^+ \tag{5.3}$$

$$[TaC_2H_2D_4]^+ \rightarrow [TaCHD(CHD_3)]^+ \xrightarrow[-CHD_3]{} [TaCHD]^+ \tag{5.4}$$

The kinetic simulation reveals that exchange reactions also occur on the second intermediates of the main reaction channel $[Ta(CH_2)(CD_2)]^+/[Ta(CHD)(CD_2)]^+$. Including H/D exchanges on the other species is not necessary to replicate the progression of the overall reaction.

Both dehydrogenation steps in the reaction of the tantalum dimer with methane show large KIE values of approximately 7-9. KIE values exceeding 2.5 evidence a C–H bond breaking in the rate-determining step (RDS) [148]. The reaction of Ta_2^+ with a mixture of CH_4 and CD_4 results in the formation of $[Ta_2CHD]^+$, *i.e.* H/D exchange occurs on the intermediates (see Fig. 5.9). Including exchange reactions on the final products $[Ta_2C_2H_xD_{4-x}]^+$ ($x = 0 - 4$) is not required for the kinetic model and lowers the quality of the fitting procedure.

The dehydrogenation of d_4-methane by Ta_3^+ is significantly slower compared to the reaction with h_4-methane, corresponding to a KIE of about 8 (see Fig. 5.10). Exposing the tantalum trimer to a CH_4/CD_4 mixture does not generate $[Ta_3CHD]^+$. The Ta_3^+ methylene clusters likely do not facilitate C–H cleavage in a second methane molecule, thereby hindering an H/D exchange.

Methane dehydrogenation and concomitant hydrogen evolution by the tantalum tetramer cation is associated with a KIE of approximately 7. However, the second reaction step, *i.e.* the formation of $[Ta_4(CH_2)_2]^+$, demonstrates a KIE of 1.69±0.55. The RDS of the first dehydrogenation reaction therefore is C–H cleavage, whereas H_2 formation and elimination likely determines the rate of the second step. Surprisingly, the exchange product $[Ta_4CHD]^+$ is not formed when Ta_4^+ is simultaneously exposed to CH_4 and CD_4. On the other hand, the intermediates $[Ta_4(CH_2)_2]^+/[Ta_4(CH_2)(CD_2)]^+/[Ta_4(CD_2)_2]^+$ undergo H/D exchange reactions to form $[Ta_4(CHD)(CH_2)]^+/[Ta_4(CHD)(CD_2)]^+$ (see Fig. 5.2 and 5.11 in Chapter 5.5.4).

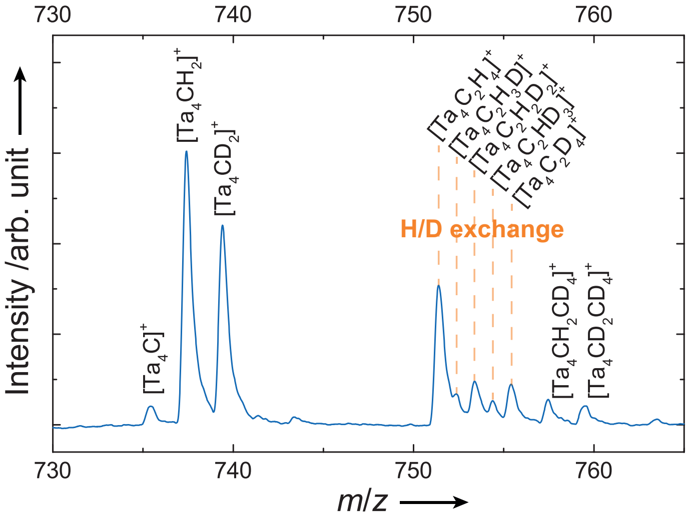

Figure 5.2: *Excerpt of a time-of-flight mass spectrum for Ta_4^+ exposed to a CH_4/CD_4 mixture ($4.6 \cdot 10^{-3}$ Pa/$4.1 \cdot 10^{-2}$ Pa) at 300 K (0.027 s). No significant amount $[Ta_4CHD]^+$ is detected, whereas H/D exchange reactions generate $[Ta_4(CHD)(CH_2)]^+$ and $[Ta_4(CHD)(CD_2)]^+$. The kinetic simulations moreover indicate a reversible H/D exchange on all Ta_4^+ complexes with a second methylene moiety. Note that the peak intensity marked $[Ta_4C_2H_4]^+$ is elevated due to a $[Ta_4N_2]^+$ contribution as the CD_4 cylinder contains a nitrogen impurity.*

5.3. Discussion

Small tantalum cluster cations (Ta_n^+, $n = 1-4$) directly dehydrogenate one or more methane molecules and concurrently eliminate dihydrogen at room-temperature reaction conditions. This behavior is also found for cationic platinum clusters [68, 71, 72, 149] and is different to most gold and palladium clusters that require co-operative coadsorption of two or more methane molecules for H_2 elimination to occur [64, 65, 160]. In contrast to Pt clusters [68, 71], the rate coefficients of Ta clusters illustrate a drastic and monotonic decrease as a function of cluster size. Several effects may be responsible for the influence of cluster size on rate coefficients as well as reaction products, which will be discussed in detail in the following.

5.3.1. Dehydrogenation mechanism

Metallic systems typically bring about CH_4 activation and concurrent H_2 elimination *via* twofold metal-mediated C–H bond insertion. In Chapter 6, quantum-chemical calculations show the same mechanism to be operative in Ta_4^+/CH_4. On the other hand, the atomic Ta cation potentially adopts a four centered Ta–H–H–C ring geometry in an alternative pathway [62]. In the case of Ta_2^+ and Ta_3^+, C–H insertion by Ta atoms may be assumed to facilitate the dehydrogenation of methane. For these insertion reactions, the charge state plays a crucial role, which was observed for cationic Pt clusters being more reactive than the neutral counterparts that are in turn more reactive than anionic clusters [66, 68, 69]. As a consequence, local charges may also affect the methane dehydrogenation rate in cationic tantalum clusters. With increasing cluster size, the single positive charge may be delocalized over an increasing number of atoms, thus elevating C–H insertion barriers and decreasing the activity. This is also evidenced by the change of the rate-determining step: dihydrogen elimination for Ta^+ and C–H cleavage for $n \geq 2$, *i.e.* the initial scission of the C–H bond becomes hindered, while H_2 liberation does not (as much). The monotonous decrease of the dehydrogenation rate as a function of size indicates a significant increase of the C–H cleavage barrier for Ta_4^+ compared to the small activation energies determined for Ta^+ [62]. The current findings imply that the barriers in the reaction of Ta_2^+ and Ta_3^+ lie somewhere between those of the atomic system and the tetramer cluster, assuming a similar exothermic driving force (see also Chapter 5.5.2). Additionally, the clusters become more saturated with increasing size, *i.e.* the number of Ta–Ta bonds increases and valence electrons available for bond breaking and making during reactions diminish. The absence of highly under-coordinated Ta atoms render an exothermic Ta–C bond formation less likely and also explains the inertness of larger clusters.

5.3.2. Comparison of cationic Pt, Au and Ta clusters

Pt cluster cations dehydrogenate methane under single-collision conditions, *i.e.* there are no significant barriers in excess of endothermicity, and larger clusters (up to $n = 20$) still demonstrate dehydrogenation activity, with a minimum occurring for Pt_4^+ [68, 69]. Cationic tantalum clusters thus demonstrate a very different behavior regarding reaction barriers compared to the corresponding platinum counterparts and the similarity to gold clusters (which adsorb single methane molecules in absence of H_2 elimination) increases with size. The different reactivity of the atomic cations has previously been related to a combination of

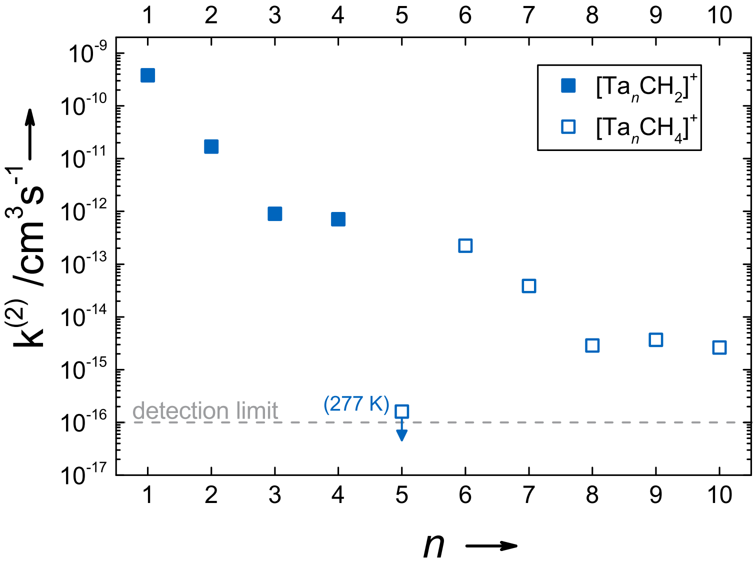

Figure 5.3: *Logarithmic plot of bimolecular rate coefficients $k^{(2)}$ for the formation of $[Ta_nCH_2]^+$ (closed squares) and $[Ta_nCH_4]^+$ (open squares) as a function of cluster size n. Dehydrogenation and concurrent dihydrogen elimination prevails for $n = 1 - 4$, demonstrating a monotonic decrease of the corresponding $k^{(2)}$, whereas larger clusters ($n \geq 5$) solely undergo molecular adsorption with a minimum $k^{(2)}$ occurring at $n = 5$. The arrow indicates an extrapolation to 300 K for the rate coefficient of the pentamer cluster obtained at 277 K.*

(i) orbital size, or more precisely the relative 6s and 5d orbital size of third-row transition metals affecting s-d hybridization, (ii) the promotion energy to adopt a $d^{n-1}s^1$ electronic state facilitating a bond to a methylene unit and (iii) exchange energy due to a loss of s-d and d-d interactions upon bonding the methylene unit [54]. As a result of the electronic configurations (Ta: $5d^3 6s^2$, Pt: $5d^9 6s^1$, Au: $5d^{10} 6s^1$), Ta^+ does not demand promotion, while Pt^+ and Au^+ require a promotion energy of 0.59 and 1.86 eV, respectively [54]. The Pt cation seemingly compensates due to a small 6s orbital with a root-mean-square radius of 1.59 Å, compared to 1.56 and 1.80 Å for Au^+ and Ta^+, respectively [54, 163]. Lastly, the exchange energy is 0.79 eV (Pt^+), 0.21 eV (Au^+) and 1.32 eV (Ta^+) [54]. Although the exchange energy required in the reactions of the corresponding clusters is unknown, the promotion energy will be a decisive factor in the reaction rate. The electronic configuration of platinum suggests an abundance of unpaired 6s and 5d electrons independent of cluster size. On the other hand, fewer unpaired 6s electrons might be available in tantalum clusters, thereby elevating the promotion energy and diminishing the reactivity.

As a result, cationic tantalum clusters become less similar to Pt clusters and more comparable to Au clusters with increasing size. This effect is reflected by a change in the rate coefficients for a reaction towards methane ($Pt^+ \approx Ta^+ > Au^+$; $Pt_2^+ > Ta_2^+ > Au_2^+$; $Pt_3^+ \gg Ta_3^+ > Au_3^+$; $Pt_4^+ \gg Ta_4^+ \approx Au_4^+$)[1] and a change in the reactivity mode (dihydrogen elimination for $n = 1 - 4$ and molecular adsorption for $n > 4$). While the rate coefficients decrease with cluster size, the Ta_2^+ and Ta_4^+ methylene species still facilitate dehydrogenation of a second methane molecule. In contrast, Pt_2^+ and Pt_4^+ do not demonstrate the same behavior and the generation of $[Pt_5C_2H_4]^+$ during the reaction with methane was attributed to the size of the cluster core, which potentially enables bonding of two methylene units [72, 73].

5.3.3. Potential product structures

The interpretation of reaction kinetics and occurrence of H/D exchange in some of the species are helpful to confirm or rule out structural motifs. Early studies simultaneously exposed Ta^+ to CH_4 and CD_4 and observed scrambling on

---

[1] Pt^+ through Pt_4^+: 4.9 [53], 8.2, 6.0 and $0.2 \cdot 10^{-10} cm^3 s^{-1}$ [72];
Ta^+ through Ta_4^+: 3.80, 0.14, 0.009 and $0.007 \cdot 10^{-10} cm^3 s^{-1}$;
Au^+ through Au_4^+: 0.12, 0.0015, 0.0011 and $<0.0028 \cdot 10^{-10} cm^3 s^{-1}$ [64, 127]

$[TaCH_2]^+$, pointing to a tantalum carbene [54]. The carbene structure of this species has been predicted previously by theoretical means [62, 159], and was confirmed and shown to be distorted due to agostic interactions, recently with the help of dissociation spectroscopy [158]. Although not conclusive, collision-induced dissociation (CID) suggests a bis-carbene structure of $[Ta(CH_2)_2]^+$ [54, 157]. The current kinetic simulations of the reaction of $[TaCH_2]^+$ with CD_4 indicate that H/D exchange occurs on $[TaCH_xD_{2-x}]^+$ and $[TaC_2H_xD_{4-x}]^+$, but not on $[TaC_3H_xD_{6-x}]^+$, $[TaC_4H_xD_{8-x}]^+$ ($x = 2, 1$) or other species. Adsorption of CH_4 to $[Ta(CH_2)_2]^+$ could induce formation of an acetelyne unit and concomitant H_2 release. A less strong binding of the acetelyne group and the methane molecule in the resulting $[Ta(C_2H_2, CH_4)]^+$ could prevent H/D exchange reactions. In addition, this type of binding situation could cause the enhanced rate of the subsequent dehydrogenation reaction that generates $[TaC_4H_8]^+$, which potentially contains a methane, an acetelyne and a methylene group. As CID of $[TaC_3H_6]^+$ and $[TaC_4H_8]^+$ primarily generates one or more H_2 molecules followed by CH_4 in likelihood, the suggested $[Ta(C_2H_2, CH_4)]^+$ and $[Ta(C_2H_2, CH_4, CH_2)]^+$ structures cannot be ruled out.

Furthermore, the observations from H/D exchange suggest a carbene structure for $[Ta_2CH_2]^+$, but are inconclusive for $[Ta_2(CH_2)_2]^+$. However, the formation rate of $[Ta_2(CH_2)_2]^+$ shows a sixfold increase compared to the previous reaction step. The high KIE implies significant barriers in both reaction steps, thus excluding thermodynamic effects. More likely, the carbene unit in $[Ta_2CH_2]^+$ is connected to a single Ta atom and polarizes the opposite Ta atom, which could reduce the C–H cleavage barrier in the subsequent reaction step. The inert nature of the resulting product could be caused by a $[H_2C{=}Ta\text{-}Ta{=}CH_2]^+$ geometry, in which each Ta atom is saturated by a carbene ligand.

No exchange reactions with CD_4 are observed for the intermediate of the trimer cluster, potentially due to a lack of C–H cleavage in a subsequently adsorbed methane molecule. Assuming a triangular geometry, $[Ta_3CH_2]^+$ could contain a methylene ligand that bridges a Ta–Ta bond. Although the adsorption of a second methane molecule would be feasible on the unligated Ta atom, the subsequent twofold C–H scission, stabilization of two H atoms and, ultimately, the combination and release of H_2 would be greatly hindered. The dehydrogenation of a second CH_4 molecule by $[Ta_3CH_2]^+$ would also be hampered in case of a triangular dihydrido-carbide structure, *i.e.* when each Ta–Ta bond is bridged by either a C atom or one of the H atoms. Such a binding situation could also explain the suppressed formation of $[Ta_3(CH_2)(CH_4)]^+$ due to a lack of unligated adsorption sites. While the methylene units on the atomic cation and the dimer are likely carbenes, the Ta_4^+ methylene species prohibits exchange reactions. The temperature-dependent behavior requires methane adsorption to $[Ta_4CH_2]^+$ to be reversible, and $[Ta_4CH_2]^+$ facilitates dehydrogenation of a second methane molecule. Thus, the absence of H/D exchange must be caused by strongly bound H atoms in $[Ta_4CH_2]^+$. The exchange reactions of the second intermediates $[Ta_4C_2H_xD_{4-x}]^+$ ($x = 0 - 4$) are evidence for less strongly bound H(D) atoms and furthermore demonstrate that C–H(D) bonds from a third methane molecule may be cleaved. These observations agree with a prediction by DFT calculations (see Chapter 6), indicating a transformation of the methylene complex, $[Ta_4CH_2]^+$, into a dihydrido carbide, $[Ta_4(C,H,H)]^+$. As the formation of this carbide (high KIE) and the subsequent reaction step (low KIE) show a similar rate, the corresponding formation of $[Ta_4(CH_2)_2]^+$ has to be associated with a significant elevated barrier for dihydrogen elimination. At the same time, this species undergoes twofold H/D exchange, again agreeing with the most stable structure determined by DFT (see Chapter 6), a dihydrido-carbide-methylene cluster complex ($[Ta_4(C,H,H,CH_2)]^+$). Similar to the binding situation in the product of the trimer cluster, the high coordination of Ta atoms in the $[Ta_4(C,H,H,CH_2)]^+$ cluster would severely hinder H_2 elimination from a third methane molecule. Although H/D exchange reactions of this species indicate C–H scission in an additionally adsorbed CH_4 (CD_4) molecule, the binding situation could exclude cleavage of a second C–H bond, recombination of the H atoms and dihydrogen release.

5.4. Summary

Surprising size effects are observed in the activation of methane by cationic tantalum clusters. Insights obtained from dehydrogenation as well as H/D exchange products and from reaction kinetics are used to elucidate these findings, relating them to an interplay of electronic and geometric effects. While small Ta clusters share traits with their Pt counterparts and liberate dihydrogen from one or more CH_4 molecules, larger clusters are inert or undergo molecular adsorption in absence of dehydrogenation, similar to cationic Au clusters. As the cluster size increases, the positive charge may become diluted and the number of unpaired 6s electrons could diminish. The barriers for the initial C–H insertion may therefore become elevated, thereby significantly decreasing the reaction rate with increasing cluster size. On the other hand, geometric effects could additionally determine the number of methane molecules dehydrogenated by the clusters, which varies non-monotonically. Coupling of methylene units *via* C–C bond formation is likely limited to the reaction mediated by Ta^+, thus causing the formation of $[TaC_4H_8]^+$. A symmetric bis-carbene structure explains the inertness of $[Ta_2(CH_2)_2]^+$ and a dihydrido-carbide geometry of $[Ta_3CH_2]^+$ potentially hinders a subsequent reaction. The tetramer cluster apparently forms a dihydrido-carbide-methylene complex, $[Ta_4(C,H,H,CH_2)]^+$, that may activate a third methane molecule, but does not bring about H_2 elimination. Consequently, these results unravel effects that stimulate the search for catalysts based on non-noble metals. The unique change in the reactivity mode will motivate further studies of tantalum systems, for example exploiting the size effects to tune the selectivity of reactions, or probing C–O coupling mechanisms and the release of oxidation products. Latter reactions will be explored in Chapter 8.

5.5. Supplementary Information

5.5.1. Rate coefficients and KIE

Table 5.1 displays bimolecular rate coefficients for reactions toward CH_4 and CD_4, as well as theoretical collision rates according to the surface charge capture (SCC) theory by Kummerlöwe and Beyer [143] of bare metal clusters with CH_4 and CD_4, $k^{\mathrm{SCC}}_{\mathrm{CH_4}}$ and $k^{\mathrm{SCC}}_{\mathrm{CD_4}}$. The kinetic isotope effect (KIE) is calculated as the ratio of the experimental rate coefficients, $k^{(2)}_{\mathrm{CH_4}}$ to $k^{(2)}_{\mathrm{CD_4}}$, multiplied by the ratio of theoretical collision rates, $k^{\mathrm{SCC}}_{\mathrm{CD_4}}$ to $k^{\mathrm{SCC}}_{\mathrm{CH_4}}$, which is approximately 90%.

Table 5.1: *Bimolecular rate coefficients $k^{(2)}$ and theoretical collision rates k^{SCC} in units of $10^{-11}\,cm^3\,s^{-1}$ in the consecutive reaction of Ta_n^+ with CH_4 and CD_4, which are used to calculate the respective kinetic isotope effect (KIE).*

Reaction product	$k^{(2)}_{\mathrm{CH_4}}$ [a]	$k^{(2)}_{\mathrm{CD_4}}$ [a]	$k^{\mathrm{SCC}}_{\mathrm{CH_4}}$ [b]	$k^{\mathrm{SCC}}_{\mathrm{CD_4}}$ [b]	KIE
$[TaCH_2]^+$	38.00±7.70	17.00±3.41	143	129	2.01±0.57
$[Ta(CH_2)_2]^+$	35.20±7.11	20.09±4.03			1.58±0.45
$[Ta(CH_2)_3]^+$	40.54±8.19	25.49±5.12			1.43±0.41
$[Ta(CH_2)_4]^+$	55.38±11.20	34.28±6.90			1.45±0.41
$[Ta(CH_2)_4(CH_4)]^+$	31.09±6.28	22.37±4.49			1.25±0.36
$[Ta(CH_2)(CH_4)]^+$	1.05±0.22	9.90±1.98			0.10±0.03
$[Ta(CH_2)(CH_4)_2]^+$	37.29±11.22	36.93±7.49			0.91±0.33
$[Ta(CH_2)_2(CH_4)]^+$	2.60±0.53	6.17±1.24			0.38±0.11
$[Ta(CH_2)_2(CH_4)_2]^+$	68.68±19.85	72.66±1.88			0.85±0.33
$[Ta_2CH_2]^+$	1.68±0.39	0.18±0.04	154	139	8.69±1.94
$[Ta_2(CH_2)_2]^+$	10.12±2.05	1.31±0.28			6.94±1.56
$[Ta_3CH_2]^+$	0.09±0.01	0.01±0.00	164	147	8.48±2.67
$[Ta_3(CH_2)(CH_4)]^+$	<0.01				
$[Ta_4CH_2]^+$	0.07±0.01	0.01±0.00	172	154	6.98±2.23
$[Ta_4(CH_2)_2]^+$	0.06±0.01	0.03±0.01			1.69±0.55
$[Ta_5CH_4]^+$	<0.01		179	160	
$[Ta_6CH_4]^+$	0.03±0.01		185	166	
$[Ta_{7-10}CH_4]^+$	<0.01				

[a] Rate coefficients referenced to $[TaCH_2]^+$ formation determined by Shayesteh *et al.* [53] (see Chapter A.5). [b] Collision rates of bare metal clusters with CH_4 and CD_4 according to SCC theory [143].

5.5.2. Temperature-dependent reactions with CH_4

This chapter provides plots to illustrate the kinetic modeling results and temperature-dependent data. The reactions of Ta_n^+ ($n = 1 - 9$) with methane are repeated at several temperatures, typically ranging from 150 to 300 K (see Figs. 5.4-5.7 and Chapter A.6 in the Appendix). As molecular adsorption becomes enhanced at lower temperatures, the cluster complexes non-dissociatively adsorb additional methane molecules (with the exception of Ta^+ and its products). Figures 5.4-5.7 include low-temperature mass spectra and Arrhenius plots of logarithmic termolecular rate coefficients (apparent pseudo-first order rate coefficients normalized to He and CH_4 particle density, see Chapter 3.4.2) versus the inverse reaction temperature, which are shown for selected reaction steps. Table 5.2 lists the as-obtained apparent activation energies. The apparent activation energies for Ta_{1-9}^+/CH_4 are subsequently discussed in the next chapter and a method to obtain underlying dehydrogenation barriers is described.

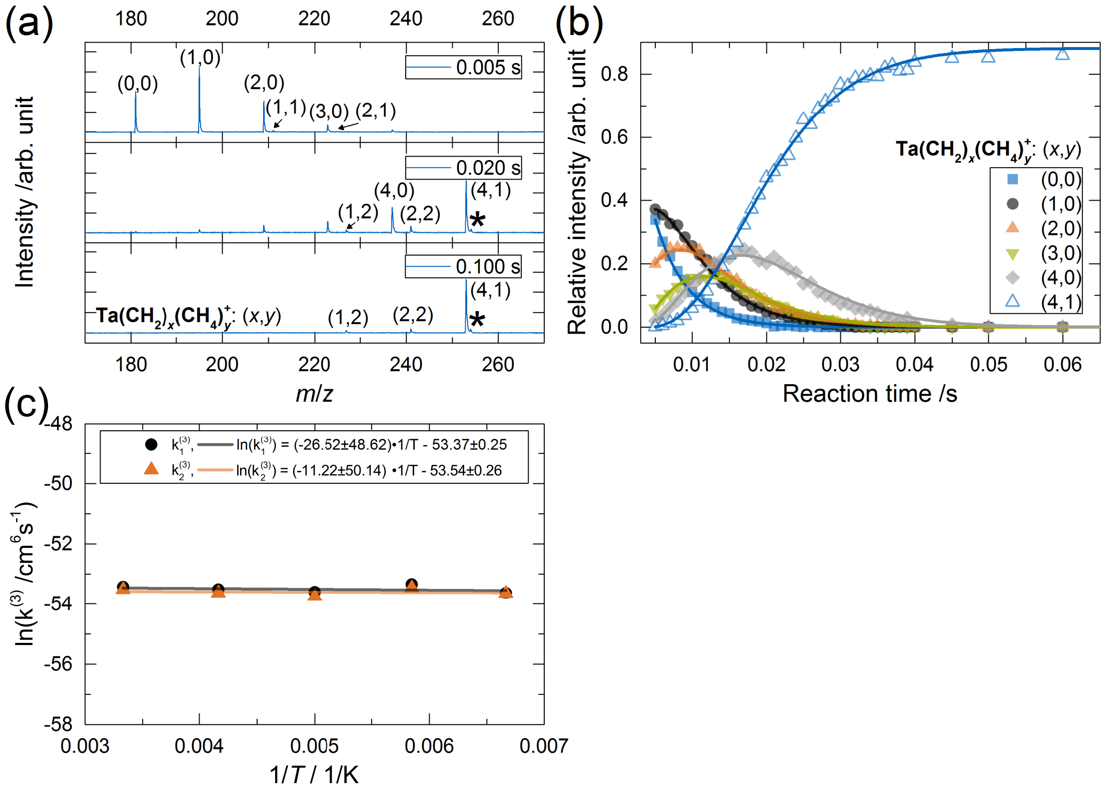

Figure 5.4: *Mass spectra (a), kinetic simulation (b) and Arrhenius plot (c) for the reaction of* Ta^+ *with methane* ($8.6 \cdot 10^{-4}$ *Pa partial pressure). The reaction consecutively produces several species,* $[Ta(CH_2)_x(CH_4)_y]^+$ *with* $x = 0 - 4$ *and* $y = 0 - 2$ *(a), and the change of ion abundances in the course of the reaction is successfully replicated* via *kinetic modeling (b). The star in the mass spectra (a) marks a final product species with a single carbon atom replaced by a naturally occurring* ^{13}C *isotope. Measurement points in (b) are depicted as symbols, while solid lines show the result of the kinetic simulation. In (c), an Arrhenius plot exemplarily shows the change of the apparent termolecular rate coefficients of the first two reaction steps as a function of temperature. The other reaction steps are similarly independent of temperature (see Tab 5.2).*

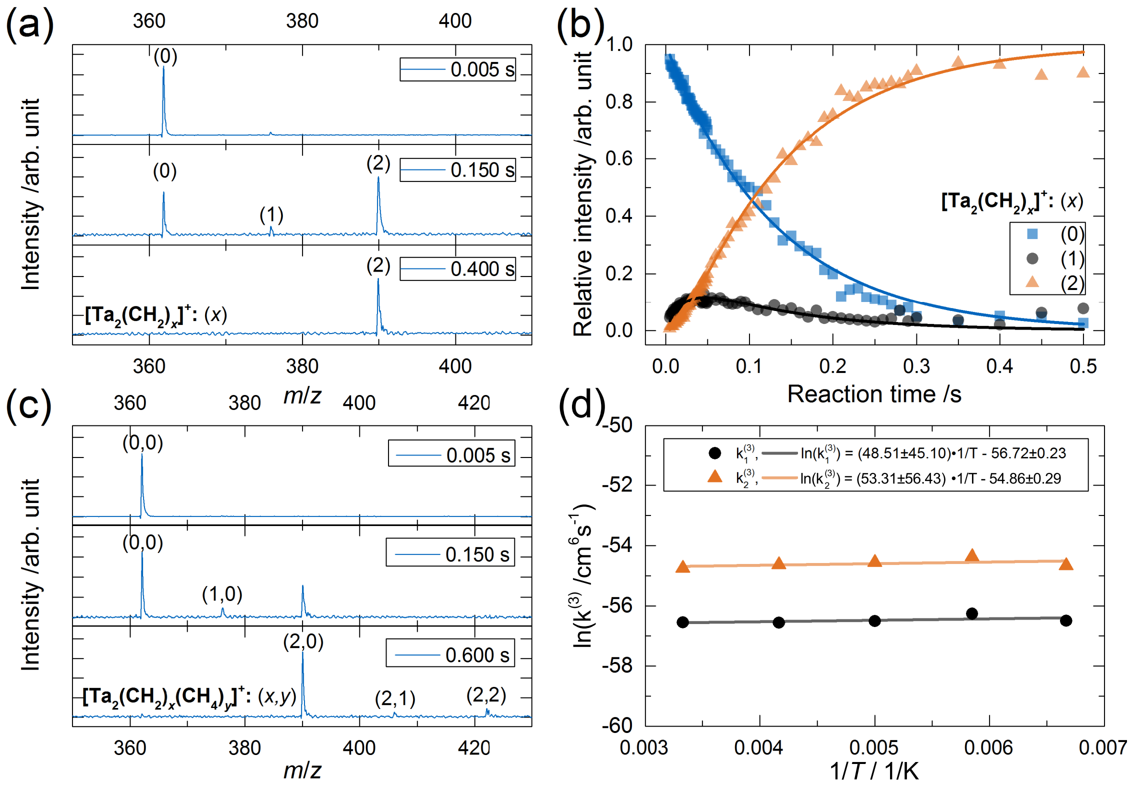

Figure 5.5: *Mass spectra (a and c), kinetic simulation (b) and Arrhenius plot (d) for the reaction of Ta$_2^+$ with methane ($9.2 \cdot 10^{-4}$ Pa partial pressure). At 300 K, the reaction produces two species, [Ta$_2$CH$_2$]$^+$ and [Ta$_2$(CH$_2$)$_2$]$^+$ (a), and the change of ion abundances in the course of the reaction is successfully replicated* via *kinetic modeling (b). Measurement points in (b) are depicted as circles, squares and triangles, while solid lines show the result of the kinetic simulation. Additional products of consecutive molecular adsorption form at lower temperatures as seen in the mass spectrum measured at 150 K (c). In (d), an Arrhenius plot illustrates the change of the apparent termolecular rate coefficients as a function of reaction temperature and the apparent activation energies are subsequently obtained by multiplying the slope of the fitted lines with the negative universal gas constant, $-R$.*

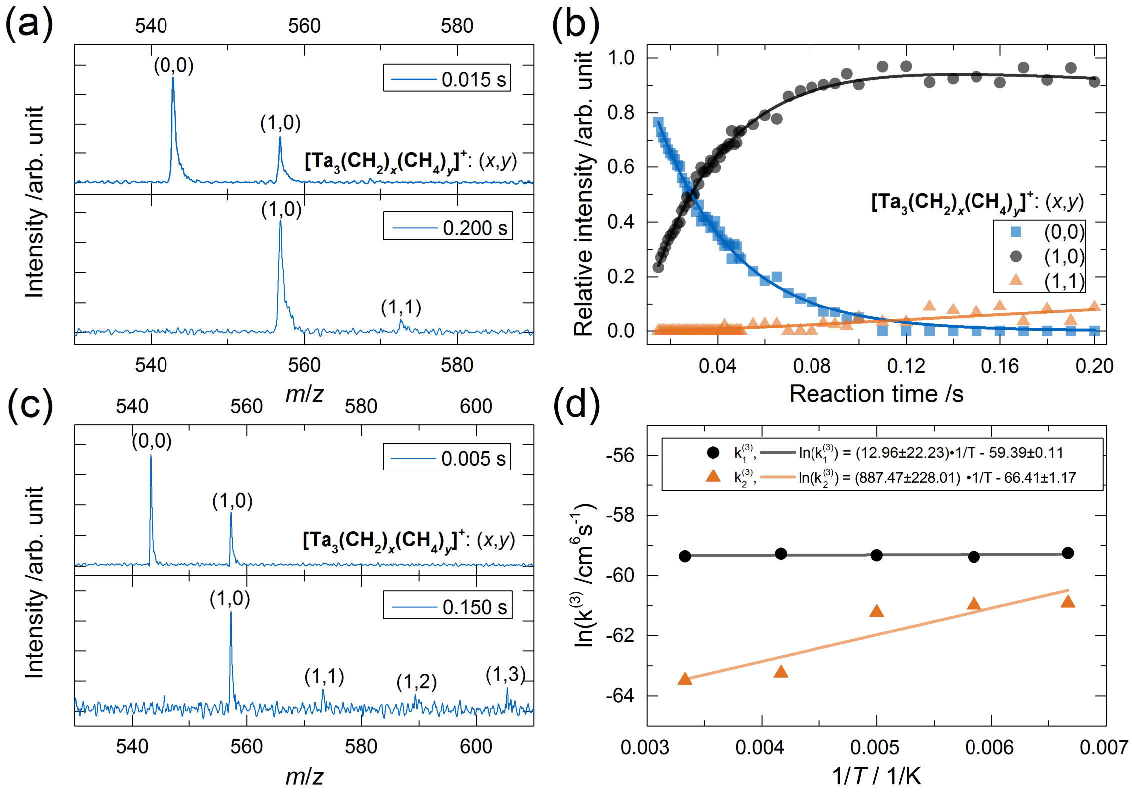

Figure 5.6: *Mass spectra (a and c), kinetic simulation (b) and Arrhenius plot (d) for the reaction of Ta_3^+ with methane ($4.6 \cdot 10^{-2}$ Pa partial pressure). At 300 K, the reaction produces two species, $[Ta_3CH_2]^+$ and $[Ta_3(CH_2)(CH_4)]^+$ (a), and the change of ion abundances in the course of the reaction is successfully replicated* via *kinetic modeling (b). Measurement points in (b) are depicted as circles, squares and triangles, while solid lines show the result of the kinetic simulation. Additional products of consecutive molecular adsorption form at lower temperatures as seen in the mass spectrum measured at 150 K (c). In (d), an Arrhenius plot illustrates the change of the apparent termolecular rate coefficients as a function of reaction temperature and the apparent activation energies are subsequently obtained by multiplying the slope of the fitted lines with the negative universal gas constant, $-R$.*

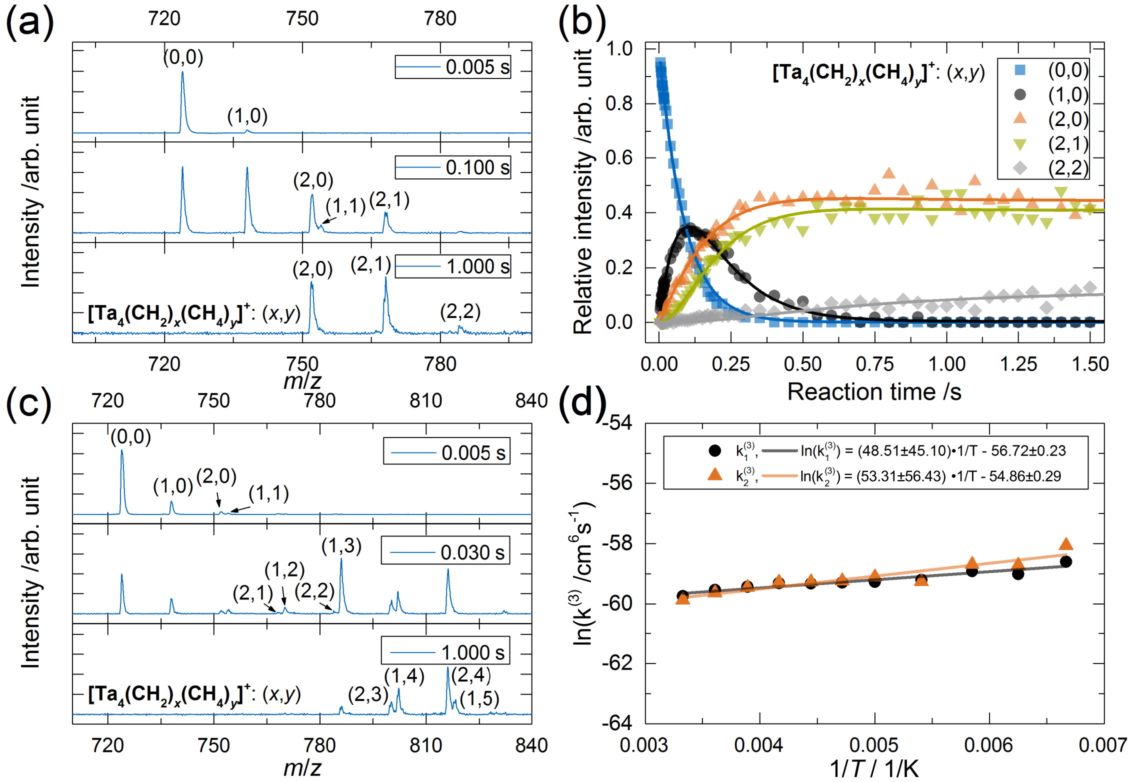

Figure 5.7: *Mass spectra (a and c), kinetic simulation (b) and Arrhenius plot (d) for the reaction of* Ta$_4^+$ *with methane* ($2.2 \cdot 10^{-2}$ *Pa partial pressure). The reaction proceeds* via *consecutive dehydrogenation of two methane molecules followed by reversible molecular adsorption (a), and the change of ion abundances in the course of the reaction is successfully replicated* via *kinetic modeling (b). Measurement points in (b) are depicted as symbols, while solid lines show the result of the kinetic simulation. Additional products of consecutive molecular adsorption form at lower temperatures as seen in the mass spectrum measured at 150 K (c). In (d), an Arrhenius plot illustrates the change of the apparent termolecular rate coefficients as a function of reaction temperature and the apparent activation energies are subsequently obtained by multiplying the slope of the fitted lines with the negative universal gas constant,* $-R$.

Table 5.2: *Apparent activation energy in the reactions of cationic tantalum clusters with methane. The apparent activation energy of the overall process* $E_A^{app}(k^{(3)})$ *and modeled activation energies of the adsorption-complex dissociation step* $E_A^{mod}(k'_d)$ *and the dehydrogenation/hydrogen elimination step* $E_A^{mod}(k'_e)$ *are displayed in units of J mol*$^{-1}$.

Product	$E_A\left(k^{(3)}\right)$ [a]	$E_A\left(k'_d\right)$	$E_A\left(k'_e\right)$ [b]
$[TaCH_2]^+$	221		
$[Ta(CH_2)_2]^+$	93		
$[Ta(CH_2)_3]^+$	915		
$[Ta(CH_2)_4]^+$	1319		
$[Ta(CH_2)_4(CH_4)]^+$	11		
$[Ta(CH_2)(CH_4)]^+$	-973		
$[Ta(CH_2)(CH_4)_2]^+$	-946		
$[Ta(CH_2)_2(CH_4)]^+$	2105		
$[Ta(CH_2)_2(CH_4)_2]^+$	306		
$[Ta_2CH_2]^+$	-403		2505
$[Ta_2(CH_2)_2]^+$	-443		2808
$[Ta_2(CH_2)_2(CH_4)]^+$	-2844	3974	
$[Ta_3CH_2]^+$	-108		7501
$[Ta_3(CH_2)(CH_4)]^+$	-7379	8759	
$[Ta_4CH_2]^+$	-403		11457
$[Ta_4(CH_2)_2]^+$	-443		10472
$[Ta_4(CH_2)_2(CH_4)]^+$	-10958	14525	
$[Ta_5CH_4]^+$	-21835		
$[Ta_6CH_4]^+$	-10381		
$[Ta_7CH_4]^+$	-16868		
$[Ta_8CH_4]^+$	-21365		
$[Ta_9CH_4]^+$	-25111		

[a] Reactions associated with $E_A^{app} < 1$ kJ mol^{-1} are virtually independent of temperature and the corresponding E_A^{app} values are affected by errors of ±100%. Otherwise errors of approximately ±30% are observed. [b] The apparent activation energy of the dehydrogenation/H_2 elimination step is estimated based on the temperature-dependent molecular adsorption of methane to yield another species in the consecutive reaction (see the following chapter).

5.5.3. Discussion of apparent activation energies

Reactions in absence of H_2 elimination become enhanced at lower temperatures (see Tab. 5.2), which is indicative of molecular adsorption under operation of a Lindemann mechanism of energy transfer (see Chapter 3.4.2). Collision of a cluster complex with methane leads to the formation of an energized intermediate, described by k_a:

$$[\mathrm{Ta}_n\,(\mathrm{CH}_2)_x]^+ + \mathrm{CH}_4 \underset{k_d}{\overset{k_a}{\rightleftharpoons}} [\mathrm{Ta}_n\,(\mathrm{CH}_2)_x\,(\mathrm{CH}_4)]^{+*} \xrightarrow[k_s]{+\mathrm{He}} [\mathrm{Ta}_n\,(\mathrm{CH}_2)_x\,(\mathrm{CH}_4)]^+ + \mathrm{He}^* \quad (5.5)$$

where $x \geq 0$ methylene moieties may be present in the cluster complex. The energized intermediate may dissociate back to the reactants (k_d) or may collide with a helium atom that removes the excess energy, which leads to stabilization of the intermediate and formation of the product (k_s). The collision with methane and helium is rather unaffected by temperature. The dissociation of the energized intermediate, however, is suppressed at lower temperatures, resulting in an increased overall reaction rate and a formally negative activation energy (see Tab. 5.2). Interestingly, the negative activation energies for molecular adsorption reactions increase with cluster size, *e.g.* from -2.8 to -11 kJ mol^{-1} for the formation of $[\mathrm{Ta}_2\,(\mathrm{CH}_2)_2\,(\mathrm{CH}_4)]^+$ and $[\mathrm{Ta}_4\,(\mathrm{CH}_2)_2\,(\mathrm{CH}_4)]^+$, respectively, and from -10 to -25 kJ mol^{-1} for the formation of $[\mathrm{Ta}_n\mathrm{CH}_4]^+$ ($n = 6 - 9$). The pentamer cluster is an exception from this trend, as the adsorption of CH_4 is hindered at 300 K and the formation of weakly bound adducts then becomes quickly enhanced at lower temperatures, resulting in a relatively large negative apparent activation energy of -22 kJ mol^{-1}.

With the experimentally determined rate coefficient of the overall process $k^{(3)}$ as a function of temperature, the temperature dependence of the dissociation step may be accessed by modeling the theoretical collision rates of the ions with methane and helium (see Chapter 3.4.2 for a detailed explanation). The following equation expresses the modeled dissociation rate coefficient k'_d as a function of the experimentally determined $k^{(3)}$ and the rate coefficients for the collision with helium and methane, k_s^{mod} and k_a^{mod}, described by the SCC model [143]:

$$k^{(3)} = \frac{k_s k_a}{k_d} \Rightarrow k'_d = \frac{k_s^{mod} k_a^{mod}}{k^{(3)}} \quad (5.6)$$

Furthermore, the dehydrogenation reactions demonstrate small, negative apparent activation energies (see Tab. 5.2). A positive dehydrogenation barrier may be masked by the temperature dependence of the adsorption-complex dissociation.

The dehydrogenation of methane may be modeled similarly to the adsorption in absence of H_2 elimination:

$$[\mathrm{Ta}_n\,(\mathrm{CH}_2)_x]^+ + \mathrm{CH}_4 \underset{k_d}{\overset{k_a}{\rightleftharpoons}} [\mathrm{Ta}_n\,(\mathrm{CH}_2)_x\,(\mathrm{CH}_4)]^{+*} \xrightarrow[-\mathrm{H}_2^*]{k_e} [\mathrm{Ta}_n\,(\mathrm{CH}_2)_{x+1}]^+ \tag{5.7}$$

The energized intermediate undergoes a dehydrogenation reaction and relaxes *via* H_2 elimination, which is described by the rate coefficient k_e. Formulating the rate law of the reaction (see Chapter 3.4.2) results in a simplified rate coefficient for the overall dehydrogenation reaction, displayed in Equation 5.8. The modeled rate coefficient for the dehydrogenation/elimination step k'_e is thus expressed as a function of the coefficients for the overall reaction ($k^{(3)}$) and the complex dissociation (k_d), and the collision rate toward methane according to SCC theory (k_a^{mod}):

$$k^{(3)} = \frac{k_e k_a}{k_e + k_d} \Rightarrow k'_e = \frac{k^{(3)} k_d}{k_a^{mod} - k^{(3)}} \tag{5.8}$$

In a direct dehydrogenation and concurrent H_2 elimination reaction, however, the coefficients for the adsorption-complex dissociation and the dehydrogenation/elimination are not independently accessible (as the adsorption-complex intermediate is not detected). In an approximation, k_d may be assumed to be identical for similar species. For example, the Ta_3^+ cluster dehydrogenates methane and the resulting $[\mathrm{Ta}_3(\mathrm{CH}_2)]^+$ species molecularly adsorbs methane. Latter adsorption reaction is used to determine k'_d (see Eq. 5.6). As the initial complex dissociation of $[\mathrm{Ta}_3(\mathrm{CH}_4)]^+$ and $[\mathrm{Ta}_3(\mathrm{CH}_2)(\mathrm{CH}_4)]^+$ are similar processes, the as-obtained k'_d is subsequently used to calculate k'_e of the dehydrogenation reaction mediated by Ta_3^+ (see Eq. 5.8). The consecutive dehydrogenation reactions of $\mathrm{Ta}_{2-4}^+/\mathrm{CH}_4$ are analyzed in this fashion and the result is displayed in Table 5.2, with a separate column for the activation energy of the dissociation coefficients k'_d utilized in the approximation of k'_e. The temperature-dependent reactions of $\mathrm{Ta}^+/\mathrm{CH}_4$ indicate an absence of molecular adsorption processes, and the aforementioned approximation is therefore unavailable. Nonetheless, this procedure results in reaction barriers in agreement with the monotonous decrease of the rate coefficients as a function of cluster size. The dehydrogenation steps in the reaction of the tantalum dimer system show barriers of ~2.5 kJ mol^{-1}, while a value of 7.5 kJ mol^{-1} is found for Ta_3^+ and the tetramer cluster system demonstrates a dehydrogenation barrier of 11.5 kJ mol^{-1} in the first and 10.5 kJ mol^{-1} in the second step. The thermochemical analysis, albeit based on rough approximations, thus qualitatively relates the decreasing methane dehydrogenation activity to reaction barriers that increase with cluster size.

5.5.4. Reactions with CD_4 and CH_4/CD_4 mixtures

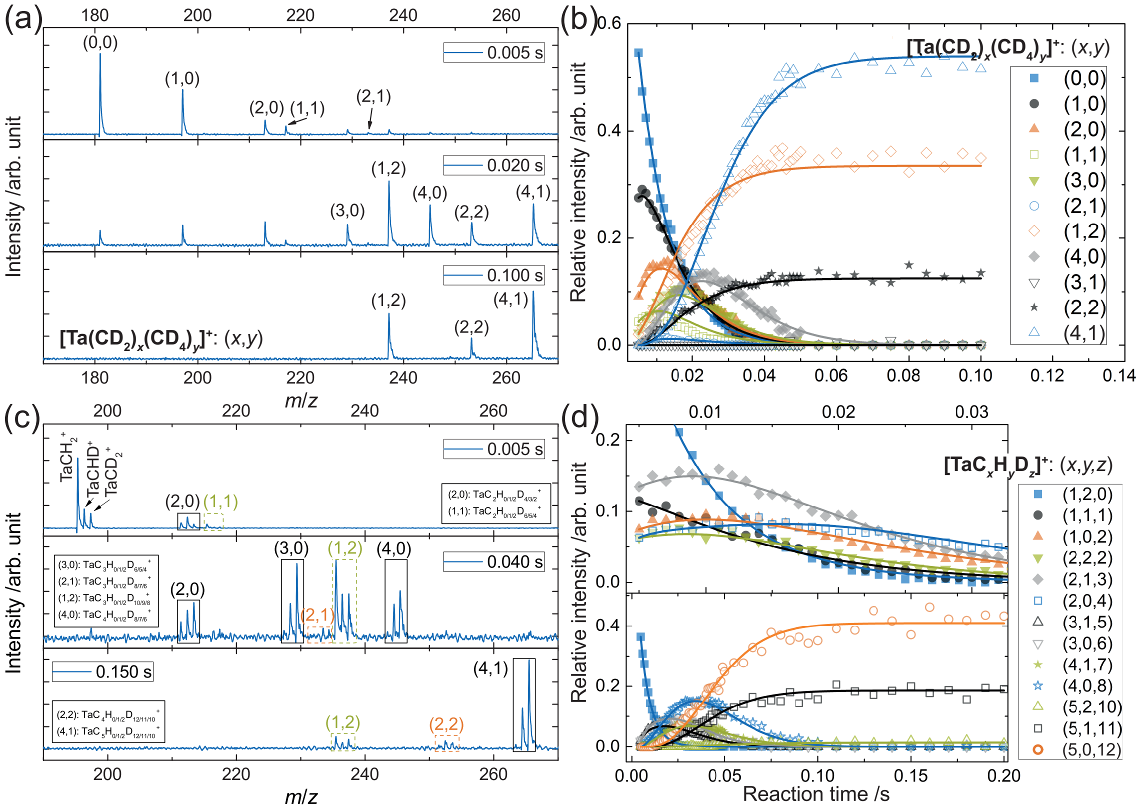

Figure 5.8: *Mass spectra in the reaction of Ta^+ with CD_4 (a, $9.2 \cdot 10^{-4}$ Pa partial pressure) and of $[TaCH_2]^+$ with CD_4 (c, $2.8 \cdot 10^{-4}$ Pa partial pressure), as well as the corresponding kinetic simulations (b and d). Consecutive dehydrogenation and molecular adsorption yields $[TaCD_2(CD_4)_2]^+$, $[Ta(CD_2)_2(CD_4)_2]^+$ and $[Ta(CD_2)_4(CD_4)]^+$ (a). Kinetic modeling nicely replicates the reaction progression (b), illustrating a shift to the byproducts compared to the reaction with h_4-methane. H/D exchange and dehydrogenation in the reaction of $[TaCH_2]^+$ with d_4-methane cause analogous species that contain 0-2 H atoms instead of 2-0 D atoms (c). The plot in (d) depicts the change of selected species as a function of reaction time (experimental data points), and the simplest reaction model (solid lines) demands H/D exchange solely on $[TaCH_2]^+$, $[TaCHD]^+$, $[TaC_2H_2D_2]^+$ and $[TaC_2HD_3]^+$.*

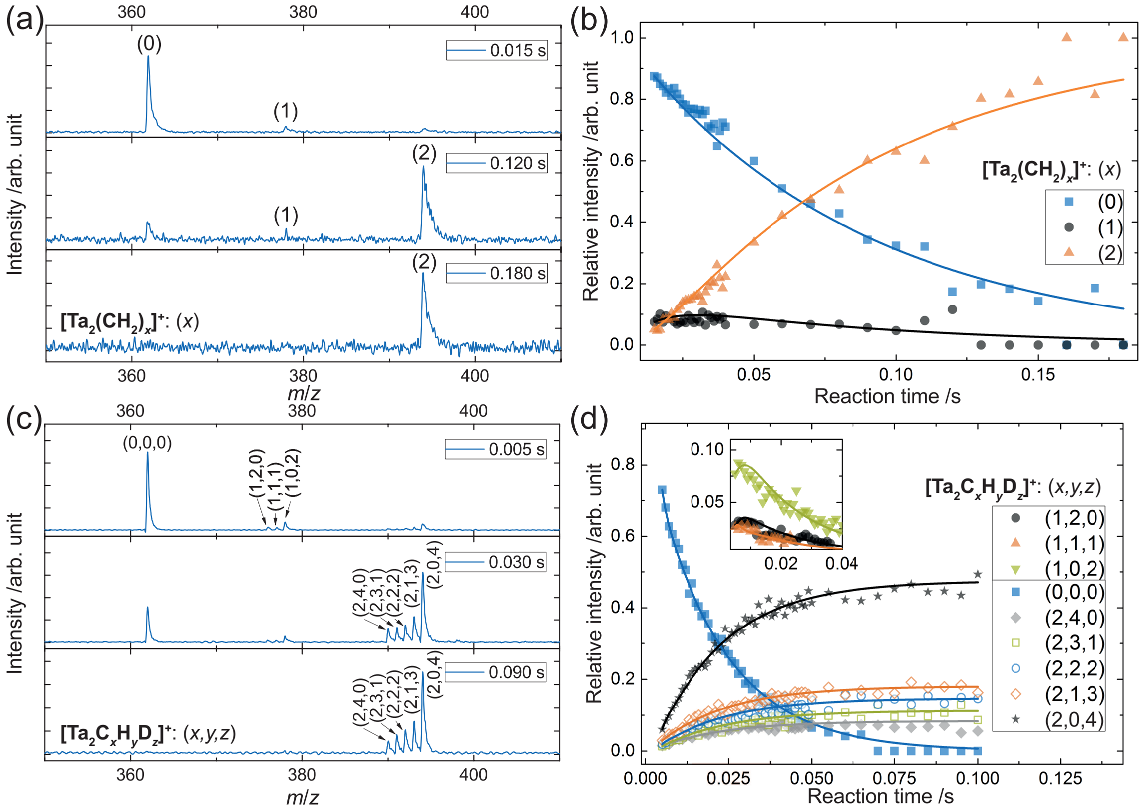

Figure 5.9: *Mass spectra of* Ta_2^+ *exposed to* CD_4 *(a,* $9.5 \cdot 10^{-3}$ *Pa partial pressure) and a* CH_4/CD_4 *mixture (c,* $1.4 \cdot 10^{-3}$ *Pa/*$1.5 \cdot 10^{-2}$ *Pa partial pressure). The results of the corresponding kinetic simulations are shown to the right in (b) and (d). Although the* CD_4 *dehydrogenation reactions are comparatively slow, the second step to generate* $[Ta_2(CD_2)_2]^+$ *is much faster than the first one, analogous to the reaction with* CH_4 *(b). H/D scrambling occurs on* $[Ta_2CH_2]^+$*,* $[Ta_2CHD]^+$ *and* $[Ta_2CD_2]^+$*, but is not needed to describe the formation of the subsequent species (c and d).*

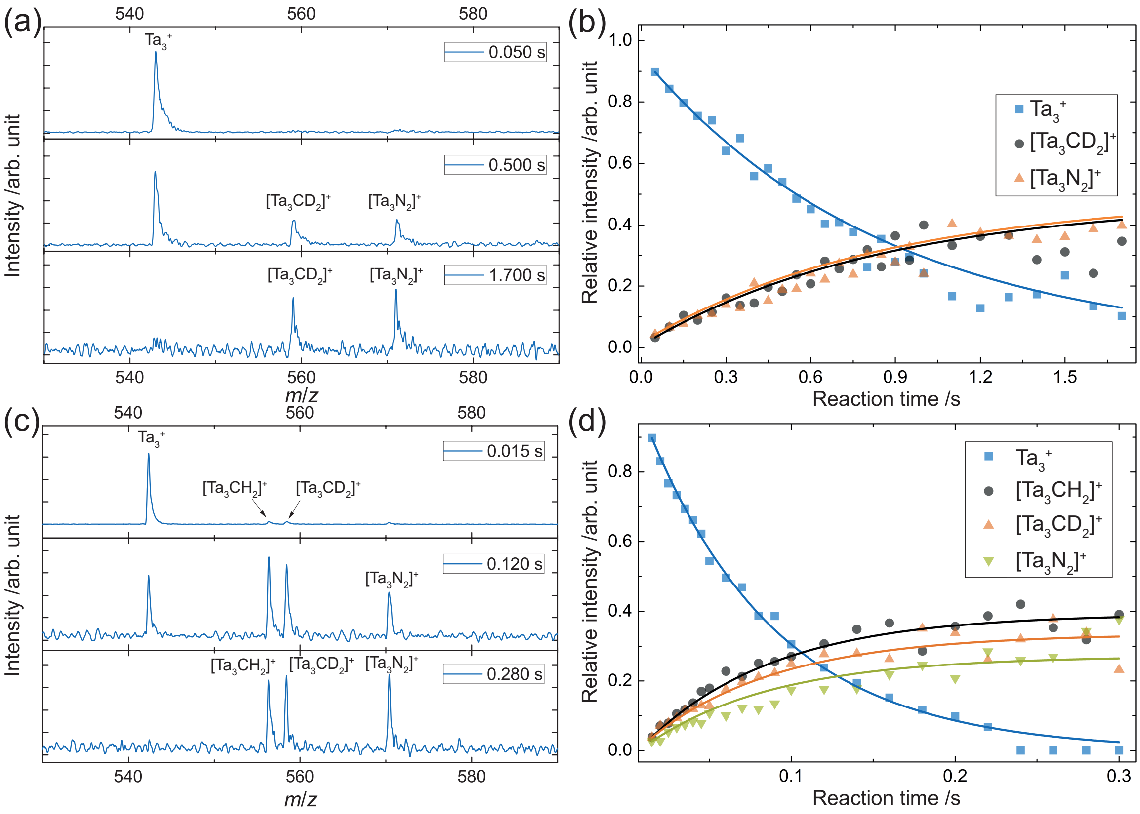

Figure 5.10: *Mass spectra of* Ta_3^+ *reacting with* CD_4 *(a,* $8.3 \cdot 10^{-3}$ *Pa partial pressure) and a* CH_4/CD_4 *mixture (c,* $7.3 \cdot 10^{-3}$ *Pa/*$6.9 \cdot 10^{-2}$ *Pa partial pressure) and the corresponding results of the kinetic modeling (b and d).* Ta_3^+ *slowly dehydrogenates a single* d_4*-methane molecule and adsorbs* N_2 *in a parallel channel due to a significant nitrogen impurity in the* d_4*-methane gas cylinder (a). However, the* N_2 *contribution does not hinder the kinetic simulation (b). When the trimer cluster is simultaneously exposed to* h_4*- and* d_4*-methane,* $[Ta_3CH_2]^+$ *and* $[Ta_3CD_2]^+$ *are generated and the H/D exchange product,* $[Ta_3CHD]^+$*, is not observed above the noise level (c).*

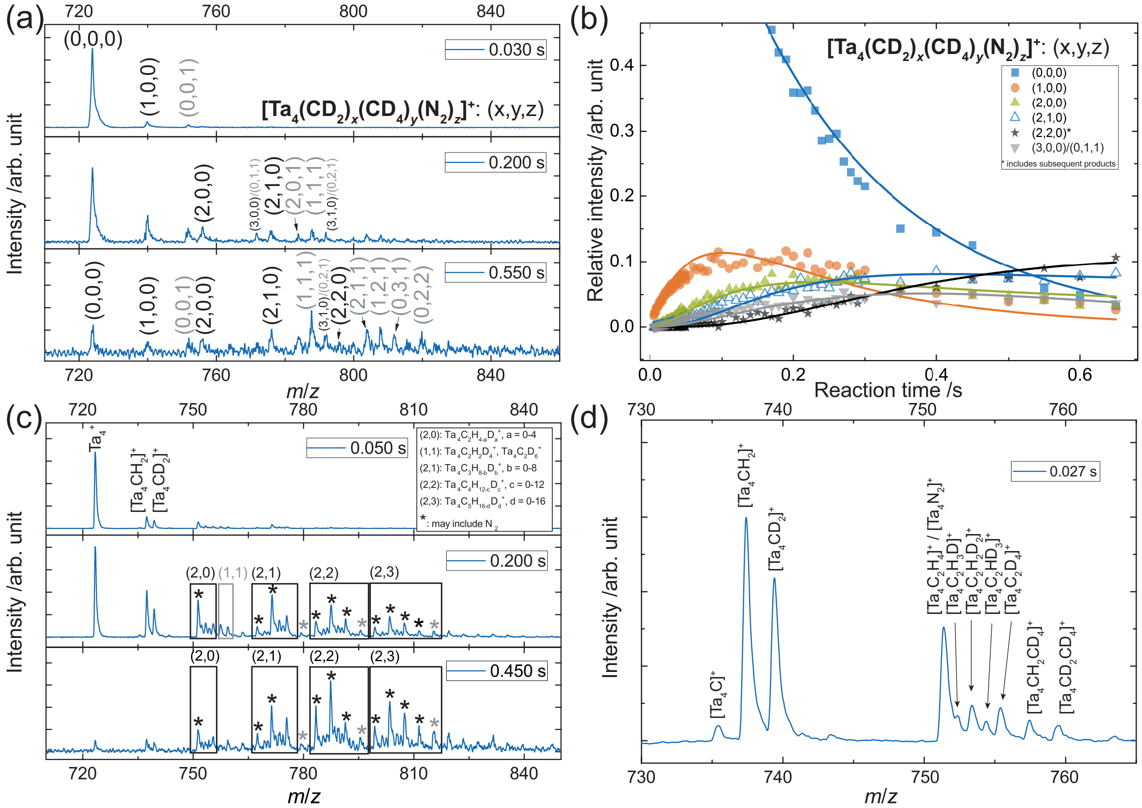

Figure 5.11: *Mass spectra of Ta_4^+ reacting with CD_4 (a, $4.8 \cdot 10^{-2}$ Pa partial pressure) and the corresponding results of the kinetic modeling (b). Dehydrogenation and molecular adsorption of d_4-methane molecules generates the analogous products observed in the reaction with h_4-methane (a). Virtually all of these species adsorb one or two nitrogen molecules (products denoted by gray numbers), due to residual N_2 in the CD_4 gas bottle. A low reaction efficiency combined with a high kinetic isotope effect in the reaction with methane cause a high intensity of these side products. Still, the reaction is successfully modeled and species of interest are depicted in (b). Nitrogen also contributes to the mass spectra of the tetramer cluster reacting with a CH_4/CD_4 mixture ($4.6 \cdot 10^{-3}$ Pa/$4.1 \cdot 10^{-2}$ Pa partial pressure) depicted in (c) and (d). Nevertheless, H/D scrambling on $[Ta_4CH_2]^+$ and $[Ta_4CD_2]^+$ can be ruled out, while it is feasible on $[Ta_4C_2H_4]^+$, $[Ta_4C_2H_2D_2]^+$ and $[Ta_4C_2D_4]^+$ (d).*

ENHACEMENT OF THERMAL METHANE DEHYDROGENATION BY OXO LIGANDS

6

The effects of ligating cationic tantalum clusters with single oxygen atoms on their reactivity are explored in the following chapter. The experimental findings resulted in a collaboration with the group of Prof. Dr. Uzi Landman. In order to obtain detailed insights on the dehydrogenation reactions, U. Landman and R. Barnett performed quantum-chemical calculations. Therefore, descriptions of the theoretical findings and the methodology as well as the corresponding illustrations were provided by the group of U. Landman.

The gas-phase reactions of $[Ta_xO_y]^+$ ($x = 4, 5$, $y = 0, 1$) with methane have been explored in a ring electrode ion trap under multi-collision conditions, and theoretically with the use of first-principles quantum simulations. While Ta_4^+ consecutively dehydrogenates two CH_4 molecules and concurrently eliminates H_2, Ta_5^+ is unreactive at room temperature. Both of the corresponding mono-oxides, $[Ta_4O]^+$ and $[Ta_5O]^+$, demonstrate significantly increased reaction rates. Remarkably, up to four tantalum atoms actively participate in the reaction, yet the oxygen atom does not form any bonds and only acts as a ligand. Clusters with such particular properties may thus become applicable in concepts for complex chemistry, surface metal-organic chemistry or heterogeneous nanocatalysis by either tuning ligands or Lewis acidity of the support.

6.1. Introduction

Methane is the most abundant natural gas and the smallest hydrocarbon, elevating the prospects of utilizing CH_4 as a venerable molecular building block to a worthwhile challenging goal. The process of activating methane, however, is hindered by intrinsic molecular properties such as strong sp^3-hydridized C–H bonds, a low pK_a value and a small polarizability, which pose a challenge to the activating agent [12, 164]. On an extended surface, silica-supported tantalum hydrides catalyze the conversion of methane into ethane [41]. Bulk metal oxides also facilitate C–H bond cleavage in methane, albeit at elevated reaction temperatures and accompanied by effects that obstruct their systematic investigation [49, 164]. Studies of gas-phase atoms and small clusters, which resemble active centers of more complex systems, may therefore provide important insights about operative molecular-level processes and mechanisms [165].

Various 5d transition metal cations, including Ta^+, dehydrogenate methane and form (distorted) carbene structures [53, 56, 158]. The reaction of $[TaO_3]^+$ with methane leads to the formation of two value-added products, formaldehyde and methanol [98]. As observed in the comparison of $[M CH_2]^+$ [62] and $[M O_2]^+$ [153] (M = V, Nb, Ta), the increased reactivity of tantalum-containing compounds is generally attributed to relativistic effects that enable the formation of very strong Ta–C bonds. Instead of dehydrogenation and concomitant H_2 evolution, a direct hydrogen atom transfer (HAT) mechanism prevails for many metal oxide systems that contain terminal [78] or bridging oxygen atoms [166] with localized spin density, *e.g.* stoichiometric vanadium and niobium oxide clusters [91]. In these systems, the local charge influences reaction barriers [167]. Lewis acid-base pairs found in metal oxide clusters may also abstract hydrogen atoms by means of a proton-coupled electron transfer (PCET) [78, 168]. While many single-collision studies focus on methane activation [57–59, 68, 70, 75, 169], such investigations under well-defined multi-collision conditions are scarcer [65, 76, 77, 160] These experiments enable the constant thermal equilibration of reactants and buffer gas, and the observation of consecutive reactions, *e.g.* metal-catalyzed C–C coupling of two reactant molecules. The catalytic reaction of Au_2^+ with CH_4 and O_2 exemplifies this benefit, as the reaction product changes from ethylene to formaldehyde with decreasing temperature [65]. Due to promising properties of tantalum clusters and the corresponding mono-oxides, illuminating their reaction mechanisms may aid the rational design of catalysts mediating C–H bond activation.

This chapter contains combined experimental and theoretical investigations on the reactions of $[Ta_xO_y]^+$ ($x = 4, 5$, $y = 0, 1$) with methane in an ion trap. It is shown that the addition of one oxygen atom to the investigated tantalum cluster cations leads to a significant increase in the dehydrogenation reaction rate. First-principles Born-Oppenheimer spin-density functional theory (SDFT) simulations (see Chapter B in the Appendix) reveal that the bridging oxygen atom only influences the electronic structure of the clusters, but never acts as a binding partner for methane and its fragments. This finding is different to many oxide systems, for which hydroxide moieties are formed via PCET/HAT mechanisms [78] or in the course of the subsequent reaction steps [101]. Ultimately, the effect of the μ_2-O ligand on the reaction mechanism is addressed and the observed outcome of consecutive reactions with multiple methane molecules is put into context with other small metal clusters.

6.2. Experimental results

Time-of-flight mass spectra and microkinetic simulations of $[Ta_xO_y]^+$ clusters exposed to a defined fraction of methane in helium buffer gas are shown in Figure 6.1. Ta_4^+ clusters facilitate H_2 elimination upon reacting with the first methane molecule and generate $[Ta_4CH_2]^+$ as an intermediate (Fig. 6.1a). The $[Ta_4CH_2]^+$ complex is also capable of releasing H_2 from a second adsorbed CH_4 molecule, thereby forming $[Ta_4(CH_2)_2]^+$. Subsequently, the reaction progresses via a consecutive slow adsorption of two additional CH_4 molecules (Fig. 6.1a-b). As H_2 is not released in these steps, the reactions become reversible. In contrast, Ta_5^+ clusters are completely inert towards methane (see Fig. 6.7 in Chapter 6.6). The reaction of $[Ta_4O]^+$ proceeds analogously to Ta_4^+, *i.e.* corresponding reaction intermediates and products are formed. However, the reaction progresses much

Table 6.1: *Bimolecular rate coefficients $k^{(2)}$ and theoretical collision rates k^{SCC} in units of $10^{-12}\,cm^3\,s^{-1}$ in the consecutive reaction of Ta_4^+, $[Ta_4O]^+$ and $[Ta_5O]^+$ with CH_4 and CD_4, which are used to calculate the respective kinetic isotope effect (KIE).*

Reaction product	$k^{(2)}_{CH_4}$ [a]	$k^{(2)}_{CD_4}$ [a]	$k^{SCC}_{CH_4}$ [b]	$k^{SCC}_{CD_4}$ [b]	KIE
$[Ta_4CH_2]^+$	0.71±0.14	0.09±0.02	1720	1540	6.98±2.23
$[Ta_4(CH_2)_2]^+$	0.64±0.14	0.34±0.08			1.69±0.55
$[Ta_4OCH_2]^+$	10.89±2.18	1.04±0.21			9.40±2.66
$[Ta_4O(CH_2)_2]^+$	3.76±0.79	0.43±0.09			7.87±2.30
$[Ta_5OCH_2]^+$	14.87±2.98	1.63±0.33	1790	1600	8.23±2.33
$[Ta_5O(CH_2)_2]^+$	0.66±0.14	0.09±0.02			6.24±2.05

[a] Rate coefficients referenced to $[TaCH_2]^+$ formation determined by Shayesteh *et al.* [53] (see Chapter A.5). [b] Theoretical collision rates of bare metal clusters with CH_4 and CD_4, $k^{SCC}_{CH_4}$ and $k^{SCC}_{CD_4}$, according to the surface charge capture (SCC) theory developed by Kummerlöwe and Beyer [143].

more quickly (Fig. 6.1c-d) and the apparent rate coefficient of the first reaction step is more than an order of magnitude larger (see Tab. 6.1). The maximum rate coefficient of all reactions is observed for $[Ta_5O]^+$ clusters forming the first intermediate $[Ta_5OCH_2]^+$. As displayed in Figure Fig. 6.1e-f, this species is generated very rapidly and also mediates activation of a second CH_4 via H_2 evolution. In a parallel reaction channel, $[Ta_5OCH_2]^+$ reacts with CH_4 by eliminating two H_2 molecules, thus forming $[Ta_5OC_2H_2]^+$. For all clusters, side reactions with possible residual gases in the vacuum chamber are ruled out as no products are formed when the clusters are stored for prolonged times without mixing methane into the buffer gas (see Fig. 6.7 in Chapter 6.6). Furthermore, isotopic labeling with

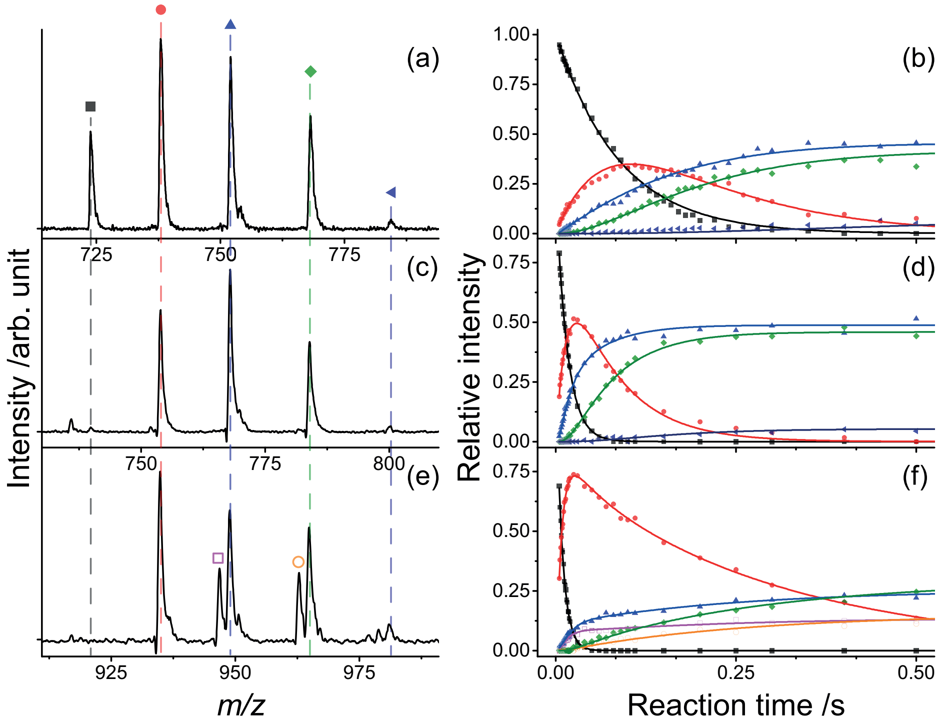

Figure 6.1: *Intensity distribution of reactants and products in the reaction of $[Ta_xO_y]^+$ ($x = 4, 5$, $y = 0, 1$) with CH_4. All reactions are conducted at 300 K in the presence of He buffer gas at a total pressure of 0.77 Pa. Mass spectra display Ta_4^+ species (a, after 0.15 s, 0.02 Pa CH_4), $[Ta_4O]^+$ species (c, after 0.07 s, 0.008 Pa CH_4) and $[Ta_5O]^+$ species (e, after 0.3 s, 0.008 Pa CH_4). The respective abundances as a function of time and reaction kinetics are shown to the right in b), d) and f). ■: $[Ta_xO_y]^+$, ●: $[Ta_xO_yCH_2]^+$, ▲: $[Ta_xO_y(CH_2)_2]^+$, ◆: $[Ta_xO_y(CH_2)_2(CH_4)]^+$, ◀: $[Ta_xO_y(CH_2)_2(CH_4)_2]^+$ □: $[Ta_5OC_2H_2]^+$, ○: $[Ta_5OC_2H_2(CH_4)]^+$.*

CD_4 confirms the product assignment (see Fig. 6.8 in Chapter 6.6), and Table 6.1 displays apparent rate coefficients for the corresponding reactions. The CD_4 dehydrogenation reactions are associated with significantly lower rate coefficients compared to the respective reactions with CH_4. This is the result of the kinetic isotope effect (KIE), which is defined as the ratio of a rate coefficient for a reaction toward CH_4, k_{CH_4}, and the corresponding rate coefficient when CD_4 is involved, k_{CD_4}. The theoretical collision rate, k^{SCC} according to the surface charge capture (SCC) model by Kummerlöwe and Beyer [143], of clusters in the investigated size range with d_4-methane is about 90% of the collision rate with CH_4 and this value is applied as a factor in the determination of the KIE. The obtained KIE values are very high, which is indicative of a metal-mediated C–H scission in the rate-determining step of each reaction (see Tab. 6.1) [148]. The formation of the $[Ta_4\,(CH_2)_2]^+$ species represents an exception with a low KIE of 1.7±0.6.

6.3. Theoretical results

Born-Oppenheimer SDFT simulations (including scalar-relativistic effects for Ta) [170, 171], predict the structures and thermochemistry of the reactants, transition-state complexes and products. Figures 6.2 and 6.3 illustrate the initial interactions of the clusters with methane, whereas Figs. 6.4 and 6.5 display the microscopic reaction pathways, including transitional activation barriers. Chapter 6.6 and Chapter B (in the Appendix) provide additional information. The ground state structure of Ta_4^+ is a slightly Jahn-Teller-distorted tetrahedron and that of Ta_5^+ is a square-base pyramid (also see Fig. 6.9). The equi-excess-spin-density hypersurfaces displayed in Figures 6.2 and 6.3 for $[Ta_xO_y]^+$ and $[Ta_xO_yCH_4]^+$ show a nearly uniform distribution of the excess spin spread over all the metal atoms, corresponding to an itinerant character of the excess spin in these clusters. The lack of spin density located at the oxygen atom thus excludes a direct HAT mechanism. The Bader charge distributions (see Figs. 6.2 and 6.3) exhibit unequal values on the metal atoms, and the effect of an added oxygen atom (in $[Ta_xO]^+$, $x = 4, 5$) is to concentrate negative charge on the oxygen atom. This results in redistribution of the Bader charges on the Ta atoms, with those directly bonded to the bridging O atom acquiring a larger positive charge. While tantalum atoms labeled 3 or 4 in Figure 6.2 and the oxygen atom in $[Ta_4O]^+$ could be expected to act as a Lewis acid-base pair in order to abstract a hydrogen

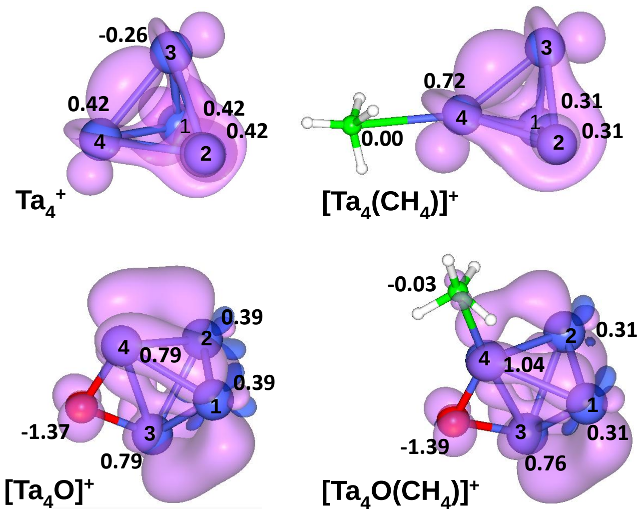

Figure 6.2: *Ground-state configurations of* $[Ta_4O_{0,1}]^+$ *clusters without and with an adsorbed* CH_4 *molecule. Ta (numbered), O, C and H atoms are represented by blue, red, green and small white spheres, respectively. Calculated Bader charges are additionally depicted next to the atoms. The itinerant nature of the excess spin is illustrated by superimposed equi-excess-spin-density hypersurfaces.*

atom, this is not found to be the case. Instead, the adsorption occurs solely on one of the Ta atoms and interestingly, the adsorbed CH_4 molecule remains neutral with the charge on the Ta atoms directly bonded to it becoming positively polarized (see Figs. 6.2 and 6.3). This reflects the nature of the polarization bonding mode, where the 8-electron closed-shell CH_4 molecule repels charge from the anchoring metal atom site (Pauli repulsion). The cluster-mediated methane dehydrogenation reaction pathways, calculated via steered first-principles simulations (see Chapter 6.6), show that CH_4 readily adsorbs on both the bare and oxo-ligated clusters. The adsorption energies are: ΔE_{ad} (Ta_4^+; $\mu = 1$) = 0.24 eV (0.22 eV); ΔE_{ad} (Ta_5^+; $\mu = 2$) = 0.40 eV (0.36 eV); ΔE_{ad} ($[Ta_4O]^+$; $\mu = 1$) = 0.58 eV (0.54 eV); ΔE_{ad} ($[Ta_5O]^+$; $\mu = 2$) = 0.28 eV (0.27 eV), with the value in parenthesis giving the zero-point-energy (zpe)-corrected adsorption energy, and μ is the number of unpaired electrons (excess spin-up over spin-down electrons). Note that the pentamer cluster possesses several isomers with the energy of the cluster having $\mu = 0$ and 2 being nearly-degenerate, and the spin isomer with $\mu = 4$ having a significantly higher energy (0.80 eV). Upon adsorption, the reaction proceeds through transition states corresponding to the dissociation of a first and a second C–H bond via "metal atom insertion" (transition states marked as 1 and 2,

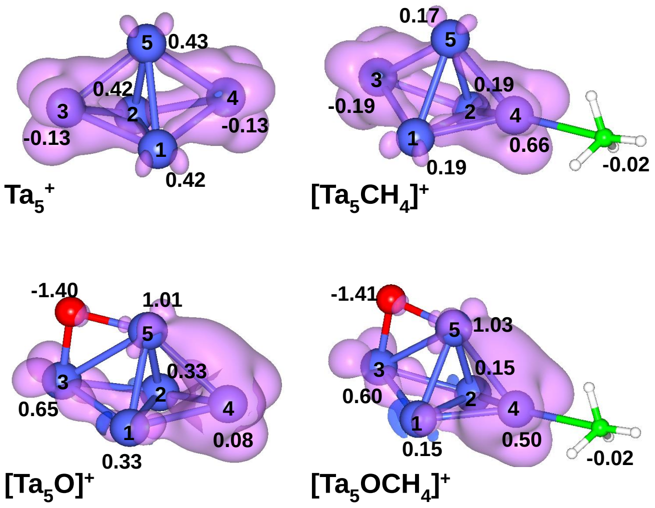

Figure 6.3: *Ground-state configurations of* $[Ta_5O_{0,1}]^+$ *clusters without and with an adsorbed* CH_4 *molecule. Ta (numbered), O, C and H atoms are represented by blue, red, green and small white spheres, respectively. Calculated Bader charges are additionally depicted next to the atoms. The itinerant nature of the excess spin is illustrated by superimposed equi-excess-spin-density hypersurfaces.*

green in Figs. 6.4 and 6.5). Scission of the first C–H bond leads to intermediates with the H and CH_3 fragments bridging two adjacent Ta–Ta bonds ($n = 1$, where n denotes the number of cleaved C–H bonds in the intermediate complex). For Ta_4^+ and $[Ta_4O]^+$, the subsequent cleavage of the second C–H bond generates a second intermediate including a Ta triangle with three Ta–Ta bonds respectively bridged by a methylene unit, the first hydrogen and the second hydrogen atom ($n = 2$). Lastly, the hydrogen atoms combine on the Ta atom opposite to the CH_2-bridged Ta–Ta bond to form H_2 (transition state marked as 3 in Fig. 6.4) and molecular hydrogen is ejected from the cluster. In addition, the third and fourth C–H bonds may be cleaved ($n = 3$ and 4), which requires participation of the fourth Ta atom and causes the generation of dihydrido carbides of the Ta_4^+ and $[Ta_4O]^+$ clusters. For Ta_5^+ and $[Ta_5O]^+$, methylene formation and H_2 elimination require four Ta atoms to take part and an additional step of hydrogen atom migration (transition state marked as 3, whereas H_2 formation is marked as 4). In the $n = 2$ intermediate of $[Ta_5O]^+/CH_4$, the Ta atom that initially acts as the CH_4 adsorption site becomes bonded to all of the three (H,H,CH_2) moieties, which bridge three individual Ta–Ta bonds.

(a) $Ta_4^+ + CH_4 \rightarrow [Ta_4CH_2]^+ + H_2$

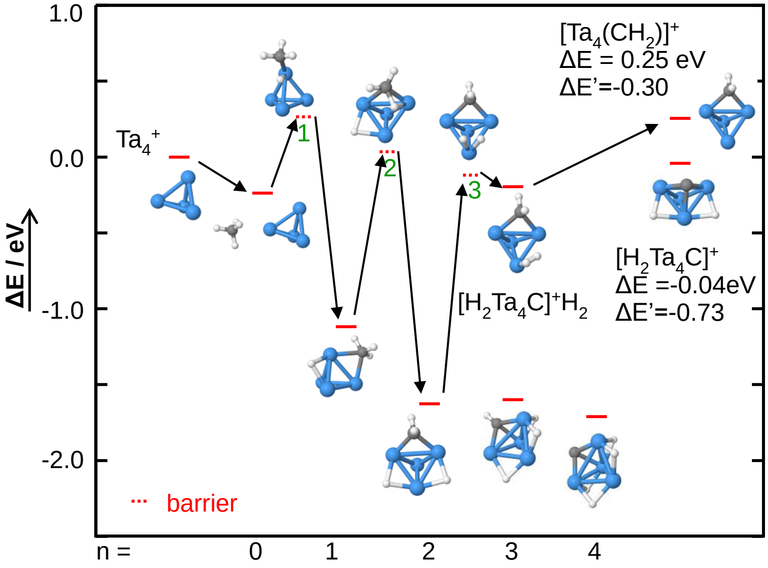

(b) $[Ta_4O]^+ + CH_4 \rightarrow [Ta_4OCH_2]^+ + H_2$

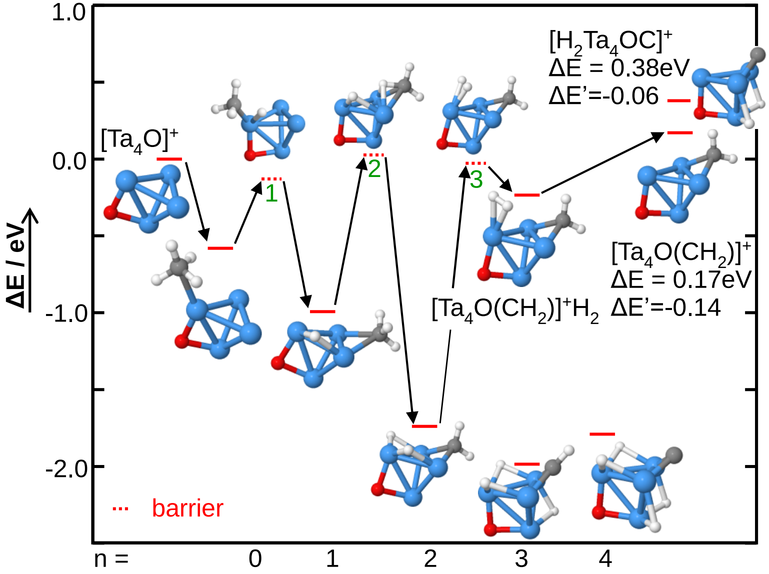

Figure 6.4: *Reaction pathways for adsorption and dehydrogenation of a methane molecule on bare* Ta_4^+ *(a) and oxygen-ligated* $[Ta_4O]^+$ *(b) clusters. Dotted horizontal lines depict the transition states (numbered, in green) and solid lines denote local minima, with the number of cleaved C–H bonds in the intermediates indicated by* n*. Ta, O, C and H atoms are displayed as blue, red, gray and white spheres, respectively.* ΔE *and* $\Delta E'$ *are the calculated energy and zpe-corrected thermochemical total energies for the reaction. The depicted energy levels correspond to non-zpe-corrected values. The values of the activation barriers and local minima are given in Chapter B of the Appendix.*

The $[Ta_5O]^+/CH_4$ system furthermore crosses from the triplet spin state of the adsorption complex ($n = 0$) into the singlet state of the first transition state to circumvent the elevated activation barrier of the triplet state. In addition, cleavage of the third C–H bond potentially generates a $[Ta_5O]^+$ methylidyne cluster. For Ta_4^+ (μ=1), $[Ta_4O]^+$ (μ=1) and $[Ta_5O]^+$ ($\mu = 2$), the hydrogen elimination reactions are exothermic, which is indicated by the zpe-corrected energetic difference of the isolated $[Ta_xO_yCH_2]^+/H_2$ products compared to the isolated $[Ta_xO_y]^+/CH_4$ reactants. The potential strongly exothermic formation of dihydrido-carbide and hydrido-methylidyne clusters ($[Ta_4CH_2]^+$ and $[Ta_5OCH_2]^+$, respectively) is remarkable as a carbene structure is more common and usually assumed for most metals, with the exception of the Ir^+ carbyne [158]. In contrast, the calculated reaction pathway of the bare Ta_5^+ clusters with methane ($\mu = 2$) would result in a very endothermic formation of products (see $\Delta E' > 0$ in Fig. 6.5). Furthermore, the zpe-corrected energy barrier for the first C–H dissociation process (marked as 1, green in Fig. 6.5) is larger for Ta_5^+ (0.73 eV) compared to Ta_4^+ (0.38 eV), $[Ta_4O]^+$ (0.32 eV) and $[Ta_5O]^+$ (0.35 eV). Due to isothermal, multi-collision conditions, the buffer gas may supply external energy to overcome activation barriers in excess of endothermicity [17]. This process enables the dehydrogenation for example mediated by Ta_4^+, but is prevented by the exceedingly high activation energy required in the reaction of Ta_5^+.

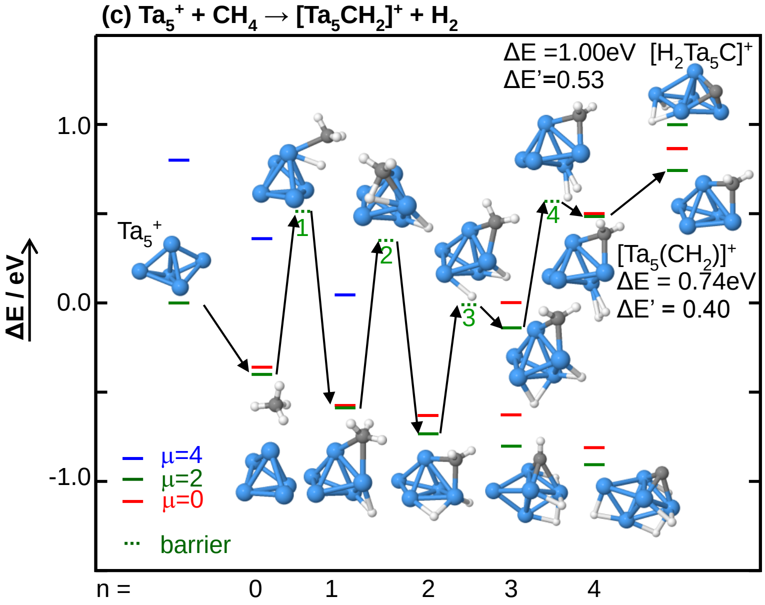

(c) $Ta_5^+ + CH_4 \rightarrow [Ta_5CH_2]^+ + H_2$

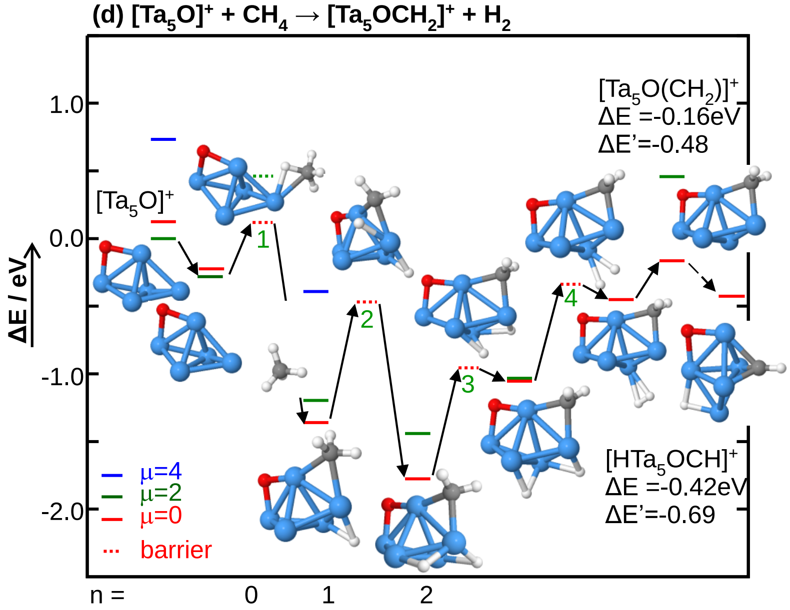

(d) $[Ta_5O]^+ + CH_4 \rightarrow [Ta_5OCH_2]^+ + H_2$

Figure 6.5: *Reaction pathways for adsorption and dehydrogenation of a methane molecule on bare* Ta_5^+ *(c) and oxygen-ligated* $[Ta_5O]^+$ *(d) clusters. Dotted horizontal lines depict the transition states (numbered, in green) and solid lines denote local minima, with the number of cleaved C–H bonds in the intermediates indicated by* n*. Ta, O, C and H atoms are displayed as blue, red, gray and white spheres, respectively. The color of the horizontal line indicates the spin state (corresponding to the number of unpaired electrons, excess-spin, electrons; note the spin transition occurring in the first activation process in (d)). The values of the activation barriers and local minima are given in Chapter B of the Appendix.*

6.4. Discussion

A repeated shift of electron density is required for the adsorption of methane, the scission of the C–H bond and the subsequent stabilization of the hydrogen and methyl fragments, as illustrated by the Bader charges in the adsorption complex, the first transition state and the resulting intermediate (see Figs. 6.10 and 6.11). Due to the adsorption of the closed-shell molecule, electron density is repulsed from the adsorption site to the neighboring Ta atoms. In the subsequent C–H cleavage, the CH_3 and H fragments become negatively charged (about -0.3 each), while the overall positive charge of Ta atoms is increased (by about +0.6). To bind the fragments, the overall positive Ta atom charge increases further (by about +0.8) and the negative charge on -H and -CH_3 is increased by approximately 0.4 each. The first transition state of Ta_4^+/CH_4 demands a significant rearrangement of electron density in every Ta atom. In the transition state of the corresponding monoxide, a single Ta atom, the adsorption site, provides the electron density required in the C–H cleavage, while the positive Bader charges of the adjacent Ta atoms become only slightly elevated compared to the adsorption complex (see Fig. 6.11).

The presence of the O ligand in $[Ta_4O]^+$ thus limits the transitional electronic rearrangements to a single Ta atom (and the CH_4 fragments), which facilitates the C–H bond scission. In contrast, the addition of an O atom likely increases barriers in the reaction of small cationic Pd clusters with methane [76]. Furthermore, the dissociated H atom is found to favor a cluster-site with excess electron charge, but contrary to other oxidic systems does not form a hydroxide on the monooxide clusters. So far, a similar role of oxygen atoms has been observed during σ-bond metathesis in the reaction of $[HMO]^+$ (M = Ti, Mo, Ta) with methane, in which scission of a single C–H bond leads to the formation of a M-CH_3 bond and simultaneous loss of H_2 [172–174]. In those systems, the oxo ligand was found to affect M–CH_3 and M–H bond strengths. For Ta_4^+ and $[Ta_5O]^+$, the first C–H dissociation is the rate-determining step, while the scission of the second C–H bond is associated with the highest barrier in the reaction of $[Ta_4O]^+$. These findings are in excellent agreement with the observed kinetic isotopic effect (KIE). An elevated KIE is characteristic for a metal-mediated C–H bond scission in the rate-determining step [78]. Accordingly, similar and high kinetic isotopic effects are observed for all reactive clusters (see Tab. 6.1), with values of about 6-9. In addition, a spin crossover facilitates the dehydrogenation reaction by the pentamer cluster monoxide. The $[Ta_5O]^+/CH_4$ system is thus another example for a two-state reactivity scenario [12, 13].

The three reactive clusters demonstrate similar reaction pathways in the subsequent consecutive reaction (with an additional side reaction for $[Ta_5O]^+$ attributed to its high reactivity): after a second CH_4 molecule is dehydrogenated and H_2 is eliminated, two methane molecules are formally molecularly adsorbed on the clusters. This adsorption could provide energy necessary to release a neutral product molecule, *e.g.* observed for ethylene generation by Au_2^+ and Pd_2^+ [64, 77]. As this does not occur, a strong binding of potential C_{2-3} hydrocarbons or separated methylene units to the tantalum clusters can be assumed. To confirm this, the dehydrogenation of a second methane molecule is investigated by theoretical means on the basis of Ta_4^+. Adsorption of methane to the Ta_4^+ methylene cluster is exothermic (-0.84 eV), as is the formation of the most stable dehydrogenation product, a dihydrido-carbide-methylene cluster complex (-0.41 eV, see Fig. 6.6). In addition, forming an ethylene unit on Ta_4^+ is thermodynamically hindered at 300 K ($\Delta E([Ta_4(C_2H_4)]^+/2\,H_2) = 1.26$ eV) and the adsorption of two ad-

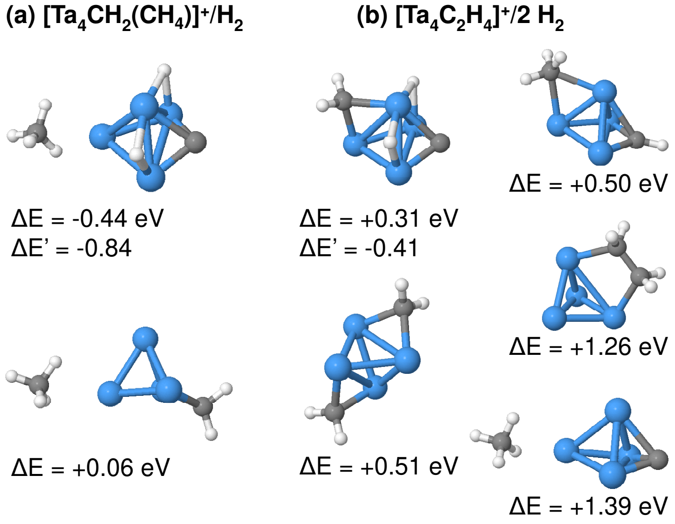

Figure 6.6: *SDFT-calculated optimized structures for $[Ta_4CH_2(CH_4)]^+$ (a) and $[Ta_4C_2H_4]^+$ (b), illustrating methane adsorption to two $[Ta_4CH_2]^+$ isomers and resulting dehydrogenation products. For $[Ta_4C_2H_4]^+$, six structural isomers are shown and the lowest-energy structure corresponds to a dihydrido-carbide-methylene complex of the tetramer cluster. The calculated energy and zpe-corrected energy (ΔE and $\Delta E'$) include the respective cluster and one (a) or two (b) hydrogen molecules in isolation, and are given in relation to the initial Ta_4^+/CH_4 reactants in isolation.*

ditional methane molecules therefore cannot induce the desorption of ethylene (see Fig. 6.6). These results suggest the formation of a Ta_4^+ dihydrido-carbide-methylene cluster complex and the absence of C–C coupling. Latter is likely the same case for the other investigated reactive clusters as these demonstrate a similar reaction progression.

6.5. Summary

To summarize, the μ_2-O ligand in $[Ta_4O]^+$ and $[Ta_5O]^+$ clusters enhances the C–H bond activation of methane. The inert nature of bare Ta_5^+ clusters is caused by an endothermic energy balance and significant activation energies. For the reactive clusters, C–H scission is the rate-determining step, as evidenced by an elevated kinetic isotope effect and quantum-chemical calculations. In addition, the corresponding barriers are decreased in the mono-oxide clusters. Up to four Ta atoms participate in the dehydrogenation reactions, whereas the additional oxygen atom does not contribute directly to the bond-breaking or -making process. The consecutive dehydrogenation reactions subsequently yield separated CH_{0-2} units and the formation of C–C coupling products is thermodynamically hindered.

The initial bonding of the CH_4 molecule involves Pauli-repulsion and polarization of the electronic charge of the metal cluster. The subsequent C–H bond activation process leads to a (negative) charging of the $–CH_3$ and –H moieties. While the itinerant character of the electron density may be crucial for a successful dehydrogenation reaction, hydrogen atom abstraction reactions are prevented by a low spin density on the oxygen atom and the absence of a Lewis acid-base pair. The addition of the μ_2-O ligand creates an electronic structure favorable for the C–H scission process, without significantly altering the clusters' geometric structure. Such a change in the electronic structure may also be brought about by tuning the Lewis acidity of the support material in heterogeneous catalysis. These studies therefore demonstrate that small metal clusters with such properties may serve as models for surface metal-organic chemistry.

6.6. Supplementary Information

6.6.1. Verification of peak assignment (reactions in He and CD_4)

The inert cluster, Ta_5^+, does not form any products when exposed to methane for prolonged storage times (see Fig. 6.7). The effect of possible contaminants on the mass spectra of the reactive species, Ta_4^+, $[Ta_4O]^+$ and $[Ta_5O]^+$, is probed by storing these clusters in pure helium buffer gas without the addition of methane. As seen in Figure 6.7, no side-reactions are observed.

In order to confirm the initial peak assignment in the reaction with methane, Ta_4^+, $[Ta_4O]^+$ and $[Ta_5O]^+$ clusters are reacted with d_4-methane (see Fig. 6.8). The consecutive reactions produce the analogous species $[Ta_xO_yCD_2]^+$, $[Ta_xO_y(CD_2)_2]^+$ and $[Ta_xO_y(CD_2)_2(CD_4)]^+$, thus verifying the species assigned in the reaction with

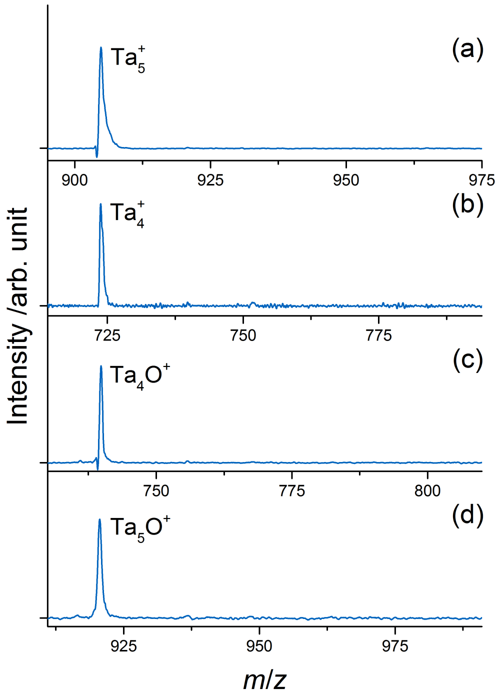

Figure 6.7: *(a) Time-of-flight mass spectrum of* Ta_5^+ *clusters exposed to methane. The absence of reaction products is shown after a reaction time of 0.5 s (0.04 Pa* CH_4*, 0.73 Pa He). Without the addition of methane to the buffer gas, no reactions are observed for* Ta_4^+*,* $[Ta_4O]^+$ *and* $[Ta_5O]^+$ *(b-d, after 0.5 s, 0.77 Pa He).*

CH_4. Due to a high nitrogen impurity stemming from the d_4-methane gas bottle[1], products containing N_2 are additionally generated, *e.g.* $[Ta_xO_yN_2]^+$. Such species are depicted by open symbols in Figure 6.8 a,c,e and do not prevent a successful kinetic analysis. As an exception, an overlap of two species occurs in the reaction of $[Ta_5O]^+$, where $[Ta_5OC_2D_2]^+$ is expected to be generated but is experimentally indistinguishable from $[Ta_5ON_2]^+$.

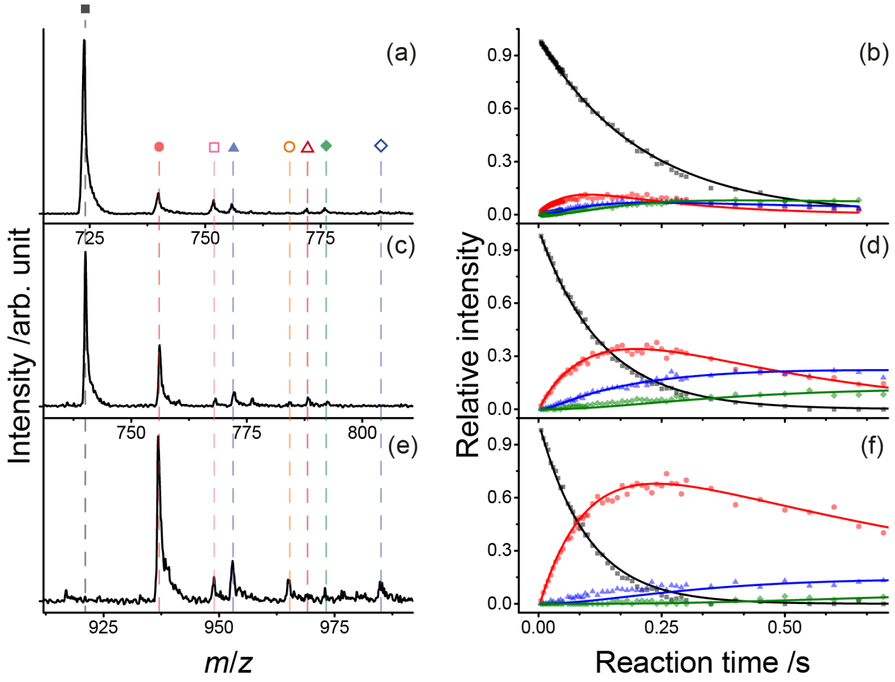

Figure 6.8: *Mass spectra (left) and time-dependent abundances (right) of reactants and products in the reaction of* $[Ta_xO_y]^+$ *(*$x = 4,5$*;* $y = 0,1$*) with* CD_4*. All reactions are conducted at 300 K in the presence of He buffer gas at a total pressure of 0.77 Pa. Mass spectra display* Ta_4^+ *species (a, after 0.075 s, 0.05 Pa* CD_4*),* $[Ta_4O]^+$ *species (c, after 0.075 s, 0.008 Pa* CD_4*) and* $[Ta_5O]^+$ *species (e, after 0.5 s, 0.008 Pa* CD_4*). The change of the corresponding ion abundances as a function of reaction time is shown on the right (b,d,f), with species of interest depicted as symbols and the results of the kinetic modeling displayed as solid lines.* ■: $[Ta_xO_y]^+$, ●: $[Ta_xO_yCD_2]^+$, ▲: $[Ta_xO_y(CD_2)_2]^+$, ♦: $[Ta_xO_y(CD_2)_2(CD_4)]^+$, □: $[Ta_xO_yN_2]^+/[Ta_5OC_2D_2]^+$, ○: $[Ta_xO_yN_2CD_2]^+$, △: $[Ta_xO_yN_2CD_4]^+$, ◇: $[Ta_xO_yN_2CD_2CD_4]^+$.

---

[1] Linde AG, methane-d4, 99 atom % D; impurities: Ar/O_2 = 100 ppm, N_2 = 220 ppm, CO_2 = 40 ppm, C_2H_6 = 180 ppm

6.6.2. Additional SDFT results

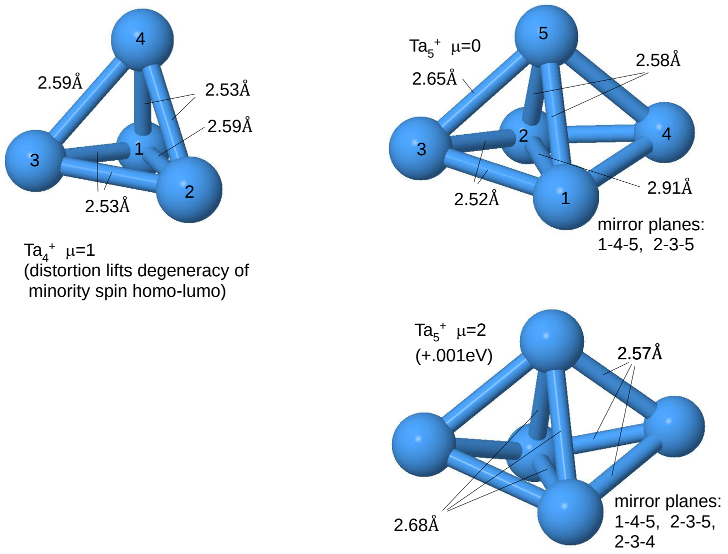

Figure 6.9: *SDFT-calculated lowest-energy optimized structures for bare* Ta_4^+ *(left) and* Ta_5^+ *(right) clusters. For* Ta_5^+ *two close-in-energy spin-isomers are shown* ($\mu = 0, 2$)*; the total energy difference between these isomers is 0.001 eV. For each cluster the difference between the number of majority and minority spins is given by* μ*. The interatomic distances are given in the figure.*

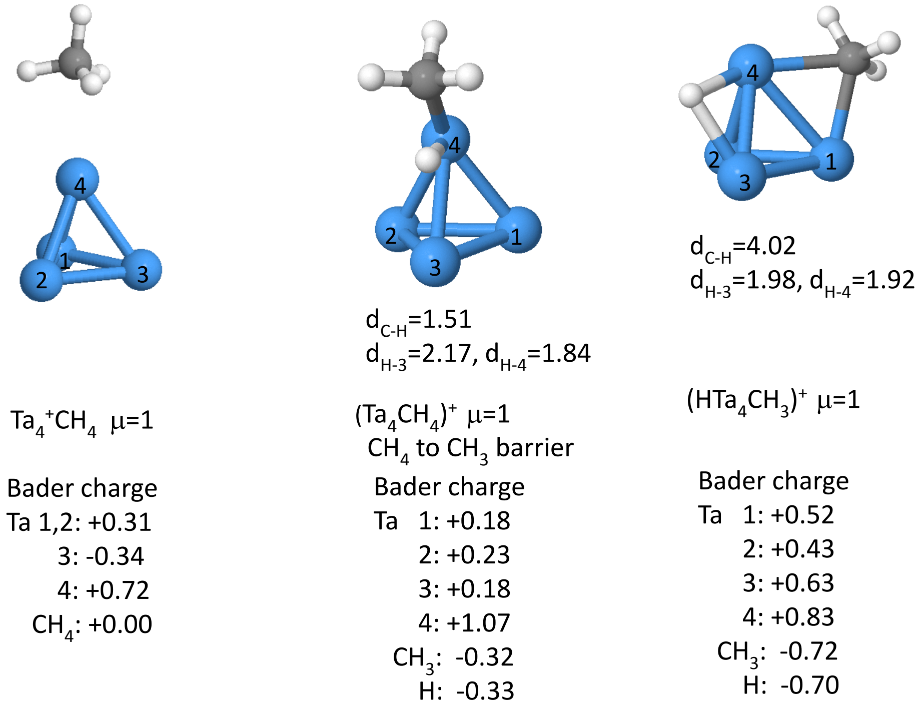

$d_{C\text{-}H}$=1.51
$d_{H\text{-}3}$=2.17, $d_{H\text{-}4}$=1.84

$d_{C\text{-}H}$=4.02
$d_{H\text{-}3}$=1.98, $d_{H\text{-}4}$=1.92

$Ta_4^+CH_4$ μ=1

Bader charge
Ta 1,2: +0.31
3: -0.34
4: +0.72
CH_4: +0.00

$(Ta_4CH_4)^+$ μ=1
CH_4 to CH_3 barrier
Bader charge
Ta 1: +0.18
2: +0.23
3: +0.18
4: +1.07
CH_3: -0.32
H: -0.33

$(HTa_4CH_3)^+$ μ=1

Bader charge
Ta 1: +0.52
2: +0.43
3: +0.63
4: +0.83
CH_3: -0.72
H: -0.70

Figure 6.10: $[Ta_4CH_2]^+$ *cluster configurations and Bader charges illustrating electronic charge rearrangements during the activation and dissociation of the C–H bond (compare to Fig. B.1, and Fig. 6.4). The configuration on the left is the equilibrium ground state, of the adsorbed* CH_4 *molecule on the* Ta_4^+ *cluster, with the adsorbed molecule remaining neutral. The middle configuration corresponds to the top of the activation barrier, showing partial negative charging of the* CH_3 *fragment (-0.32). The configuration on the right is the relaxed configuration (past the activation barrier), showing increased negative electron charge on the* CH_3 *fragment upon dissociation.*

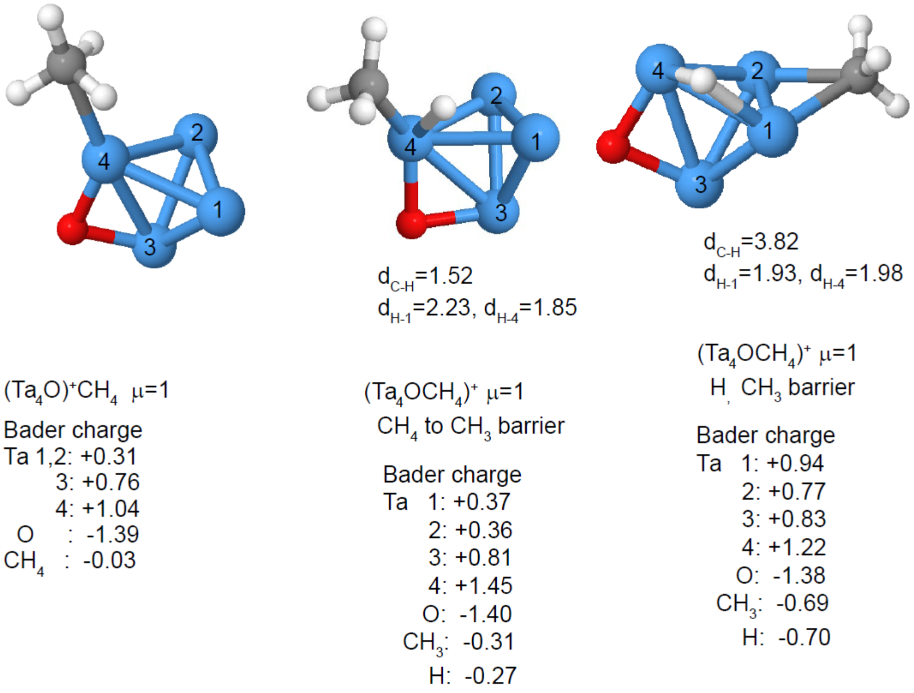

Figure 6.11: $[Ta_4OCH_2]^+$ *cluster configurations and Bader charges illustrating electronic charge rearrangements during the activation and dissociation of the C–H bond (compare to Fig. B.2, and Fig. 6.4). The configuration on the left is the equilibrium ground state, of the adsorbed* CH_4 *molecule on the* $[Ta_4O]^+$ *cluster, with the adsorbed molecule remaining neutral. The middle configuration corresponds to the top of the activation barrier, showing partial negative charging of the* CH_3 *fragment. The configuration on the right is the relaxed configuration (past the activation barrier), showing increased negative electron charge on the* CH_3 *fragment upon dissociation.*

MECHANISTIC VARIANTS OF METHANE ACTIVATION BY TANTALUM DIMER OXIDES

7

Mass-selected cationic tantalum dimer oxides $Ta_2O_{0\text{-}6}{}^+$ are stored in a ring electrode ion trap at 300 K, in order to probe methane activation reactions under well-defined multi-collision conditions. Consecutive reaction schemes and rate coefficients are obtained through kinetic modeling, and experiments with d_4-methane deliver additional mechanistic insights. Three distinct reactivity modes are described as a precise function of the number of oxygen atoms and an additional mode is observed for a reaction intermediate.

7.1. Introduction

Transition metals typically cause the activation of methane *via* metal-mediated insertion into a C–H bond, which may result in the elimination of dihydrogen and the formation of a metal carbene [12, 13, 54, 55]. The atomic cation of tantalum activates methane in this manner [53–55, 62, 158]. The dehydrogenation reaction can be enhanced by introducing ligands that, for example, change the electronic structure of the participating metal atoms. Ligation with an O atom was found to drastically increase the reactivity of Ta_4^+ toward methane and, moreover, turns the inert Ta_5^+ cluster into $[Ta_5O]^+$, which is more reactive than the tetramer monoxide (see Chapter 6). The cationic tantalum dioxide $[TaO_2]^+$ cleaves a C–H bond in methane (forming $[Ta(O)(OH)(CH_3)]^+$) and demonstrates an enhanced reactivity compared to the corresponding V and Nb oxides [153]. This is the result of an increased thermodynamic driving force: due to relativistic effects [62] a Ta–C bond is formed that is stronger than the metal-carbon bonds in the vanadium and niobium system [153]. Furthermore, the reaction of the closed-shell $[TaO_3]^+$ and methane yields two value-added products, formaldehyde and methanol, and a spin flip additionally causes the release of a $^3CH_2$ group [98].

Metal oxide clusters, in general, demonstrate an additional mode of methane activation, which is the abstraction of atomic hydrogen and the concomitant release of a methyl radical [12, 78]. Two mechanisms lead to this reaction outcome. In a hydrogen atom transfer (HAT) mechanism, an oxygen atom with a high density of unpaired spin directly accepts a hydrogen radical from methane [78–80]. On the other hand, a Lewis acid-base pair is required in a proton-coupled electron transfer (PCET) mechanism, in which a Lewis acidic metal atom intermittently binds a CH_3 moiety and a Lewis basic oxygen atom binds a proton [78–80]. The accessibility of a PCET mechanism depends strongly on the Lewis acidity of the participating metal atoms, whereas localized spin is less important [79]. A HAT reaction is mediated by oxygen-centered radicals. Terminal oxygen atoms with latter characteristics are present in a metal oxide cluster $M_xO_y^q$, when $2y-nx+q = 1$, with the number of valence electrons n in the metal M and the charge state q [91, 175]. $Ta_2O_5^+$ and $Ta_4O_{10}^+$, for example, were shown to mediate HAT, but this previous study was performed without mass-selection and lacks a comparative analysis of rate coefficients [87]. Investigating mass-selected tantalum cluster oxides with a precise number of oxygen atoms – ranging from bare clusters, monoxides, to the stoichiometric oxide – under multi-collision conditions reveals distinct changes in the reaction mechanism, as will be shown in this chapter.

7.2. Results and discussion

As illustrated in Figure 7.1, three principle reactivity modes are operative in the reactions of $Ta_2O_x{}^+$ (x = 0–6) with CH_4: molecular adsorption, dehydrogenation with concurrent H_2 elimination, and abstraction of atomic hydrogen. Metal-mediated dehydrogenation and concomitant elimination of hydrogen is observed for Ta_2^+ and $[Ta_2O_2]^+$ (see Eq. 7.1). These reactions occur in a consecutive manner and may be followed by non-dissociative adsorption of methane.

$$[Ta_2O_x]^+ + CH_4 \rightarrow [Ta_2O_xCH_2]^+ + H_2 \qquad \text{for } x = 0, 2 \tag{7.1}$$

Equation 7.2 describes that methane undergoes hydrogen atom transfer in the reaction with $[Ta_2O_5]^+$. This process competes with non-dissociative adsorption and is followed by the same.

$$[Ta_2O_5]^+ + CH_4 \rightarrow [Ta_2O_5H]^+ + CH_3 \tag{7.2}$$

The remainder of the clusters solely demonstrates the irreversible adsorption of CH_4 in absence of H_2 elimination (see Eq. 7.3). The amount of adsorbed molecules varies as a function of the oxygen content.

$$[Ta_2O_x]^+ + CH_4 \rightarrow [Ta_2O_xCH_4]^+ \qquad \text{for } x = 1, 3, 4, 6 \tag{7.3}$$

All of the experiments are repeated with isotopically labeled methane to confirm the peak assignment. Additionally, the reaction with CH_4 is compared to the reaction with CD_4 and the ratio of of the corresponding rate coefficients is defined as the kinetic isotope effect (KIE), which is indicative of the mechanism in the rate-determining step [148].

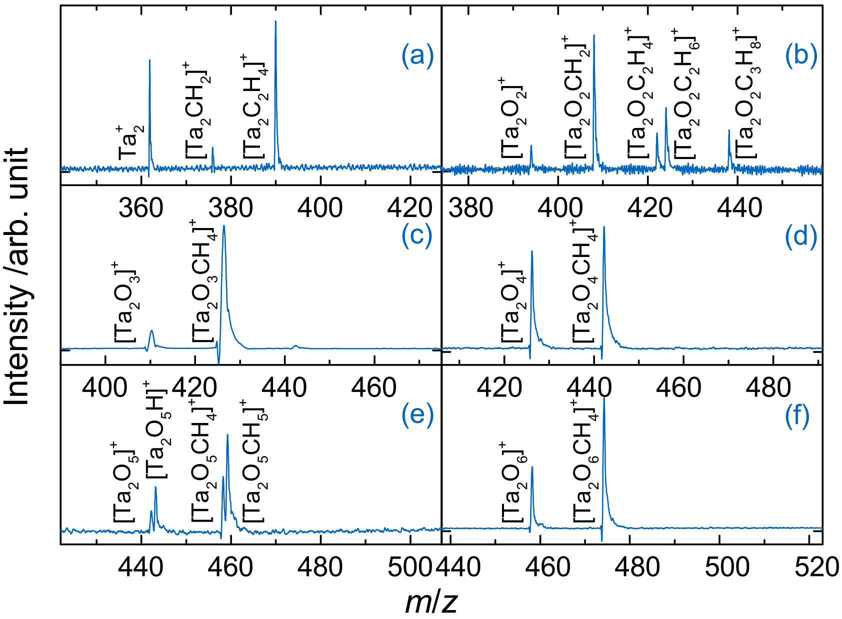

Figure 7.1: *Time-of-flight mass spectra of tantalum dimer oxides exposed to methane, demonstrating different reaction mechanisms as a function of oxygen content.* Ta_2^+ *with* $6.2 \cdot 10^{-4}$ *Pa* CH_4 *after 0.150 s (a),* $Ta_2O_2^+$ *with* $4.4 \cdot 10^{-4}$ *Pa* CH_4 *after 0.050 s (b),* $Ta_2O_3^+$ *with* $2.4 \cdot 10^{-4}$ *Pa* CH_4 *after 0.025 s (c),* $Ta_2O_4^+$ *with* $1.1 \cdot 10^{-3}$ *Pa* CH_4 *after 0.050 s (d),* $Ta_2O_5^+$ *with* $2.5 \cdot 10^{-4}$ *Pa* CH_4 *after 0.035 s (e) and* $Ta_2O_6^+$ *with* $2.2 \cdot 10^{-4}$ *Pa* CH_4 *after 0.025 s (f). All reactions were conducted at 300 K in He buffer gas at a total pressure of 0.77 Pa.*

7.2.1. Molecular adsorption

Four tantalum dimer oxides, $Ta_2O_{1,3,4,6}{}^+$, react with methane in a non-dissociative manner, predominantly generating the corresponding $[Ta_2O_{1,3,4,6}CH_4]^+$ species.

Ta_2O^+ and $Ta_2O_6^+$ adsorb a single methane molecule, whereas up to two molecules attach to $Ta_2O_3^+$, and $Ta_2O_4^+$ reacts with up to three methane molecules. The bimolecular rate coefficients $k^{(2)}$ associated with the adsorption reactions are significantly affected by the number of oxygen atoms in the cluster. The maximum coefficient ($5.43 \cdot 10^{-10}$ cm^{3}s^{-1}) is observed for the first reaction step of $Ta_2O_3^+$, which corresponds to a high reaction efficiency ϕ of 0.56 ($\phi = k^{(2)}/k_{LGS}$, with the theoretical collision rate k_{LGS} according to the Langevin-Giousmousis-Stevenson model) [136]. On the other hand, the adsorption to Ta_2O^+ is barely exceeding the detection limit for the reaction with CD_4, resulting in a rate coefficient of $8.31 \cdot 10^{-14}$ cm^{3}s^{-1} ($\phi = 8.6 \cdot 10^{-5}$). As this process is very slow, it competes with reactions to background gases, *e.g.* H_2O (see Fig. 7.5 in the Supplementary Information). In contrast to the tetramer and pentamer clusters, addition of an O atom to the bare Ta_2^+ drastically hinders the reaction with methane. Attaching the oxygen atom may remove electrons from the Ta atoms that are imperative for the interaction with methane. Indicated by molecular adsorption to $Ta_2O_6^+$, the additional oxygen atom (in comparison to $Ta_2O_5^+$) apparently causes the absence of an oxygen atom with significant unpaired spin and thereby prevents a HAT reaction. While the trioxide cluster demonstrates the highest overall reactivity, there is no experimental evidence for the cleavage of C–H bonds.

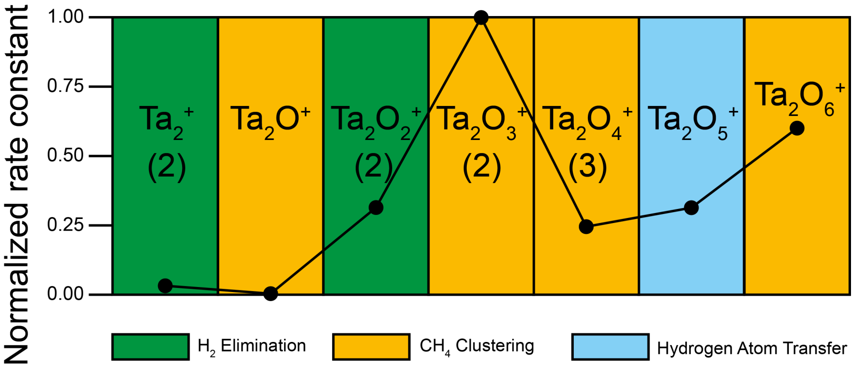

Figure 7.2: *Overview of main reactivity modes operative in the reaction of* $Ta_2O_x^+$ *with methane; corresponding rate coefficients of the first reaction step are normalized and displayed in an overlay. Molecular adsorption (shown in yellow) occurs for* $x = 1,3,4,6$, *with* Ta_2O^+ *being almost inert and a maximum activity for* $Ta_2O_3^+$. *Compared to bare* Ta_2^+, *the dioxide cluster demonstrates an enhanced activity for dehydrogenation and concurrent* H_2 *elimination (green). The pentoxide cluster abstracts atomic hydrogen from methane (blue).*

7.2.2. Dehydrogenation reactions

The bare tantalum dimer cation, Ta_2^+, was shown to dehydrogenate methane and concurrently eliminate dihydrogen (see Chapter 5), as depicted in Equation 7.1 and Figure 7.1. The resulting dimer methylene complex facilitates H_2 elimination from a second methane molecule. These two reactions are associated with apparent bimolecular rate coefficients of 0.17 and $1.01 \cdot 10^{-10}$ cm^3s^{-1} and reaction efficiencies of 0.02 and 0.11, respectively. This consequently shows that the second dehydrogenation reaction is enhanced by a factor of 6. Similar to the bare dimer, two methane molecules are dehydrogenated in the reaction of $[Ta_2O_2]^+$, consecutively generating $[Ta_2O_2CH_2]^+$ and $[Ta_2O_2C_2H_4]^+$ (see Fig. 7.5b). The corresponding rate coefficients are $1.69 \cdot 10^{-10}$ cm^3s^{-1} ($\phi = 0.18$) and $0.23 \cdot 10^{-10}$ cm^3s^{-1} ($\phi = 0.02$). Even though the first reaction step demonstrates a high efficiency, $[Ta_2O_2]^+$ is less reactive than the bare tantalum cation ($\phi = 0.39$) [53]. The main product of the reaction, $[Ta_2O_2C_2H_6]^+$, is formed through irreversible methane adsorption to $[Ta_2O_2CH_2]^+$ and is associated with a rate coefficient of $0.32 \cdot 10^{-10}$ cm^3s^{-1} (see also Fig. 7.6 in the Supplementary Information). Slow molecular adsorption to the main product additionally generates two minor products, $[Ta_2O_2C_3H_{10}]^+$ and $[Ta_2O_2C_4H_{14}]^+$. Note that the kinetic model excludes a reaction from $[Ta_2O_2C_2H_6]^+$ to $[Ta_2O_2C_3H_8]^+$. Instead, this C_3 species is produced from $[Ta_2O_2C_2H_4]^+$ *via* adsorption of CH_4 in absence of H_2 elimination. The two consecutive dehydrogenation reactions are associated with KIE values of 2.6 and 2.0, indicating a

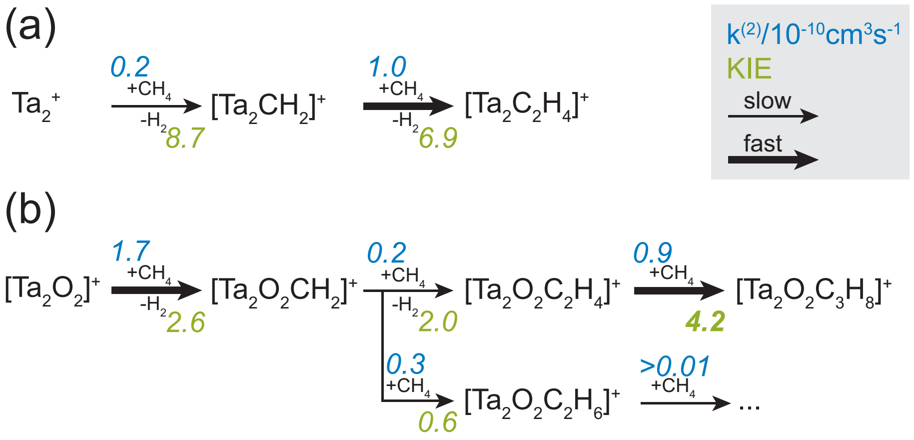

Figure 7.3: *Reaction scheme for Ta_2^+/CH_4 (a) and $[Ta_2O_2]^+/CH_4$ (b). Bimolecular rate coefficients for the reaction toward CH_4 are depicted in blue, while the kinetic isotope effect is shown in green.*

C–H bond scission in the rate-determining step. Interestingly, the formation of $[Ta_2O_2C_3(H/D)_8]^+$ is significantly hindered with CD_4 (KIE of 4.2), despite the lack of H_2 elimination, which becomes especially apparent in the ion abundances as a function of reaction time (see Fig. 7.6 in the Supplementary Information). This high KIE implies the scission of a C–H bond. As a result, at least one bond in the CH_4 molecule that reacts with $[Ta_2O_2C_2H_4]^+$ is broken (see also the full reaction scheme in Fig. 7.3).

Comparing the bare tantalum dimer cation to the corresponding dioxide, one could apply a simplistic model for the dehydrogenation of methane and concurrent elimination of H_2. Three steps will affect the process:

- the initial interaction of the cluster with the closed-shell CH_4 (the entrance channel),
- the activation of C–H bonds, and
- the stabilization of the methylene unit and elimination of dihydrogen.

Both clusters, Ta_2^+ and $[Ta_2O_2]^+$, readily facilitate the release of H_2 from two methane molecules, which points to exothermic reactions due to the formation of strong Ta–C bonds. However, the second dehydrogenation reaction is greatly enhanced for the bare cluster, while it is suppressed for the dioxide cluster. This difference may be explained accordingly: in the reaction of Ta_2^+, the initial interaction with methane may be the limiting factor, and the presence of an end-on carbene in the intermediate $[Ta_2CH_2]^+$ polarizes the opposite Ta atom. Less electron density has to be repulsed when the closed-shell CH_4 molecule approaches the polarized Ta atom, thereby increasing the rate coefficient of the second reaction step. The higher oxidation state of Ta atoms in the dimer dioxide may be beneficial for the initial interaction with the first methane molecule. However, the reduced number of valence electrons localized on the Ta atoms in the resulting intermediate may hamper the binding to a second methylene group. The change in the rates of consecutive dehydrogenation reactions may thus be explained by an initial entrance channel limitation for Ta_2^+ and an exit channel limitation for $[Ta_2O_2]^+$.

In addition, $[Ta_2\,(CH_2)_2]^+$ is rather inert and facilitates further molecular adsorption only at lower temperatures (see Chapter 5). On the other hand, $[Ta_2O_2\,(CH_2)_2]^+$ seemingly activates a third methane molecule. Consequently, the absence of H_2 elimination from $[Ta_2O_2\,(CH_2)_2\,(CH_4)]^+$ could stem from the scission of only one instead of two C–H bonds, or from the saturation of the tantalum atoms, which would cause a highly endothermic energy balance for the binding of an additional methylene unit.

7.2.3. Abstraction of atomic hydrogen

The pentoxide cluster $[Ta_2O_5]^+$ abstracts a hydrogen atom from methane and releases a methyl radical, thereby generating $[Ta_2O_5H]^+$ (see Eq. 7.2), with a rate coefficient of $1.70 \cdot 10^{-10}$ cm^3s^{-1} and a reaction efficiency of 0.18. As expected for a HAT process [148], this reaction is moreover associated with a low KIE of 1.4. HAT reaction efficiencies in similar systems range from 0.15 in $[Zr_2O_5]^+/CH_4$ to 0.48 in $[V_2O_5]^+/CH_4$ [87]. The HAT process occurs directly, *i.e.* a terminal oxygen atom with a high unpaired density $O_t^\bullet$ accepts a hydrogen radical from methane without any direct involvement of a metal atom in the bond-making or -breaking process [81]. As a result, potentially stronger Ta–C bonds (compared to V–C bonds) [56, 153] are inconsequential and the reaction of the vanadium pentoxide cluster cation is more efficient, which is caused by another effect. Local charges were found to play a role in HAT reactions by yttrium doped vanadium clusters: species with more positive charge at metal-bound oxygen radical centers M–$O^\bullet$ are more reactive [167]. Vibrational spectroscopy assigned $[V_2O_5]^+$ to contain two bridging O atoms, two terminal O atoms bonded to one V atom and a single terminal O atom bonded to the other V atom [176, 177]. Calculations indicate the same structural motifs in the most stable geometry of $[Nb_2O_5]^+$ [178] (with potential experimental evidence for other isomers), and vibrational spectroscopy evidences a general similarity of Nb and Ta oxide clusters structures [179]. If $[Ta_2O_5]^+$ adopts a similar geometric arrangement and an electronic structure with less positive charge around the M–$O^\bullet$ center than in the vanadium counterpart, the reaction efficiency would consequently be diminished.

Under multi-collision conditions, additional species are formed. Adsorption of CH_4 to $[Ta_2O_5]^+$ and $[Ta_2O_5H]^+$ yields $[Ta_2O_5CH_4]^+$ and $[Ta_2O_5CH_5]^+$, respectively (see the reaction scheme in Fig. 7.4). The adsorption reaction to $[Ta_2O_5]^+$ is associated with a rate coefficient of $1.77 \cdot 10^{-10}$ cm^3s^{-1} and no significant KIE (0.9). In contrast, a lower rate coefficient of $0.88 \cdot 10^{-10}$ cm^3s^{-1} and a low KIE of of 0.4 correspond to the adsorption reaction to $[Ta_2O_5H]^+$. Such an inverse KIE (enhanced reaction with CD_4) may be caused by an increased lifetime of an intermediate

$[Ta_2O_5D(CD_4)]^+$ complex compared to the analogous species in the reaction with CH_4 [153].

Following the progression of the reaction, the abundance of $[Ta_2O_5CH_4]^+$ decreases after 40 ms and $[Ta_2O_5CH_5]^+$ increases further, which implies a transformation of the former to the latter (see Fig. 7.4). Moreover, the kinetic modeling requires the inclusion of the reaction from $[Ta_2O_5CH_4]^+$ to $[Ta_2O_5CH_5]^+$, in order to replicate the experimentally determined ion abundances, illustrated in Figure 7.4. An alternative scheme, excluding this reaction and including a reversible adsorption of methane to the pentoxide cluster, yields an insufficient description of the experimental findings: this model significantly overestimates the $[Ta_2O_5]^+$ abundance and underestimates the $[Ta_2O_5CH_5]^+$ abundance. The reaction from $[Ta_2O_5CH_4]^+$ to $[Ta_2O_5CH_5]^+$ formally corresponds to a HAT-type process. However, this process requires a hydrogen radical to be accepted by an

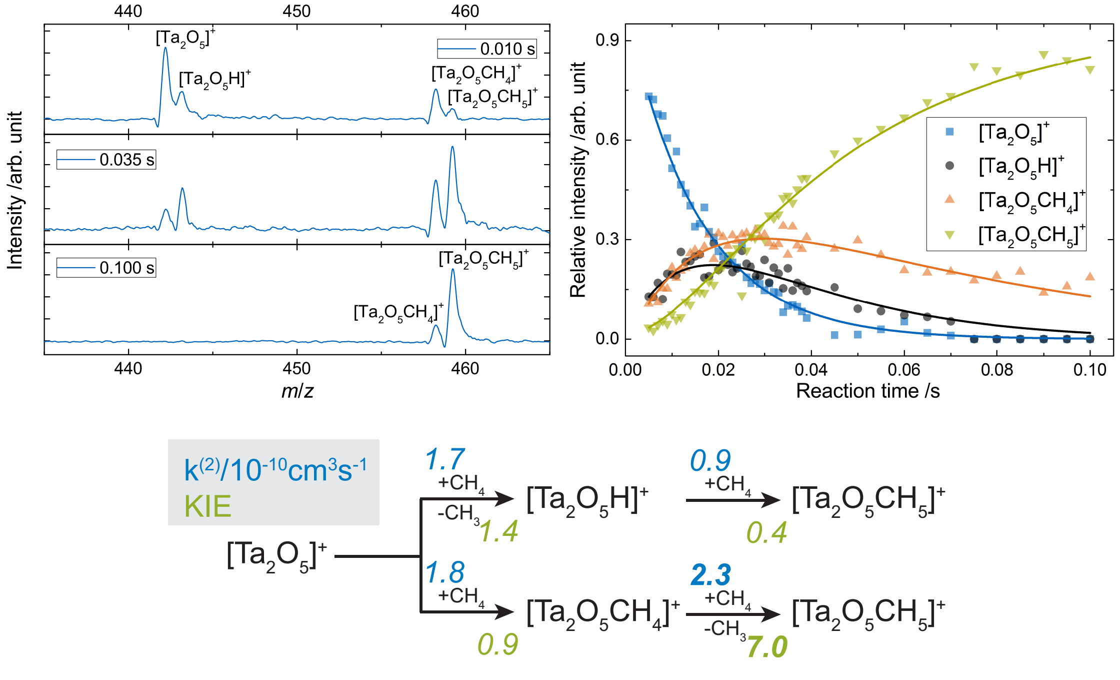

Figure 7.4: *Time-of-flight mass spectra for three storage times (top left) and kinetic simulation (top right) in the reaction of* $Ta_2O_5^+$ *with* CH_4 *and corresponding reaction scheme (bottom). Hydrogen atom abstraction yields* $[Ta_2O_5H]^+$ *and molecular adsorption to this species and the pentoxide cluster causes the formation of* $[Ta_2O_5CH_4]^+$ *and* $[Ta_2O_5CH_5]^+$*. Kinetic modeling additionally evidences a reaction of the former to the latter. Bimolecular rate coefficients for the reaction toward* CH_4 *are depicted in blue, while the kinetic isotope effect is shown in green.*

oxygen-centered radical, *i.e.* the radical nature of $[Ta_2O_5]^+$ would need to be unperturbed in the corresponding adsorption complex. While this already seems unlikely, the rate coefficient ($2.30{\cdot}10^{-10}$ cm^3s^{-1}) is actually enhanced compared to the initial HAT reaction. More importantly, the reaction from $[Ta_2O_5CH_4]^+$ to $[Ta_2O_5CH_5]^+$ is associated with a KIE of 7.0, ruling out a direct HAT process. The elevated KIE rather indicates a PCET-type mechanism: [79, 180] a Lewis basic O atom and a Lewis acidic Ta atom work in tandem to bind a H atom and a CH_3 moiety, respectively, and a methyl radical is subsequently ejected. The PCET reaction of $[Ta_2O_5CH_4]^+$ demonstrates a relatively high efficiency ($\phi = 0.24$) that exceeds the one observed for $[Al_2O_2]^{\bullet+}/CH_4$ ($\phi = 0.10$) [79, 168]. $[Ta_2O_5H]^+$ and $[Ta_2O_5CH_4]^+$ both react with methane to generate $[Ta_2O_5CH_5]^+$. This species potentially corresponds to two isomers, *i.e.* the two reactions result in species that share the same mass but demonstrate a different structure. The existence of two isomers is likely, if the Lewis basic oxygen atom O_b in the PCET reaction of $[Ta_2O_3O_tO_bCH_4]^+$ is not the terminal oxygen atom with radical character O_t in the HAT reaction of $[Ta_2O_3O_tO_b]^+$. Due to a potential different location of the hydroxyl moiety, the structural isomers would correspond to $[Ta_2O_3O_t\,(O_b\text{–}H)\,CH_4]^+$ and $[Ta_2O_3\,(O_t\text{–}H)\,O_bCH_4]^+$.

In conclusion, the reaction of the pentoxide cluster branches into hydrogen atom transfer and methane association. Surprisingly, the product of the latter process remains highly reactive. In this parallel reaction channel, the initial adsorption of methane and resulting interaction apparently disturb the radical nature of the cluster. These findings suggest that a PCET mechanism becomes operative instead, in which $[Ta_2O_5CH_4]^+$ reacts with methane, a C–H bond is broken and an $[H_3C\text{–}Ta_2O_4OH\,(CH_4)]^+$ intermediate is formed. This species subsequently ejects a methyl radical. As there is no evidence of a PCET mechanism in the first reaction step, CH_4 adsorption seemingly alters the electronic structure of the cluster, thereby enabling an efficient PCET reaction.

7.3. Summary

Mechanisms in the reactions of cationic tantalum dimer oxides toward methane were elucidated with the help of kinetic modeling. The exact number of oxygen atoms in the clusters non-monotonically determines the reactivity mode and the associated rate coefficient. The monoxide cluster, Ta_2O^+, is almost completely inert, whereas $Ta_2O_3^+$ demonstrates the highest overall reactivity and adsorbs methane molecularly. Similar to the bare dimer cation, $Ta_2O_2^+$ mediates dehydrogenation and dihydrogen elimination from two methane molecules. Though, the reaction of $Ta_2O_2^+$ demonstrates different limitations, potentially due to electronic effects, and causes the activation (in absence of H_2 ejection) of a third molecule as evidenced by reaction kinetics. The pentoxide cluster, $Ta_2O_5^+$, abstracts atomic hydrogen from methane as expected from the predicted terminal oxygen radical. Surprisingly, evidence for a consecutive PCET reaction is found: the intermediate of molecular adsorption, $[Ta_2O_5CH_4]^+$, also cleaves a C–H bond upon reaction with a second molecule and concurrently ejects a methyl radical. The adsorption of methane in the first reaction step affects the electronic structure of the cluster, seemingly leading to a Ta–O Lewis acid-base pair that efficiently activates a second methane molecule. In contrast to a direct hydrogen atom transfer, this reaction is associated with an elevated kinetic isotope effect and, thus, corresponds to a distinctly different mechanism.

7.4. Supplementary Information

7.4.1. Reactions with CD_4

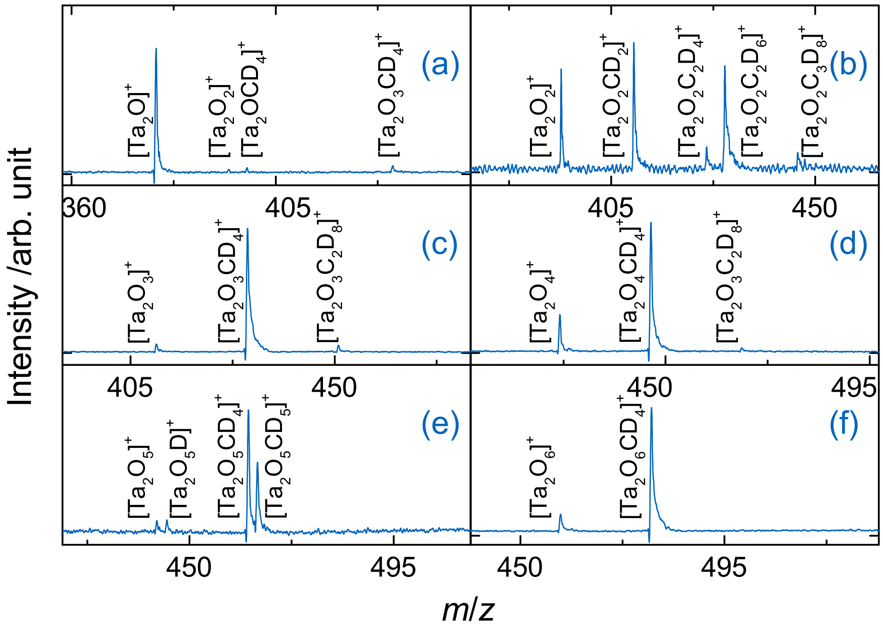

Figure 7.5: *Time-of-flight mass spectra of tantalum dimer oxides exposed to d_4-methane, demonstrating different reaction mechanisms as a function of oxygen content. Ta_2O^+ with $3.9 \cdot 10^{-2}$ Pa CD_4 after 0.025 s (a), $Ta_2O_2^+$ with $9.8 \cdot 10^{-4}$ Pa CD_4 after 0.035 s (b), $Ta_2O_3^+$ with $4.4 \cdot 10^{-4}$ Pa CD_4 after 0.030 s (c), $Ta_2O_4^+$ with $4.2 \cdot 10^{-4}$ Pa CD_4 after 0.030 s (d), $Ta_2O_5^+$ with $3.4 \cdot 10^{-4}$ Pa CD_4 after 0.025 s (e) and $Ta_2O_6^+$ with $4.2 \cdot 10^{-4}$ Pa CD_4 after 0.025 s (f). All reactions are conducted at 300 K and in presence of He buffer gas at a total pressure of 0.77 Pa.*

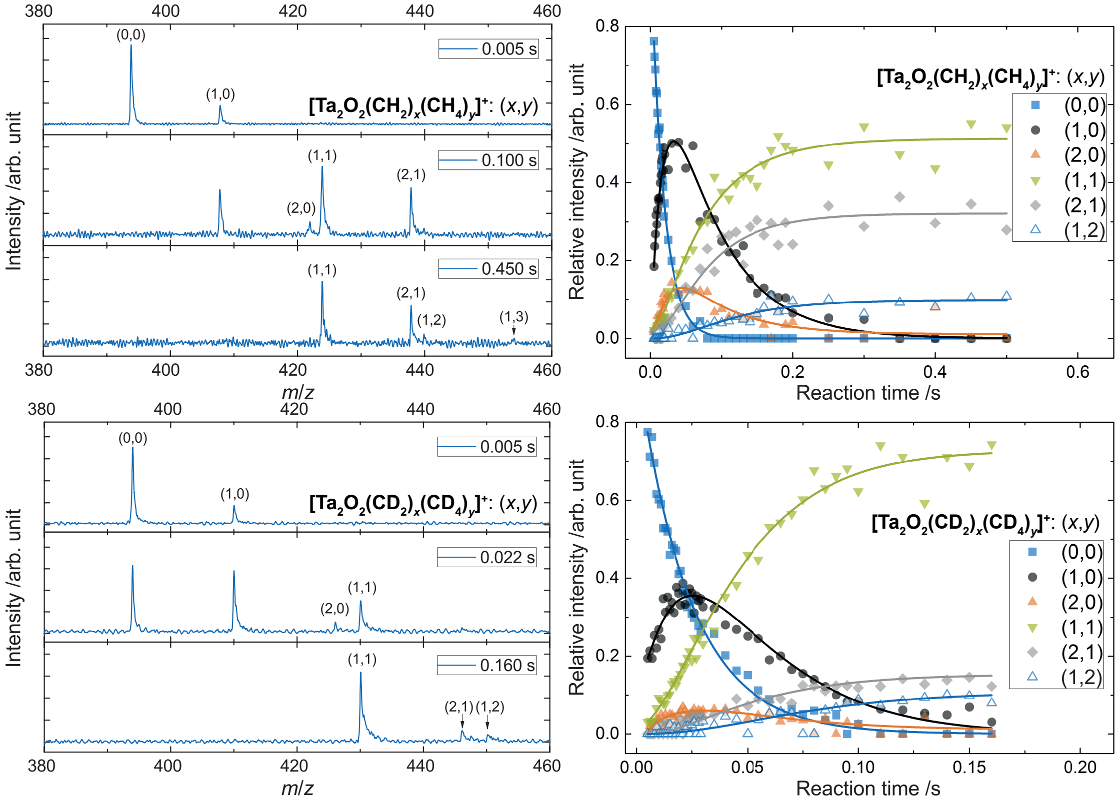

Figure 7.6: *Time-of-flight mass spectra of $Ta_2O_2^+$ exposed to $2.5{\cdot}10^{-4}$ Pa CH_4 (top left) and corresponding kinetic simulation (top right). Time-of-flight mass spectra of $Ta_2O_2^+$ exposed to $3.4{\cdot}10^{-4}$ Pa CD_4 (bottom left) and corresponding kinetic simulation (bottom right). The reaction of $[Ta_2O_2(CD_2)_2]^+$ to $[Ta_2O_2(CD_2)_2(CD_4)]^+$ is significantly suppressed compared to the analogous reaction with CH_4, which implies C–H(D) cleavage in absence of dihydrogen elimination. All reactions are conducted at 300 K and in presence of He buffer gas at a total pressure of 0.77 Pa.*

7.4.2. Rate coefficients and KIE

Table 7.1 displays rate coefficients for the reactions of $[Ta_2O_x]^+$ ($x = 0-6$) toward CH_4 and CD_4. Theoretical collision rates k^{LGS} obtained from the Langevin-Giousmousis-Stevenson model [136] are utilized to determine the corresponding reaction efficiencies ($\phi = k^{(2)}/k^{\mathrm{LGS}}$). The ratio of theoretical collision rates is applied as a correction factor in order to calculate the kinetic isotope effect (KIE):

$$\begin{aligned}\mathrm{KIE} &= \frac{k^{(2)}_{\mathrm{CH_4}}}{k^{(2)}_{\mathrm{CD_4}}} \cdot \frac{k^{\mathrm{LGS}}_{\mathrm{CD_4}}}{k^{\mathrm{LGS}}_{\mathrm{CH_4}}} \\ &\approx \frac{k^{(2)}_{\mathrm{CH_4}}}{k^{(2)}_{\mathrm{CD_4}}} \cdot 0.9\end{aligned}$$

Table 7.1: *Bimolecular rate coefficients* $k^{(2)}$ *in units of* $10^{-11}\,cm^3 s^{-1}$ *and kinetic isotope effects (KIE) in the consecutive reaction of* $[Ta_2O_x]^+$ $(x = 0 - 6)$ *with* CH_4 *and* CD_4*. Reaction efficiencies* ($\phi = k^{(2)}/k^{LGS}$) *are additionally displayed.*

Reaction	$k^{(2)}_{CH_4}$ [a]	$k^{(2)}_{CD_4}$ [a]	ϕ_{CH_4}	ϕ_{CD_4}	KIE
$Ta_2^+ + CH_4 \rightarrow [Ta_2CH_2]^+ + H_2$	1.69±0.34	0.18±0.03	0.018	0.002	8.69±1.94
$[Ta_2CH_2]^+ + CH_4 \rightarrow [Ta_2C_2H_4]^+ + H_2$	10.12±2.05	1.31±0.28	0.104	0.015	6.94±1.56
$[Ta_2O]^+ + CH_4 \rightarrow [Ta_2OCH_4]^+$	N/A[b]	>0.01	N/A[b]	$1 \cdot 10^{-4}$	N/A[b]
$[Ta_2O_2]^+ + CH_4 \rightarrow [Ta_2O_2CH_2]^+ + H_2$	16.96±3.44	5.83±1.17	0.176	0.067	2.62±0.75
$[Ta_2O_2CH_2]^+ + CH_4 \rightarrow [Ta_2O_2C_2H_4]^+ + H_2$	2.33±0.51	1.05±0.26	0.024	0.012	1.99±0.65
$[Ta_2O_2CH_2]^+ + CH_4 \rightarrow [Ta_2O_2C_2H_6]^+$	3.15±0.64	4.41±0.89	0.033	0.051	0.64±0.18
$[Ta_2O_2C_2H_4]^+ + CH_4 \rightarrow [Ta_2O_2C_3H_8]^+$	9.17±2.20	1.97±1.31	0.095	0.015	4.19±2.98
$[Ta_2O_3]^+ + CH_4 \rightarrow [Ta_2O_3CH_4]^+$	54.28±10.86	27.30±5.46	0.564	0.315	1.79±0.51
$[Ta_2O_4]^+ + CH_4 \rightarrow [Ta_2O_4CH_4]^+$	13.24±2.65	17.23±3.45	0.138	0.200	0.69±0.20
$[Ta_2O_5]^+ + CH_4 \rightarrow [Ta_2O_5H]^+ + CH_3$	16.98±3.46	10.99±2.35	0.177	0.127	1.39±0.41
$[Ta_2O_5]^+ + CH_4 \rightarrow [Ta_2O_5CH_4]^+$	17.67±3.59	16.88±3.48	0.184	0.196	0.94±0.27
$[Ta_2O_5H]^+ + CH_4 \rightarrow [Ta_2O_5CH_5]^+$	8.78±1.84	17.97±3.87	0.091	0.208	0.44±0.13
$[Ta_2O_5CH_4]^+ + CH_4 \rightarrow [Ta_2O_5CH_5]^+ + CH_3$	23.02±4.70	2.95±0.65	0.240	0.034	7.02±2.11
$[Ta_2O_6]^+ + CH_4 \rightarrow [Ta_2O_6CH_4]^+$	32.52±6.52	29.67±5.94	0.339	0.344	0.99±0.28

[a] Rate coefficients referenced to $[TaCH_2]^+$ formation determined by Shayesteh *et al.* [53] (see Chapter A.5). [b] Not available due to a reaction rate toward CH_4 below the detection threshold.

COUPLING REACTIONS OF TANTALUM-METHYLENE COMPLEXES WITH DIOXYGEN

8

Cationic tantalum complexes $[TaCH_2]^+$ and $[Ta_4CH_2]^+$, products of thermal methane dehydrogenation, are collected and stored in a ring electrode ion trap. In there, C–O coupling reactions are probed by exposing the tantalum complexes to dioxygen in presence of helium buffer gas, thereby facilitating reactions underwell defined multi-collision conditions at 300 K. Time-of-flight mass spectrometry determines the time-dependent reaction products and kinetic modeling is used to analyze the reaction progression, illustrating a drastic difference in the selectivity.

8.1. Introduction

The purposeful transformation of methane to value-added products is a highly sought-after goal. A route to this end is transition metal-mediated dehydrogenation of methane followed by oxidative coupling of the resulting metal carbene species to a target molecule [66, 181]. Platinum catalyzes a reaction of this kind in the Degussa process, which couples methane to ammonia, yielding hydrogen cyanide and dihydrogen [35, 36, 50, 51, 73, 182, 183]. Studying isolated reactive centers, *e.g.* cationic metal atoms and clusters in the gas phase, elucidates fundamental effects due to the absence of perturbing interactions. Accordingly, insights obtained by reacting $[PtCH_2]^+$ with NH_3 in a Fourier-transform ion cyclotron mass spectrometer (FT-ICR) provide a conceptual framework for reaction steps occurring in the Degussa process [50–52]. Koszinowski *et al.* have also studied the reactions of platinum cluster carbenes ($[Pt_nCH_2]^+$, n = 1–5) with dioxygen, methane and water, consequently revealing cluster size-dependent selectivities: in contrast to atomic platinum, the cationic clusters favor the generation of carbides, which corresponds to soot formation on an extended metallic system.

Furthermore, the atomic cation of tantalum mediates coupling of methane and carbon dioxide, resulting in the formation of ethenone, dihydrogen and carbon monoxide [50, 152]. However, Ta^+ is consumed in the course of the reaction by formation of $[TaO_2]^+$. While the atomic cation of tantalum has also been shown to dehydrogenate methane under elimination of H_2 by several groups [53–55, 62, 152, 157–159], the corresponding clusters (Ta_n^+, $n = 2$–4) have only recently been found to demonstrate the same behavior (see Chapter 5). Although the size effects observed for $[Pt_nCH_2]^+$ motivates studies of other metal cluster systems, literature on reactions of free metal cluster carbenes is extremely scarce. The oxidation of $[TaCH_2]^+$ and $[Ta_4CH_2]^+$ may subsequently provide valuable insights of C–O coupling mechanisms on systems based on metals more abundant than platinum.

8.2. Generation of tantalum-methylene complexes

Reacting the atomic cation of tantalum with methane in the ring electrode ion trap results in dehydrogenation and concomitant dihydrogen elimination, and the same occurs for small tantalum cluster cations:

$$Ta_n^+ + CH_4 \rightarrow [Ta_nCH_2]^+ + H_2 \qquad \text{for } n < 5 \tag{8.1}$$

In order to investigate subsequent reactions with oxygen, selected tantalum methylene species[1] are generated by pulsing CH_4 into a second collision volume inside of the laser vaporization cluster source. Previous investigations evidence reaction conditions in the source comparable to the ion trap studies and estimate a temperature of below 250 K (see Chapter 4.3). Previously generated $[Ta_{1,4}CH_2]^+$ clusters are mass selected and exposed to CH_4 in the ion trap to compare the reactivity to the consecutive reactions of the corresponding bare clusters, and the in-source formed cluster complexes are found to generate the same products (see Chapter 8.6). While structural isomers cannot be ruled out by mass spectrometry, the rate coefficients are identical within the error of the experiment (see Tab. 8.3), which strongly evidences a similar geometric and electronic structure compared to the reaction products of the bare clusters in the ion trap.

---

[1] Due to a low natural abundance of the dimer and trimer clusters (see Ref. [184] and also Chapter A.6) combined with inefficient dehydrogenation reactions, the production of $[Ta_2CH_2]^+$ and $[Ta_3CH_2]^+$ with sufficient intensity was not feasible.

8.3. Results

The following chapter individually describes the reactions of $[TaCH_2]^+$ and $[Ta_4CH_2]^+$ toward oxygen in detail, and is followed by a discussion and comparison of the two systems.

8.3.1. $[TaCH_2]^+ + O_2$

Figure 8.1 displays the consecutive reactions of $[TaCH_2]^+$ with dioxygen. The oxidation reactions generate two main intermediates, $[TaO]^+$ and $[TaOH]^+$, and a main reaction product, $[TaO_2]^+$. Minor species include $[TaOCH_2]^+$, $[TaO_2H]^+$, $[TaO_3]^+$, $[TaO_3H_2]^+$ and $[TaO_4H]^+$ as depicted in Fig. 8.1a. Reactions with traces of background gases are ruled by conducting experiments with isotopically labeled dioxygen, $^{18}O_2$ (see Fig. 8.8 in Chapter 8.6).

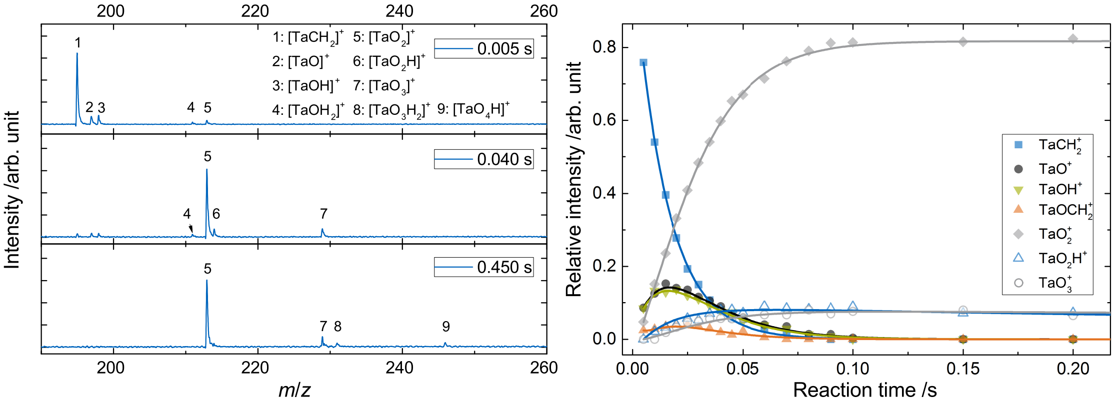

Figure 8.1: *Time-of-flight mass spectra (left) and corresponding kinetic simulation (right) of* $[TaCH_2]^+$ *reacting with* $4.1 \cdot 10^{-5}$ *Pa* O_2 *at 300 K. In the main reaction channel,* $[TaO]^+$ *is formed via release of "*CH_2O*" and is subsequently oxidized to* $[TaO_2]^+$.

Kinetic modeling perfectly replicates the progression of the reaction (see Fig. 8.1), thereby revealing the reaction channels and the corresponding rate coefficients. The tantalum carbene forms six species with varying branching ratios (BR). Albeit included in the kinetic simulation, the generation of $[TaO_2H_2]^+$ is not shown in the following scheme due to a BR of below 2%.

As uptake of dioxygen corresponds to an additional mass of 32, tantalum monoxide formation (additional mass of 2) requires the loss of neutral species with a mass of 30. This "CH_2O" fragment corresponds to the release of formaldehyde or the simultaneous loss of CO/H_2. The formation of the tantalum hydroxide in

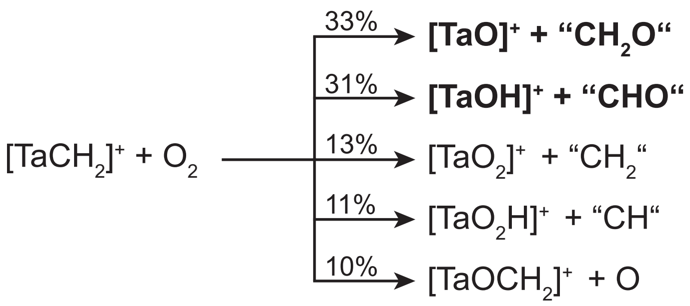

a second reaction channel similarly implies ejection of one oxygen, carbon and hydrogen atom, *e.g.* a formyl radical CHO. While direct oxidation of the tantalum carbene and the concurrent release of a methylene fragment generates the tantalum dioxide cation, oxidation of $[TaO]^+$ and $[TaOH]^+$ in a second reaction step also produces $[TaO_2]^+$ via the ejection of O and OH, respectively. The loss of a methylidyne radical causes the formation of $[TaO_2H]^+$ and the remainder of the minority species is formed (in subsequent reaction steps) via uptake of dioxygen and release of an O atom. The reaction steps displayed in the above scheme are associated with rate coefficients in the order of 10^{-10} cm^{3}s^{-1} and comparing these values to theoretical collision rates (according to the surface charge capture model by Kummerlöwe and Beyer [143]) yields high to medium reaction efficiencies (between $7.27 \cdot 10^{-10}$ cm^{3}s^{-1} and 84% to $1.25 \cdot 10^{-10}$ cm^{3}s^{-1} and 14% for $[TaO]^+$ and $[TaOCH_2]^+$ formation, respectively; see Tab. 8.1 in Chapter 8.6). Considering that the sum of all efficiencies in this first reaction step should not exceed unity and yet it does, the surface charge capture model seemingly fails to provide an upper limit for the collision rate. This finding is furthermore evidenced by efficiencies up to 200% for the subsequent reaction steps, in which $[TaO]^+$ and $[TaOH]^+$ form the tantalum dioxide cation (see Tab. 8.1 in Chapter 8.6).

8.3.2. $[Ta_4CH_2]^+ + O_2$

When $[Ta_4CH_2]^+$ reacts with dioxygen, $[Ta_4O]^+$, $[Ta_4CO_2]^+$ and $[Ta_4O_3]^+$ are initially generated in the high-mass range (see Figure 8.2). However, the reaction additionally yields products of oxidative degradation. While those include $[Ta_3O]^+$ and $[TaO]^+$ in the first reaction step, the previously mentioned species undergo further consecutive reactions with O_2, causing the formation of $[Ta_xO_y]^+$ ($x < 4$, $y > 1$). The main products of the oxidation reactions are $[TaO_2]^+$ and $[Ta_2O_6]^+$ as shown in Figure 8.2.

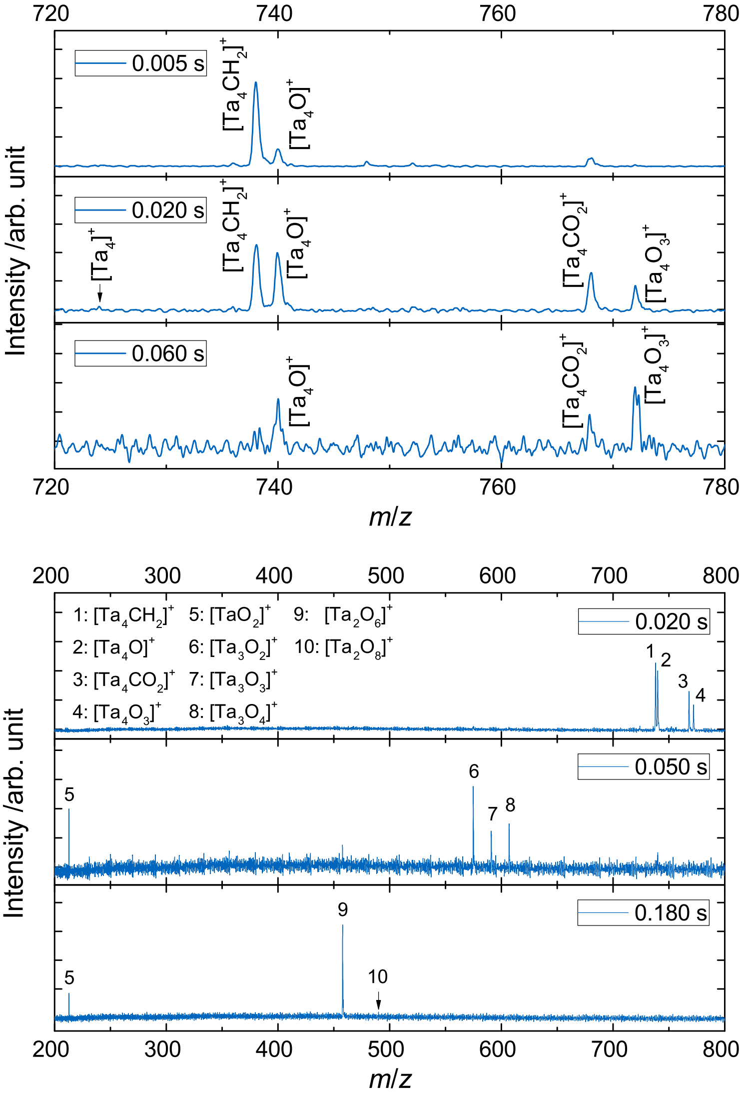

Figure 8.2: *Time-of-flight mass spectra of* $[Ta_4CH_2]^+$ *exposed to* $5.2 \cdot 10^{-5}$ *Pa* O_2 *in He buffer gas at 300 K for various reaction times. Spectra on the bottom illustrate consecutive oxidative degradation, yielding* $[TaO_2]^+$ *and* $[Ta_2O_6]^+$*, whereas spectra on top show the initial oxidation to* $[Ta_4O]^+$, $[Ta_4CO_2]^+$ *and* $[Ta_4O_3]^+$*.*

Again, kinetic modeling is successfully employed to determine all reaction channels and the associated rate coefficients (see Tab. 8.2 in Chapter 8.6). The as-obtained BR values for the products of the first reaction step range from 4% for the bare tetramer cluster to 56% for the mono-oxide of the tetramer cluster.

Similar to the reaction of $[TaCH_2]^+$, the formation of $[Ta_4O]^+$ suggests the release of "CH_2O". $[Ta_4CH_2]^+$ also reacts with residual H_2O, forming $[Ta_4O]^+$ and CH_4 (see Fig. 8.7). This background reaction does not interfere with the following reaction scheme as it occurs extremely slowly. Furthermore, the main products are

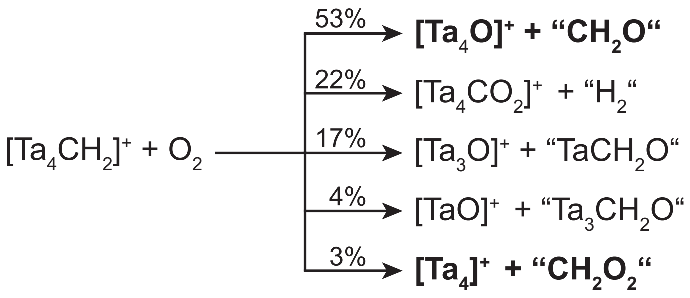

also confirmed by conducting experiments with $^{18}O_2$ (see Figs. 8.9 and 8.10 in Chapter 8.6). As expected, a significant isotope effect is not observed for the reaction. Ejection of H_2 in the reaction of $[Ta_4CH_2]^+$ with O_2 leads to the generation of $[Ta_4CO_2]^+$, which subsequently reacts to $[Ta_4O_3]^+$ via release of CO. The intermittent adsorption complex $[Ta_4CH_2O_2]^+$ may also relax through loss of "$TaCH_2O$" or "Ta_3CH_2O", respectively forming $[Ta_3O]^+$ and $[TaO]^+$. Lastly, a small abundance of the bare tetramer cluster is generated. Although the amount of $[Ta_4]^+$ is close to the noise level, the kinetic modeling is able to replicate the trend of an initial increase of relative abundance followed by a decrease due to the subsequent reaction to $[Ta_3O]^+$ (see Fig. 8.3). The formation of $[Ta_4]^+$ requires the release of formic acid, HCOOH, or a concerted ejection of either CO/H_2O or CO_2/H_2. The rate coefficients for the first reaction steps as depicted in the scheme lie between

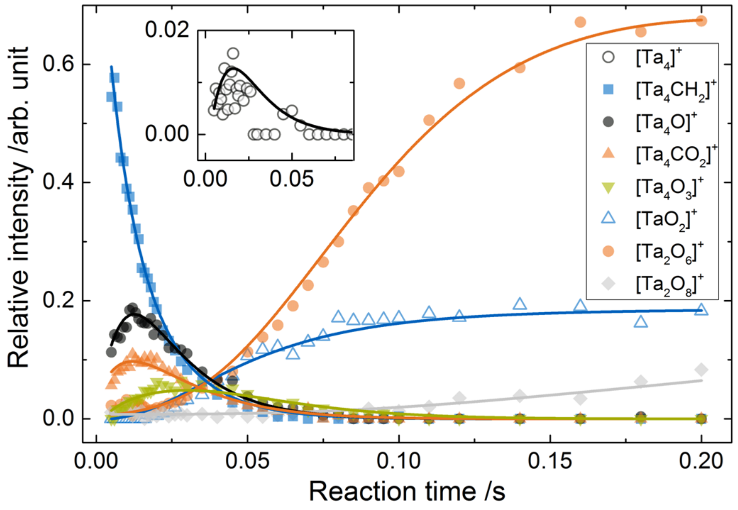

Figure 8.3: *Kinetic simulation of* $[Ta_4CH_2]^+$ *reacting with* $5.2{\cdot}10^{-5}$ *Pa* O_2 *at 300 K. Symbols depict measured ion abundances, whereas solid lines show the results of kinetic modeling. As seen in the inset, the trend for the generation and subsequent reaction of* $[Ta_4]^+$ *is replicated qualitatively.*

11.69 (for the generation of $[Ta_4CH_2]^+$) to $0.74 \cdot 10^{-10}$ cm^3s^{-1} (for the formation of the bare tetramer cluster cation, see Tab. 8.2 in Chapter 8.6). Latter is affected by a large error due to the very low abundance of the species. One should note that a reaction model including the subsequent oxidation of $[Ta_4CH_2]^+$ via $[Ta_4C]^+$ to $[Ta_4CO_2]^+$ is also able to replicate the general experimental findings. However, the tantalum tetramer carbide barely exceeds the noise level, the abundance shows no clear trend as a function of reaction time, and the oxidation reaction would have to proceed with a reaction efficiency of ten times the collision rate predicted by the SCC model. Thus, this alternative reaction model seems very unlikely and is therefore discarded in the following discussion.

8.4. Discussion

Both tantalum methylene complexes, the mononuclear as well as the tetramer system, release carbon upon oxidation through C–O coupling reactions. The main pathway of both systems progresses via the formation of the corresponding mono-oxide and the ejection of "CH_2O". This reaction outcome was also observed by Koszinowski *et al.* when the cationic platinum carbene was exposed to dioxygen. The released neutral molecule was assigned to be formaldehyde as it is thermodynamically favorable compared to a concerted release of CO/H_2 [73]. The tantalum tetramer cluster complex $[Ta_4CH_2]^+$ heavily favors formaldehyde formation with a BR of 56%, whereas $[TaCH_2]^+$ shows a more balanced release of either "CH_2O" or "CHO" (33% and 31% BR). In contrast, the reaction of $[PtCH_2]^+$ with O_2 was found to produce minor amounts of $[PtO]^+$/"CH_2O" (30% BR) and predominantly Pt^+/"CH_2O_2" (70% BR) [73, 185]. The release of "CHO", "CH_2", "CH" and O by $[TaCH_2]^+$ evidences a "hot" reaction: the O–O bond scission and subsequent Ta-O bond formation feed sufficient energy into the system that facilitates the ejection of these unsaturated fragments. On the other hand, $[Ta_4CH_2]^+$ and the corresponding reaction intermediates cleave additional O–O bonds and relax by releasing neutral tantalum-containing fragments. This process, oxidative degradation, was previously observed in the reaction of bare tantalum cluster cations with dioxygen [120, 154]. Compared to the tantalum monomer carbene, the cluster core possesses more vibrational modes and may function as an intermittent energy reservoir that prevents a higher BR for degradation processes as well as the immediate ejection of unstable neutrals.

$[Ta_4CH_2]^+$ furthermore reacts via $[Ta_4CO_2]^+$ to $[Ta_4O_3]^+$, concurrently generating H_2 in the first step and CO in the second step. As $[Ta_4CH_2]^+$ stems from methane dehydrogenation, this process accordingly represents an analogue to steam reforming of CH_4. Lastly, "CH_2O_2" and $[Ta_4]^+$ are generated in a minor reaction channel. The generation of the bare metal species was previously identified as the major reaction in the oxidation of $[Pt_nCH_2]^+$ ($n = 1, 3 - 5$) [73]. Interestingly, this process is associated with very similar rate coefficients for the tantalum ($7.4 \cdot 10^{-11}$ cm^{3}s^{-1}) and the platinum tetramer cluster complex ($9.0 \cdot 10^{-11}$ cm^{3}s^{-1}). Based on theoretical calculations for the platinum monomer carbene, "CH_2O_2" was assigned to a mixture of HCOOH, CO_2/H_2 and CO/H_2O [73, 185]. The distribution of the neutral products in the reaction of the tantalum cluster might be shifted compared to the platinum counterpart: quantum-chemical calculations (see Chapter 6) predict that a dihydrido-carbide structure of $[Ta_4CH_2]^+$ is more stable than the corresponding cluster-methylene isomer. However, significant isomerization may occur in the energized $[Ta_4CH_2O_2]^+$ collision complex.

As methane dehydrogenation and concomitant H_2 elimination generates $[Ta_4CH_2]^+$, the reaction step of $[Ta_4]^+$ formation corresponds to the back-reaction of a catalytic cycle, in which the tetramer cluster oxidizes methane to "CH_2O_2". Although, the prospects of this cycle are diminished by a low selectivity and oxidative degradation that occurs when the bare cluster, in lieu of the corresponding methylene complex, is exposed to oxygen. The degradation processes are different to the behavior of the platinum cluster carbenes, which preferentially release "CH_2O_2" (with the exception of $[Pt_2CH_2]^+$) [73].

8.5. Conclusion

To summarize, these results elucidate C–O coupling reactions of isolated metal-methylene complexes that depend on the size of the metal core and the metal itself. In general, $[TaCH_2]^+$ and $[Ta_4CH_2]^+$ exhibit different oxidation pathways with different branching ratios. For both species, the formal ejection of formaldehyde and metal monoxide formation is the dominant reaction channel. Only about one third of the atomic carbenes react accordingly, whereas the branching ratio increases to over 50% for $[Ta_4CH_2]^+$. The atomic system undergoes "hot" reactions, which may become suppressed in case of a more efficient transfer of excess energy to the environment, *e.g.* to a potential support material. Likewise, the oxidation products of $[Ta_nCH_2]^+$ ($n = 1, 4$) show that the tetramer cluster is a more "realistic" model for a reactive center of an extended system, and a potential catalytic cycle for the activation of methane (similar to the platinum system [73]) was identified, albeit with significant limitations. While the tantalum species investigated in this work demonstrate larger rate coefficients than previously studied platinum carbenes, they also show channels corresponding to over-oxidation of the methylene fragment and degradation of the cluster. The comparison with platinum consequently reveals that tantalum-based systems may indeed be potential catalysts for activating methane, but they are also more prone to oxidative degradation than their noble-metal counterparts.

8.6. Supplementary Information

8.6.1. Rate coefficients and theoretical collision rates

Tables 8.1 and 8.2 show rate coefficients for the reactions of $[TaCH_2]^+$ and $[Ta_4CH_2]^+$ toward $^{16}O_2$ and $^{18}O_2$. Theoretical collision rates with $^{16}O_2$ and $^{18}O_2$, $k^{SCC}_{^{16}O_2}$ and $k^{SCC}_{^{18}O_2}$, are calculated according to the surface charge capture (SCC) theory developed by Kummerlöwe and Beyer [143]. Theoretical collision rates for the ligated atomic system were determined neglecting the change in geometric cross section, only accounting for the increased mass.

Table 8.1: *Bimolecular rate coefficients $k^{(2)}$ in units of $10^{-10} cm^3 s^{-1}$ in the consecutive reaction of $[TaCH_2]^+$ with $^{16}O_2$ and $^{18}O_2$. Theoretical collision rates k^{SCC} are modeled by surface charge capture (SCC) theory developed by Kummerlöwe and Beyer [143] and the corresponding reaction efficiencies ($\phi = k^{(2)}/k^{SCC}$) are additionally shown.*

Reaction	$k^{(2)}_{^{16}O_2}$ [a]	$k^{(2)}_{^{18}O_2}$ [a]	$k^{SCC}_{^{16}O_2}$	$k^{SCC}_{^{18}O_2}$	$\phi_{^{16}O_2}$	$\phi_{^{18}O_2}$
$[TaCH_2]^+ + O_2 \rightarrow [TaO]^+$ + ”CH$_2$O”	7.27±1.52	7.45±1.53	8.70	8.28	0.84	0.90
$[TaCH_2]^+ + O_2 \rightarrow [TaOH]^+$ + ”CHO”	6.71±1.40	9.27±1.92	8.70	8.28	0.77	1.12
$[TaCH_2]^+ + O_2 \rightarrow [TaO_2]^+$ + ”CH$_2$”	2.89±0.68	2.94±0.75	8.70	8.28	0.33	0.36
$[TaCH_2]^+ + O_2 \rightarrow [TaO_2H]^+$ + ”CH”	2.51±0.51	2.54±0.52	8.70	8.28	0.29	0.31
$[TaCH_2]^+ + O_2 \rightarrow [TaOCH_2]^+ + O$	1.25±0.40	N/A[b]	8.70	8.28	0.14	N/A[b]
$[TaO]^+ + O_2 \rightarrow [TaO_2]^+ + O$	17.71±3.68	17.06±3.89	8.71	8.28	2.03	2.06
$[TaOH]^+ + O_2 \rightarrow [TaO_2]^+$ + ”OH”	13.64±2.89	20.11±4.26	8.71	8.29	1.57	2.43

[a] Rate coefficients referenced to $[TaCH_2]^+$ formation determined by Shayesteh *et al.* [53] (see Chapter A.5). [b] Not available due to a mass overlap of $[Ta^{18}OCH_2]^+$ and $[Ta^{16}O_2]^+$.

Table 8.2: *Bimolecular rate coefficients* $k^{(2)}$ *in units of* $10^{-10}\text{cm}^3 s^{-1}$ *in the consecutive reaction of* $[Ta_4CH_2]^+$ *with* $^{16}O_2$ *and* $^{18}O_2$. *Theoretical collision rates* k^{SCC} *of the bare cluster are modeled by surface charge capture (SCC) theory developed by Kummerlöwe and Beyer [143] and the corresponding reaction efficiencies* ($\phi = k^{(2)}/k^{SCC}$) *are additionally shown.*

Reaction	$k^{(2)}_{^{16}O_2}$ [a]	$k^{(2)}_{^{18}O_2}$ [a]	$k^{SCC}_{^{16}O_2}$	$k^{SCC}_{^{18}O_2}$	$\phi_{^{16}O_2}$	$\phi_{^{18}O_2}$
$[Ta_4CH_2]^+ + O_2 \rightarrow [Ta_4O]^+ +$ ”CH_2O”	11.69±3.48	13.84±3.93	10.32	9.75	1.13	1.42
$[Ta_4CH_2]^+ + O_2 \rightarrow [Ta_3O]^+ +$ ”$TaCH_2O$”	3.84±6.27	N/A[b]	10.32	9.75	0.37	N/A[b]
$[Ta_4CH_2]^+ + O_2 \rightarrow [Ta_4CO_2]^+ +$ ”H_2”	5.00±1.26	6.78±1.93	10.32	9.75	0.48	0.70
$[Ta_4CH_2]^+ + O_2 \rightarrow [TaO]^+ +$ ”Ta_3CH_2O”	0.95±0.31	N/A[b]	10.32	9.75	0.09	N/A[b]
$[Ta_4CH_2]^+ + O_2 \rightarrow [Ta_4]^+ +$ ”CH_2O_2”	0.74±6.21	0.06±0.56	10.32	9.75	0.07	0.01
$[Ta_4CO_2]^+ + O_2 \rightarrow [Ta_4O_3]^+ +$ ”CO	17.29±7.71	4.53±1.29	10.32	9.75	1.68	0.46

[a] Rate coefficients referenced to $[TaCH_2]^+$ formation determined by Shayesteh *et al.* [53] (see Chapter A.5). [b] Not available due to a lower extent of the degradation reactions in the investigated storage time and a kinetic model without individual degradation steps (*i.e.* the sum of the abundances of all degraded clusters was treated as a single species).

8.6.2. Assignment of species (reactions in He, CH$_4$ and ^{18}O$_2$)

Table 8.3: *Bimolecular rate coefficients for tantalum complexes* $[Ta_{1,4}CH_2]^+$ *generated in the cluster source (CS) reacting with* CH_4 *in the ring electrode ion trap (RET),* $k^{(2)}_{CS}$, *and for bare clusters undergoing consecutive reactions toward* CH_4 *in the RET,* $k^{(2)}_{RET}$, *in units of* $10^{-11}cm^3 s^{-1}$.

Reaction product	$k^{(2)}_{\text{CS}}$ [a]	$k^{(2)}_{\text{RET}}$ [a]
$[Ta\,(CH_2)_2]^+$	38.65±7.80	35.20±7.11
$[Ta\,(CH_2)_3]^+$	53.44±10.79	40.54±8.19
$[Ta\,(CH_2)_4]^+$	57.49±11.61	55.38±11.20
$[Ta\,(CH_2)_4\,(CH_4)]^+$	20.74±4.19	31.09±6.28
$[Ta_4\,(CH_2)_2]^+$	0.05±0.01	0.06±0.01
$[Ta_4\,(CH_2)_2\,(CH_4)]^+$	0.02±0.02	0.05±0.01

[a] Rate coefficients referenced to $[TaCH_2]^+$ formation determined by Shayesteh *et al.* [53] (see Chapter A.5).

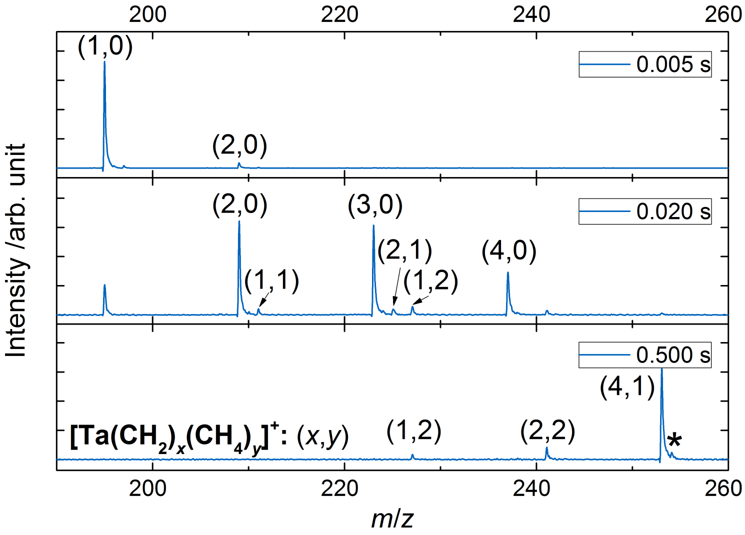

Figure 8.4: *Time-of-flight mass spectra of* $[TaCH_2]^+$ *formed in the cluster source, reacting with* CH_4 *in the ion trap at 300 K. The spectra depict a consecutive reaction toward* $[Ta(CH_2)_2]^+$, $[Ta(CH_2)_3]^+$, $[Ta(CH_2)_4]^+$ *and* $[Ta(CH_2)_4(CH_4)]^+$ *as well as* $[Ta(CH_2)(CH_4)]^+$, $[Ta(CH_2)(CH_4)_2]^+$, $[Ta(CH_2)_2(CH_4)]^+$ *and* $[Ta(CH_2)_2(CH_4)_2]^+$ *as minor species. The asterisk marks a* $[Ta(CH_2)_4(CH_4)]^+$ *species shifted by a single mass unit as it contains a naturally occurring* ^{13}C *isotope. The same products are observed when* Ta^+ *is exposed to methane (see Chapter 5).*

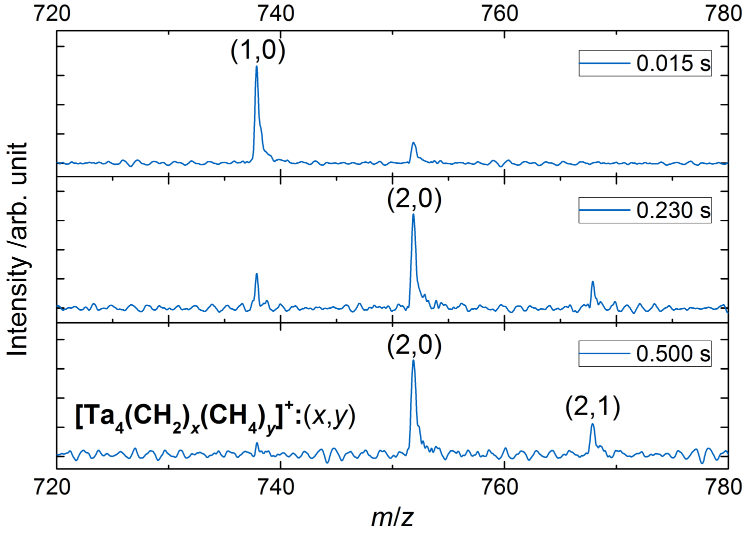

Figure 8.5: *Time-of-flight mass spectra of* $[Ta_4CH_2]^+$ *formed in the cluster source and exposed to* CH_4 *in the ion trap at 300 K, which generates* $[Ta_4(CH_2)_2]^+$ *and* $[Ta_4(CH_2)_2(CH_4)]^+$ *as seen in the reaction of the bare cluster with methane (see Chapter 5).*

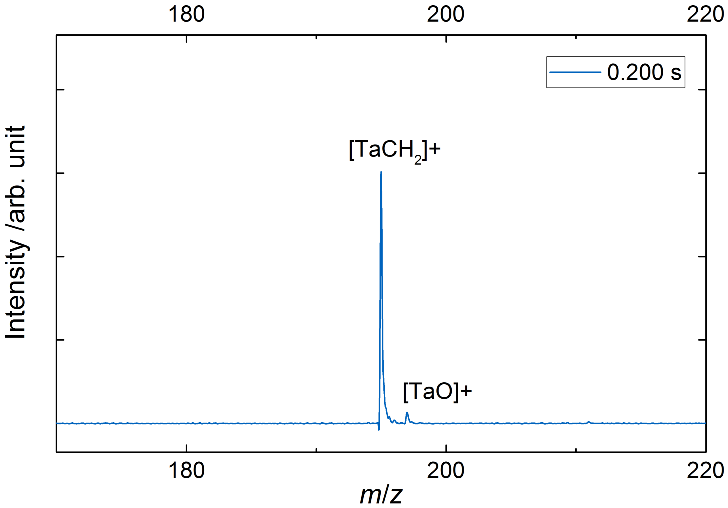

Figure 8.6: *Time-of-flight mass spectra of* $[TaCH_2]^+$ *stored in helium buffer gas at 300 K, illustrating a reaction with background water that generates a small amount of* $[TaO]^+$.

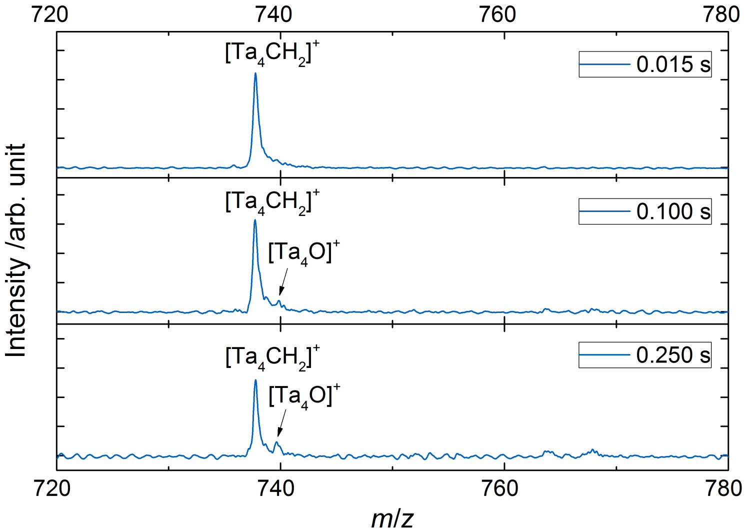

Figure 8.7: *Time-of-flight mass spectra of* $[Ta_4CH_2]^+$ *stored in helium buffer gas at 300 K, illustrating a reaction with background water that generates a small amount of* $[Ta_4O]^+$.

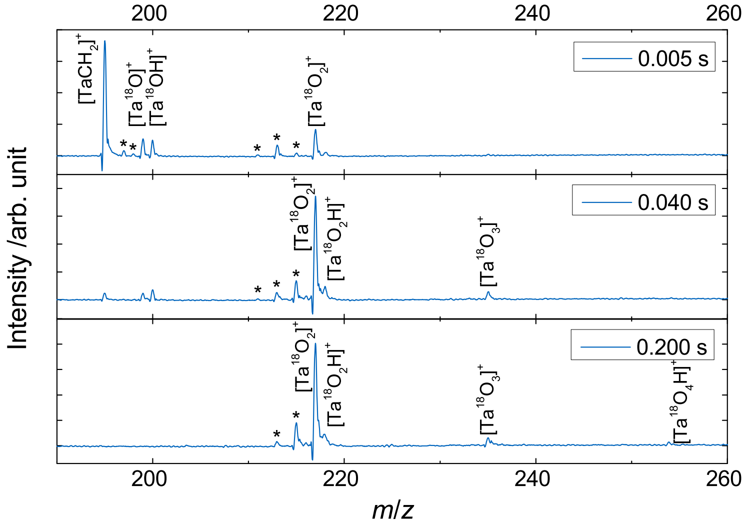

Figure 8.8: *Time-of-flight mass spectra of* $[TaCH_2]^+$ *exposed to* $2.8{\cdot}10^{-5}$ *Pa* $^{18}O_2$ *at 300 K for reaction times of 5, 40 and 200 ms. Products analogous to the ones formed in the reaction with* $^{16}O_2$ *are observed. Additionally,* $^{16}O_2$ *and* $^{16}O^{18}O$*, impurities in the* $^{18}O_2$ *gas cylinder, generate minority species marked by asterisks (*$[Ta^{16}O]^+$, $[Ta^{16}OH]^+$, $[Ta^{16}OCH_2]^+$ *and* $[Ta^{16}O^{18}O]^+$*).*

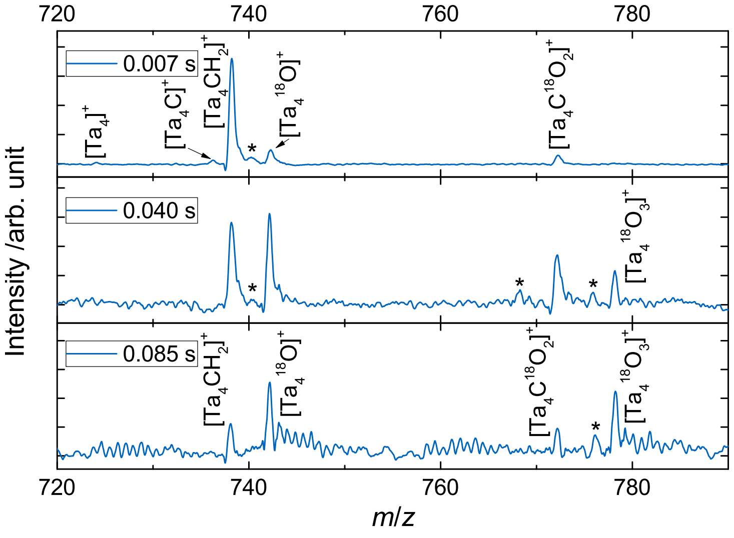

Figure 8.9: *High-mass range excerpts of time-of-flight mass spectra illustrating the reaction of* $[Ta_4CH_2]^+$ *with* $1.8{\cdot}10^{-5}$ *Pa* $^{18}O_2$ *at 300 K for reaction times of 7, 40 and 85 ms. The oxidation reactions produce species analogous to the ones observed in the reactions with* $^{16}O_2$*, i.e. the monoxide, trioxide and carbon-dioxide of the tantalum tetramer cluster cation. In addition, the contaminants in the gas bottle,* $^{16}O^{18}O$ *and* $^{16}O_2$*, cause the formation of three side products,* $[Ta_4^{16}O]^+$, $[Ta_4C^{16}O_2]^+$ *and* $[Ta_4{}^{16}O^{18}O_2]^+$*, which are respectively marked by asterisks.*

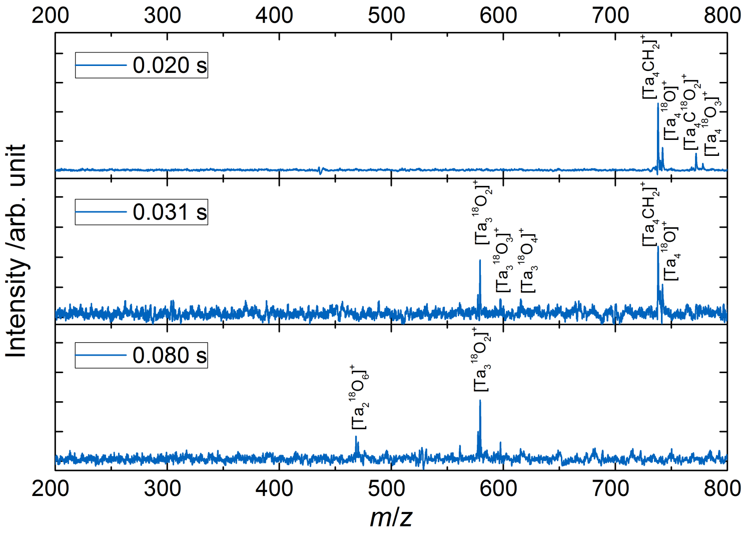

Figure 8.10: *Time-of-flight mass spectra for the consecutive oxidation of* $[Ta_4CH_2]^+$ *with* $1.8{\cdot}10^{-5}$ *Pa* $^{18}O_2$ *at 300 K for reaction times of 7, 40 and 85 ms. Successive oxidative degradation yields clusters* $[Ta_x{}^{18}O_y]^+$ $(x < 4, y > 1)$*, analogous to the species observed in the reactions with* $^{16}O_2$*.*

EXPLORATORY INVESTIGATIONS 9

Several more tantalum-oxygen systems were studied in this thesis, as were more intricate reactions, for example in the simultaneous presence of methane and oxygen. While the investigations presented in this chapter hint at certain insights, additional measurements, *e.g.* peak assignment confirmation through isotopic labeling or further temperature-dependent experiments, are required to render a complete picture of the observed phenomena. The data discussed in the following chapter may thus provide a basis for future studies.

9.1. Oxo-ligation of larger tantalum clusters

The effect of adding oxygen atoms to cationic tantalum clusters was also studied for larger species, for example $[Ta_7O_x]^+$ ($x = 0 - 3$). The bare Ta_7^+ species slowly adsorbs methane in absence of hydrogen elimination (see Chapter 5). The addition of an oxygen atom to the cluster facilitates dehydrogenation of methane and concurrent elimination of H_2, yielding $[Ta_7OCH_2]^+$ (see Fig. 9.1). This behavior is similar to the pentamer clusters, for which the bare cluster cation is inert and $[Ta_5O]^+$ readily dehydrogenates methane as shown in Chapter 6. However, $[Ta_7O]^+$ demonstrates another reaction channel in parallel. The molecular adsorption of CH_4 leads to the reversible formation of $[Ta_7OCH_4]^+$. Surprisingly, the $[Ta_7O]^+$ cluster represents the first species investigated in this work that mediates **methane dehydrogenation and molecular adsorption** in the first reaction step at the same time, whereas solely intermediates of $Ta_nO_x^+/CH_4$ reactions have demonstrated a similar behavior beforehand, for example $[Ta_4CH_2]^+$. The formation of a side product moreover indicates a strong interaction of $[Ta_7O]^+$ and methane: a degradation reaction generates $[Ta_6OCH_4]^+$. Disregarding a potential reaction with background oxygen (and the assignment of the latter species to $[Ta_6O_2]^+$), the activation of methane on $[Ta_7O]^+$ may result in an exothermic

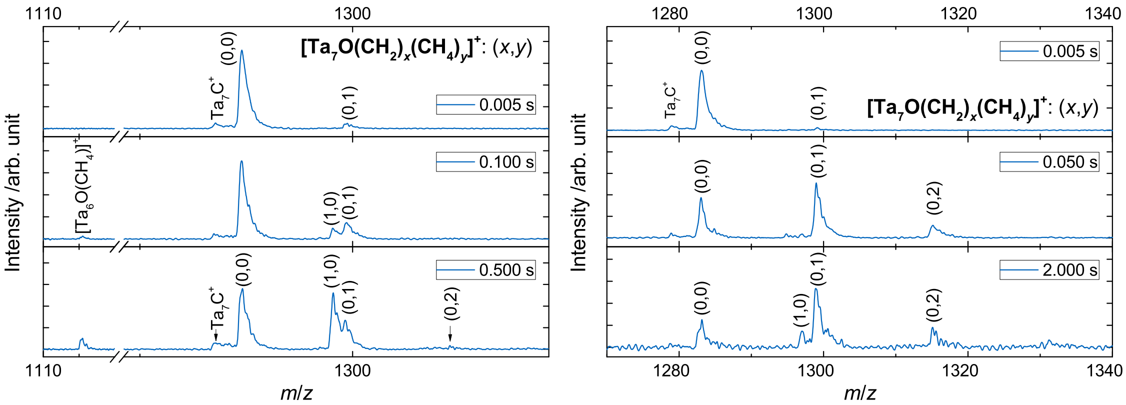

Figure 9.1: *Mass spectra illustrating the reaction of [Ta$_7$O]$^+$ toward methane at 300 K (left) and at 240 K (right). The reactions occur in the presence of* $4 \cdot 10^{-2}$ *Pa CH$_4$ in helium buffer gas at a total pressure of 0.77 Pa.*

formation of a Ta–C bond, which could release energy into the system that triggers the relaxation *via* ejection of a neutral Ta atom. Again, the [Ta$_7$O]$^+$/CH$_4$ couple would be the first investigated system to undergo such a reaction. At 240 K (see Fig. 9.1), this degradation reaction is suppressed. At the same time a high abundance of [Ta$_7$OCH$_4$]$^+$ is generated, while only small amounts of the cluster-methylene complex [Ta$_7$OCH$_2$]$^+$ are detected. Although these findings imply a significant barrier for the dehydrogenation reaction, the kinetic analysis proves the opposite. Actually, the dehydrogenation and molecular adsorption reactions compete, and the rate coefficient associated with the formation of the cluster-methylene complex is rather unaffected by temperature. Instead, the reversible molecular adsorption of methane to [Ta$_7$O]$^+$ becomes significantly enhanced at 240 K, *i.e.* the equilibrium shifts to [Ta$_7$OCH$_4$]$^+$ and fewer [Ta$_7$O]$^+$ clusters are available to mediate the dehydrogenation reaction.

The dioxide of the heptamer cluster cation, [Ta$_7$O$_2$]$^+$, does not bring about hydrogen elimination from methane. After 100 ms, reversible adsorption of methane causes a chemical equilibrium between [Ta$_7$O$_2$]$^+$ and [Ta$_7$O$_2$CH$_4$]$^+$ (see Fig. 9.2). On the other hand, the [Ta$_7$O$_3$]$^+$ cluster shares traits with the monoxide species. In the first reaction step, reversible molecular adsorption and dehydrogenation reactions occur in parallel (see Fig. 9.2). The resulting [Ta$_7$O$_3$CH$_2$]$^+$ and [Ta$_7$O$_3$CH$_4$]$^+$ complexes additionally adsorb two more methane molecules in absence of H$_2$ elimination, consecutively forming [Ta$_7$O$_3$(CH$_2$)(CH$_4$)]$^+$/[Ta$_7$O$_3$(CH$_4$)$_2$]$^+$ and [Ta$_7$O$_3$(CH$_2$)(CH$_4$)$_2$]$^+$/[Ta$_7$O$_3$(CH$_4$)$_3$]$^+$. In contrast to the methylene complex of the heptamer monoxide, [Ta$_7$O$_3$CH$_2$]$^+$ mediates the dehydrogenation and H$_2$

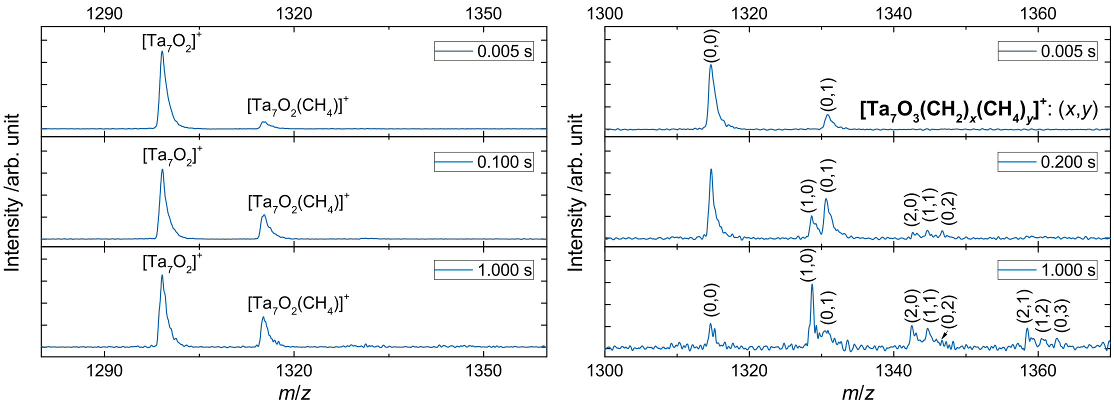

Figure 9.2: *Mass spectra of $[Ta_7O_2]^+$ (left) and $[Ta_7O_3]^+$ (right) reacting with methane ($4 \cdot 10^{-2}$ Pa partial pressure). The reactions are conducted in helium buffer gas at a total pressure of 0.77 Pa and at a temperature of 300 K.*

elimination from a second methane molecule, thus generating $[Ta_7O_3(CH_2)_2]^+$. Note that experiments with d_4-methane would have to be performed in order to validate the mass assignment of all the previously discussed species.

The dehydrogenation reaction of $[Ta_7O]^+$ is associated with a small rate coefficient $k^{(2)}$ of $4.7 \cdot 10^{-14}$ cm^3s^{-1}, corresponding to a **vanishing reaction efficiency** $\phi \approx 2 \cdot 10^{-5}$ (with $\phi = k^{(2)}/k^{SCC}$, where k^{SCC} describes the theoretical collision rate according to the surface charge capture model [143]). Coefficients of 7.3 and $3.2 \cdot 10^{-14}$ cm^3s^{-1} ($\phi \approx 4 \cdot 10^{-5}$ and $2 \cdot 10^{-5}$) are determined for the formation of $[Ta_7O_3CH_2]^+$ and $[Ta_7O_3(CH_2)_2]^+$, respectively. The heptamer oxide clusters therefore demonstrate a drastically lower reactivity than the Ta_4^+ species, for which the dehydrogenation reaction is associated with a rate coefficient of $70.8 \cdot 10^{-14}$ cm^3s^{-1}. Nevertheless, these findings moreover illustrate that each oxygen atom in tantalum clusters affects the reaction mechanism.

In addition, the potential of very large tantalum oxide clusters toward methane activation was investigated. In previous studies (see Chapter 4) bare tantalum cluster cations were exposed to oxygen in the ring electrode ion trap. It was found that larger clusters with more than nine Ta atoms consecutively pick up O_2 units and form specific intermediates and final products. The size-dependent composition and the reaction kinetics indicate that these final oxidation products consists of a Ta core and an outer Ta oxide shell. In order to generate species with the same stoichiometry, tantalum clusters were reacted with oxygen in the expansion channel of the laser vaporization source (see Chapter 4.3). Two clusters with

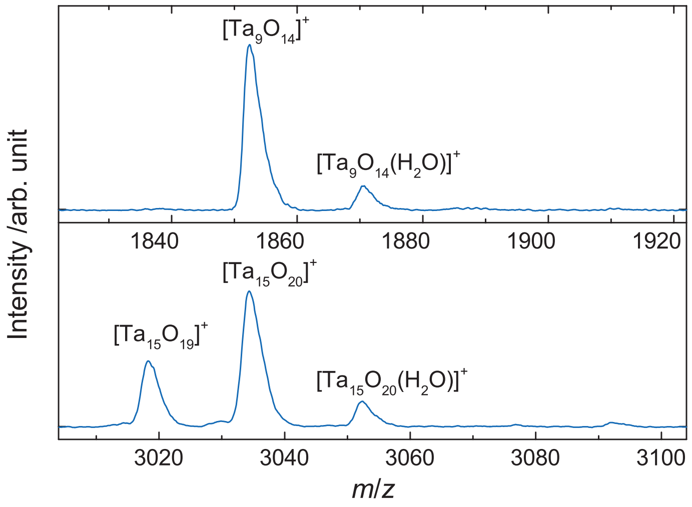

Figure 9.3: *Mass spectra of* $Ta_9O_{14}^+$ *(top) stored for 0.5 s in a* CH_4*/He gas mixture (0.12 and 0.65 Pa, respectively) and of* $Ta_{15}O_{19/20}^+$ *clusters stored under the same conditions (bottom). The oxide clusters are inert and slowly adsorb water.*

the formal composition of final oxidation products, $[Ta_9O_{14}]^+$ and $[Ta_{15}O_{20}]^+$, were selected and exposed to a fraction of methane in helium buffer gas in the ion trap. Interestingly, when $[Ta_9O_{14}]^+$ clusters are exposed to CH_4, neither dehydrogenation nor molecular adsorption occurs. After prolonged storage times, solely small amounts of cluster-water complexes are formed ($[Ta_9O_{14}(H_2O)]^+$, see Fig. 9.3). Similarly, $[Ta_{15}O_{20}]^+$ clusters are inert toward methane and demonstrate a slow molecular adsorption of water (see Fig. 9.3). Note that an insufficient mass selection leads to the presence of $[Ta_{15}O_{19}]^+$ clusters in the ion trap. These clusters may adsorb methane, yielding $[Ta_{15}O_{19}CH_4]^+$, which would overlap with $[Ta_{15}O_{20}]^+$ in the mass spectrum.

More importantly, $[Ta_9O_{14}]^+$ and $[Ta_{15}O_{20}]^+$ were observed as final products in the reaction of bare clusters with oxygen, and potentially contain a tantalum core that is oxidized on the surface (see Chapter 4). The reaction behavior of these clusters toward methane indicates that the **absence of accessible Ta atoms** on the cluster surface apparently prevents any reaction toward methane and renders the oxide clusters inert.

9.2. On the complex scheme in the reaction of $Ta_8O_2{}^+$

When $Ta_8O_2^+$ is exposed to methane, a cluster-methylene complex $[Ta_8O_2CH_2]^+$ is quickly formed. A slow consecutive dehydrogenation reactions yields $[Ta_8O_2(CH_2)_2]^+$ and methane adsorbs to $Ta_8O_2^+$ in absence of hydrogen elimination in a parallel reaction channel (see Fig. 9.4). The initial dehydrogenation reaction to form $[Ta_8O_2CH_2]^+$ is associated with a bimolecular rate coefficient $k^{(2)}$ of $1.27{\cdot}10^{-10}$ cm^3s^{-1}, corresponding to reaction efficiency ϕ of 6.5% ($\phi = k^{(2)}/k^{SCC}$, where k^{SCC} denotes the theoretical collision rate according to the SCC model [143]). The reactivity of $Ta_8O_2^+$ clusters is therefore comparable to the cationic tantalum dimer and exceeds the tetramer and pentamer monoxide cations. Surprisingly, the relative abundances of $Ta_8O_2^+$ and $[Ta_8O_2CH_2^+]$ indicate quasi-steady state conditions. In fact, a model including a reaction from the cluster-methylene complex back to the reactant cluster perfectly replicates the experimentally determined ion abundances as a function of time (see the kinetic simulation in Fig. 9.4):

$$Ta_8O_2^+ + CH_4 \underset{k_{-1}}{\overset{k_1}{\rightleftarrows}} [Ta_8O_2CH_2]^+ + H_2 \qquad K = \frac{k_1}{k_{-1}} \tag{9.1}$$

The two species, $Ta_8O_2^+$ and $[Ta_8O_2CH_2]^+$, seemingly are in equilibrium and parallel reactions, *i.e.* the molecular adsorption of methane and the second dehydrogenation reaction, draw relative abundance from this equilibrium. As the release

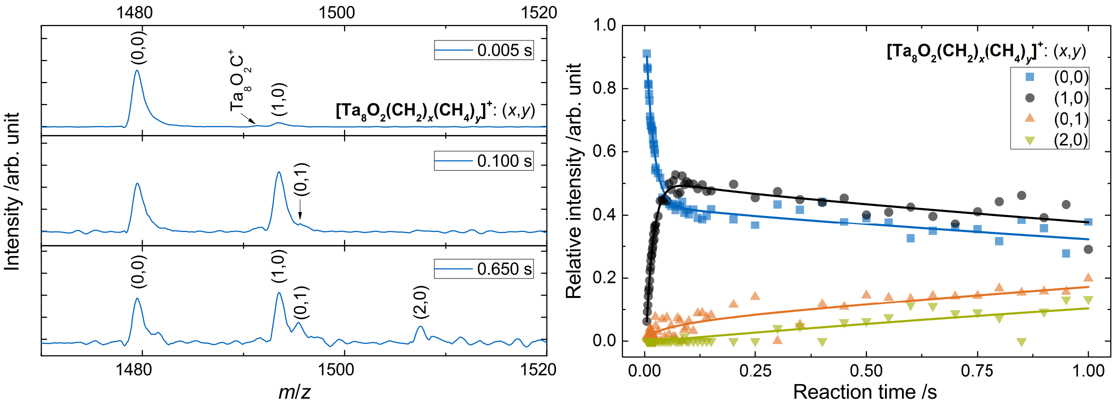

Figure 9.4: *Mass spectra (left) and kinetic simulation (right) for the reaction of* $Ta_8O_2^+$ *toward* $3.5 \cdot 10^{-4}$ *Pa methane in 0.77 Pa He buffer gas at 300 K. Dehydrogenation and concomitant* H_2 *elimination quickly generate the majority species,* $[Ta_8O_2CH_2]^+$*, that equilibrates with the initial* $Ta_8O_2^+$ *cluster. Side reactions additionally produce* $[Ta_8O_2CH_4]^+$ *and* $[Ta_8O_2C_2H_4]^+$*.*

of a methylene fragment from $[Ta_8O_2CH_2]^+$ or a recombination with extremely dilute hydrogen are unlikely, the equilibrium evidences a more complicated reaction scheme. When the reaction is repeated with an increased methane partial pressure, the equilibrium constant remains unchanged ($K = 1.17$ and $K = 1.21$ for 3.5 and $18.3 \cdot 10^{-4}$ Pa CH_4, respectively). Thus, the forward and backward reaction displayed in Equation 9.1 have to be of the same order with regard to the methane concentration. The rate coefficient associated with the back-reaction of the cluster-methylene complex (k_{-1}) is a function of the methane partial pressure, thereby further evidencing a complicated reaction scheme that involves a methane molecule in the back-reaction. Since a second CH_4 molecule participates in the reaction from $[Ta_8O_2CH_2]^+$ to $Ta_8O_2^+$, the back-reaction may proceed *via* a $[Ta_8O_2C_2H_6]^+$ intermediate. In order to regenerate the initial $Ta_8O_2^+$ cluster, the intermediate needs to release a neutral molecule, for example ethane:

$$[Ta_8O_2CH_2]^+ + CH_4 \xrightarrow{k_2} [Ta_8O_2C_2H_6]^+ \xrightarrow{k_3} Ta_8O_2^+ + C_2H_6 \tag{9.2}$$

The apparent rate coefficient k_{-1} associated with the back-reaction depicted in Equation 9.1 is therefore a function of the intermediate formation, k_2, and the actual regeneration of the reactant cluster, k_3. If the release of the neutral molecule is much faster than the formation of the intermediate ($k_3 \gg k_2$), the $[Ta_8O_2C_2H_6]^+$ species will not be detectable in the experiment.

Similarly, the catalytic cycle of the cationic gold dimer, that leads to the formation of ethylene, also requires the participation of an intermediate, which is not experimentally detected [63]. When the formation of the $[Ta_8O_2C_2H_6]^+$ intermediate becomes enhanced or the subsequent reaction is suppressed, the abundance of the intermediate species will increase and may be observed in the experiment.

Indeed, a significant amount of $[Ta_8O_2C_2H_6]^+$ clusters is detected when the reaction is conducted at 200 K (see Fig. 9.5). The reaction quickly results in a chemical equilibrium between $Ta_8O_2^+$, $[Ta_8O_2CH_2]^+$ and $[Ta_8O_2C_2H_6]^+$. Similar to 300 K, parallel reactions at 200 K yield $[Ta_8O_2CH_4]^+$ and $[Ta_8O_2C_2H_4]^+$. The reaction model for the kinetic simulation (see Fig. 9.5) includes a reaction from the $[Ta_8O_2C_2H_6]^+$ intermediate to the $Ta_8O_2^+$ cluster as depicted in Equation 9.2. This proposed model replicates the experimentally determined ion abundances and results in equilibrium conditions after approximately 100 ms. Note that a high methane partial pressure during the low-temperature measurement quickly lead

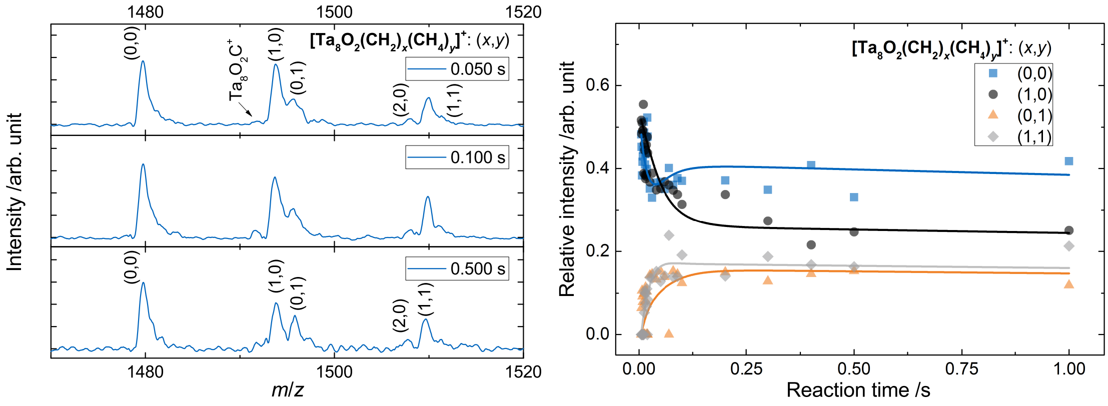

Figure 9.5: *Low-temperature mass spectra (left) for the reaction of $Ta_8O_2^+$ toward methane ($7.7 \cdot 10^{-3}$ Pa), illustrating an equilibrium between $Ta_8O_2^+$, $[Ta_8O_2CH_2]^+$ and $[Ta_8O_2C_2H_6]^+$. The ion abundances are displayed with the result of the kinetic simulation (right) and demonstrate a quick increase of the cluster-methylene complex (caused by a high methane partial pressure), followed by a decrease due to the formation of the $[Ta_8O_2C_2H_6]^+$ species. A reaction model including a catalytic cycle consequently replicates the measured ion abundances.*

to a 50/50 distribution of the $Ta_8O_2^+$ and $[Ta_8O_2CH_2]^+$ species, *i.e.* the initial rise of the cluster-methylene complex is not temporally resolved.

Figure 9.6 displays the generalized reaction scheme of $Ta_8O_2^+$. A cluster-methylene complex is formed *via* dehydrogenation of methane and concurrent H_2 elimination, and adsorption of methane to this complex generates a $[Ta_8O_2C_2H_6]^+$ species. In this intermediate, C–C coupling potentially mediates the formation of a C_2 hydrocarbon moiety that is subsequently ejected from the cluster, thereby regenerating the initial $Ta_8O_2^+$ reactant. The reaction scheme moreover includes parallel reactions: the product of molecular adsorption $[Ta_8O_2CH_4]^+$ may be stabilized through collisions with the buffer gas and $[Ta_8O_2CH_2]^+$ also brings about H_2 elimination from a second methane molecule. Additional molecular adsorption is observed when the reaction is conducted with an elevated methane partial pressure at 300 K, thus forming $[Ta_8O_2C_2H_8]^+$ and $[Ta_8O_2C_3H_8]^+$.

At near room temperature, the release of the neutral hydrocarbon is much faster than the formation of the intermediate, and $[Ta_8O_2C_2H_6]^+$ remains undetected, and is only evidenced by the reaction order in regard to the methane concentration. In contrast, the gold dimer system requires cooperative co-adsorption of a second methane molecule to mediate the elimination of hydrogen, and the release of the neutral product (ethylene) limits the catalytic cycle [63]. In the case of

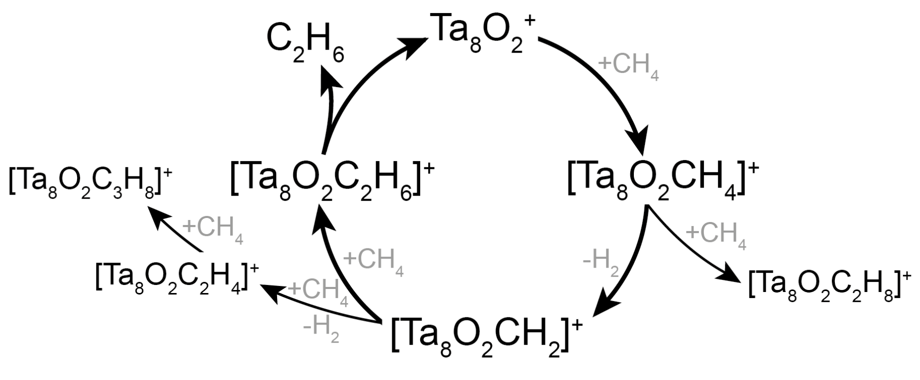

Figure 9.6: *Proposed scheme for the consecutive reaction of* $Ta_8O_2^+$ *toward methane. Dehydrogenation of methane yields a cluster-methylene complex that subsequently adsorbs methane in absence of* H_2 *elimination, and the resulting intermediate releases a neutral hydrocarbon to regenerate the* $Ta_8O_2^+$ *cluster.*

$Ta_8O_2^+$, a strong Ta–C bond of the cluster-methylene complex may enable a direct, exothermic dehydrogenation reaction of $Ta_8O_2^+/CH_4$. A potentially high bond dissociation energy in comparison to gold [56] may be required to transform the cluster-methylene complex in the subsequent reaction step. The **formation of the C–C coupling product** thus limits the overall reaction, whereas the experimental findings indicate a facilitated release of the neutral product.

In order to plausibly confirm the proposed reaction model, the reaction has to be repeated at a temperature that allows the detection of all involved species, ideally using a low partial pressure of deuterated methane. This approach will simultaneously allow the verification of the reaction scheme and of the peak assignment. Furthermore, a systematic variation of the reaction temperature may enable the determination of activation energies. At 300 K, the equilibrium constant (see Eq. 9.1) can be probed at several additional methane molecule densities (ranging over more than one order of magnitude). An unaffected equilibrium constant will confirm the order of the back reaction, which would additionally evidence the operation of the proposed catalytic cycle at near room temperature. Moreover, a spectroscopic and/or theoretical investigation of the $[Ta_8O_2C_2H_6]^+$ species would clarify the proposed C–C coupling mechanism.

9.3. Simultaneous reactions toward methane and oxygen

The methylene complexes of the cationic tantalum atom and the tetramer cluster were previously generated, isolated and exposed to oxygen (see Chapter 8). A low natural abundance of the cationic tantalum dimer in combination with a low reactivity toward methane prohibited the generation of $[Ta_2CH_2]^+$ in the cluster source. In order to study C–O coupling reactions of the dimer system, Ta_2^+ ions were subjected to a mixture of methane and oxygen in the ion trap at 300 K. The mass spectra in Figure 9.7 illustrate the high number of species that are generated in consecutive reactions. In agreement with the previously studied dehydrogenation reactions, $[Ta_2CH_2]^+$ and $[Ta_2C_2H_4]^+$ are formed initially. Similar to the oxidation of the atomic methylene complex, the oxidation of $[Ta_2CH_2]^+$ yields the monoxide and hydroxide of the cationic tantalum dimer, $[Ta_2O]^+$ and $[Ta_2OH]^+$ (see Fig. 9.7, 0.050 s). The reaction of $[Ta_2CH_2]^+$ to $[Ta_2O]^+$ also requires the formal ejection of a formaldehyde equivalent, "CH_2O", whereas the formation of the hydroxide species demands the release of a formyl radical. Furthermore, the methy-

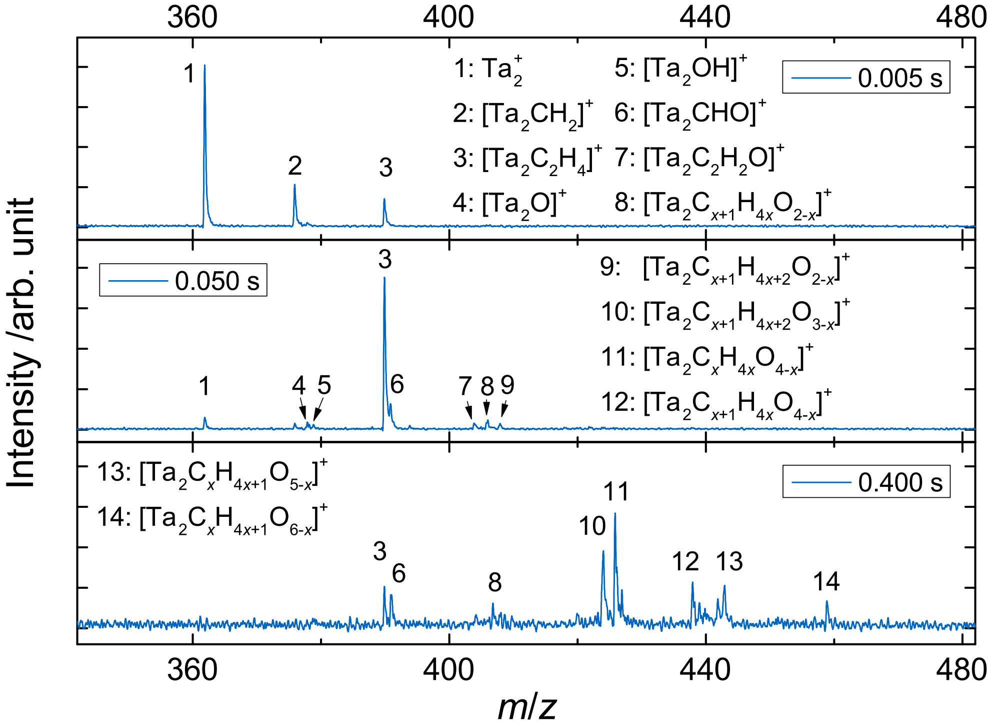

Figure 9.7: *Time-of-flight mass spectra depicting consecutive reactions of* Ta_2^+ *clusters stored in a He/*CH_4*/*O_2 *mixture (partial pressures of 0.77,* $4{\cdot}10^{-3}$ *and* $7{\cdot}10^{-5}$ *Pa, respectively) at 300 K.*

lene complex reacts with oxygen and forms $[Ta_2CHO]^+$ *via* elimination of an OH moiety. The bis-methylene cluster $[Ta_2C_2H_4]^+$ ejects a water molecule when exposed to dioxygen, thus forming $[Ta_2C_2H_2O]^+$. Products with higher masses can no longer be assigned to single species due to a negligible mass difference of a methane molecule and an oxygen atom. For example, a species with an additional mass of 64 u compared to the bare dimer could correspond to $[Ta_2C_4H_{16}]^+$ or $[Ta_2O_4]^+$ or certain combinations of oxygen, carbon and hydrogen atoms. The species is therefore denoted as $[Ta_2C_xH_{4x}O_{4-x}]^+$, with $x = 0 - 4$. The product with the highest mass may similarly be assigned to $[Ta_2C_xH_{4x+1}O_{6-x}]^+$ where $x = 0 - 6$. The existence of many species between the former two products evidences a rich chemistry that prevails in the simultaneous presence of oxygen and methane. The high number and ambiguous assignment of reaction species prevents the determination of a reaction scheme for longer storage times. In addition, oxidative degradation generates $[TaO]^+$ and $[TaO_2]^+$, which is not depicted in Figure 9.7.
A repetition of the experiment with isotopically labeled methane or dioxygen would allow the assignment of all involved species and facilitate the full kinetic characterization of the consecutive reactions. A variation of the CH_4/O_2 partial pressure ratio would furthermore bring additional insights, *e.g.* about the C–O coupling mediated by the tantalum dimer-methylene complex. Compared to noble metal clusters, the tantalum system demonstrates a high reactivity toward oxygen, resulting in the formation of many reaction products and a hampered characterization of the reaction.

The bare tantalum tetramer cation was simultaneously exposed to oxygen and a significant fraction of methane in helium buffer gas. Initially, consecutive dehydrogenation reactions produce $[Ta_4CH_2]^+$ and $[Ta_4C_2H_4]^+$ (see Fig. 9.8). However, subsequent reactions toward oxygen (and methane) lead to a distinct change in the mass spectra. In the mass range between 775 und 850 u, more than 25 cluster complexes are generated. The potential mass overlap of different species again prevents a clear assignment. As a result, the clusters are exemplarily denoted with a generally applicable formula. Some of these ions are spaced by a single mass unit, indicating a variety of reaction mechanisms. Moreover, the mass spectrum converges to fewer species for longer reaction times. After 250 ms, two of the most abundant clusters correspond to $[Ta_4O_{8-x}C_xH_{4x}]^+$ and $[Ta_4O_{10-x}C_xH_{4x}]^+$. The oxidation reactions potentially generate highly oxidized clusters and con-

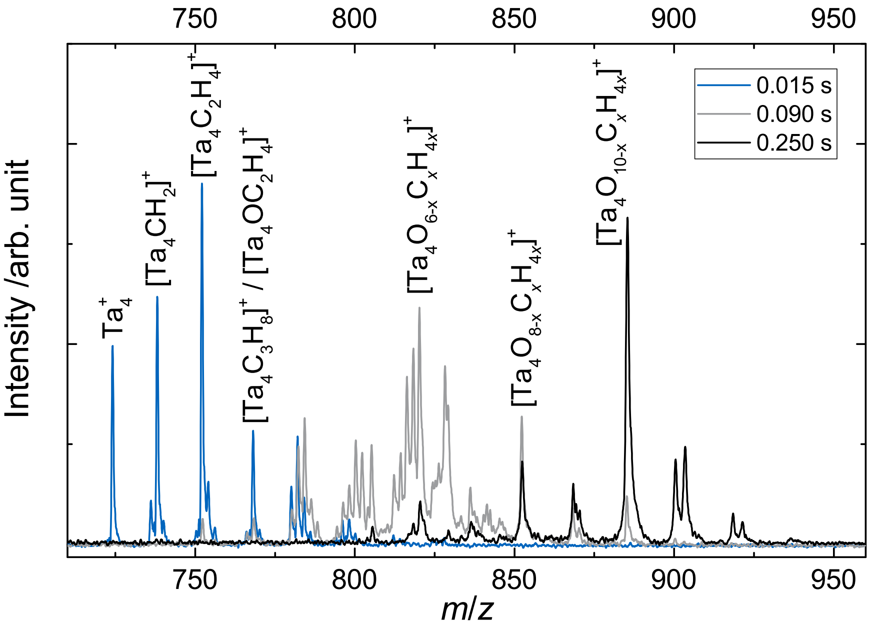

Figure 9.8: *Time-of-flight mass spectra depicting consecutive reactions of* Ta_4^+ *clusters stored in a* $He/CH_4/O_2$ *mixture (partial pressures of 0.54, 0.23 and* $7{\cdot}10^{-5}$ *Pa, respectively) at 300 K.*

currently release various neutral hydrocarbons, thus reducing the number of present species. In addition, the high concentration of methane in the buffer gas seemingly hinders oxidative degradation reactions. Although not depicted in Figure 9.8, only 10% of the clusters undergo degradation and eject a neutral Ta-containing fragment. The CH_4 molecules could provide an enhanced collisional stabilization due to the increased internal degrees of freedom compared to helium atoms, thereby suppressing degradation reactions.

Again, reactions with isotopically labeled reactive gases are required to determine the mass assignment. While the high number of species in the consecutive reactions impede a clarification of the reaction mechanism, a systematic variation of the methane/dioxygen ratio may reveal further information.

9.4. Summary

Exploratory studies revealed preliminary insights about larger tantalum oxide clusters and reactions in the simultaneous presence of oxygen and methane. The reactivity of $[Ta_7O_x]^+$ clusters resonates with the results obtained from the comparison of the cationic dimer oxides (see Chapter 7): the amount of oxygen atoms contained in the tantalum clusters non-linearly affects the reaction mechanism. The concept "each atom counts" [186] does not only apply to the number of metal atoms in a cluster, but, moreover, to the total chemical composition of a metal or metal-oxide cluster. Tantalum oxide clusters composed of a preserved metal core and an outer oxide shell are inert toward methane, likely due to a lack of accessible Ta atoms. The $[Ta_8O_2]^+$ cluster potentially catalyzes the formation and release of ethane, although further studies are necessary to verify the proposed reaction model. The high number of cluster complexes generated in the simultaneous presence of oxygen and methane hinders a detailed characterization of the consecutive reactions, and at the same time illustrates an intriguing variety of different reaction mechanisms. The insights presented in this chapter are of an speculative nature and are therefore not included in the conclusion of the overall thesis. However, the confirmation of these findings through additional experiments may promise to be rewarding.

CONCLUSION 10

Metal clusters serve as models of active sites in catalytic processes, and the micro-kinetic investigation of gas-phase reactions unravels effects and mechanisms operative on a molecular level. Tantalum compounds have been shown to demonstrate properties advantageous in the activation of methane, *e.g.* the formation of strong Ta–C bonds that provide a thermodynamic driving force [62, 153] and the release of value-added products [41, 98, 152]. During the time of this work, however, a comprehensive study on the reactivity of size-selected tantalum clusters toward methane is not available in other publications.

10.1. Summary

A cryogenic ring electrode ion trap was used to study reactions of isolated particles under well-defined multi-collision conditions in the presence of buffer gas. Kinetic modeling was employed to determine reaction schemes for the consecutive reactions and to obtain associated rate coefficients. Initial investigations exposed cationic tantalum clusters to a commonly used oxidant, dioxygen. The observed reaction pathways are a function of cluster size and correspond to different **relaxation mechanisms**. Highly exothermic Ta–O bond formation in small clusters leads to the ejection of neutral TaO fragments and the generation of highly oxidized clusters [154]. In contrast, the core of larger clusters mediates internal vibrational relaxation, thus suppressing degradation pathways [119]. These oxidation reactions subsequently produce various types of metal-oxygen species: partially oxidized clusters, stoichiometric metal oxides and large clusters with a preserved core and an oxidized surface [120].

Bare tantalum clusters cations were consequently subjected to methane, in order to investigate their potential as C–H bond activation catalysts. Small tantalum cluster cations dehydrogenate methane and concurrently eliminate dihydrogen, whereas clusters with five or more atoms solely demonstrate non-dissociative adsorption. The **monotonic decrease in dehydrogenation activity** is related to C–H bond scission barriers that increase with cluster size, potentially stemming from local charge effects or fewer unpaired 6s electrons for bond-making processes. With the exception of the tantalum monomer, the dehydrogenation reactions are limited by the cleavage of C–H bonds, indicated by the magnitude of the kinetic isotope effect. Methylene complexes of the tantalum monomer and dimer undergo H/D exchange reactions, thereby evidencing a carbene-type structure. In contrast, $[Ta_4CH_2]^+$ does not exchange hydrogen atoms and quantum-chemical calculations predict a (dihydrido) carbide structure.

Through a modification of the laser vaporization cluster source, $[TaCH_2]^+$ and $[Ta_4CH_2]^+$ were generated, isolated and individually exposed to dioxygen. Both complexes undergo **C–O coupling reactions** and preferentially release the equivalent of formaldehyde. The reaction products of $[TaCH_2]^+/O_2$ indicate an additional ejection of unstable neutral molecules, whereas $[Ta_4CH_2]^+/O_2$ resembles a more realistic model system. Minor amounts of the bare tetramer cluster are regenerated in a side reaction, corresponding to a catalytic cycle similar to the analogous platinum system [73]. The tantalum species are more reactive than the platinum counterparts, but the tantalum tetramer cluster system demonstrates significant oxidative degradation and reaction channels associated with over-oxidation of the methylene group.

The cluster source modification also enabled the synthesis of clusters with a specific amount of oxygen atoms. Addition of an oxygen atom to the tetramer and the inert pentamer cluster drastically increases the reactivity. The oxygen atom acts as a ligand by manipulating the electronic structure of the clusters and is not directly involved in the bond-making or -breaking process. During the initial C–H scission in $[Ta_4CH_4]^+$, the calculated charges demonstrate a significant **transitional electronic rearrangement** of all Ta atoms, whereas a single Ta atom in $[Ta_4OCH_4]^+$ acts as the adsorption site and provides most of the electron density necessary in the C–H cleavage and stabilization of the resulting moieties. Furthermore, the subsequent steps in the reaction of Ta_4^+, $[Ta_4O]^+$ and $[Ta_5O]^+$, *i.e.* the second C–H cleavage, hydrogen migration, H_2 formation and elimination, require the participation of up to four tantalum atoms, evidenced by results from computational chemistry.

Oxides of the cationic tantalum dimer illustrate that reactivity modes and associated rate coefficients do not scale linearly with the number of oxygen atoms. For example, $[Ta_2O]^+$ is virtually inert, whereas the dioxide demonstrates a higher reactivity than the bare cluster. In the stoichiometric oxide, $[Ta_2O_5]^+$, the presence of a terminal oxygen radical facilitates a direct hydrogen atom transfer. The adsorption of CH_4 in a parallel channel leads to the formation of a Lewis-acidic Ta atom and a Lewis-basic O atom in $[Ta_2O_5CH_4]^+$. This Lewis acid-base pair abstracts hydrogen from a second methane molecule in a proton-coupled electron transfer mechanism.

10.2. Conclusion and outlook

In conclusion, the study of free tantalum cluster cations resulted in molecular-level insights of C–H activation mechanisms. These non-noble metal particles mediate the dehydrogenation of methane, and the reactivity decreases with increasing cluster size. The dehydrogenation reactions are partially driven by the formation of strong Ta–C bonds due to the stabilization of the 6s orbital. Coupling of carbon atoms is likely limited to the monomer system as there is no structural evidence or release of $C_{n\geq2}$ hydrocarbon groups on the larger particles. To quote Sandra Lang and Thorsten Bernhardt: "[...] the selective catalytic conversion of methane to higher hydrocarbons or potentially to oxidized reaction products requires a detailed balance of C–H bond activation activity, C–C bond formation capability, and the ability to eventually release newly formed products." [77] While Ta_4^+ readily activates two methane molecules, the resulting structure with two isolated $CH_{0,2}$ groups is very stable and the formation of an ethylene unit is extremely endothermic. Strong Ta–C bonds thus limit the **C–C bond formation capability** of tantalum clusters. Nevertheless, when $[Ta_4CH_2]^+$ is exposed to O_2, evidence for the release of value-added C–O coupling products and for the existence of a potential catalytic cycle is found. The prospects of the catalytic cycle, however, are limited due to oxidative degradation of the system in parallel reaction channels, *e.g.* another oxidant than dioxygen would have to be used. Moreover, the **role of oxygen atoms** as components of metal clusters was illuminated. Oxygen atoms may behave like a ligand that manipulates the electronic structure of the cluster, thereby affecting C–H scission barriers. In stoichiometric metal oxide clusters, *e.g.* $[Ta_2O_5]^+$, oxygen radical centers directly accept a hydrogen radical from methane and a methyl radical is released. A unique effect in the consecutive reaction of $[Ta_2O_5]^+$ was additionally observed: adsorption of the first CH_4 molecule promotes a Lewis acid-base (Ta–O) pair, and hydrogen from a second methane molecule is abstracted in a PCET instead of a HAT mechanism. On a similar note, the activity of the $[Ta_2CH_2]^+$ intermediate is enhanced sixfold compared to the bare dimer cluster. These findings consequently emphasize an advantage of multi-collision conditions, *viz.* the facilitated observation of effects that occur during consecutive reactions.

A more detailed characterization of the analyzed systems will benefit the understanding of operative mechanisms, evidenced by the additional insights obtained from the quantum-chemical simulation of selected dehydrogenation reactions. Further computational studies by external collaborators are currently underway in order to describe the influence of the electronic structure of small cationic tantalum clusters on the methane activation reactions. Future spectroscopic studies and collision-induced dissociation experiments may also aid in the determination of cluster-complex structures. When methane dehydrogenation products are generated in the cluster source, the current quadrupole mass filter/ion trap apparatus may be adapted to facilitate high-energy collisions with inert gas atoms, and to subsequently analyze the dissociation product composition. The cryogenic ring electrode ion trap presented in this work is furthermore an ideal tool for spectroscopic investigations [112]. A sophisticated **structural characterization** technique will be available if an infrared laser system is added to the experimental setup. Excitation of characteristic vibrational modes leads to the frequency-dependent dissociation of cluster-inert atom complexes (so-called messenger tagging, *e.g.* with argon [187]). The combination of this and similar spectroscopic methods with DFT calculations enabled the groups of André Fielicke [179, 187–190] and Knut Asmis [112, 176, 177, 191] to determine the structure of many transition metal and metal oxide clusters.

Other cluster systems of interest will be studied in the future. For example, methane monooxygenase catalyzes the oxidation of CH_4 in nature. This enzyme consists of a di-iron core, in which the iron atoms are connected *via* oxygen atoms [192]. In addition, supported iron oxide species transform methane to formaldehyde [193]. The study of free **iron oxide clusters** with specific compositions may thus yield further information on the mechanistic aspects of methane activation.

ABBREVIATIONS AND NOMENCLATURE

ADO	average dipole orientation
CID	collision-induced dissociation
DC	direct current
DFT	density functional theory
EXT	extractor plate of a TOF-MS
FT-ICR	Fourier-transform ion cyclotron resonance
HAT	hydrogen atom transfer
HOMO	highest occupied molecular orbital
KIE	kinetic isotope effect
LC	inductor (L) and capacitor (C) components in a resonant circuit
LGS	Langevin Giousmousis Stevenson
LUMO	lowest unoccupied molecular orbital
MCP	micro-channel plate, component of ion detectors
PCET	proton-coupled electron transfer
QMF	quadrupole mass filter
RDS	rate-determining step
REP	repeller plate of a TOF-MS
RET	ring electrode ion trap
ReTOF-MS	reflectron time-of-flight mass spectrometer
RF	radio frequency, relating to alternating current potentials
RGA	residual gas analyzer, specific type of QMF
RRKM	Rice Ramsperger Kassel Marcus
SCC	surface charge capture
TOF-MS	time-of-flight mass spectrometer
TSR	two-state reactivity

bar	unit of pressure, 1 bar = 10^5 Pa
C	coulomb, SI unit of electric charge
E	energy
E_A	activation energy
e	elementary charge, 1 $e \approx 1.602 \cdot 10^{-19}$ C
Hz	Hertz, SI unit of frequency, 1 Hz = 1 s^{-1}
J	Joule, SI unit of energy
K	Kelvin, SI unit of temperature
k	rate coefficient, where $k^{(i)}$ refers to the i-th order of the reaction
k_B	Boltzmann constant, $k_B \approx 1.38 \cdot 10^{-23}$ J·K^{-1}
kg	kilogram, SI unit of mass
$M_n{}^{-/0/+}$	anionic, neutral or cationic cluster comprising n atoms of the metal M
mol	mole, SI unit of the amount of a substance
m	meter, SI unit of length
m	mass
$(n/V)_\mathrm{X}$	volumetric density of particles X, typically in units of cm^{-3}
p	pressure
Pa	Pascal, SI unit of pressure
q	charge of an ion, multiple z of the elementary charge e
R	universal gas constant, $R \approx 8.3145$ J·K^{-1} · mol^{-1}
r	reaction rate
s	second, SI unit of time
T	temperature
U	electric potential
u	unified atomic mass unit, 1 u $\approx 1.66 \cdot 10^{-27}$ kg
v	velocity
[X]	concentration of a species X
z	multiple of the electronic charge, for example two in a doubly charged ion

REFERENCES

[1] E. I. Rabinowitch, *Photosynthesis And Related Processes. Vol. I.* Interscience Publishers, Inc.; New York, **1945**.

[2] H. Hers, *Biochim. Biophys. Acta* **1960**, *37*, 120–126.

[3] J. Laidler K., *A glossary of terms used in chemical kinetics, including reaction dynamics (IUPAC Recommendations 1996)*, *Vol. 68*, **2009**, p. 149.

[4] H. Blaser, F. Spindler, M. Studer, *Appl. Catal. A.* **2001**, *221*, 119–143.

[5] J. W. Erisman, M. A. Sutton, J. Galloway, Z. Klimont, W. Winiwarter, *Nat. Geosci.* **2008**, *1*, 636.

[6] R. Schlögl, *Eur. Phys. J. D* **2003**, *115*, 2050–2055.

[7] J. R. Jennings, *Catalytic ammonia synthesis: fundamentals and practice*, Springer Science & Business Media, **2013**.

[8] G. Ertl, *J. Vac. Sci. Technol* **1983**, *1*, 1247–1253.

[9] G. Ertl, *Angew. Chem. Int. Ed.* **2008**, *47*, 3524–3535.

[10] K.-i. Aika, L. J. Christiansen, I. Dybkjaer, J. B. Hansen, P. E. H. Nielsen, P. Nielsen, A .and Stoltze, K. Tamaru, *Ammonia: catalysis and manufacture*, Springer Science & Business Media, **2012**.

[11] A. Caballero, P. J. Perez, *Chem. Soc. Rev.* **2013**, *42*, 8809–8820.

[12] H. Schwarz, *Angew. Chem. Int. Ed.* **2011**, *50*, 10096–10115.

[13] H. Schwarz, *Isr. J. Chem.* **2014**, *54*, 1413–1431.

[14] H. Häkkinen, S. Abbet, A. Sanchez, U. Heiz, U. Landman, *Angew. Chem. Int. Ed.* **2003**, *42*, 1297–1300.

[15] A. S. Wörz, K. Judai, S. Abbet, U. Heiz, *J. Am. Chem. Soc.* **2003**, *125*, 7964–7970.

[16] M. J. Berr, F. F. Schweinberger, M. Döblinger, K. E. Sanwald, C. Wolff, J. Breimeier, A. S. Crampton, C. J. Ridge, M. Tschurl, U. Heiz, F. Jäckel, J. Feldmann, *Nano Lett.* **2012**, *12*, 5903–5906.

[17] S. M. Lang, T. M. Bernhardt, *Phys. Chem. Chem. Phys.* **2012**, *14*, 9255–9269.

[18] S. M. Lang, I. Fleischer, T. M. Bernhardt, R. N. Barnett, U. Landman, *J. Phys. Chem. C* **2015**, *119*, 10881–10887.

[19] S. M. Lang, T. M. Bernhardt, D. M. Kiawi, J. M. Bakker, R. N. Barnett, U. Landman, *Angew. Chem. Int. Ed.* **2015**, *54*, 15113–15117.

[20] S. M. Lang, T. M. Bernhardt, D. M. Kiawi, J. M. Bakker, R. N. Barnett, U. Landman, *Phys. Chem. Chem. Phys.* **2016**, *18*, 15727–15737.

[21] S. Feyel, *Gaseous Vanadium, Vanadium Oxide and Hydroxide Clusters: From Clusters to Model Catalysts*, Logos Verlag Berlin GmbH, **2008**.

[22] D. R. Stull, E. F. Westrum, G. C. Sinke, *The chemical thermodynamics of organic compounds*, J. Wiley New York, **1969**.

[23] J. Berkowitz, G. B. Ellison, D. Gutman, *J. Phys. Chem.* **1994**, *98*, 2744–2765.

[24] G. B. Ellison, P. Engelking, W. Lineberger, *J. Am. Chem. Soc.* **1978**, *100*, 2556–2558.

[25] C.-G. Zhan, J. A. Nichols, D. A. Dixon, *J. Phys. Chem. A* **2003**, *107*, 4184–4195.

[26] M. Meunier, N. Quirke, D. Binesti, *Mol. Simulat.* **1999**, *23*, 109–125.

[27] J. Berkowitz, J. P. Greene, H. Cho, B. Ruscić, *J. Chem. Phys.* **1987**, *86*, 674–676.

[28] G. Bieri, L. Åsbrink, *J. Electron Spectrosc.* **1980**, *20*, 149–167.

[29] P. Tang, Q. Zhu, Z. Wu, D. Ma, *Energy Environ. Sci* **2014**, *7*, 2580–2591.

[30] H. D. Gesser, N. R. Hunter, C. B. Prakash, *Chem. Rev.* **1985**, *85*, 235–244.

[31] J. Xu, G. F. Froment, *AlCHe J.* **1989**, *35*, 88–96.

[32] F. Endter, *Chem. Ing. Tech.* **1958**, *30*, 305–310.

[33] S. Mukhopadhyay, A. T. Bell, *Chem. Commun.* **2003**, 1590–1591.

[34] M. E. Dry, *Catal. Today* **2002**, *71*, 227–241.

[35] D. Hasenberg, L. D. Schmidt, *J. Catal.* **1987**, *104*, 441–453.

[36] D. Hasenberg, L. D. Schmidt, *J. Catal.* **1986**, *97*, 156–168.

[37] M. Aschi, M. Brönstrup, M. Diefenbach, J. N. Harvey, D. Schröder, H. Schwarz, *Angew. Chem. Int. Ed.* **1998**, *37*, 829–832.

[38] L. Andrussow, *Angew. Chem. Ger. Ed.* **1935**, *48*, 593–595.

[39] S. Mukhopadhyay, A. T. Bell, *Angew. Chem. Int. Ed.* **2003**, *42*, 1019–1021.

[40] S. Nemana, B. C. Gates, *Catal. Lett.* **2007**, *113*, 73–81.

[41] D. Soulivong, S. Norsic, M. Taoufik, C. Coperet, J. Thivolle-Cazat, S. Chakka, J.-M. Basset, *J. Am. Chem. Soc.* **2008**, *130*, 5044–5045.

[42] S. Soignier, M. Taoufik, E. Le Roux, G. Saggio, C. Dablemont, A. Baudouin, F. Lefebvre, A. de Mallmann, J. Thivolle-Cazat, J.-M. Basset, G. Sunley, B. M. Maunders, *Organometallics* **2006**, *25*, 1569–1577.

[43] A. E. Shilov, G. B. Shul'pin, *Chem. Rev.* **1997**, *97*, 2879–2932.

[44] B. G. Hashiguchi, C. H. Hövelmann, S. M. Bischof, K. S. Lokare, C. H. Leung, R. A. Periana in *Encyclopedia of Inorganic and Bioinorganic Chemistry*, John Wiley & Sons, Ltd, **2011**.

[45] R. A. Periana, O. Mironov, D. Taube, G. Bhalla, C. Jones, *Science* **2003**, *301*, 814–818.

[46] O. A. Mironov, S. M. Bischof, M. M. Konnick, B. G. Hashiguchi, V. R. Ziatdinov, W. A. Goddard III, M. Ahlquist, R. A. Periana, *J. Am. Chem. Soc.* **2013**, *135*, 14644–14658.

[47] G. Luinstra, L. Wang, S. Stahl, J. Labinger, J. Bercaw, *J. Organomet. Chem.* **1995**, *504*, 75 –91.

[48] J. A. Labinger, J. E. Bercaw, *Nature* **2002**, *417*, 507.

[49] K. Kwapien, J. Paier, J. Sauer, M. Geske, U. Zavyalova, R. Horn, P. Schwach, A. Trunschke, R. Schlögl, *Angew. Chem. Int. Ed.* **2014**, *53*, 8774–8778.

[50] S. Zhou, J. Li, M. Schlangen, H. Schwarz, *Acc. Chem. Res.* **2016**, *49*, 494–502.

[51] M. Diefenbach, M. Brönstrup, M. Aschi, D. Schröder, H. Schwarz, *J. Am. Chem. Soc.* **1999**, *121*, 10614–10625.

[52] R. Horn, G. Mestl, M. Thiede, F. C. Jentoft, P. M. Schmidt, M. Bewersdorf, R. Weber, R. Schlögl, *Phys. Chem. Chem. Phys.* **2004**, *6*, 4514–4521.

[53] A. Shayesteh, V. V. Lavrov, G. K. Koyanagi, D. K. Bohme, *J. Phys. Chem. A* **2009**, *113*, 5602–5611.

[54] K. K. Irikura, J. L. Beauchamp, *J. Phys. Chem.* **1991**, *95*, 8344–8351.

[55] K. K. Irikura, W. A. Goddard, *J. Am. Chem. Soc.* **1994**, *116*, 8733–8740.

[56] P. B. Armentrout, *Chem. Eur. J.* **2017**, *23*, 10–18.

[57] R. Liyanage, X.-G. Zhang, P. B. Armentrout, *J. Chem. Phys.* **2001**, *115*, 9747–9763.

[58] F. Liu, X.-G. Zhang, R. Liyanage, P. B. Armentrout, *J. Chem. Phy* **2004**, *121*, 10976–10990.

[59] M. Citir, F. Liu, P. B. Armentrout, *J. Chem. Phys.* **2009**, *130*, 054309.

[60] N. Aristov, P. B. Armentrout, *J. Phys. Chem.* **1987**, *91*, 6178–6188.

[61] M. Sievers, Y.-M. Chen, C. Haynes, P. B. Armentrout, *Int. J. Mass Spectrom.* **2000**, *195*, 149–170.

[62] L. G. Parke, C. S. Hinton, P. B. Armentrout, *J. Phys. Chem. C* **2007**, *111*, 17773–17787.

[63] S. M. Lang, T. M. Bernhardt, R. N. Barnett, U. Landman, *J. Phys. Chem. C* **2011**, *115*, 6788–6795.

[64] S. M. Lang, A. Frank, T. M. Bernhardt, *Catal. Sci. Technol.* **2013**, *3*, 2926–2933.

[65] S. M. Lang, T. M. Bernhardt, *Faraday Discuss.* **2011**, *152*, 337–351.

[66] D. J. Trevor, D. M. Cox, A. Kaldor, *J. Am. Chem. Soc.* **1990**, *112*, 3742–3749.

[67] U. Achatz, M. Beyer, S. Joos, B. S. Fox, G. Niedner-Schatteburg, V. E. n. Bondybey, *J. Phys. Chem. A* **1999**, *103*, 8200–8206.

[68] U. Achatz, C. Berg, S. Joos, B. S. Fox, M. K. Beyer, G. Niedner-Schatteburg, V. E. Bondybey, *Chem. Phys. Lett.* **2000**, *320*, 53–58.

[69] G. Kummerlöwe, I. Balteanu, Z. Sun, O. P. Balaj, V. E. Bondybey, M. K. Beyer, *Int. J. Mass Spectrom.* **2006**, *254*, Ion Catalysis Special Issue, 183 –188.

[70] C. Adlhart, E. Uggerud, *Chem. Commun.* **2006**, 2581–2582.

[71] C. Adlhart, E. Uggerud, *Chem. Eur. J.* **2007**, *13*, 6883–6890.

[72] K. Koszinowski, D. Schröder, H. Schwarz, *J. Phys. Chem. A* **2003**, *107*, 4999–5006.

[73] K. Koszinowski, D. Schröder, H. Schwarz, *Organometallics* **2003**, *22*, 3809–3819.

[74] K. Koszinowski, D. Schröder, H. Schwarz, *ChemPhysChem* **2003**, *4*, 1233–1237.

[75] G. Albert, C. Berg, M. Beyer, U. Achatz, S. Joos, G. Niedner-Schatteburg, V. E. Bondybey, *Chem. Phys. Lett.* **1997**, *268*, 235 –241.

[76] S. M. Lang, A. Frank, T. M. Bernhardt, *J. Phys. Chem. C* **2013**, *117*, 9791–9800.

[77] S. M. Lang, A. Frank, T. M. Bernhardt, *Int. J. Mass Spectrom.* **2013**, *354-355*, Detlef Schröder Memorial Issue, 365 –371.

[78] N. Dietl, M. Schlangen, H. Schwarz, *Angew. Chem. Int. Ed.* **2012**, *51*, 5544–5555.

[79] J. Li, S. Zhou, J. Zhang, M. Schlangen, T. Weiske, D. Usharani, S. Shaik, H. Schwarz, *J. Am. Chem. Soc.* **2016**, *138*, 7973–7981.

[80] H. Schwarz, P. González-Navarrete, J. Li, M. Schlangen, X. Sun, T. Weiske, S. Zhou, *Organometallics* **2017**, *36*, 8–17.

[81] S. Feyel, J. Döbler, D. Schröder, J. Sauer, H. Schwarz, *Angew. Chem. Int. Ed.* **2006**, *45*, 4681–4685.

[82] S. Feyel, J. Döbler, R. Höckendorf, M. Beyer, J. Sauer, H. Schwarz, *Angew. Chem. Int. Ed.* **2008**, *47*, 1946–1950.

[83] Z.-C. Wang, T. Weiske, R. Kretschmer, M. Schlangen, M. Kaupp, H. Schwarz, *J. Am. Chem. Soc.* **2011**, *133*, 16930–16937.

[84] M. Schlangen, H. Schwarz, *Catal. Lett.* **2012**, *142*, 1265–1278.

[85] X. Sun, S. Zhou, M. Schlangen, H. Schwarz, *Chem. Eur. J.* **2017**, *23*, 1498–1501.

[86] X.-L. Ding, Y.-X. Zhao, X.-N. Wu, Z.-C. Wang, J.-B. Ma, S.-G. He, *Chem. Eur. J.* **2010**, *16*, 11463–11470.

[87] Y.-X. Zhao, X.-N. Wu, Z.-C. Wang, S.-G. He, X.-L. Ding, *Chem. Commun.* **2010**, *46*, 1736–1738.

[88] J.-B. Ma, B. Xu, J.-H. Meng, X.-N. Wu, X.-L. Ding, X.-N. Li, S.-G. He, *J. Am. Chem. Soc.* **2013**, *135*, 2991–2998.

[89] X.-N. Wu, X.-L. Ding, Z.-Y. Li, Y.-X. Zhao, S.-G. He, *J. Phys. Chem. C* **2014**, *118*, 24062–24071.

[90] J.-H. Meng, X.-J. Deng, Z.-Y. Li, S.-G. He, W.-J. Zheng, *Chem. Eur. J.* **2014**, *20*, 5580–5583.

[91] X.-L. Ding, D. Wang, X.-N. Wu, Z.-Y. Li, Y.-X. Zhao, S.-G. He, *J. Chem. Phys.* **2015**, *143*.

[92] J.-B. Ma, L.-L. Xu, Q.-Y. Liu, S.-G. He, *Angew. Chem. Int. Ed.* **2016**, *55*, 4947–4951.

[93] M.-Q. Zhang, Y.-X. Zhao, Q.-Y. Liu, X.-N. Li, S.-G. He, *J. Am. Chem. Soc.* **2017**, *139*, 342–347.

[94] A. Božović, S. Feil, G. K. Koyanagi, A. A. Viggiano, X. Zhang, M. Schlangen, H. Schwarz, D. K. Bohme, *Chem. Eur. J.* **2010**, *16*, 11605–11610.

[95] D. Schröder, H. Schwarz, *Angew. Chem. Int. Ed.* **1990**, *29*, 1433–1434.

[96] D. Schröder, H. Schwarz, D. E. Clemmer, Y. Chen, P. Armentrout, V. I. Baranov, D. K. Böhme, *Int. J. Mass Spectrom.* **1997**, *161*, 175 –191.

[97] N. Dietl, C. van der Linde, M. Schlangen, M. K. Beyer, H. Schwarz, *Angew. Chem. Int. Ed.* **2011**, *50*, 4966–4969.

[98] S. Zhou, J. Li, M. Schlangen, H. Schwarz, *Angew. Chem. Int. Ed.* **2016**, *55*, 7257–7260.

[99] B. K. Mai, Y. Kim, *Angew. Chem. Int. Ed.* **2015**, *54*, 3946–3951.

[100] M. Schlangen, H. Schwarz, *Helv. Chim. Acta* **2008**, *91*, 2203–2210.

[101] Y.-X. Zhao, Z.-Y. Li, Z. Yuan, X.-N. Li, S.-G. He, *Angew. Chem. Int. Ed.* **2014**, *126*, 9636–9640.

[102] U. Heiz, F. Vanolli, L. Trento, W.-D. Schneider, *Rev. Sci. Instrum.* **1997**, *68*, 1986–1994.

[103] D. E. Powers, S. G. Hansen, M. E. Geusic, A. C. Puiu, J. B. Hopkins, T. G. Dietz, M. A. Duncan, P. R. R. Langridge-Smith, R. E. Smalley, *J. Phys. Chem.* **1982**, *86*, 2556–2560.

[104] J. L. Gole, J. H. English, V. E. Bondybey, *J. Phys. Chem.* **1982**, *86*, 2560–2563.

[105] L. Ruby, *Am. J. Phys.* **1996**, *64*, 39–44.

[106] É. Mathieu, *J. Math. Pures Appl.* **1868**, *13*, 137–203.

[107] D. Neuwirth, J. F. Eckhard, K. Lange, B. Visser, M. Wiedemann, R. Schröter, M. Tschurl, U. Heiz, *Int. J. Mass Spectrom.* **2015**, *387*, 8 –15.

[108] U. Boesl, R. Weinkauf, E. Schlag, *Int. J. Mass Spectrom. Ion Processes* **1992**, *112*, 121 –166.

[109] U. Boesl, R. Weinkauf, C. Weickhardt, E. W. Schlag, *Int. J. Mass Spectrom. Ion Processes* **1994**, *131*, 87–124.

[110] U. Boesl, *J. Phys. Chem.* **1991**, *95*, 2949–2962.

[111] D. Gerlich, *Adv. Chem. Phys.* **1992**, 1–176.

[112] D. J. Goebbert, G. Meijer, K. R. Asmis, *AIP Conf. Proc.* **2009**, *1104*, 22–29.

[113] K. J. Laidler, *Chemical kinetics*, **1987**.

[114] T. M. Bernhardt, *Int. J. Mass Spectrom.* **2005**, *243*, 1 –29.

[115] T. M. Bernhardt, J. Hagen, S. M. Lang, D. M. Popolan, L. D. Socaciu-Siebert, L. Wöste, *J. Phys. Chem. A* **2009**, *113*, 2724–2733.

[116] G. Van Rossum et al. in USENIX Annual Technical Conference, *Vol. 41*, **2007**, p. 36.

[117] A. C. Hindmarsh, *ACM SIGNUM Newslett.* **1980**, *15*, 10–11.

[118] D. W. Marquardt, *SIAM J. Appl. Math.* **1963**, *11*, 431–441.

[119] D. Neuwirth, J. F. Eckhard, B. R. Visser, M. Tschurl, U. Heiz, *Phys. Chem. Chem. Phys.* **2016**, *18*, 8115–8119.

[120] J. F. Eckhard, D. Neuwirth, M. Tschurl, U. Heiz, *Phys. Chem. Chem. Phys.* **2017**, *19*, 10863–10869.

[121] W. L. H. Jeffrey I. Steinfeld, Joseph S. Fransisco, *Chemical Kinetics and Dynamics*, 2nd ed., Pearson, Prentice Hall: Upper Saddle River, NJ, **1999**.

[122] A. W. Castleman, K. G. Weil, S. W. Sigsworth, R. E. Leuchtner, R. G. Keesee, *J. Chem. Phys.* **1987**, *86*, 3829–3835.

[123] S. M. Lang, T. M. Bernhardt, *Eur. Phys. J. D* **2009**, *52*, 139–142.

[124] R. A. Marcus, *J. Chem. Phys.* **1952**, *20*, 359–364.

[125] D. M. Wardlaw, R. Marcus, *Chem. Phys. Lett.* **1984**, *110*, 230 –234.

[126] M. J. Pilling, I. W. Smith, *Modern gas kinetics*, Blackwell Scientific Publications, **1987**.

[127] S. M. Lang, T. M. Bernhardt, R. N. Barnett, U. Landman, *ChemPhysChem* **2010**, *11*, 1570–1577.

[128] K. Eller, H. Schwarz, *Int. J. Mass Spectrom. Ion Processes* **1989**, *93*, 243 –257.

[129] C. Berg, T. Schindler, G. Niedner-Schatteburg, V. E. Bondybey, *J. Chem. Phys.* **1995**, *102*, 4870–4884.

[130] C. Berg, M. Beyer, U. Achatz, S. Joos, G. Niedner-Schatteburg, V. E. Bondybey, *J. Chem. Phys.* **1998**, *108*, 5398–5403.

[131] M. Zakin, R. Brickman, D. Cox, A Kaldor, *J. Chem. Phys.* **1988**, *88*, 5943–5947.

[132] D. Cox, R. Brickman, K. Creegan, A. Kaldor, *Z. Phys. D* **1991**, *19*, 353–355.

[133] S. Arrhenius, *Z. Phys. Chem.* **1889**, *4*, 226–248.

[134] M. Langevin in Ann. chim. phys. *Vol. 5*, **1905**, pp. 245–288.

[135] H. Eyring, J. Hirschfelder, H. S. Taylor, *J. Chem. Phys.* **1936**, *4*, 479–491.

[136] G. Gioumousis, D. P. Stevenson, *J. Chem. Phys.* **1958**, *29*, 294–299.

[137] T. Su, M. T. Bowers, *J. Chem. Phys.* **1973**, *58*, 3027–3037.

[138] T. Su, M. T. Bowers, *Int. J. Mass Spectrom. Ion Phys.* **1973**, *12*, 347 –356.

[139] L. Bass, T. Su, W. Chesnavich, M. Bowers, *Chem. Phys. Lett.* **1975**, *34*, 119 –122.

[140] T. Su, W. J. Chesnavich, *J. Chem. Phys.* **1982**, *76*, 5183–5185.

[141] T. Su, *J. Chem. Phys.* **1988**, *88*, 4102–4103.

[142] T. Su, *J. Chem. Phys.* **1988**, *89*, 5355–5355.

[143] G. Kummerlöwe, M. K. Beyer, *Int. J. Mass Spectrom.* **2005**, *244*, 84 –90.

[144] H. Eyring, *J. Chem. Phys.* **1935**, *3*, 107–115.

[145] J. Bigeleisen, M. Wolfsberg, *Theoretical and experimental aspects of isotope effects in chemical kinetics*, Wiley Online Library, **2007**, pp. 15–76.

[146] F. Westheimer, *Chem. Rev.* **1961**, *61*, 265–273.

[147] V. Leskovac, *Kinetic Isotope Effects*, Springer Science & Business Media, **2003**, pp. 353–390.

[148] D. Schröder, H. Schwarz, *Proc. Natl. Acad. Sci. U.S.A* **2008**, *105*, 18114–18119.

[149] C. Heinemann, R. Wesendrup, H. Schwarz, *Chem. Phys. Lett.* **1995**, *239*, 75–83.

[150] X.-G. Zhang, R. Liyanage, P. B. Armentrout, *J. Am. Chem. Soc.* **2001**, *123*, 5563–5575.

[151] D. Schröder, H. Schwarz, *Can. J. Chem.* **2005**, *83*, 1936–1940.

[152] R. Wesendrup, H. Schwarz, *Angew. Chem. Int. Ed.* **1995**, *34*, 2033–2035.

[153] S. Zhou, J. Li, M. Schlangen, H. Schwarz, *Chem. Eur. J.* **2016**, *22*, 7225–7228.

[154] J. F. Eckhard, D. Neuwirth, C. Panosetti, H. Oberhofer, K. Reuter, M. Tschurl, U. Heiz, *Phys. Chem. Chem. Phys.* **2017**, *19*, 5985–5993.

[155] T. Masubuchi, J. F. Eckhard, K. Lange, B. Visser, M. Tschurl, U. Heiz, *Rev. Sci. Instrum.* **2018**, *89*, 023104.

[156] D. K. Böhme, H. Schwarz, *Angew. Chem. Int. Ed.* **2005**, *44*, 2336–2354.

[157] S. W. Buckner, T. J. MacMahon, G. D. Byrd, B. S. Freiser, *Inorg. Chem.* **1989**, *28*, 3511–3518.

[158] V. J. F. Lapoutre, B. Redlich, A. F. G. van der Meer, J. Oomens, J. M. Bakker, A. Sweeney, A. Mookherjee, P. B. Armentrout, *J. Phys. Chem. A* **2013**, *117*, 4115–4126.

[159] N. Sändig, W. Koch, *Organometallics* **1997**, *16*, 5244–5251.

[160] S. M. Lang, T. M. Bernhardt, R. N. Barnett, U. Landman, *Angew. Chem. Int. Ed.* **2010**, *49*, 980–983.

[161] S. M. Lang, T. M. Bernhardt, V. Chernyy, J. M. Bakker, R. N. Barnett, U. Landman, *Angew. Chem. Int. Ed.* **2017**, *56*, 13406–13410.

[162] D. J. Harding, C. Kerpal, G. Meijer, A. Fielicke, *Angew. Chem. Int. Ed.* **2012**, *51*, 817–819.

[163] G. Ohanessian, M. J. Brusich, W. A. Goddard, *J. Am. Chem. Soc.* **1990**, *112*, 7179–7189.

[164] R. Horn, R. Schlögl, *Catal. Lett.* **2015**, *145*, 23–39.

[165] S. Zhou, J. Li, M. Schlangen, H. Schwarz, *Angew. Chem. Int. Ed.* **2017**, *56*, 413–416.

[166] J. Li, X.-N. Wu, M. Schlangen, S. Zhou, P. González-Navarrete, S. Tang, H. Schwarz, *Angew. Chem. Int. Ed.* **2015**, *54*, 5074–5078.

[167] Z.-Y. Li, Y.-X. Zhao, X.-N. Wu, X.-L. Ding, S.-G. He, *Chem. Eur. J.* **2011**, *17*, 11728–11733.

[168] J. Li, S. Zhou, J. Zhang, M. Schlangen, D. Usharani, S. Shaik, H. Schwarz, *J. Am. Chem. Soc.* **2016**, *138*, 11368–11377.

[169] D. J. Harding, A. Fielicke, *Chem. Eur. J.* **2014**, *20*, 3258–3267.

[170] R. N. Barnett, U. Landman, *Phys. Rev. B* **1993**, *48*, 2081–2097.

[171] H. Häkkinen, M. Moseler, U. Landman, *Phys. Rev. Lett.* **2002**, *89*, 033401.

[172] R. Kretschmer, M. Schlangen, H. Schwarz, *Angew. Chem. Int. Ed.* **2013**, *52*, 6097–6101.

[173] M. Firouzbakht, S. Zhou, P. González-Navarrete, M. Schlangen, M. Kaupp, H. Schwarz, *Chem. Eur. J.* **2017**, *23*, 12346–12352.

[174] M. Firouzbakht, N. J. Rijs, P. González-Navarrete, M. Schlangen, M. Kaupp, H. Schwarz, *Chem. Eur. J.* **2016**, *22*, 10581–10589.

[175] Y.-X. Zhao, X.-L. Ding, Y.-P. Ma, Z.-C. Wang, S.-G. He, *Theor. Chem. Acc.* **2010**, *127*, 449–465.

[176] K. R. Asmis, J. Sauer, *Mass Spectrom. Rev.* **2007**, *26*, 542–562.

[177] K. R. Asmis, G. Meijer, M. Brümmer, C. Kaposta, G. Santambrogio, L. Wöste, J. Sauer, *J. Chem. Phys.* **2004**, *120*, 6461–6470.

[178] X.-N. Wu, J. Li, M. Schlangen, S. Zhou, P. González-Navarrete, H. Schwarz, *Chem. Eur. J.* **2017**, *23*, 788–792.

[179] A. Fielicke, G Von Helden, G. Meijer, *Eur. Phys. J. D* **2005**, *34*, 83–88.

[180] S. Zhou, J. Li, M. Schlangen, H. Schwarz, *Angew. Chem. Int. Ed.* **2016**, *55*, 14867–14871.

[181] F. Xia, Z. Cao, *Organometallics* **2007**, *26*, 6076–6081.

[182] N Waletzko, L. Schmidt, *AlCHe J.* **1988**, *34*, 1146–1156.

[183] A Bockholt, I. Harding, R. Nix, *J. Chem. Soc. Faraday Trans.* **1997**, *93*, 3869–3878.

[184] M. Sakurai, K. Watanabe, K. Sumiyama, K. Suzuki, *J. Chem. Phys.* **1999**, *111*, 235–238.

[185] M. Pavlov, M. R. A. Blomberg, P. E. M. Siegbahn, R. Wesendrup, C. Heinemann, H. Schwarz, *J. Phys. Chem. A* **1997**, *101*, 1567–1579.

[186] U. Heiz, A. Sanchez, S. Abbet, W.-D. Schneider, *Eur. Phys. J. D* **1999**, *9*, 35–39.

[187] A. Fielicke, G. Meijer, G. von Helden, *Eur. Phys. J. D* **2003**, *24*, 69–72.

[188] A. Fielicke, G. Meijer, G. von Helden, *J. Am. Chem. Soc.* **2003**, *125*, 3659–3667.

[189] A. Fielicke, P. Gruene, M. Haertelt, D. J. Harding, G. Meijer, *J. Phys. Chem. A* **2010**, *114*, 9755–9761.

[190] P. Gruene, A. Fielicke, G. Meijer, *J. Chem. Phys.* **2007**, *127*, 234307.

[191] K. R. Asmis, T. Wende, M. Brummer, O. Gause, G. Santambrogio, E. C. Stanca-Kaposta, J. Dobler, A. Niedziela, J. Sauer, *Phys. Chem. Chem. Phys.* **2012**, *14*, 9377–9388.

[192] L. Shu, J. C. Nesheim, K. Kauffmann, E. Münck, J. D. Lipscomb, L. Que, *Science* **1997**, *275*, 515–518.

[193] F. Arena, G. Gatti, G. Martra, S. Coluccia, L. Stievano, L. Spadaro, P. Famulari, A. Parmaliana, *J. Catal.* **2005**, *231*, 365–380.

[194] R. C. Bell, K. A. Zemski, D. R. Justes, A. W. Castleman, *J. Chem. Phys.* **2001**, *114*, 798–811.

[195] M. Neumaier, F. Weigend, O. Hampe, M. M. Kappes, *J. Chem. Phys.* **2005**, *122*, 104702.

[196] N. Troullier, J. L. Martins, *Phys. Rev. B* **1991**, *43*, 1993–2006.

[197] J. P. Perdew, K. Burke, M. Ernzerhof, *Phys. Rev. Lett.* **1996**, *77*, 3865–3868.

[198] T. Bernhardt, U. Heiz, U. Landman, *Chemical and Catalytic Properties of Size-Selected Free and Supported Clusters*, Springer Berlin Heidelberg, Berlin, Heidelberg, **2007**, pp. 1–191.

[199] E. Sanville, S. D. Kenny, R. Smith, G. Henkelman, *J. Comput. Chem.* **2007**, *28*, 899–908.

[200] W. Tang, E. Sanville, G. Henkelman, *J. Phys.: Condens. Matter* **2009**, *21*, 084204.

[201] M. Yu, D. R. Trinkle, *J. Chem. Phys.* **2011**, *134*, 064111.

ACKNOWLEDGMENTS

I am extremely grateful for many people dear to me, colleagues, friends, and family.

After my Bachelor's thesis, I eagerly accepted a position as "studentische Hilfskraft" offered by Ueli Heiz. This position culminated in my Master's thesis at the Chair of Physical Chemistry and finally in the work toward my doctorate. Ueli's trust and continuing guidance throughout these years lead me to where I am today. Kathrin Lange and Brad Visser welcomed me to the world of experimental science and demonstrated how to relish life in- and outside of the lab. In the first years of my postgraduate work, I enjoyed the company of Daniel Neuwirth, whose work ethic set a great example, and whose experimental and technical expertise facilitated many subsequent studies. Martin Tschurl has been an outstanding group leader, never short of advice, and always pushing me to do my best. In the lab, I later on thankfully came to benefit from the support and knowledge of Tsugunosuke Masubuchi.

My gratitude also goes to all the members (former and current) of the Heiz group for contributing to a constantly enjoyable work environment. I will fondly remember many of the fierce Badminton matches and invigorating dinners afterward with Fabian Knoller and Alexander von Weber. I cherished the banter with the members of the photocat lab, Constantin Walenta, whose literature proficiency and barbecuing ingenuity outrank everybody, and Sebastian Kollsmannsberger, whose talents with the racket and at the "Kicker" are second to none. I am also grateful for the time with the members of the nanocat lab, Maximilian Krause, who embodies scientific curiosity, and Marian Rötzer, whose joyful attitude to life made me moreover appreciate bavarian culture.

I owe all of my achievements to the support and care of my parents, Barbara and Joachim, my sister, Julia, and my beloved girlfriend, Carla.

LIST OF PUBLICATIONS

The following list shows work published during the period of this dissertation, including the corresponding bibliographic information. The content of publications relating to the modification of the laser vaporization cluster source and the oxidation reactions of bare tantalum clusters was briefly summarized in Chapter 4, whereas excerpts of the publication that discusses the ring electrode ion trap are provided in Chapter 3.3. At the end, this list includes an overview of manuscripts that are currently in preparation. The experimental work displayed in Chapters 5–8 serves as a basis for these future publications, which will be complemented by quantum-chemical calculations of external collaborators.

Published Manuscripts

1. T. Masubuchi, **J. F. Eckhard**, K. Lange, B. Visser, M. Tschurl and U. Heiz (2018). *An efficient laser vaporization source for chemically modified metal clusters characterized by thermodynamics and kinetics*. Review of Scientific Instruments, 89(2), 023104.

2. **J. F. Eckhard**, D. Neuwirth, M. Tschurl, and U. Heiz (2017). *From oxidative degradation to direct oxidation: size regimes in the consecutive reaction of cationic tantalum clusters with dioxygen*. Physical Chemistry Chemical Physics, 19(17), 10863-10869.

3. **J. F. Eckhard**, D. Neuwirth, C. Panosetti, H. Oberhofer, K. Reuter, M. Tschurl, and U. Heiz (2017). *Consecutive reactions of small, free tantalum clusters with dioxygen controlled by relaxation dynamics*. Physical Chemistry Chemical Physics, 19(8), 5985-5993.

4. D. Neuwirth, **J. F. Eckhard**, B. R. Visser, M. Tschurl, and U. Heiz (2016). *Two reaction regimes in the oxidation of larger cationic tantalum clusters* (Ta_n^+, $n = 13 - 40$) *under multi-collision conditions*. Physical Chemistry Chemical Physics, 18(11), 8115-8119.

5. D. Neuwirth, **J. F. Eckhard**, K. Lange, B. Visser, M. Wiedemann, R. Schröter, M. Tschurl and U. Heiz (2015). *Using controlled ion extraction to combine a ring electrode trap with a reflectron time-of-flight mass spectrometer*. International Journal of Mass Spectrometry, 387, 8-15.

6. K. Lange, B. Visser, D. Neuwirth, **J. F. Eckhard**, U. Boesl, M. Tschurl, K. H. Bowen and U. Heiz (2015). *Size-dependent gas phase reactivity of tantalum cluster cations with small alcohols*. International Journal of Mass Spectrometry, 375, 9-13.

Manuscripts in preparation

7. **J. F. Eckhard**, T. Masubuchi, M. Tschurl, R. Barnett, U. Landman and U. Heiz. *Thermal Methane Activation Mediated by Bare Tantalum Cluster Cations*. In preparation.
8. **J. F. Eckhard**, T. Masubuchi, M. Tschurl, R. Barnett, U. Landman and U. Heiz. *Thermal Dehydrogenation of Methane Enhanced by Oxo Ligands in Tantalum Clusters Cations* $[Ta_xO_y]$ $(x = 4, 5)$. In preparation.
9. T. Masubuchi, **J. F. Eckhard**, G. Goddard, M. Tschurl, and U. Heiz. *C–O Coupling Reactions of Tantalum-Methylene Complexes* $[Ta_{1,4}CH_2]^+$ *with* O_2. In preparation.
10. **J. F. Eckhard**, T. Masubuchi, G. Goddard, M. Tschurl, and U. Heiz. *Mechanistic Variants of Methane Activation by Tantalum Dimer Oxides* $[Ta_2O_x]^+$ $(x = 0–6)$. In preparation.

Appendices

EXPERIMENTAL DETAILS A

A.1. Sequence of vaporization laser and gas valve triggers

Tantalum clusters are generated through the irradiation of a tantalum target by a vaporization laser and the introduction of a high-pressure carrier gas by a piezo-electric valve (see Chapter 3.1). Figure A.1 displays the corresponding triggering scheme. Shortly after the extraction from the ion trap, a high-voltage pulse is applied to the acceleration plates of the TOF-MS to analyze the clusters based on their mass-to-charge ratio. In order to produce various tantalum cluster oxides, a solenoid valve may introduce oxygen gas into the nozzle of the cluster source (see Chapter 4.3).

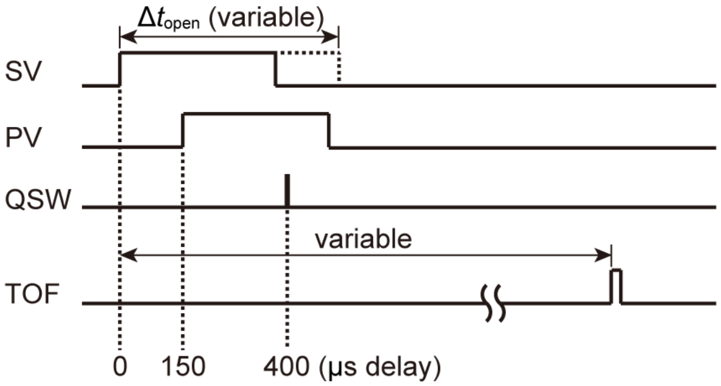

Figure A.1: *Temporal sequence for the trigger pulses of the solenoid valve (SV) to introduce reactant gas, the piezo-electric valve (PV) to introduce helium carrier gas, the Q-switch (QSW) of the ablation laser and the voltage applied to the TOF-MS acceleration plates. Reproduced with permission from [155]. Copyright AIP PUBLISHING LLC.*

A.2. Vacuum pumps and gases

Each of the main components of the experimental setup is housed in an individual, stainless-steel ultra-high-vacuum chamber. These chambers are evacuated by turbomolecular pumps (see Tab. A.1), which are connected to pre-vacuum (rotary vane) pumps. The chamber of the laser vaporization cluster source is an exception as it is evacuated by a roots pump during operation of the carrier gas valve. Table A.2 lists all gases used in the experiments, including purities and suppliers of the gas cylinders.

Table A.1: *Roots, turbomolecular, and rotary vane pumps used in the evacuation of the experimental apparatus.*

Chamber	Pump type	Backing pump
Laser vaporization source	Ruvac WS 1001	Busch R5 RA 0205
Ion bender	Pfeiffer TPU 2200	Pfeiffer Duo 060 A
Quadrupole mass filter	Pfeiffer TPU 240	Pfeiffer Duo 65 M[a]
Ring electrode ion trap	Pfeiffer HiPace 700M	Pfeiffer Duo 20 M
TOF-MS	Pfeiffer TPU 510	Pfeiffer Duo 65 M[a]
Reflectron	Pfeiffer TMU 260	Pfeiffer Duo 65 M[a]
Gas-mixing	Pfeiffer TMU 260	Leybold TRIVAC D 65 B

[a] The same rotary vane pump evacuates three turbomolecular pumps simultaneously.

Table A.2: *Carrier, buffer and reactive gases employed during experiments. Next to the purity, the supplier of the gas cylinders is shown.*

Gas	purpose	purity /%	supplier
He	Carrier gas (laser vaporization source)	99.9990	Westfalen
He	Buffer gas (ring electrode ion trap)	99.9999	Westfalen
O_2 in He	Reactive gas/buffer gas mixture	99.9999	Westfalen
$^{18}O_2$ (95.4 atom-% ^{18}O)	Reactive gas	99.0000	Isotec, Inc.
CH_4	Reactive gas	99.9995	Riessner Gase
CD_4 (99 atom-% D)	Reactive gas	99.9460	Linde AG

A.3. Pressure determination

Gas mixtures are prepared in a home-built UHV chamber, which is connected to the ion trap *via* a mass flow controller (model 179C, MKS), a gas channel feedthrough and, ultimately, a Teflon capillary. The gas-mixing chamber is evacuated by a turbomolecular pump that is gated off when gases are introduced into the chamber, in order to either flush the chamber or to produce gas mixtures. Several gas cylinders containing helium buffer gas (He 6.0, Westfalen) as well as reactive gases are connected to the gas-mixing chamber *via* leak valves, and the chamber pressure is monitored by a combined Pirani/hot-filament ionization pressure gauge (ITR90, Leybold, $5 \cdot 10^{-10}$–1000 mbar range) and a capacitance gauge (baratron model 722B, MKS, 1-10000 mbar range). The measurement of the absolute pressure in the gas-mixing chamber is used to produce specific gas dilutions. For example, methane (CH_4 5.5, Riessner Gase) is dosed to a chamber pressure of 5 mbar and helium is added to achieve a total pressure of 1000 mbar. Reactive gas concentrations are precisely determined under reaction conditions by a residual gas analyzer (RGA200, SRS) located in the ion trap UHV chamber. When gas is introduced into the RET, the base pressure of the ion trap UHV chamber rises from ~$2{\cdot}10^{-9}$ mbar to ~$2{\cdot}10^{-4}$ mbar and the pressure in the ion trap itself increases from <$1{\cdot}10^{-5}$ mbar to $7.7{\cdot}10^{-3}$ mbar. The reactive gas particle density in the ion trap, for example $\left(\frac{n}{V}\right)_{\mathrm{CH_4}}$, is assumed to be a function of the absolute abundance, $p^{\mathrm{RGA}}_{\mathrm{CH_4}}$, determined by the RGA in the ion trap chamber[1] relative to the absolute helium abundance, $p^{\mathrm{RGA}}_{\mathrm{He}}$, and the absolute pressure in the RET, P_m, monitored by a second baratron connected to the ion trap (model 722B, MKS, $1 \cdot 10^{-5}$–1 mbar range). Assuming a behavior of highly diluted gases according to the ideal gas law, one arrives at the following expression for the methane particle density:

$$\left(\frac{n}{V}\right)_{\mathrm{CH_4}} = \left(\frac{p^{\mathrm{RGA}}_{\mathrm{CH_4}}}{p^{\mathrm{RGA}}_{\mathrm{He}}} P_m\right) \frac{1}{k_B \cdot T} \tag{A.1}$$

with the Boltzmann constant k_B and the gas temperature T. Figure A.2 illustrates the validity of this approach. Gas-phase reactions of extremely diluted ions are assumed to be of pseudo-first order, as the concentration of reactant gas

---

[1] Molecules demonstrate different ionization cross sections and a cracking pattern as a result of the ionization process. The analysis of abundances accounts for these two effects.

molecules (in tremendous excess compared to the ions)[2] remains constant during the reaction. This assumption was tested by exposing Ta_4^+ to a wide range of different methane particle densities and evaluating the first-order rate coefficients. The rate coefficient scales linearly with the particle density according to Eq. A.1, thus verifying the pseudo-first order of the reactions and the approach used in the determination of the methane particle density.

Typical gas contaminations are water, oxygen and nitrogen, which are suppressed by repeatedly flushing the gas-mixing chamber with helium and subsequent evacuation to high-vacuum pressure conditions. Oxygen levels are routinely suppressed below the detection limit of the RGA, *i.e.* $3.6 \cdot 10^{-10}$ mbar at a chamber pressure of $\sim 2 \cdot 10^{-4}$ mbar (simultaneously corresponding to the He fraction measured by the RGA). On the other hand, extremely diluted amounts of water and nitrogen remain in the gas mixture (typically 5 and $9 \cdot 10^{-10}$ mbar, respectively).

The mass flow controller injects a constant stream of gas into the capillary that is wrapped around the copper block and leads into the RET, and the resulting pressure is measured by a baratron located outside of the vacuum chamber. One has to account for thermal transpiration when the ion trap (and buffer gas) temperature T_a differs from the temperature of the second baratron T_m [114, 194]. The necessary correction of the measured pressure P_m to obtain the actual pressure P_a is expressed by Equation A.2.

$$P_a = P_m \sqrt{\frac{T_a}{T_m}} \tag{A.2}$$

---

[2] At 0.77 Pa and a concentration of 0.5%, approximately 10^{11} methane molecules occupy one cubic centimeter, whereas the total RET volume typically contains $10^5 - 10^6$ ions [107].

A.4. Evaluation of reaction order

The dehydrogenation reactions $[\mathrm{Ta}_x\mathrm{O}_y]^+ + \mathrm{CH}_4 \rightarrow [\mathrm{Ta}_x\mathrm{O}_y\mathrm{CH}_2]^+ + \mathrm{H}_2$ are assumed to be of first order. In order to verify this assumption, the rate of $[\mathrm{Ta}_4\mathrm{CH}_2]^+$ formation is determined at various methane concentrations in the buffer gas. Figure A.2 illustrates the linear dependence of the pseudo-first order rate coefficient on the methane partial pressure in the ion trap ($\chi_{\mathrm{CH}_4} = \frac{p^{\mathrm{RGA}}_{\mathrm{CH}_4}}{p^{\mathrm{RGA}}_{\mathrm{He}}} \cdot P_m$, see also Eq. A.1). As the pseudo-first order rate coefficient scales linearly with χ_{CH_4}, reactions may be conducted at various methane partial pressures in the investigated regime and the rate coefficient obtained by kinetic modeling may be normalized to those values.

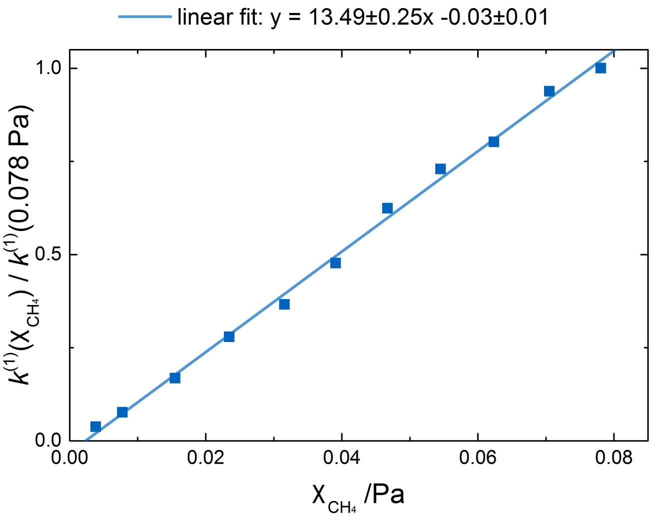

Figure A.2: *Pseudo-first order rate coefficient associated with the formation of* $[\mathrm{Ta}_4\mathrm{CH}_2]^+$ *as a function of the methane partial pressure. The rate coefficient scales linearly and a vanishing (negative) value is extrapolated for a partial pressure of zero.*

A.5. Rate coefficient normalization and uncertainties

The biggest source of error for the normalized rate coefficients derives from the determination of the total pressure inside of the RET. The RET is, due to its design, comparatively gas-tight and differentially pumped from the axial openings, while the buffer gas enters the ion trap *via* a center electrode [107]. The baratron is connected to an electrode halfway between the first and the center electrode. As a result, there is an unknown pressure gradient throughout the RET and a local pressure is measured by the baratron that may deviate from the mean pressure and will subsequently bring about a large systematic error [107]. Groups with similar setups estimate the absolute error of the pressure measurement to be 50% [195] and the same error was assumed in the initial oxidation studies of our group (see Chapter 4) [119, 120, 154]. However, the absolute pressure is constant for all experiments and results in small relative errors around 20% when measurements are compared. For the subsequent reactivity studies toward methane, the pressure was referenced by repetition and evaluation of a measurement reported in literature. Previous studies have shown $[TaCH_2]^+$ formation (*via* methane dehydrogenation) under single-collision conditions in a guided ion beam [62] and an FT-ICR experiment [54] and under multi-collision conditions in a flow-tube reactor [53], with bimolecular rate coefficients of 2.9 ± 1.2, 3.4 ± 0.9 and $3.8 \pm 1.1 \cdot 10^{-10}$ $cm^3 s^{-1}$, respectively. In our experiment, a bimolecular rate coefficient of $11.5 \pm 2.3 \cdot 10^{-10}$ $cm^3 s^{-1}$ is found due to the deviation of the measured pressure from the mean pressure. As the flow-tube reactor shares the multi-collision conditions similar to the present ion trap experiment, the corresponding rate coefficient is used to determine a correction factor that is applied to all of the rate coefficients obtained with the present setup. Note that the systematic error caused by the absolute pressure and the subsequent correction for it has no impact on the relative error. The relative error of the rate coefficients (and the kinetic isotope effect) is determined by propagating uncertainties of the kinetic fitting procedure, the calculation of the particle densities, and of the temperature measurement.

A.6. Additional mass spectra

Chapter 5 investigates the reactions of Ta_{1-10}^{+} toward methane and illustrations provided therein focus on Ta_{1-4}^{+}. Additional spectra of the clusters stored for prolonged times in pure helium (Fig. A.4) and Ta_{7-10}^{+} reacting with methane (Fig. A.5) are displayed in the following. The temperature-dependent behavior of larger clusters is shown exemplarily for the pentamer and hexamer cluster cations (see Fig. A.3).

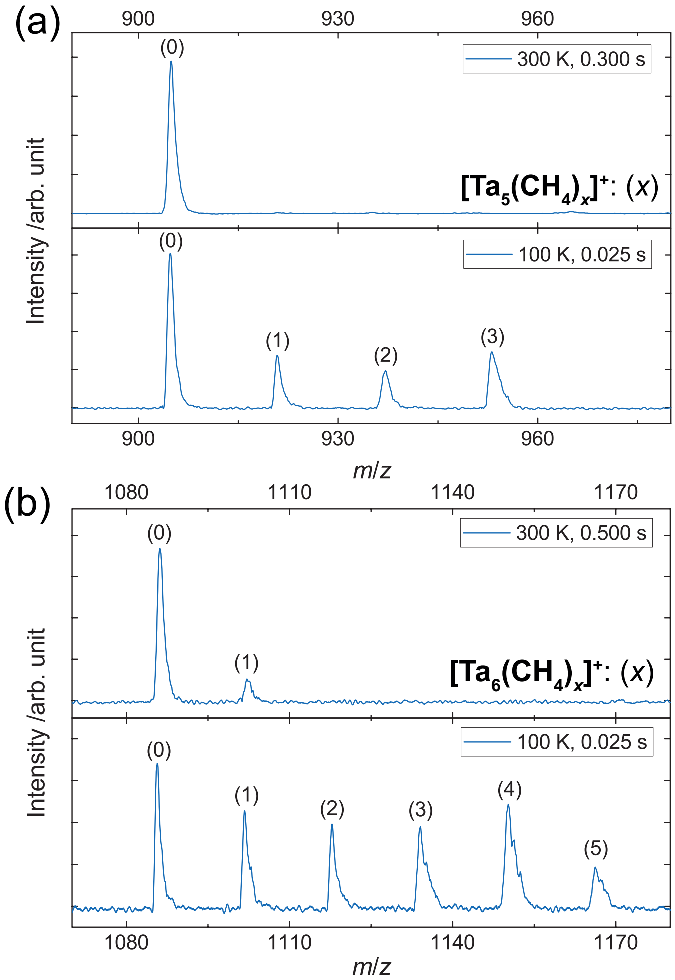

Figure A.3: *Mass spectra for the reaction of Ta_5^+ (a) and Ta_6^+ (b) with methane. The pentamer cluster is unreactive at 300 K and weakly-bound adducts form at 100 K. At 300 K, Ta_6^+ slowly adsorbs a CH_4 molecule and the adsorption of up to five molecules is facilitated at 100 K. Ta_{7-9}^{+} clusters demonstrate the identical behavior,* i.e. *slow adsorption of methane in absence of hydrogen elimination that becomes enhanced at lower temperatures.*

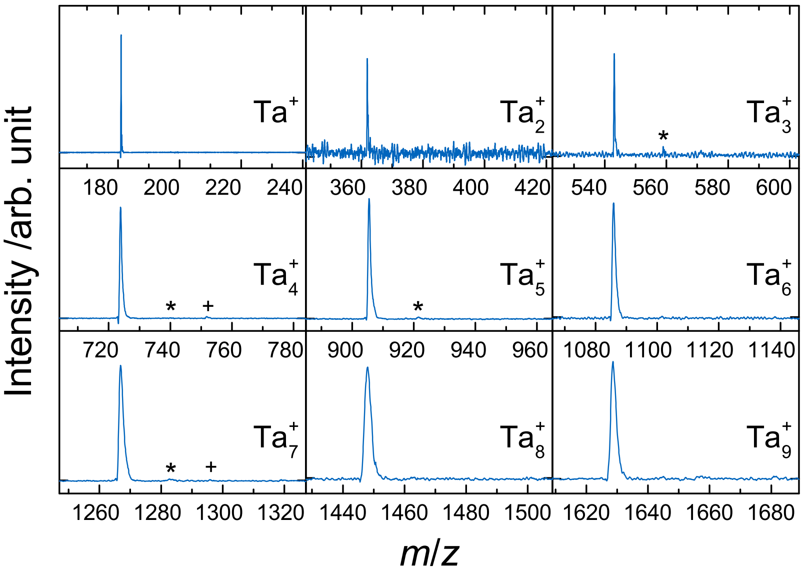

Figure A.4: *Mass spectra of Ta_{1-9}^+ stored for 0.5 s in helium buffer gas. Negligible amounts of cluster monoxides (marked by asterisks) and cluster-nitrogen complexes (marked by plus signs) are produced due to reactions with background water and nitrogen, respectively. For Ta_3^+ and especially Ta_2^+, a low natural abundance [184] causes a lower signal-to-noise ratio.*

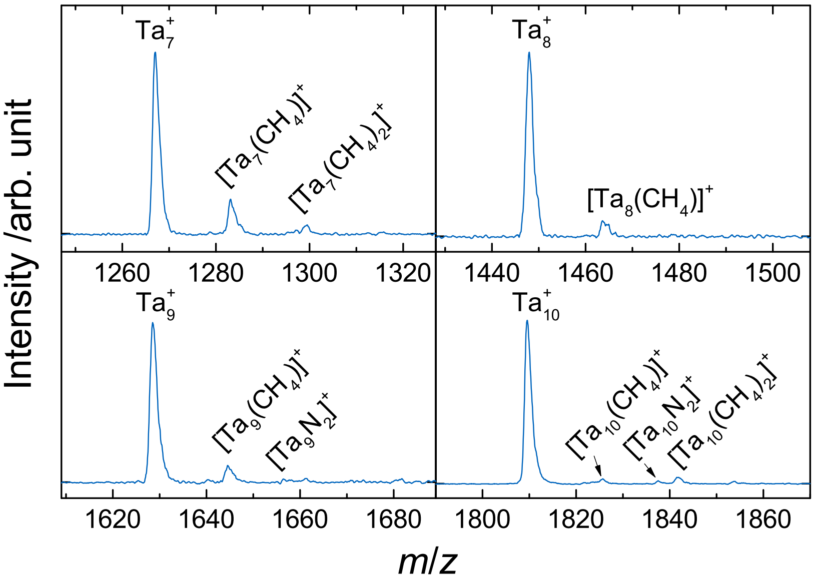

Figure A.5: *Time-of-flight mass spectra for Ta_{7-10}^+ exposed to methane for 0.5 s in helium buffer gas. These clusters slowly adsorb CH_4 in absence of hydrogen elimination. Reactions with background nitrogen additionally generate traces of side products,* e.g. *$[Ta_{10}N_2]^+$.*

SDFT ON $[\mathrm{Ta}_{4,5}\mathrm{O}_{0,1}]^{+}/\mathrm{CH}_4$ B

B.1. Theoretical Methods

B.1.1. Spin-density functional methodology

The theoretical explorations of the atomic arrangements and electronic structures of the tantalum clusters and their derivatives were performed with the use of the Born-Oppenheimer spin density-functional theory molecular dynamics (BO-SDFT-MD) method [170] with norm-conserving soft (scalar relativistic for Ta) pseudopotentials [196] and the generalized gradient approximation (GGA) [197] for electronic exchange and correlations. In these calculations a plane-wave basis was used with a kinetic energy cut-off E_c = 62 Ry, which yields convergence. This corresponds to a real-space grid spacing of 0.4 a_0 (Bohr radius); the real-space grid spacing for the density (and potential) was 0.133 a_0 corresponding to E_c = 555 Ry. In the construction of the Ta pseudopotentials the valence electrons, $5d^3$ and $6s^2$, were characterized by core radii $r_c(s) = 2.55\ a_0$ and $r_c(d) = 2.00\ a_0$, with the s orbital treated as local, and (unoccupied) $6p^0$ core radius $r_c(p) = 3.00\ a_0$. Additionally for Ta there is a non-linear core correction with the pseudo-core containing 10% of the $[\mathrm{Xe}]4f^{14}$ core. For the carbon atom pseudopotential the valence $2s^2$ and $2p^2$ electrons were treated with $r_c(s) = r_c(p) = 1.45\ a_0$, with the p orbital treated as local. The 1s electron of the H atoms was described by local pseudopotential with $r_c(s) = 0.95\ a_0$. The oxygen $2s^2$ and $2p^4$ core radii are $r_c(s) = r_c(p) = 1.45\ a_0$ with p local.

The BO-SDFT-MD method [170] is particularly suitable for investigations of charged systems since it does not employ a supercell (*i.e.*, no periodic replication of the ionic system is used). In all the calculations the dependence on spin multiplicity has been checked, and the reported results correspond to the spin multiplicities with the lowest energies. In particular, it is pertinent to note here that in all calculations the spin-degree of freedom is optimized and used in the compu-

tation, unless a particular spin configuration (spin multiplicity) is prescribed. At each step of the calculation the energy levels of the SDFT up-spin and down-spin manifolds in the vicinity of the Fermi level are examined, and the occupation is adjusted such that the spin-Kohn-Sham level with the lower energy eigenvalue gets occupied. When a particular spin configuration is desired, the corresponding numbers of electrons with up and down spins are kept fixed throughout the calculation (that is N_s electrons with spin s = ↑ or ↓, so that the spin excess is given by $\mu = N_\uparrow - N_\downarrow$).
The energy minimization to find the optimal cluster geometry was done with a steepest-descent method. The convergence criteria were that the maximum force magnitude on any particle is less than 0.0005 Hartree/Bohr and that the average over all particles is less than 0.00025 Hartree/Bohr. In some cases BO-SDF-MD simulations of typically a few picosecond duration at 300 K (that is, canonical, constant temperature, simulations, with stochastic thermalization) were used to ensure that the resulting optimal configurations were stable; a time-step of 0.25 fs was used in these simulations.

B.1.2. Spin Isomers

For the Ta_4^+ and $[Ta_4O]^+$ clusters, both in the bare clusters and with adsorbed CH_n, the ground state always has the lowest possible spin, *i.e.* $\mu = 1$ (μ is the difference between numbers of majority and minority spin electrons). The calculated energy differences of the two higher-spin isomers with respect to the ground state isomer are: $\Delta E\,[Ta_4^+(\mu = 3)] - \Delta E\,[Ta_4^+(\mu = 1)] = 0.92$ eV; $\Delta E\,[Ta_4^+CH_4(\mu = 3)] - \Delta E\,[Ta_4^+CH_4(\mu = 1)] = 0.86$ eV; $\Delta E\,[(HTa_4CH_3)^+(\mu = 3)] - \Delta E\,[(HTa_4CH_3)^+(\mu = 1)] = 0.60$ eV. The energy differences between spin isomers for the Ta_5^+ and $[Ta_5O]^+$ clusters are smaller and for $[Ta_5O]^+CH_4$ the ground state changes from $\mu = 2$ to $\mu = 0$ after the first deprotonation as shown in Figure 6.5.

B.1.3. Reaction pathway calculations

In the first-principles SDFT calculations of the reaction profiles (shown in Figs. 6.4 and 6.5 of the main text) the total energy of the system is calculated using the SDFT method as a function of a sequence of values of a judiciously chosen reaction coordinate; i.e., steered SDFT simulations. The reaction coordinate can be the distance between two atoms or a function involving several interatomic distances, angles, etc. For example, for the case of activation and dissociation of a C–H bond of a CH_4 molecule adsorbed on $[Ta_xO_y]^+$ clusters ($x = 4, 5$ and $y = 0, 1$), that is $[Ta_xO_yCH_4]^+ \rightarrow [Ta_xO_y\,(H_d,CH_3)]^+$, the reaction coordinate can be the distance between the activated bond length r(C–H_d), where H_d is the dissociating hydrogen atom, or the ratio between that bond length and the distance between H_d and chosen Ta* atom of the metal cluster, *i.e.* $r(C\text{–}H_d)/r(Ta^*\text{–}H_d)$. In the calculations, the C–H_d bond for the first deprotonation and the aforementioned distance-ratio choice was used for subsequent deprotonation. The H–H bond length was used for the barrier to the adsorbed H_2 molecule. For each value of the reaction coordinate, the total energy of the system was optimized through unconstrained relaxation of all of the other degrees of freedom of the system; as aforementioned, the relaxation process includes optimization with respect to the spin degrees of freedom. The reaction profile (reaction path) was obtained via incrementing the reaction coordinate by small steps to find the local minima and barrier configurations. These calculations yield results that are the same as, or close to, those obtained by other methods, *e.g.*, the nudged elastic band and variants thereof; see the discussion on pp. 89 and 90 in Reference [198].

B.1.4. Bader charge analysis

The wave-functions resulting from the SDFT calculations were used in evaluation of the partial charges on the atoms of the cluster systems, using the Bader-charge analysis [199–201]. This analysis gives the partial charge associated with each of the atoms in the cluster complex, and allows one to estimate the gain or loss of charge on each atom in the cluster environment.

B.2. Reaction pathways

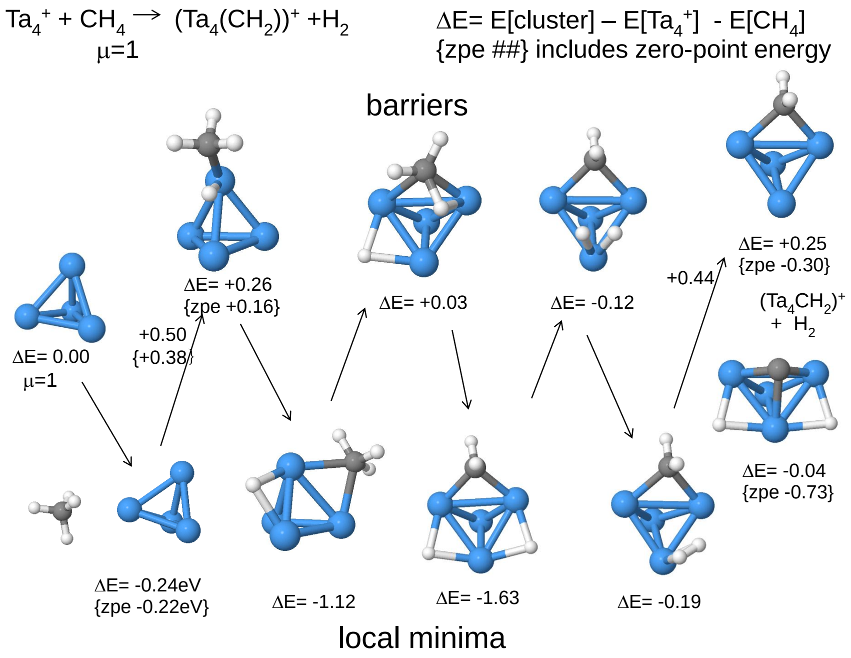

Figure B.1: *SDFT-calculated pathway for the cluster-mediated reaction $Ta_4^+ + CH_4 \rightarrow [Ta_4CH_2]^+ + H_2$ (compare Fig. 6.4). Energies are given relative to that of the initial state of the isolated reactants Ta_4^+ and CH_4; zero-point-energy (zpe)-corrected values are given in brackets. The initial spin state of the metal cluster is indicated by μ (the excess of majority spin electrons). Barrier configurations are shown in the upper row, and local minima are depicted in the bottom row. Two possible products of the dehydrogenated cluster complex are shown on the right. Ta atoms are depicted as blue spheres, carbon in gray, and hydrogen atoms as small white spheres.*

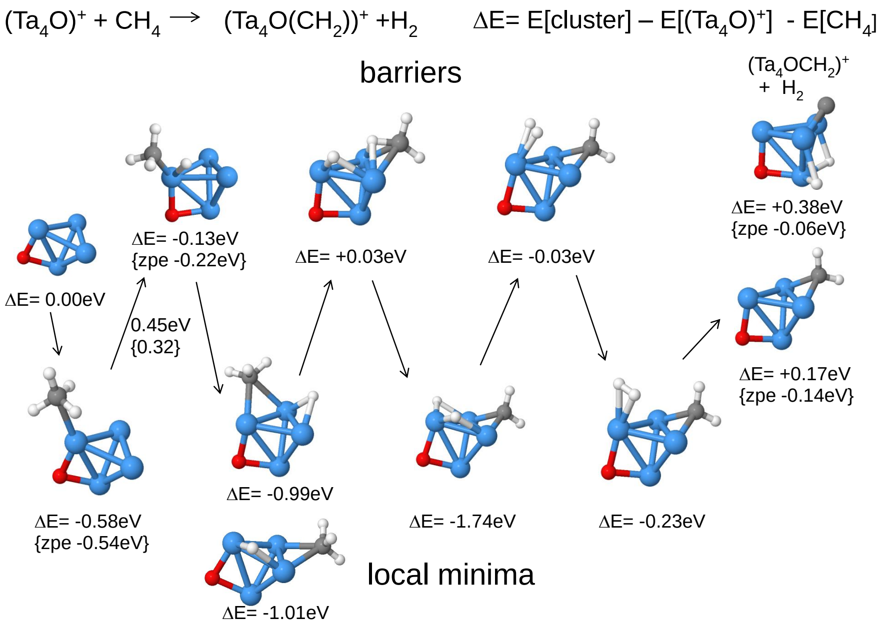

Figure B.2: *SDFT-calculated pathway for the cluster-mediated reaction* $[Ta_4O]^+ + CH_4 \rightarrow [Ta_4OCH_2]^+ + H_2$ *(compare Fig. 6.4). Energies are given relative to that of the initial state of the isolated reactants* $[Ta_4O]^+$ *and* CH_4*; zero-point-energy (zpe)-corrected values are given in brackets. The initial spin state of the metal cluster is indicated by* μ *(the excess of majority spin electrons). Barrier configurations are shown in the upper row, and local minima are depicted in the bottom row. Two possible products of the dehydrogenated cluster complex are shown on the right. Ta atoms are depicted as blue spheres, carbon in gray, and hydrogen atoms as small white spheres.*

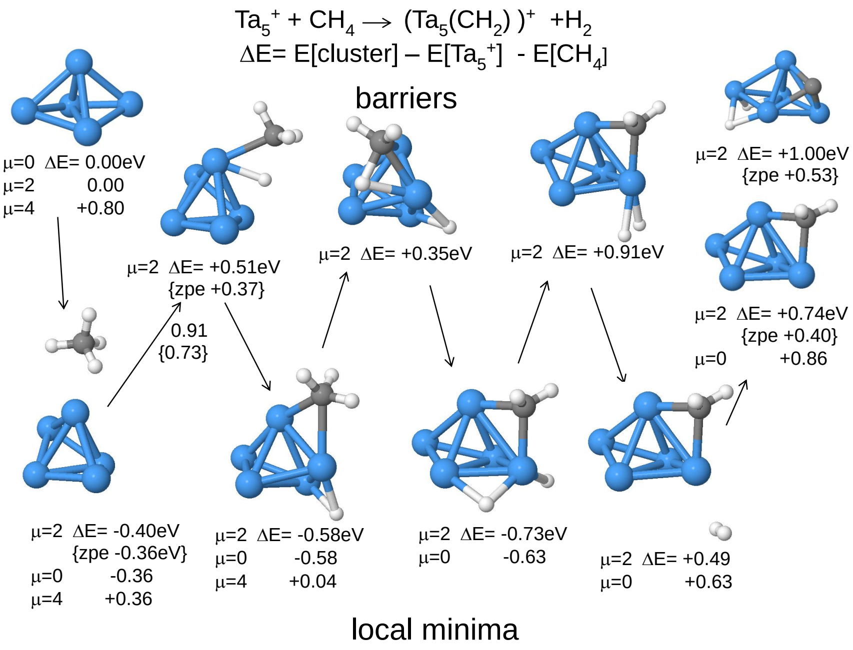

Figure B.3: *SDFT-calculated pathway for the cluster-mediated reaction*$Ta_5^+ + CH_4 \rightarrow [Ta_5CH_2] + H_2$ *(compare Fig. 6.5). Energies are given relative to that of the initial state of the isolated reactants* Ta_5^+ *and* CH_4*; zero-point-energy (zpe)-corrected values are given in brackets. The spin state of the metal cluster is indicated by* μ *(the excess of majority spin electrons). Barrier configurations are shown in the upper row, and local minima are depicted in the bottom row. Two possible products of the dehydrogenated cluster complex are shown on the right. Ta atoms are depicted as blue spheres, carbon in gray, and hydrogens as small white spheres.*

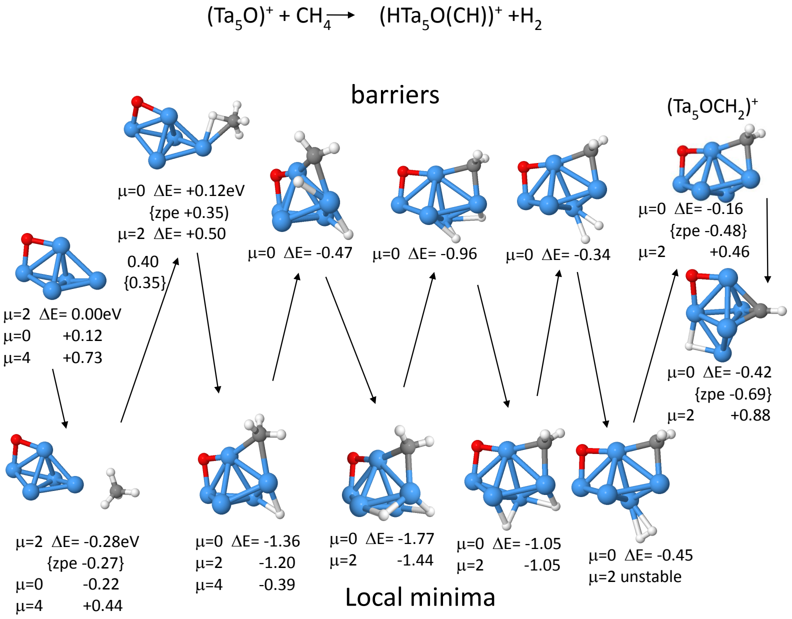

Figure B.4: *SDFT-calculated pathway for the cluster-mediated reaction* $[Ta_5O]^+ + CH_4 \rightarrow [Ta_5OCH_2]^+ + H_2$ *(compare Fig. 6.5). Energies are given relative to that of the initial state of the isolated reactants* $[Ta_5O]^+$ *and* CH_4*; zero-point-energy (zpe)-corrected values are given in brackets. The spin state of the metal cluster is indicated as* μ *(the excess of majority spin electrons). Barrier configurations are shown in the upper row, and local minima are depicted in the bottom row. Two possible products of the dehydrogenated cluster complex are shown on the right. Ta atoms are depicted as blue spheres, carbon in gray, oxygen in red, and hydrogens as small white spheres.*